

The Pennsylvania State University
The Graduate School
Department of Materials Science and Engineering

**BISMUTH MAGNESIUM TITANATE – LEAD TITANATE THIN FILMS FOR HIGH
TEMPERATURE FERROELECTRIC MEMORY**

A Dissertation in
Materials Science and Engineering
by
Carl Sebastian Morandi

© 2018 Carl Morandi

Submitted in Partial Fulfillment
of the Requirements
for the Degree of

Doctor of Philosophy

December 2018

The dissertation of Carl Morandi was reviewed and approved* by the following:

Susan Trolier-McKinstry
Professor of Ceramic Science and Engineering
Dissertation Advisor
Chair of Committee

Clive A. Randall
Professor of Materials Science and Engineering

Thomas R. ShROUT
Emeritus Professor of Materials Science and Engineering

Douglas E. Wolfe
Professor of Materials Science and Engineering
Department Head of the Advanced Coatings at the Applied Research Laboratory

Suzanne Mohney
Professor of Materials Science and Engineering and Electrical Engineering
Chair, Intercollege Graduate Degree Program in Materials Science and Engineering

*Signatures are on file in the Graduate School

ABSTRACT

This work provides a comprehensive study on the development of $35\text{Bi}(\text{Mg}_{1/2}\text{Ti}_{1/2})\text{O}_3$ - 65PbTiO_3 thin films deposited by pulsed laser deposition, detailing the effects of processing variables on the film composition and resulting electrical properties. The primary application focus is on a potential high temperature ferroelectric layer for ferroelectric random access memory (FeRAM) devices. To assess whether 35BiMT - 65PT thin films are of interest for this application, the films were assessed by determining the switchable polarization, the dielectric properties and their thickness dependence, the high temperature polarization and dielectric properties, and the retention characteristics.

For pulsed-laser deposited 35BiMT - 65PT films on 36 nm thick PbTiO_3 or 16 nm thick 5 mol% La-doped PbTiO_3 seed layers, the processing window for developing a perovskite structure was found to be wide. Within the detection limits of x-ray diffraction, scanning electron microscopy and transmission electron microscopy, the films were found to be phase pure perovskite for growth temperatures from 600 °C to 700 °C at $\text{O}_2(90\%)/\text{O}_3(10\%)$ background pressures of 100-300 mTorr. Target compositions from 10 mol% to 85 mol% excess Pb produced phase pure perovskite films when depositing at 700 °C and a 10 Hz laser repetition rate.

The film composition was found to vary as a function of processing parameters. As the chamber pressure during deposition decreased, the film Mg and Pb concentration decreased, while the concentration of Bi increases. For films on 36 nm PbTiO_3 seed layers, the remanent polarization, P_r , increased 64% to $\approx 21 \mu\text{C}/\text{cm}^2$ and the polarization – electric field loops rotated counterclockwise as the deposition pressure increased from 60 mTorr to 340 mTorr. Decreasing

the seed layer thickness from 36 to 16 nm led to a decrease in P_r to $\approx 14 \mu\text{C}/\text{cm}^2$. Adjusting the target composition allowed the deposition of films which had near-stoichiometric Bi and Mg concentrations, but in all cases, the grown films were lead deficient. These films had remanent polarizations of 18 to $20 \mu\text{C}/\text{cm}^2$. If the lead content of the target was increased too far, the remanent polarization decreased, possibly due to the need to evolve more PbO from defective growth layers. Finally, the deposition rate showed no substantial effect on the film composition, but did have a significant impact on the ferroelectric properties. As the deposition rate decreased, the P_r increased to $\approx 22 \mu\text{C}/\text{cm}^2$ presumably due to enhanced crystalline quality and time for atomic rearrangement. At laser frequencies of 5 Hz, a Mg-rich pyrochlore phase begins to form and films showed a maximum $P_r \approx 22 \mu\text{C}/\text{cm}^2$. The optimal processing window for the maximum in ferroelectric properties shifts to higher PbO excess contents in the target as the deposition rate decreased. A film deposited at 5 Hz with a 65 mol% Pb, 20 mol% Bi, and 10 mol% Mg excess target had the maximum $P_r \approx 25 \mu\text{C}/\text{cm}^2$. The processing-composition behavior is explained via preferential adsorption of Bi on the A-site, which results in lead vacancies.

The dielectric, polarization and leakage properties of 35BiMT-65PT thin films with varying levels of A-site deficiency were investigated as a function of thickness and/or temperature. PbTiO_3 seed layers utilized to nucleate the perovskite phase in A-site deficient films induced a thickness dependence to the ferroelectric hysteresis and dielectric permittivity. Adjusting for this, the dielectric response of the 35BiMT-65PT films is ≈ 960 . The dielectric permittivity maximum was 430°C at 1 MHz for A-site deficient films. The transition temperature is independent of film thickness to 85 nm. $\text{Tan}(\delta)$ remains less than 15% at 1 MHz, regardless of film thickness and temperature up to 585°C . High temperature polarization-electric field hysteresis measurements show charge injection which is exacerbated on

increasing temperature, while PUND measurements show little temperature dependence of P_r up to temperatures of 200 °C. Poole-Frenkel emission dominated the high field leakage behavior. The refractive index measured by ellipsometry is 2.58 at 633 nm. All samples show significant retention loss. As the stoichiometry improves, retention improves such that >40% of the initial ΔP is retained over ≈ 280 min. at room temperature.

To remove the influence of the PbTiO_3 seed layers on the apparent thickness dependence of 35BiMT-65PT, films without a PbTiO_3 seed layer were deposited. Similar to their seed layer counterparts, seedless films show phase purity within the same target composition range investigated for films on seed layers. Phase pure films show somewhat reduced thickness dependent dielectric properties with respect to seeded films. P_r measured at 10 kHz for seedless films was $\approx 22\text{-}25 \mu\text{C}/\text{cm}^2$ until thicknesses of ≈ 200 nm and decreased to $15.5 \mu\text{C}/\text{cm}^2$ for films that were ≈ 100 nm thick. I-V measurements of seedless films deposited under nominally the same conditions as seeded films resulted in higher leakage compared to seeded films. Deposition under an Ar/O_2 atmosphere decreased the leakage behavior by up to five times. Films grown under the optimum 50% O_2 /50% Ar atmosphere demonstrate little temperature dependence in P_r up to 200 °C. As temperature increases, the DC dielectric breakdown strength of seedless films decreases faster compared to seeded films. Retention analysis shows similar behavior to that of seeded films.

TABLE OF CONTENTS

| | |
|---|------|
| List of Figures..... | viii |
| List of Tables..... | xv |
| Acknowledgements | xvi |
| Chapter 1 Introduction and Organization of Thesis..... | 1 |
| 1.1 Dielectrics and Ferroelectrics..... | 1 |
| 1.2 Dielectrics and Ferroelectrics..... | 4 |
| 1.3 References..... | 6 |
| Chapter 2 Literature Review | 8 |
| 2.1 Dielectrics and Ferroelectrics..... | 8 |
| 2.2 Perovskite Structure and Tolerance Factor..... | 13 |
| 2.3 Ferroelectric Random Access Memory..... | 21 |
| 2.4 Bi-Based Solid Solutions..... | 24 |
| 2.5 References..... | 35 |
| Chapter 3 Experimental Procedures..... | 40 |
| 3.1 PLD Target Processing..... | 40 |
| 3.2 PLD Substrate Processing..... | 41 |
| 3.3 PLD Processing..... | 43 |
| 3.4 Structural and Composition Characterization..... | 43 |
| 3.5 Electrical Characterization..... | 44 |
| 3.5.1 Ferroelectric Property Measurement and Retention..... | 44 |
| 3.5.2 Dielectric Property Measurements and I-V Measurements..... | 45 |
| 3.5.3 Optical Property..... | 47 |
| 3.6 References..... | 48 |
| Chapter 4 Influence of Processing on Composition, Microstructure and Ferroelectric Hysteresis..... | 49 |
| 4.1 Introduction..... | 49 |
| 4.2 35BiMT-65PT Thin Film Structure and Processing Window | 51 |
| 4.3 Deposition Pressure – Composition – Ferroelectric Property Relationships | 61 |
| 4.4 Target Composition – Ferroelectric Property Relationship..... | 65 |
| 4.5 Laser Deposition Rate – Film Composition – Ferroelectric Property Relationships..... | 67 |
| 4.6 Defect Chemistry..... | 70 |
| 4.6 Conclusions | 72 |
| 4.7 References..... | 73 |

| | | |
|------------|--|-----|
| Chapter 5 | Influence of A-site Deficiency and Thickness Scaling on Electrical Properties . | 78 |
| 5.1 | Introduction | 78 |
| 5.2 | Thickness dependence..... | 79 |
| 5.3 | Temperature Dependence..... | 83 |
| 5.4 | High Voltage/Temperature Leakage | 87 |
| 5.5 | Retention | 94 |
| 5.6 | Conclusions | 96 |
| 5.7 | References..... | 96 |
| Chapter 6 | Development of Seedless 35 Bi(Mg _{1/2} Ti _{1/2})O ₃ -65PbTiO ₃ Thin Films | 99 |
| 6.1 | Introduction | 99 |
| 6.2 | Seedless 35BiMT-65PT Thin Film Growth and Microstructure..... | 100 |
| 6.3 | Ferroelectric Hysteresis and Thickness Dependence of Seedless Thin Films..... | 106 |
| 6.4 | Controlling Defect Chemistry/Charge Injection in Seedless Films..... | 111 |
| 6.5 | High Temperature Leakage, Polarization and Retention of Seedless Films | 118 |
| 6.6 | Conclusions | 123 |
| 6.7 | References..... | 124 |
| Chapter 7 | Conclusions and Future Work | 125 |
| 7.1 | Conclusions | 125 |
| 7.2 | Future Work – Developing Relationships Between A-Site stoichiometry Control, Electrical Properties and Retention..... | 127 |
| 7.3 | Future Work – Control of A-Site Stoichiometry in BiMT-PT Films..... | 128 |
| 7.4 | Future Work – Other Bi-Based-PbTiO ₃ Compositions..... | 130 |
| 7.5 | Future Work – HfO ₂ -ZrO ₂ Ferroelectric Thin Films..... | 139 |
| 7.6 | References..... | 140 |
| Appendix A | Material Tolerance Factor and Cubic Transition Temperature | 142 |
| Appendix B | Refractive Index Estimation from High Temperature I-V Measurements..... | 145 |
| Appendix C | 35BiMT-65PT Thin Film Processing-Composition-Lattice Parameter-Property Relationships..... | 151 |

LIST OF FIGURES

- Figure 1.1 - Perovskite cubic transition temperature vs tolerance factor.²⁶ For reference, PbTiO_3 is marked. The tolerance factor was calculated based on radii determined by Shannon and Prewitt.²⁷ 3
- Figure 2.1 - Schematic dielectric permittivity vs frequency showing the four primary mechanisms that contribute to the relative dielectric permittivity. ¹ 10
- Figure 2.2 – Diagram showing the relationship between the 32 point groups and pyroelectric/ferroelectric properties³ 12
- Figure 2.3 – Polarization and relative dielectric permittivity vs electric field responses for (a) ideal linear and (b) ferroelectric dielectric. Data from a 1.7 μm thick PZT thin film sample was provided by Wanlin Zhu for (b). Description of P-E loop parameters from Jaffe.⁴ 13
- Figure 2.4 - An ideal cubic perovskite (ABO_3) unit cell. 14
- Figure 2.5 –(a) Lattice parameter and phase of a BaTiO_3 single crystal as a function of temperature.²⁷ (b) The dielectric permittivity of a BaTiO_3 ceramic as a function of temperature showing the dielectric anomaly at the phase transition temperatures.³⁰ 18
- Figure 2.6 – The dielectric permittivity, pyroelectric coefficient and spontaneous polarization of PbTiO_3 as a function of temperature.³¹ The abrupt change in the P_s at the Curie point shows the first order transition of PbTiO_3 . The P_s is calculated based on phenomenological theory.²⁹ 19
- Figure 2.7 – (a) Effect of grain size on the room temperature dielectric permittivity of BaTiO_3 .^{33, 34, 36, 38, 41} (b) Comparison of the dielectric permittivity vs temperature of a free standing single crystal, small grain sized ceramic, rigid film films and a flexible film. ^{33, 38–40, 42, 43} Figures (a) and (b) reproduced from reference.³³ 20
- Figure 2.8 – Effect of misfit strain on the phase diagram of BaTiO_3 .²⁵ 21
- Figure 2.9 – (a) Proposed ferroelectric translating device proposed by Ross for data storage.⁴⁷ Metal-ferroelectric-insulator-semiconductor (MFS) and metal-ferroelectric-metal-insulator-semiconductor (MFMS) FET FeRAM schematics (b) Schematic FeRAM structure with a similar design as that of a DRAM device.^{60, 61} 22
- Figure 2.10 – Schematic operation of an FeRAM device based on a 1 Transistor / 1 Capacitor (1T1C) design. (A)-(C) Application of a voltage showing the switching of a ferroelectric capacitor with a 1T1C design. In this case the ferroelectric starts in the down polarization and is switched to the up polarization state when the word and plate line voltages are applied. C_s , C_{bit} , and V_{dd} are the capacitance of the switched ferroelectric, the capacitance of the parasitic bit line and the power supply voltage, respectively ⁶² 23
- Figure 2.11 – MPB Curie temperature vs. end member tolerance factor in PbTiO_3 solid solutions.¹¹ The ionic radii are taken from Shannon and the ionic radius of Bi^{3+} in 12 coordination was extrapolated to be 1.34Å.^{11, 84} 26

- Figure 2.12 – Mole fraction of PbTiO_3 at the MPB of a solid solution vs the tolerance factor of the non- PbTiO_3 end member. Different data points correspond to different types of solid solutions (i.e. Pb, Bi, or a different cation on the A site and/or single/double cations on the B-site). The shaded region corresponds to the MPB for systems with Pb or Bi on the A-site of the non- PbTiO_3 end member.¹⁸ 27
- Figure 2.13 – Case 1 Bi-based- PbTiO_3 solid solutions showing a continuous decrease in T_c with decreasing PbTiO_3 . T_c vs composition data shown for $\text{Bi}(\text{Mg}_{3/4}\text{W}_{1/4})\text{O}_3$ (BMW) and $\text{Bi}(\text{Mg}_{2/3}\text{Nb}_{1/3})\text{O}_3$ (BMN) end members.⁸⁰ 28
- Figure 2.14 – Case 2 Bi-based- PbTiO_3 solid solutions showing a maximum in the T_c between the end members of the solid solution. T_c vs composition data shown for $\text{Bi}(\text{Mg}_{1/2}\text{Ti}_{1/2})\text{O}_3$ (BMT), BiInO_3 (BI), $\text{Bi}(\text{Ni}_{1/2}\text{Ti}_{1/2})\text{O}_3$ (BNT), $\text{Bi}(\text{Zn}_{2/3}\text{Nb}_{1/3})\text{O}_3$ (BZN), and BiScO_3 (BS).⁸⁰ 29
- Figure 2.15 – Case 3 Bi-based- PbTiO_3 solid solutions showing a continuous increase in the T_c as the PbTiO_3 concentration decreases. T_c vs composition data shown for BiFeO_3 (BF) and $\text{Bi}(\text{Zn}_{1/2}\text{Ti}_{1/2})\text{O}_3$ (BZT).^{78, 80} 29
- Figure 2.16 – (a) Phase diagram of BS-PT.⁸⁶ (b) Lattice parameter and c/a ratio for tetragonal BS-PT compositions.⁷⁷ 31
- Figure 2.17 - Phase diagram of the BiMT-PT system. Reported data (black squares⁸³, blue upward triangle⁸⁰, green down triangle⁸⁷, and purple diamond¹⁸) is based on combined high temperature X-ray diffraction, differential scanning calorimetry and dielectric vs temperature measurements. The blue line corresponds to a 2nd order polynomial fit as performed by Stringer et al., but for all known data. The shaded region corresponds to 3rd order polynomial fits and the uncertainty in the transition temperature. 33
- Figure 2.18 - BiMT-PT diagram replotted from Stringer et al.⁸⁰ The black line is the data fit according to Stringer's fitting parameters and the red line is the refitted data. The blue line corresponds a 2nd order polynomial fit to all reported data. 34
- Figure 3.1- Process flow diagram for developing PbTiO_3 solutions. 42
- Figure 3.2 – Film thickness vs solution molarity of PbTiO_3 seed layers. Thickness measurements were determined via scanning electron microscope cross section images..... 42
- Figure 3.3 – Schematic PUND pulse sequence (left) and resulting charges when the field is applied and removed (right). P^* and P_r^* refer to charges from the total switching current. P^\wedge and P_r^\wedge refer to charges not associated with ferroelectric switching. The difference between the “*” and “^” calculates ΔP . Ideally ΔP and ΔP_r are equal..... 45
- Figure 3.4 – Schematic diagram showing a cross-section of the home built high temperature probe station (top) and top-down view illustrating the microscope view (bottom). All samples were placed in the same position with respect to the bonded thermocouple. ... 47
- Figure 4.1 - (a) XRD patterns of films deposited between 40 and 400 mTorr background pressure. Peaks marked with a star come from the substrate. (b)-(c) STEM-HAADF image and STEM-HAADF image overlaid with color EDS elemental maps of elements of interest for a

film grown at a chamber pressure of 340 mTorr. The thin layer between the Pt and Bi maps corresponds to the PbTiO_3 seed layer. TEM samples and analysis were provided by Wes Auker and Jenn Gray..... 55

Figure 4.2 – TEM cross section of (a) 35BiMt-65PT deposited at 100 mTorr and (b) 60 mTorr oxygen (90%)/ozone (10%) pressure on 36 nm PbTiO_3 seed layers. Compared to Figure 4.1, the films show a reduced surface roughness with decreasing deposition pressure. (c) Shows the interface of the BiMT-PT showing the PT seed layer. Surface texture in (c) is expected to be due to beam damage at the very surface of the sample. The texture is only visible in STM-TEM mode. The bulk of the sample is undamaged by the beam. The very top of some samples have redeposited material / gallium induced defects. TEM samples and analysis were provided by Wes Auker and Jenn Gray. (d)-(e) AFM images of 35BiMT-65PT thin films deposited at 340 mTorr (d) and 60 mTorr (e) deposition background pressure.... 56

Figure 4.3 – (a) XRD patterns of samples deposited from a 10 mol% excess Pb target varying the deposition pressure from 100-300 mTorr. (b) XRD patterns of samples deposited from a 10 mol% excess Pb target varying the deposition temperature from 600 °C to 700 °C. 57

Figure 4.4 – (a) and (b) XRD patterns of room temperature deposited films at 160 mTorr and 100 mTorr, respectively. The films were crystallized between 700 °C and 760 °C. (c) Growth of 35BiMT-65PT from a 20Pb10Bi0Mg target (RTA crystallized film). The RTA crystallized film comes from a broken piece of the sample in (b) labeled 760 °C Large Piece..... 58

Figure 4.5 – XRD patterns of 35BiMT-65PT thin films deposited at room temperature for 45 seconds at chamber pressures of (a) 60 mTorr, (b) 80 mTorr, and (c) 100 mTorr. All films were crystallized between 700 °C and 760 °C as noted in the legend..... 59

Figure 4.6 – SEM images of 35BiMT-65PT RTA crystallized for 1 minute in flowing O_2 . The deposition pressures are 60, 80 and 100 mTorr from left to right. The deposition temperatures are 700 °C, 720 °C, 740 °C, and 760 °C from top to bottom respectively. 60

Figure 4.7 – Microstructure of a 700 °C film grown on top of the “seed” layer shown in Figure 4.6. The microstructure shows only perovskite grains where triangular grains, flat square-like grains, and long rectangular grains correspond to (111), (100)_c, and (110)_c oriented grains, respectively. 61

Figure 4.8 – (a) Ideal composition fraction without vs with adjusting to the Ti fraction as a function of the chamber background pressure in oxygen(90%)/ozone(10%). (a – right) ratio of species X, where X is Pb, Mg, or Bi as a function of chamber background pressure. The compositions are normalized to the Ti concentration. A stoichiometric composition would have the composition fractions for all cations equal to 1. (b) 1 kHz ferroelectric hysteresis response of 670-720 nm thick films with a 36 nm PbTiO_3 seed layer deposited between 60 and 340 mTorr. (c) PUND switching (P^*) and (d) non-switching (P^\wedge) charge with a 1ms pulse and 1 ms 0 V holds..... 64

Figure 4.9 - (a) Normalized composition of 600-700 nm films grown using a 16 nm PbTiO_3 seed layer. The BiMT-PT film was deposited using a 20Pb10Bi0Mg target on a 36 nm PbTiO_3 seed for composition analysis. The seed layer was avoided during the cross-sectional

- analysis. (b) Ferroelectric hysteresis (1kHz) response as a function of target composition (all on 16 nm seed). (c) Sample PUND data for ≈ 600 -700 nm thick films measured using 1 ms pulses and 1 ms 0 V holds. 66
- Figure 4.10 - (a) Composition of films deposited at laser pulse frequencies between 5 and 20 Hz. (b) Ferroelectric P-E hysteresis (1kHz) of films deposited between 1 and 20 Hz. 68
- Figure 4.11 – (a) HAADF-STEM image of cross-section from sample from 35BiMT-65PT deposited at 5 Hz using a 48Pb20Bi10Mg target at 340 mTorr. Dark regions correspond to a Pb/Bi deficient secondary phase. (b) Mg quantitative EDS elemental map (atomic %). (c) Pb quantitative elemental EDS map (atomic %). Yellow circles highlight regions with decreased Pb concentrations. (d) Combined Pb and Mg elemental maps showing the overlap between Pb deficient regions and Mg rich regions. 69
- Figure 4.12 - Ferroelectric P-E hysteresis (1kHz) of films deposited between 10 Hz and 5 Hz laser frequency with varying target compositions. 70
- Figure 5.1 - Ferroelectric P-E (a) and PUND (b) of 35BiM-65PT thin films grown on 16 nm 5 mol% La doped-PbTiO₃ seed layer as a function of thickness. The reported thickness is the total film thickness (seed and grown film). 80
- Figure 5.2 - (a) $1/C_{\text{total}}$ vs thickness plot showing the capacitor in series relationship for seeded 35BiMT-65PT thin films. (b) Adjusted film ϵ_r vs total thickness 82
- Figure 5.3 - Switching (P^*) and non-switching (P^\wedge) charges vs the effective electric field across the BiMT-PT film of varying thickness. The effective field was calculated assuming the % voltage drop in the dielectric measurements is constant at all fields and then recalculating the new electric field..... 83
- Figure 5.4 - (a) ϵ_r vs. temperature for a 582 nm thick film. (b) ϵ_r vs. temperature for an 85 nm thick film. (c) ϵ_r vs temperature for films deposited using targets of different compositions. The values refer to the mol% excess of each cation added to the target. Permittivity measurements are at 1 MHz with a 30 mV excitation. Film thicknesses are 582 nm (squares) and 632 nm (circles). (d) a variety of film thicknesses showing the thickness independence of T_{max} in 35BiMT-65PT thin films 85
- Figure 5.5- (a) High temperature P-E response for a ≈ 600 nm 35BiMT-65PT thin film. (b) Corresponding PUND for the negative polarization state vs. temperature showing temperature independence up to 200 °C..... 87
- Figure 5.6 - (a) I-V measurement of 35BiMT-65PT thin films deposited under various deposition pressures. (b) Calculated refractive index based on linear fits using Poole-Frenkel and Schottky models vs deposition pressure. (c) Measured refractive index based on ellipsometry models.^{29,30} 91
- Figure 5.7 - (a)-(b) I-V measurement of 35BiMT-65PT thin films deposited at (a) 100 mTorr and (b) 340 mTorr. (c) Calculated refractive index based on linear fits using Poole-Frenkel and Schottky models for films grown at different deposition pressures. See appendix for fitted data in part (c)..... 92

- Figure 5.8 – ψ and Δ data and fits of 35BiMT-65PT on SrTiO₃. See chapter 3 for growth conditions..... 93
- Figure 5.9 - I-V measurement of a 582 nm 35 BiMT-65PT deposited on a 16 nm 5 mol% La doped PbTiO₃ seed layer. The I-V measurements were done on 50 μ m electrodes. For comparison, the positive polarity measurements from a film deposited on 36 nm PbTiO₃ seeds are included in solid lines..... 93
- Figure 5.10 – Estimated trap energy level calculated from I-V vs T measurements. 94
- Figure 5.11 – Room temperature retention of 580-630 nm 35BiMT-65PT thin films as a function of target composition. Retention analysis was done with 300 kV/cm and 1 ms pulses. (a) The overall switching response. (b) The switching charge. (c) The non-switching charge. 95
- Figure 6.1 – SEM of the etched platinum surface after depositing 35BiMT-65PT at 340 mTorr, 700 °C, 6 cm target to substrate distance, 340 mTorr O₂/O₃, and 10 Hz. The targets utilized are (a) 20Pb10Bi0Mg and (b) 30Pb15Bi5Mg..... 101
- Figure 6.2 - XRD patterns of 35 BiMT-65PT 600-650 nm thick thin films deposited using the same target compositions as seeded growth. 102
- Figure 6.3 - XRD patterns of 35 BiMT-65PT 100-700 nm thick thin films deposited using the 48Pb20Bi10Mg composition target..... 103
- Figure 6.4 – (a) XRD patterns of 35 BiMT-65PT 580-630 nm thick films deposited with varying O₂/Ar background gas mixtures. Films were deposited from the 48Pb20Bi10Mg target at 340 mTorr and constant mass flow rate 50 sccm. (b) XRD patterns of 35BiMT-65PT \approx 670 nm – \approx 720 nm thick films deposited on 36 nm PbTiO₃ between 60 mTorr and 340 mTorr background deposition pressure (90% O₂/10% O₃). Films were deposited from a 20Pb10Bi0Mg target. 105
- Figure 6.5 – Ferroelectric hysteresis of seedless 35BiMT-65PT thin films as a function of target composition at 1 kHz frequency, 250 kV/cm applied field (a), and 500 kV/cm (b). (c) Sample PUND data measured using 1 ms pulses and 1 ms 0 V holds. 107
- Figure 6.6 – (a) $1/C_{\text{total}}$ vs thickness plot showing the capacitor in series relationship for seedless 35BiMT-65PT thin films. (b) ϵ_r vs thickness comparison between seeded 35BiMT-65PT and seedless 35BiMT-65PT thin films. (c) Adjusted vs total film ϵ_r vs thickness..... 109
- Figure 6.7 – Thickness dependence of ferroelectric hysteresis at 10 kHz for (a) 5 mol% La-doped PbTiO₃ seeded 35BiMT-65PT thin films and (b) Unseeded 35BiMT-65PT thin films .. 110
- Figure 6.8 - Thickness dependence of ferroelectric hysteresis at 1 kHz for (a) 5 mol% La-doped PbTiO₃ seeded 35BiMT-65PT thin films and (b) Unseeded 35BiMT-65PT thin films. . 111
- Figure 6.9 - Thickness dependence of ferroelectric PUND with 1 ms pulses and 0V hold times for (a) 5 mol% La-doped PbTiO₃ seeded 35BiMT-65PT thin films and (b) Unseeded 35BiMT-65PT thin films..... 111

- Figure 6.10 – Ferroelectric hysteresis (1kHz) of seedless films as function O₂/Ar background deposition gas mixture at 300 kV/cm (a) and 500 kV/cm (b). (c) Remanent polarization as a function of oxygen concentration measured at 300 kV/cm. 114
- Figure 6.11 – PUND measurements as a function of electric field and oxygen concentration of seedless 35BiMT-65PT thin films. (b) and (c) Corresponding P* (switching) and P[^] (non-switching) charges, respectively. 115
- Figure 6.12 – Room temperature I-V measurement of 35BiMT-65PT thin films deposited under various O₂/Ar atmospheres during growth. The solid lines are data taken from 36 nm PbTiO₃ seeded 35BiMT-65PT films from Chapter 5. The seeded film data provides the maximum difference in leakage values seen in Chapter 5. 116
- Figure 6.13 – I-V vs temperature measurements of a seedless 35BiMT-65PT thin film deposited under a 50% O₂ / 50% Ar background gas atmosphere. 119
- Figure 6.14 – (a) High temperature P-E of a seedless 35BiMT-65PT thin films at 10 kHz. The seedless film was deposited using a 50% O₂ / 50%Ar deposition background gas atmosphere. P-E is normalized at the maximum in electric field. (b) Corresponding P_r vs temperature as a function of electric field for the 35 BiMT-65Pt thin film. The P_r was determined from PUND measurements with 1 ms pulses and 1 ms 0V hold periods. ... 120
- Figure 6.15 – (a) Room temperature retention of the optimized seedless 35 BiMT-65PT thin film. Same state retention at 85 °C of the optimized seedless 35 BiMT – 65 PT thin film. The retention analysis was done at 300 kV/cm and 1 ms pulses / 0 V holds. 122
- Figure 7.1 – I-V measurement of a 200 nm 20BiMT-80PT thin film by Zhang et al. (in supplemental section of the paper).² 130
- Figure 7.2 – XRD patterns of 20BiZT-80PT thin films deposited on 5 mol% La-doped PbTiO₃ seed layers. The film thickness varied from ≈580 nm – 630 nm..... 133
- Figure 7.3 – STEM-HAADF images of 20 BiZT-80PT thin films at low (a) and high magnification (b). Yellow circles identify secondary phases in the film near the electrode interface. (c) Elemental maps of Bi, Pb and Zn at high magnification showing the contrast in composition between the BiZT-PT film and the secondary phases..... 134
- Figure 7.4 – Dielectric permittivity and loss tangent vs Target Zn excess (mol%) of 20BiZT-80PT thin films. Thin film thickness varied between 580 nm – 630 nm..... 135
- Figure 7.5 – (a) Dielectric permittivity and loss tangent vs temperature of a 610 nm thick 20BiZT-80PT thin film. (b) Comparison of ε_r vs temperature between 35BiMT-65PT and 20BiZT-80PT. (c) Comparison of tan(δ) vs temperature between 35BiMT-65PT and 20BiZT-80PT 136
- Figure 7.6 – (a) Ferroelectric hysteresis of 20BiZT-80PT thin films at 10 kHz as a function of the excess Zn in the targets. (b) Corresponding PUND measurements on the negative polarization state from with 1 ms pulses and 1 ms 0V holds..... 138

Figure 7.7 – Total charge (P^*) on the positive polarization state during the PUND measurement in
Figure 7.6 (b) as a function to the target Zn excess..... 139

LIST OF TABLES

| | |
|---|-----|
| Table 2.1 - 2 nd order polynomial fits: $a + bx + cx^2$ where “a” is assumed to be the PbTiO ₃ Curie transition temperature of 495 °C. The predicted $T_{c,max}$ composition and $T_{c,max}$ are provided for each fitting. | 33 |
| Table 3.1 – List of target compositions investigated throughout this thesis. | 41 |
| Table 3.2 - Deposition parameters for growing 35BiMT-65PT on single crystal SrTiO ₃ substrates. | 47 |
| Table 3.3 - SrTiO ₃ fitted Sellmeier model parameters. Parameter correlation was less than 0.9 for fitted parameters. | 48 |
| Table 4.1 - List of target compositions investigated. | 65 |
| Table 5.1 - Compositions of films as a function of deposition pressure. The compositions were normalized such that the Ti concentration equals the ideal concentration. The oxygen concentration was calculated assuming typical valences for each cation. | 88 |
| Table 5.2 - 35BiMT-65PT fitted Sellmeier model parameters. Parameter correlation was less than 0.9 for fitted parameters. | 90 |
| Table 7.1 – Process parameters for growing 20BiZT-80PT thin films. | 132 |

ACKNOWLEDGEMENTS

First and foremost, I would like to thank my advisor Prof. Susan Troler-McKinstry for the last four years of guidance and patience in my journey through this program. It astounds me and many of those that I know just how much she gives to each student that works under her even with the large size of her group. In my experience, most advisors either cannot or chose not to devote their time to their students to the same degree. During my transition after finishing my Masters in the Messing group, there was a time I thought I may not be able to continue through the Ph.D. program. Prof. Troler-McKinstry was kind enough to take a chance on me. I cannot be thankful enough for the opportunity I was given.

The work provided in this thesis would not have been possible without Texas Instruments who funded the project. In addition, I appreciate all of the monthly technical discussions with my partners at Texas Instruments: Kezhakkedath Udayakumar, John Rodriguez, and Bhaskar Srinivasan. All of you were very encouraging to me and helped shape the last part of my graduate career. You were all very patient with me even when the research hit snags and focused on subjects not directly related to what you wanted out of it.

Due to the time that I have been at Penn State, there may not be a single person that I have met between 2011 and 2018 that should not be acknowledged. One of my goals when I first became a graduate student was to be a jack of all trades. I wanted to broaden my knowledge. To that end I worked with almost every equipment staff member that was even tangentially related to my research at one point or another. Thus, I would like to acknowledge the staff members in the Materials Science and Engineering Department, Materials Research Institute (MRI), and the Materials Characterization Laboratory for all of the help on the various research projects I took on. Wes Auker, Jenn Grey, and Trevor Clark all provided direct contributions to my work in this thesis and provided guidance to me in both SEM and TEM characterization. Nicole Wonderling and Gino Tambourine helped me numerous times with structure analysis. They were also relatively “understanding” of my “different” work

schedule. The entire nanofabrication staff helped me with one problem or another at some point. Whether it was Mike Labella and Kathleen Gehoski helping me with lithography or finding a transparent sample that fell on the floor, or Bill Drawl and Beth Jones dealing with me calling them late at night because something went wrong with the sputter tool, they all always helped. Numerous times Guy Lavallee and Bill provided me with the vacuum knowledge I needed to take care the PLD lab. Beth Jones and Amanda Baker both provided me with ceramic processing knowledge and equipment I needed for all the research I have done. Eric Sagmuller and Tim Klinger helped me countless times with various tool building, tool repair, and equipment set up. They have helped keep my research on schedule as well as the rest of the Trolier-McKinstry group. Finally, I would like to thank Jeff Long, Steve Perini, and Sarah Eichfeld. Jeff and Steve both provided me with a much deeper understanding of all of the electronic equipment I used for processing and electrical measurements. Sarah and Jeff have help kept me safe during the most dangerous parts of my work here such as rebuilding the PbO rapid thermal annealing furnace.

My time at Penn State spans both my Masters and PhD. I have been fortunate to have been able to work with Prof. Messing and Prof. Trolier-McKinstry's groups during my time here. I would not be where I am if it were not for all of the guidance, science discussions, kindness and friendship everyone has given to me. I thank Stephen Potelerala, Ozgur Ozer, Yunfei Change, and Prof. Messing for getting through my Masters and on my way to my Ph.D. I also thank Dan Marincel, Adarsh Rajashekhar Ryan Keech, Smith Shetty, Jonathon Bock, Betul Akkopru, Trent Borman, Lyndsey Denis, Dixion Wang, Jason Chan, Margeaux Wallace, Aaron Welsh, Song Won Ko, Charley Yeager, Hong Goo Yeo, Lizz Michael, Tianning Liu, Christopher Cheng, Kathleen Coleman, Leonard Jacques, Nicole Kirchner-Hall, Jung In Yang, Wanlin Zhu, and Lauren Garten, from the STM group. Outside of my research groups, I had the distinct pleasure to work with numerous other graduate students that I both taught and learned from. I thank Xuan Liu, Bi-Cheng Zhou, Richard Otis, Austin Ross, Cassie Marker, Welley Loc, Brian Vanleeuwen, Jason Britson, Katie Kragh-Beutow, Brian Babcox, Brian Zakrzewski, Jason Lapano, Ryan

Haislmaier, Neal Kelly, James Kally, Seth Berbano and many others. Besides the science, many of you also took part in the weekly game nights that Stephen Potelerala started and I continued almost every Saturday during my time here. I cherish my memories of all the crazy board and video games we played as we got our minds off of work.

Last and certainly not least I would like to thank my family back home and my family in the Penn State Martial Arts Group. My father, step mother, and little brother have been continuously supportive of me and have wished nothing, but the best for me in my life. They have loved me a great deal and have missed me every day that I have been in Pennsylvania. My time with my PSMAG family has been worthwhile and quite the learning experience in life lessons. While I consider everyone I know in PSMAG part of my family, I give special thanks to Master Mike Kaye, Anthony Guidotti, Susan Nahvi, Adam Bolotsky, Marissa Hartleb, and Wenxin Chen for all the support in my times of need as I have narrowly missed going mentally insane over these years. I am forever indebted to each of you.

Chapter 1

Introduction and Organization of Thesis

1.1 Dielectrics and Ferroelectrics

Technological development necessitates both improvements in established materials and development of the next generation of materials. For over half a century, researchers have overseen significant improvements in transistors. In recent years, technological development has focused on the scaling, reliability, and multifunctionality of integrated circuits.

In the same way, ferroelectrics are a class of material with an array of applications, including capacitors, pyroelectrics, electrooptics, ultrasonic transducers, energy harvesters, microelectromechanical devices, ferroelectric random access memory (FeRAM) and many more.¹⁻¹² However, some of these technologies are materials limited (e.g. by the magnitude of the property coefficients, the temperature/stress/voltage range required for operation, or by property degradation on scaling). In order to move beyond current limitations, new designs and/or materials are required. As new materials are identified, the processing-microstructure-property relationships must be explored to determine feasibility for large scale production.

A decade after the discovery of BaTiO₃, ferroelectric memory devices were conceived in the 1950's at Bell Laboratories and IBM.¹³⁻¹⁷ Significant interest was generated for these non-volatile memory based devices due to their resistance to radiation. However, the technology was plagued by a combination of inadequate materials (e.g. hygroscopic KNO₃), inadequate localization of switching due to the electrode patterns employed, and the large sample thicknesses utilized (causing large driving voltages and slow read/write speeds). However, in the

1980's significant developments were made in producing $\text{Pb}(\text{Zr,Ti})\text{O}_3$ thin films through chemical solution deposition and sputtering. This solved two problems, first allowing the growth of thin films for low driving voltages, and second introducing an inert material with sufficiently low and sharp coercive field (E_c) and large remanent polarization (P_r). Since then, PZT and $\text{SrBi}_2\text{TaO}_9$ (SBT) ferroelectric memories have been commercialized due to significant engineering developments in terms of processing technique, processing temperature, choice of electrodes, and choice of dopants.¹⁸⁻²² However, current state of the art FeRAM devices are limited to a usage temperature 85°C for a 10 year life time due to imprint failure.^{20, 23}

The high temperature limitation of FeRAM devices prompted a search for ferroelectric materials which surpass the current state-of-the-art FeRAM. One means of improving the usage temperature is to utilize a ferroelectric with a transition temperature exceeding that of PZT or SBT. The tolerance factor may be used as a guide for determining candidate materials. The tolerance factor is a geometric measure of the stability of the cubic perovskite phase.^{24, 25} Figure 1.1 shows a plot of perovskite candidate materials vs. the perovskite tolerance factor.²⁶ It is observed that as the tolerance factor deviates from 1, the transition temperature increases. However, there are not many pure materials with transition temperatures above that of PbTiO_3 . Those that utilize cations which have multiple valences allow for electron hopping conduction. Ferroelectric memory devices require low leakage due to their nature of detecting the charge of capacitors to determine 0 and 1 bits. The mixture of leakage and ferroelectric switching currents

makes it difficult to determine these different states. Thus, these types of materials are not viable options to replace PZT or SBT.

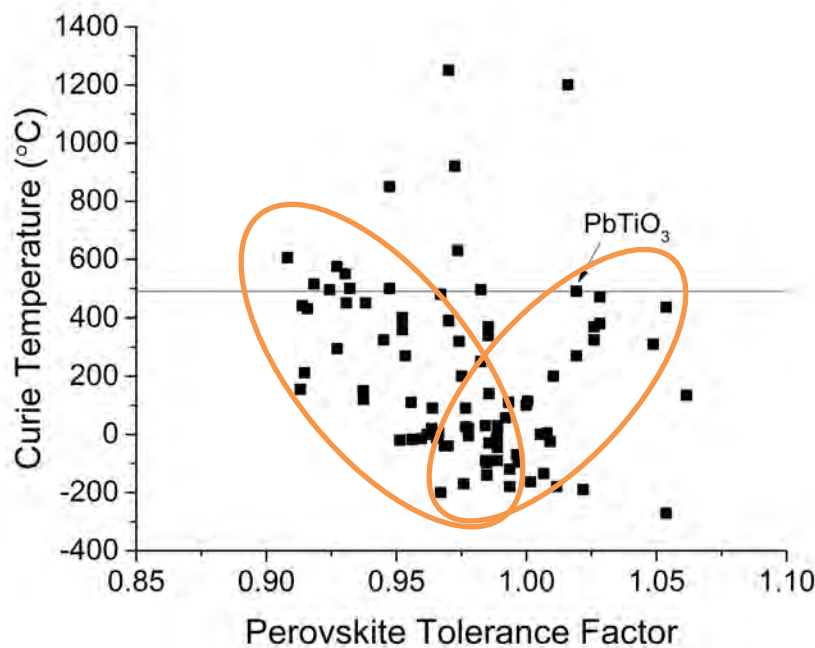


Figure 1.1 - Perovskite cubic transition temperature vs tolerance factor.²⁶ For reference, PbTiO_3 is marked. The tolerance factor was calculated based on radii determined by Shannon and Prewitt.²⁷

Eitel *et al.* utilized the perovskite tolerance factor to predict solid solutions with T_c 's greater than that of PZT.²⁵ They predicted a series of Bi-based PbTiO_3 solid solutions which significantly increased T_c 's above that of PZT or PbTiO_3 . This discovery offers new possibilities for FeRAM technology. One promising material system is the $\text{Bi}(\text{Mg}_{1/2}\text{Ti}_{1/2})\text{O}_3$ - PbTiO_3 solid solution with a maximum transition temperature of ≈ 525 - 535 °C.

To integrate such materials into devices, this thesis discusses the various processing-microstructure-properties for developing $\text{Bi}(\text{Mg}_{1/2}\text{Ti}_{1/2})\text{O}_3$ - PbTiO_3 thin films. The following section describes the organization of this thesis.

1.2 Dielectrics and Ferroelectrics

This thesis provides a comprehensive study on the development of $35\text{Bi}(\text{Mg}_{1/2}\text{Ti}_{1/2})\text{O}_3$ - 65PbTiO_3 thin films deposited by pulsed laser deposition. The primary application focus is on a potential high temperature ferroelectric layer for FeRAM. In order to assess the feasibility of 35BiMT - 65PT as a high temperature FeRAM material, several key aspects were investigated:

- High temperature polarization and dielectric properties
- The switchable polarization and dielectric thickness dependence
- The retention characteristics

Chapter 2 provides a review of relevant background literature. First, a brief introduction on dielectrics is provided. Second, FeRAM technology history, design and material properties are reviewed. Finally, Bi-based perovskite solid solutions are discussed extensively.

Chapter 3 discusses the experimental procedures and characterization techniques utilized in this thesis.

Chapter 4 discusses the development of 35BiMT - 65PT thin films through a series of experiments which explore the processing window of 35BiMT - 65PT . The film composition and microstructure was studied using scanning tunneling electron microscopy and energy dispersive x-ray spectroscopy. Relationships between the processing-composition-ferroelectric properties were examined. Based on these relationships a defect mediated model is proposed to explain the composition of these films. Parts of this chapter have been published in Transactions on Ultrasonics, Ferroelectrics, and Frequency Control.

Chapter 5 discusses the implications of A-site deficiency and thickness scaling on the electrical properties of 35BiMT - 65PT thin films. Films exhibited thickness dependent

ferroelectric and dielectric properties due to the PbTiO_3 seed layer present. A-site deficient films exhibited a T_{max} maximum at 430°C at 1 MHz which increases as stoichiometry improves. The transition temperature is independent of film thickness to at least 85 nm. High temperature polarization-electric field loops and positive up negative down (PUND) measurements demonstrate little dependence of remanent polarization to 200°C , but show significant charge injection with increasing temperature. Leakage measurements at high electric fields agree with Poole-Frenkel emission. Refractive index measurements measured with ellipsometry agree with the refractive index calculated from the Poole-Frenkel emission model. Parts of this chapter have been published in Transactions on Ultrasonics, Ferroelectrics, and Frequency Control.

Chapter 6 discusses the growth and electrical properties of 35BiMT-65PT thin films without the use of a PbTiO_3 seed layer. Removing the PbTiO_3 seed layer was done to limit the thickness dependent properties of the thin films. Phase pure films show reduced thickness dependent properties with respect to seeded films. I-V measurements of seedless films deposited under nominally the same conditions as seeded films resulted in higher leakage. Deposition under an Ar/O_2 atmosphere changed the leakage behavior of 35BiMT-65PT thin films. Films grown under the optimum $50\%\text{O}_2/50\%\text{Ar}$ atmosphere demonstrate little temperature dependence in P_r up to 200°C , as well as similar leakage behavior as seeded films. Retention of seedless 35BiMT-65PT thin films is equivalent to seeded films at room temperature, but drastically decreases with increasing temperature due to defects present.

Chapter 7 provides a summary of conclusions and potential future on the 35BiMT-65PT system and other systems.

1.3 References

- 1 T. Fujii and S. Watanabe, "Feedback Positioning Cantilever Using Lead Zirconate Titanate Thin Film for Force Microscopy Observation of Micropattern," *Appl. Phys. Lett.*, **68** [4] 467 (1996).
- 2 F. Griggio, C.E.M. Demore, J. Gigliotti, T.N. Jackson, R.L. Tutwiler, S. Cochran, and S. Trolrier-McKinstry, "Micromachined Diaphragm Transducers for Miniaturised Ultrasound Arrays," pp. 1–4 in *2012 IEEE Int. Ultrason. Symp.* IEEE, 2012.
- 3 J. Baborowski, N. Ledermann, and P. Muralt, "Piezoelectric Micromachined Ultrasonic Transducers Based on PZT Films," *Mat. Res. Soc. Symp. Proc.*, **741** J12.4.1-J12.4.5 (2003).
- 4 S.P. Beeby, M.J. Tudor, and N.M. White, "Energy Harvesting Vibration Sources for Microsystems Applications," *Meas. Sci. Technol.*, **17** [12] R175–R195 (2006).
- 5 P.D. Mitcheson, E.K. Reilly, T. Toh, P.K. Wright, and E.M. Yeatman, "Performance Limits of the Three MEMS Inertial Energy Generator Transduction Types," *J. Micromechanics Microengineering*, **17** [9] S211–S216 (2007).
- 6 J.J. Bernstein, S.L. Finberg, K. Houston, L.C. Niles, H.D. Chen, L.E. Cross, K.K. Li, and E. Udayakumar, "Micromachined High Frequency Ferroelectric Sonar Transducers," *IEEE Trans. Ultrason. Ferroelectr. Freq. Control*, **44** [5] 960–969 (1997).
- 7 N. Ledermann, J. Baborowski, A. Seifert, B. Willing, S. Hiboux, P. Muralt, N. Setter, and M. Forster, "Piezoelectric Cantilever Microphone for Photoacoustic Gas Detector," *Integr. Ferroelectr.*, **35** [1–4] 177–184 (2001).
- 8 Y. Nemirovsky, A. Nemirovsky, P. Muralt, and N. Setter, "Design of Novel Thin-Film Piezoelectric Accelerometer," *Sensors Actuators A Phys.*, **56** [3] 239–249 (1996).
- 9 D.M. Newns, B.G. Elmegreen, X.-H. Liu, and G.J. Martyna, "High Response Piezoelectric and Piezoresistive Materials for Fast, Low Voltage Switching: Simulation and Theory of Transduction Physics at the Nanometer-Scale.," *Adv. Mater.*, **24** [27] 3672–7 (2012).
- 10 D.M. Newns, B.G. Elmegreen, X.-H. Liu, and G.J. Martyna, "The Piezoelectronic Transistor: A Nanoactuator-Based Post-CMOS Digital Switch with High Speed and Low Power," *MRS Bull.*, **37** [11] 1071–1076 (2012).
- 11 R. Kandilian, A. Navid, and L. Pilon, "The Pyroelectric Energy Harvesting Capabilities of PMN–PT Near the Morphotropic Phase Boundary," *Smart Mater. Struct.*, **20** [5] 55020 (2011).
- 12 G. Teowee, J.T. Simpson, T. Zhao, M. Mansuripur, J.M. Boulton, and D.R. Uhlmann, "Electro-Optic Properties of Sol-Gel Derived PZT and PLZT Thin Films," *Microelectron. Eng.*, **29** [1–4] 327–330 (1995).
- 13 D.H. Looney, Semiconductive Translating Device, U.S. Patent 2 791 758, 1957.
- 14 W.L. Brown, Semiconductive Device, U.S. Patent 2 791 259, 1957.
- 15 I.M. Ross, Semiconductive Translating Device, U.S. Patent 2 791 760, 1957.
- 16 J.A. Morton, Electrical Switching and Storage, U.S. Patent 2 791 761, 1957.
- 17 Y. Arimoto and H. Ishiwara, "Current Status of Ferroelectric Random Access Memory," *MRS Bull.*, 823–828 (2004).
- 18 S. Kawashima and J.S. Cross, "FeRAM," pp. 279–328 in *Embed. Memories Nano-Scale VLSIs*. 2009.
- 19 H. Ishiwara, "Ferroelectric Random Access Memories," *J. Nanosci. Nanotechnol.*, **12** 7619–7627 (2012).
- 20 J. Rodriguez, K. Remack, J. Gertas, L. Wang, C. Zhou, K. Boku, K.R. Udayakumar, S. Summerfelt, T. Moise, D. Kim, J. Groat, J. Eliason, M. Depner, and F. Chu, "Reliability of Ferroelectric Random Access Memory Embedded within 130nm CMOS," pp. 750–758 in *Reliab. Phys. Symp. (IRPS), 2010 IEEE*. 2010.
- 21 K.R. Udayakumar, T. San, J. Rodriguez, S. Chevacharoenkul, D. Frystak, J. Rodriguez-Latorre, C. Zhou, M. Ball, P. Ndai, S. Madan, H. McAdams, S. Summerfelt, and T. Moise, "Low-Power

- Ferroelectric Random access Memory Embedded in 180nm Analog Friendly CMOS Technology,” *2013 5th IEEE Int. Mem. Work. IMW 2013*, 128–131 (2013).
- 22 D.C. Yoo, B.J. Bae, D.H. Im, S.O. Park, H.S. Kim, J.T. Moon, and B.I. Ryu, “Highly Reliable 50nm-thick PZT Capacitor and Low Voltage FRAM Device using Ir/SrRuO₃ /MOCVD PZT Capacitor Technology,” pp. 148–149 in *Symp. VLSI Technol.* 2005.
- 23 N. Inoue and Y. Hayashi, “Effect of Imprint on Operation and Reliability of Ferroelectric Random Access Memory (FeRAM),” *IEEE Trans. Electron Devices*, **48** [10] 2266–2272 (2001).
- 24 V.M. Goldschmidt, “Die Gesetze der Krystallochemie,” *Naturwissenschaften*, **14** [21] 477–485 (1926).
- 25 R.E. Eitel, C.A. Randall, T.R. Shrout, P.W. Rehrig, W. Hackenberger, and S.-E. Park, “New High Temperature Morphotropic Phase Boundary Piezoelectrics Based on Bi(Me)O₃-PbTiO₃ Ceramics,” *Jpn. J. Appl. Phys.*, **40** 5999–6002 (2001).
- 26 M.E. Lines and A.M. Glass, *Principles and Applications of Ferroelectrics and Related Materials*. Oxford University Press, 1977.
- 27 R.D. Shannon, “Revised Effective Ionic Radii and Systematic Studies of Interatomic Distances in Halides and Chalcogenides,” *Acta Cryst.*, **A32** 751–767 (1976).

Chapter 2

Literature Review

2.1 Dielectrics and Ferroelectrics

Electroceramics are a class of materials whose varied functionalities make them useful in many device applications. The properties can be tailored to specific functionalities, including conduction, magnetism, superconductivity, and ferroelectricity. Electroceramics cover the electrical property gambit as conductors, semiconductors and insulators, depending on their composition and defects. For the purposes of this thesis, an insulating ferroelectric material was required. Hence, this background starts with a number of the key factors that describe the properties of ferroelectric films.

For example, dielectric permittivity describes the response when an electric field is applied to an insulator, wherein instead of conducting, it polarizes due to a separation of positive and negative charge centers within the crystals. The separated charge can be described by the dielectric displacement D :¹

$$D = \epsilon_0 E + P \quad \text{Eq. 2.1}$$

E is the electric field, P is the polarization density, and ϵ_0 is the permittivity of free space. Many insulators are linear dielectrics, where their dielectric permittivity does not change with the field.¹ Thus, the dielectric displacement and polarization can be written as:¹

$$D = \epsilon_0 E + \chi_c \epsilon_0 E = (1 + \chi_c) \epsilon_0 E \quad \text{Eq. 2.2}$$

$$P = \epsilon_0 \chi_c E = \epsilon_0 (\epsilon_r - 1) E \quad \text{Eq. 2.3}$$

where χ_c is the dielectric susceptibility and ϵ_r is the relative permittivity. If the dielectric susceptibility is very large, then the polarization is simplified to:¹

$$P \sim \epsilon_r \epsilon_0 E \quad \text{Eq. 2.4}$$

Much of the work in this thesis studies the induced dielectric permittivity and polarization responses of materials with large relative permittivities.

The dielectric permittivity is a complex property which can be expressed as:

$$\varepsilon_r^* = \varepsilon_r' + \varepsilon_r'' \quad \text{Eq. 2.5}$$

where ε_r' is the real and ε_r'' is the imaginary components of the complex permittivity.¹ For an ideal capacitor under an alternating field, the current and voltage are 90° out of phase.¹ During charging, the current is 0 and the voltage is maximum. Conversely, the voltage is 0 during discharging and current is maximum. However, the phase angle of actual dielectrics is not 90° due to losses either from conduction or internal dissipation of the capacitor.¹ The lossiness of a dielectric is often described by the loss tangent $\tan \delta$:

$$\tan(\delta) = \frac{\varepsilon_r''}{\varepsilon_r'} \quad \text{Eq. 2.6}$$

The four primary mechanisms that contribute dielectric polarization are electronic, ionic, dipolar (orientation), and space charge polarizability.¹ All materials experience electronic polarization due to the displacement of the electronic clouds with respect to the nucleus. Ionic polarization arises due to the displacement of ions from their equilibrium positions in the crystal, creating dipoles due to an applied field. Dipolar polarization occurs when pre-existing dipoles within the material change their orientation under an applied field. Finally, space charge is related to long-range carrier migration under a field until the carrier is blocked by an insulating interface. Each of these mechanisms contributes to the net dielectric response up until the AC frequencies at which the mechanism can no longer keep up with the field, as seen in Figure 2.1. When the field exceeds the response frequency (either a resonance or a

relaxation depending on whether or not there is a restoring force), there is a maximum in the imaginary component of the dielectric response.

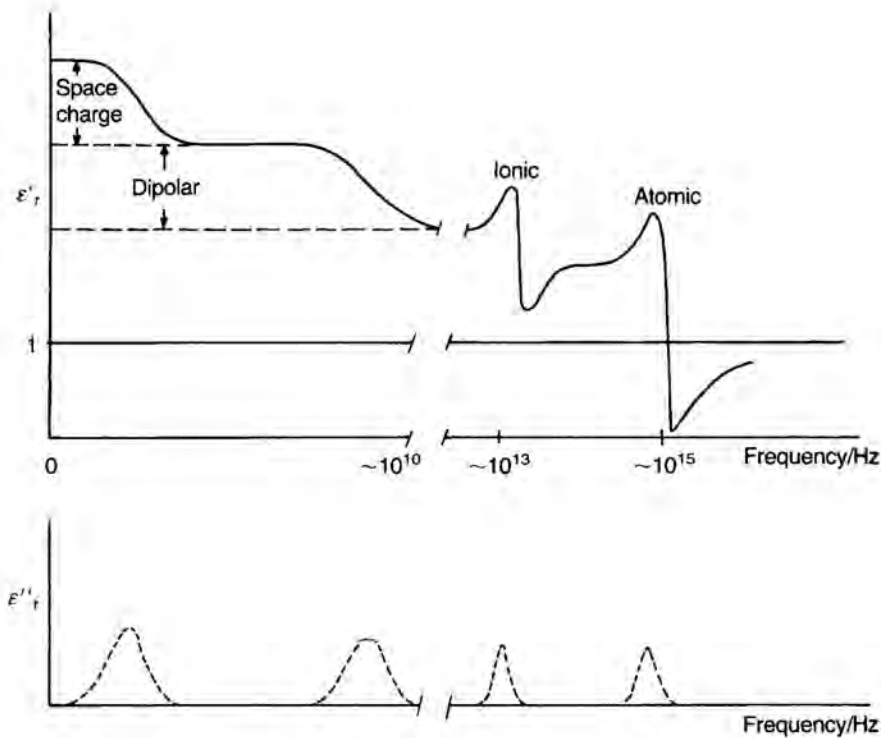


Figure 2.1 - Schematic dielectric permittivity vs frequency showing the four primary mechanisms that contribute to the relative dielectric permittivity.¹

Not all materials exhibit all of the polarization mechanisms. For instance, diamond ideally only exhibits electronic polarizability as it is not ionic and does not have any built-in dipole moment. All dielectrics exhibit electronic polarization. Many ionic linear dielectrics will only exhibit atomic, ionic and space charge polarizations, depending on the field frequency. Some materials which exhibit dipolar polarization exhibit non-linear dielectric permittivity responses.

Ferroelectrics are a class of polar crystals that can be switched between equilibrium, crystallographically-defined polarization states upon application of an electric or stress field. Neumann's principle states that for any physical property of a material, the property must exhibit the point group symmetry of the material.² Considering all 32 crystallographic point groups, only 20 point groups are non-centrosymmetric and can exhibit piezoelectricity. Only 10 are polar and thus contain a spontaneous

polarization. Ferroelectrics are a subset of the polar crystals in which the spontaneous polarization can be reoriented between crystallographically-defined states by an applied electric field. Figure 2.2 shows the point groups arranged as to whether they are piezoelectric, pyroelectric, or potentially ferroelectric.

A comparison between the polarization-electric field and dielectric response of a linear dielectric and non-linear ferroelectric is seen in Figure 2.2. The ferroelectric hysteresis shown has six important values considered in this work: the maximum polarization (P_{\max}), the remanent polarization (P_r) and the coercive field (E_c) for both positive and negative states. Assuming the ferroelectric is composed of an array of domains whose dipoles cancel, the net polarization is equal to zero to start. Each region for which the polarization is pointed in the same orientation (or at least nearly so) is a domain. Upon application of an electric field, the polarization increases in a non-linear fashion until P_{\max} is reached. At P_{\max} the material is a single domain only in the limit of an appropriately oriented single crystal. When the electric field is returned to zero, a P_r remains due to the majority of dipoles pointing in approximately the same direction. It is not until an opposite electric of sufficient value, the coercive field, that the polarization goes to zero, before switching to a negative orientation, where the process repeats. Figure 2.2 (b) shows that the dielectric permittivity maximum vs. electric field of a ferroelectric undergoes maxima at the coercive fields of the ferroelectric.

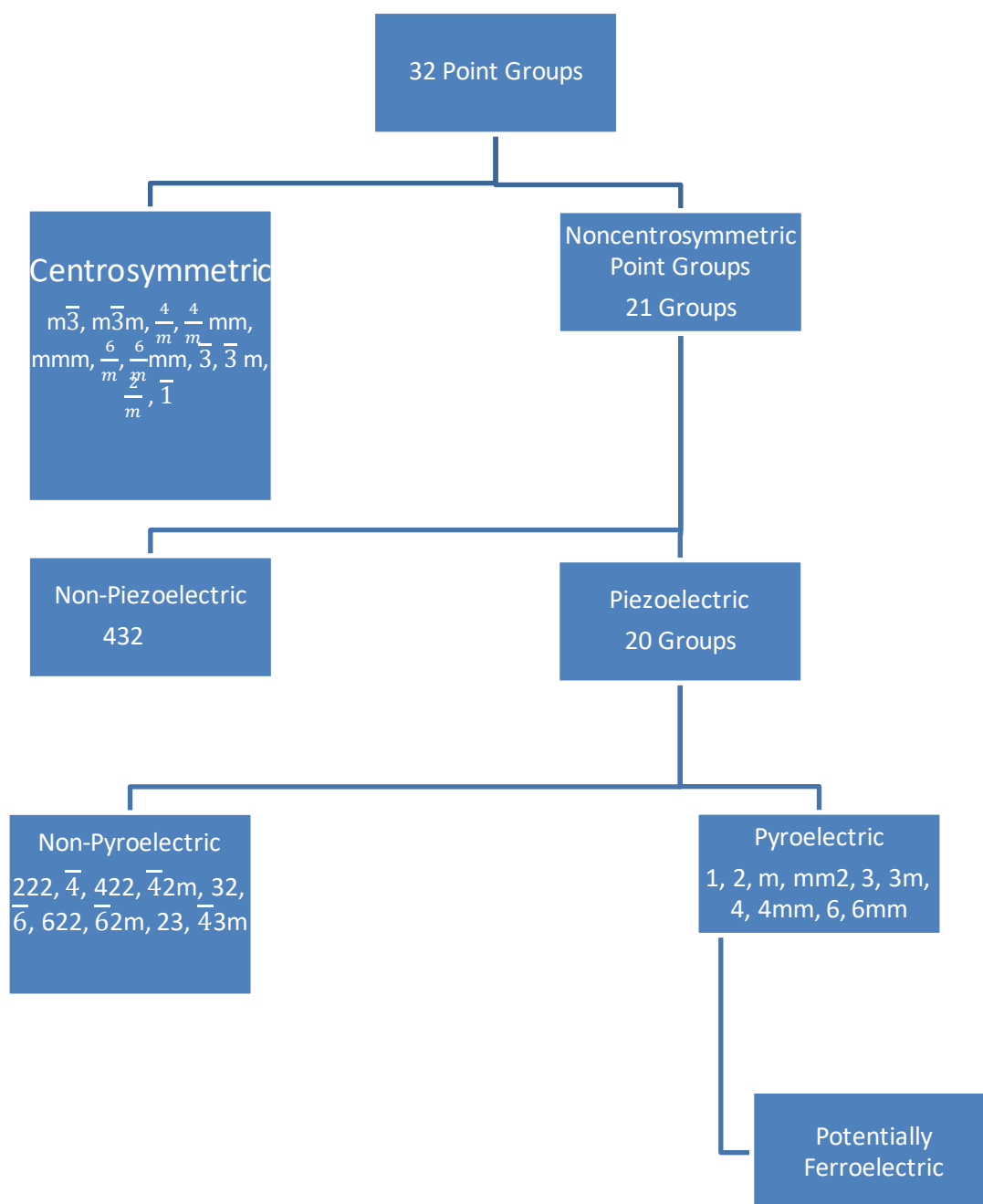


Figure 2.2 – Diagram showing the relationship between the 32 point groups and pyroelectric/ferroelectric properties³

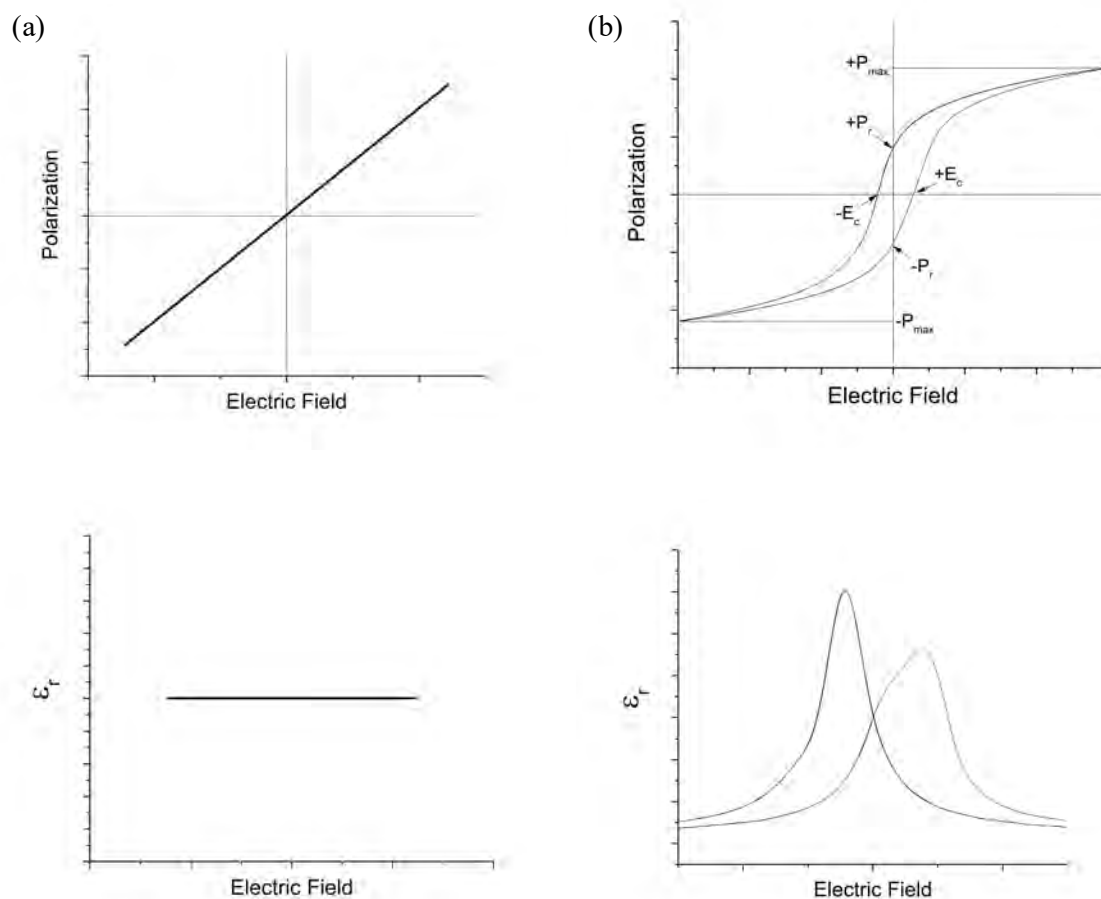


Figure 2.3 – Polarization and relative dielectric permittivity vs electric field responses for (a) ideal linear and (b) ferroelectric dielectric. Data from a 1.7 μm thick PZT thin film sample was provided by Wanlin Zhu for (b). Description of P-E loop parameters from Jaffe.⁴

2.2 Perovskite Structure and Tolerance Factor

Many ferroelectric materials, including the ones analyzed in this thesis, have the perovskite crystal structure. The structure has an ABX_3 stoichiometry. Figure 2.4 demonstrates the cubic perovskite structure. The highest symmetry variant is the cubic space group $\text{Pm}\bar{3}\text{m}$ for the paraelectric phase. The cubic perovskite unit cell is often thought of as a cage of large 12-coordinated A cations on the corners surrounding a central octahedrally coordinated B cation. Anions are located at the face centers of the

cube. For the purpose of this thesis, the focus of the work is on the oxide variants of the perovskite structure.

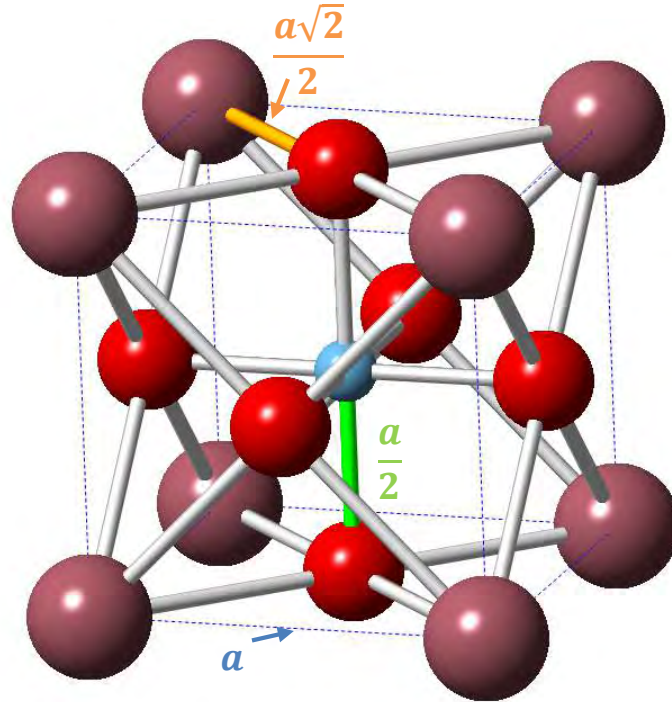


Figure 2.4 - An ideal cubic perovskite (ABO_3) unit cell.

While Figure 2.4 shows the ideal cubic perovskite structure, many perovskites do not exhibit a cubic crystal structure at standard temperature and pressure. The ideal cubic perovskite structure can be described geometrically where the unit cell lattice parameter is a , as:

$$2a^2 = (2r_A + 2r_o)^2 \longrightarrow a = \frac{(2r_A + 2r_o)}{\sqrt{2}} \quad \text{eq. 2.5}$$

$$a = 2r_B + 2r_o \quad \text{eq. 2.6}$$

where r_A and r_B are the radius of cations A and B (or the weighted average for solid solutions); r_o is the oxygen radius. Eqs. 2.5 and 2.6 are two ways to solve for the lattice parameter a based on either the bonding of the A cation to Oxygen or B cation to Oxygen. In order to form a perfect cube, these two equations must equal:

$$\frac{(2r_A + 2r_o)}{\sqrt{2}} = 2r_B + 2r_o \longrightarrow \frac{a}{a} = t = 1 = \frac{(2r_A + 2r_o)}{\sqrt{2}(2r_B + 2r_o)} \quad \text{eq. 2.7}$$

where t is the tolerance factor. The tolerance factor is a measure of the perovskite stability as proposed by Goldschmidt.⁵ When t is not equal to 1, the cubic perovskite phase becomes less stable and may distort.

There are three ways for the perovskite cell to distort; distortion of the octahedra, tilting of the octahedra, and displacement of ions in the octahedra.⁶ Distorting the octahedra requires that the degeneracies of the d electron energy levels of the octahedral metal cation to be lifted, leading to asymmetric bonding between the cation and anion.⁶ Jahn-Teller distortions are an example of this. Jahn-Teller distortions are caused by crystal field in which the anion coordination around the transition metal cation creates lower and higher energy states for the d electrons. For d^4 and d^9 ions in octahedral coordination, the energy can be further lowered by distorting the octahedron.⁶ KCuF_3 and $\text{La}_{1-x}\text{Ca}_x\text{MnO}_3$ are examples of perovskites with Jahn-Teller distortions.^{7,8} Tilting of the octahedra is the most common distortion, whereby the $\text{B}_{\text{cation}} - \text{X} - \text{B}_{\text{cation}}$ bond angle deviates from 180° typically because the A_{cation} is too small.^{6,9,10} Similar to Jahn-Teller distortions, displacement of the B_{cation} is related to electronic instabilities of the metal octahedral ion, but the B site displaces from the center site, breaking symmetry.⁶ The prototypical example is that of BaTiO_3 , where the Ti^{4+} ion displaces closer to one of the surrounding 6 oxygen. This ultimately leads to the spontaneous polarization in ferroelectric materials. The focus of this work is on materials which exhibit displacement of the octahedral cation.

The perovskite tolerance factor changes depending on the radius of the A and B cations. The stability of the perovskite was predicted to be $0.77 \leq t \leq 0.99$ using octahedral coordination for the A-site cation.¹¹ Correcting the radii for the 12 coordinated A-site predicts a tolerance factor of $0.88 \leq t \leq 1.09$.¹¹ The tolerance factor does not necessarily determine if a perovskite is ferroelectric, but, it is typically observed that if $t > 1$, a ferroelectric phase will tend to be tetragonal, while for $t < 1$ a rhombohedral or monoclinic ferroelectric phase is preferred.¹²⁻¹⁵ Tilting distortions, instead of ferroelectric distortions, are particularly prevalent as $t \leq 0.965$ due to the small A_{cation} radius.¹⁶

The tolerance factor is a reasonable predictor of the perovskite phase stability, but it has a limitation. The bonding type is assumed to be purely ionic, when inherently there is some amount of

covalency in any perovskite material.¹⁷ Thus, predicting trends in property behavior based on the tolerance factor alone may exhibit data scatter. In spite of this, the perovskite tolerance factor has been used to determine trends in the transition temperature of the Morphotropic Phase Boundary (MPBs) and magneto-resistance, the position of the MPBs in solid solutions, the temperature coefficient of capacitance, the heat of formation, and the indirect band gap transition.^{11, 18-21}

2.2.1 Perovskite Phase Transitions and Properties

In addition to the composition, temperature, pressure, strain and electric field are all stimuli which can induce phase transitions in perovskites.²²⁻²⁶ The most commonly studied and relevant to this work are phase transitions caused by changes in temperature. Since ferroelectric materials are a subclass of pyroelectrics, their properties are inherently temperature dependent. A perovskite material may undergo multiple phase transitions at various temperatures.²⁷ Two of the most well studied systems are BaTiO₃ and PbTiO₃. Figure 2.4 shows the lattice parameter and dielectric behavior of BaTiO₃ with increasing temperature. The cubic perovskite only exists at high temperatures. With decreasing temperature, the Ti⁴⁺ ion displaces to produce first tetragonal, then orthorhombic and finally rhombohedral symmetries. The corresponding dielectric permittivity is seen in Figure 2.4(b). The dielectric permittivity is a function of crystallographic direction due to the tetragonal symmetry as well as temperature.²⁸ At each phase transition there is a corresponding increase in the dielectric response. The transition between the paraelectric and ferroelectric phase is important as it defines when the material is no longer ferroelectric. In normal ferroelectrics undergoing first order phase transitions, the dielectric permittivity follows Curie-Weiss behavior above the Curie point (T_c):

$$\varepsilon = \frac{A}{T - \theta_c}$$

where C is the Curie constant, T is the temperature and θ_c is the Curie-Weiss temperature (which is near T_c).¹

Figure 2.6 shows the dielectric permittivity, pyroelectric coefficient and calculated spontaneous polarization of a single crystal PbTiO_3 . With increasing temperature, the spontaneous polarization decreases. At T_c , the spontaneous polarization goes to 0 due to the loss of the ferroelectric phase. Based on the behavior of the P_s vs temperature, the phase transition can be determined to be first or second order. PbTiO_3 and BaTiO_3 are examples of ferroelectrics with a first order phase transition where there is a discontinuity in the P_s vs temperature diagram at T_c (see first 2.6).^{27,29} Second order phase transitions exhibit a continuous decrease to 0 at T_c .

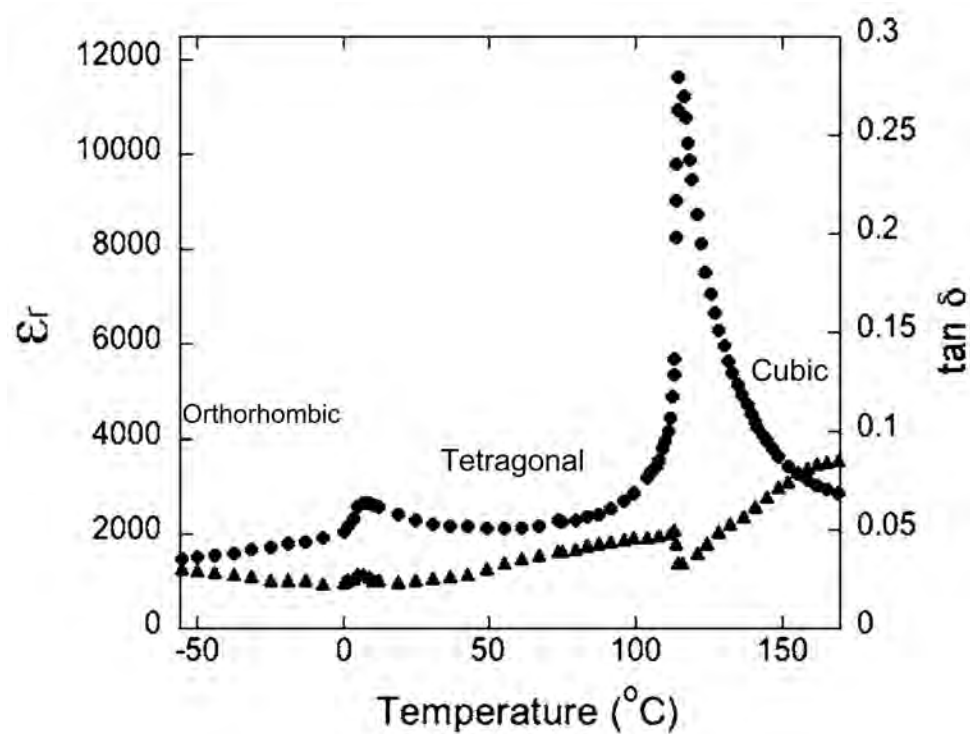
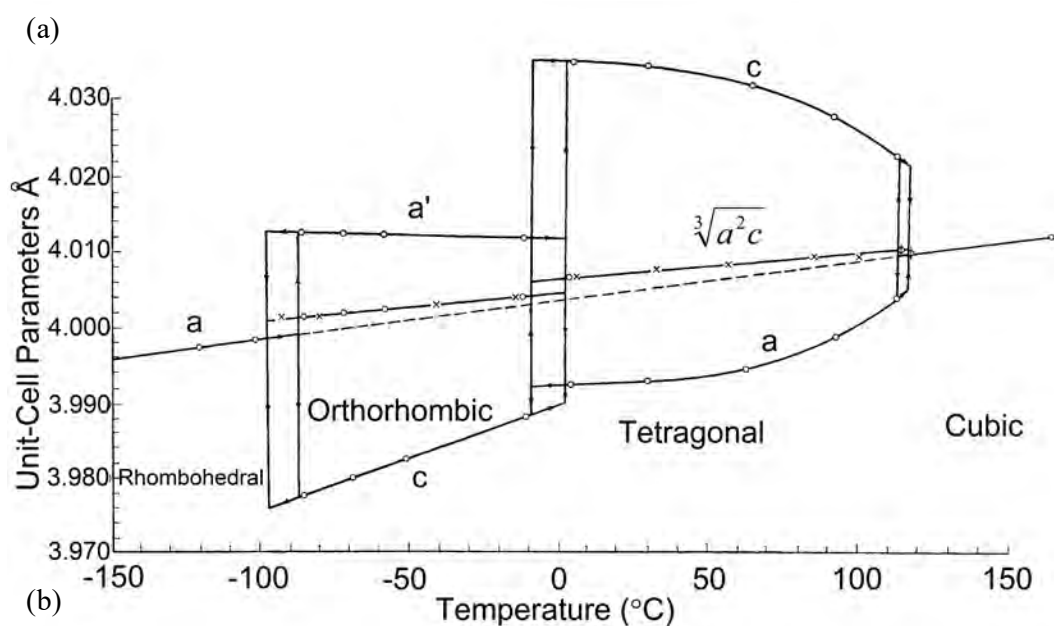


Figure 2.5 –(a) Lattice parameter and phase of a BaTiO_3 single crystal as a function of temperature.²⁷ (b) The dielectric permittivity of a BaTiO_3 ceramic as a function of temperature showing the dielectric anomaly at the phase transition temperatures.³⁰

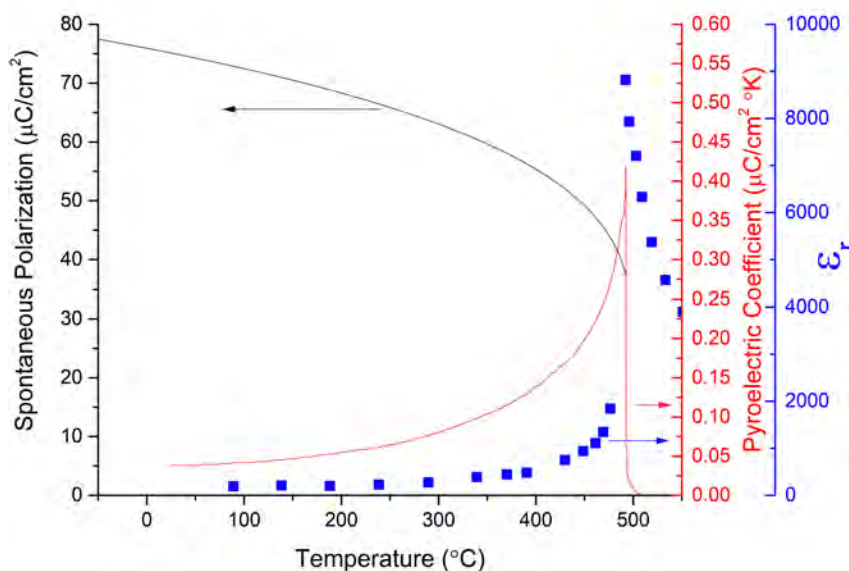


Figure 2.6 – The dielectric permittivity, pyroelectric coefficient and spontaneous polarization of PbTiO_3 as a function of temperature.³¹ The abrupt change in the P_s at the Curie point shows the first order transition of PbTiO_3 . The P_s is calculated based on phenomenological theory.²⁹

Thickness scaling of a material may also influence the high temperature transition behavior. The change in ferroelectric properties with changes in grain size or thickness are attributed to intrinsic limits and extrinsic contributions. PbTiO_3 requires at least 3 unit cells of thickness to be ferroelectric.³² However, ferroelectrics show changes in dielectric and piezoelectric properties at significantly greater thicknesses. In bulk BaTiO_3 and PZT, it has been demonstrated that the room temperature relative permittivity as a function of grain size saturates above $>10\mu\text{m}$, goes through a maximum at $\approx 1\mu\text{m}$, and decreases below $1\mu\text{m}$.^{33,34} The primary reason for the change in properties with decreasing grain size and thickness is attributed to changes in domain configuration, domain wall mobility and density. Arlt *et al.* demonstrated that the domain size $\propto (\text{grain size})^{1/2}$.³⁴ An enhancement in the permittivity and piezoelectric properties occurs due to the increased extrinsic contributions.³⁵ Below $1\mu\text{m}$, the domain wall density or mobility is decreased. In addition, domain nucleation and growth becomes more difficult as the grain size or thickness approaches the dimensions of a single domain.^{35–37} Grain size also affects the permittivity at T_c . Thin films and bulk ceramics with fine grain sizes demonstrate suppressed

permittivity at T_c and/or decreased T_c with decreasing grain size.^{36–39} However, Saad *et al.* demonstrated that a 75 nm thick free-standing single crystal exhibits bulk-like properties and no reduction in T_c .⁴⁰ Thus, mechanical clamping from the substrates or mis-oriented grains, and dilution of properties due to grain boundary phases strongly affect the behavior at T_c . Figure 2.7 shows the relationship between ceramic grain size and functional properties in BaTiO_3 .

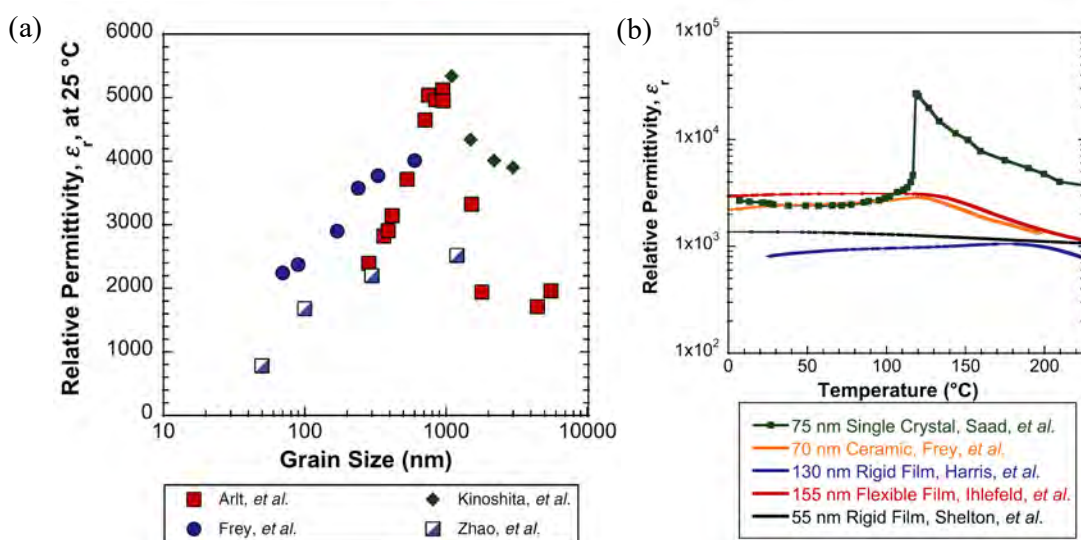


Figure 2.7 – (a) Effect of grain size on the room temperature dielectric permittivity of BaTiO_3 .^{33, 34, 36, 38, 41} (b) Comparison of the dielectric permittivity vs temperature of a free standing single crystal, small grain sized ceramic, rigid film films and a flexible film.^{33, 38–40, 42, 43} Figures (a) and (b) reproduced from reference.³³

A final factor known to affect the ferroelectric-paraelectric transition is strain. The largest strains are generated in epitaxial thin films, where large misfit strains may occur. Depending on the misfit strain in the epitaxial film, the T_c of the film will increase. Figure 2.8 shows the misfit strain phase diagram of BaTiO_3 . Strains as high as $\approx 1.5\%$ are seen to increase the T_c of BaTiO_3 by more than 500°C .

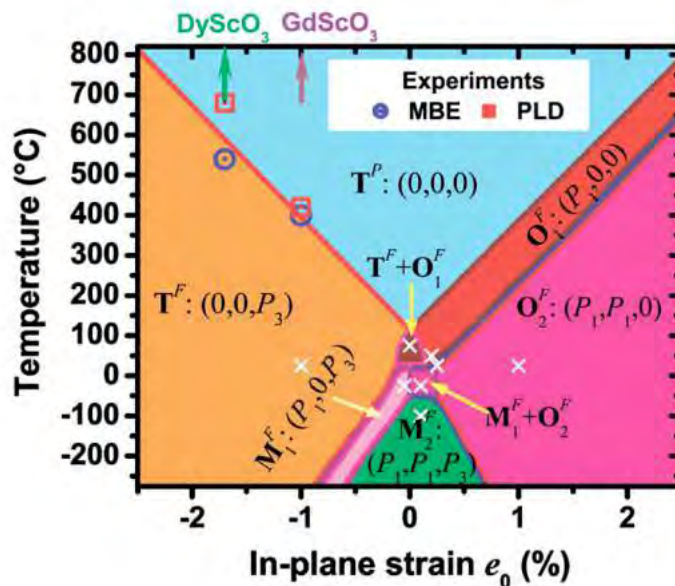


Figure 2.8 – Effect of misfit strain on the phase diagram of BaTiO₃.²⁵

2.3 Ferroelectric Random Access Memory

The ferroelectric random access memory device utilizes the different polarization states in a ferroelectric to store data in 0 and 1 bits. Since the 1950's, ferroelectrics have been seen as a means of storing information.^{44–48} The first experiments to store information in a ferroelectric and control the surface charges of a semiconductor were done by Moll and Tarui in 1963.⁴⁹ The device developed by Moll and Tarui was utilized to create a variable resistor. Rohrer showed that KNO₃ films could be made sufficiently thin to operate at less than 5V, making them complementary metal-oxide-semiconductor (CMOS) compatible.⁵⁰ In 1974, Wu successfully recorded data utilizing a metal-ferroelectric-semiconductor (MFS) memory where the oxide gate of a metal-oxide-semiconductor (MOS) was replaced with a ferroelectric.⁵¹ During the mid to late 1970's and early 1980's, Pb(Zr,Ti)O₃ (PZT) was studied as a candidate material for various thin film applications.^{52–55} It was not until 1987 that Krysalis Corporation successfully developed a ferroelectric memory device with stacked MOS transistors and a ferroelectric

capacitor.^{56,57} In 1988, Ramtron International Corporation began releasing the first commercial FeRAM product.⁵⁷

There are two primary designs utilized to make an FeRAM device today. One is based on a similar design to the work done by Wu *et al.* and proposed by Ross.^{47,51} In this design, the ferroelectric replaces the oxide gate in a CMOS transistor, allowing data storage and logic calculations simultaneously. However, that design is still only in the prototype stage.^{58,59} Commercial FeRAM utilizes a design similar to dynamic random access memory (DRAM), but replaces the paraelectric capacitor with a ferroelectric capacitor. Figure 2.9 compares the two device structures. The ideal structure to utilize would be that proposed by Ross as it allows for a greater density of memory as well as multifunctionality. However, currently there is a challenge with increasing the retention time for these type of structures.^{58,59}

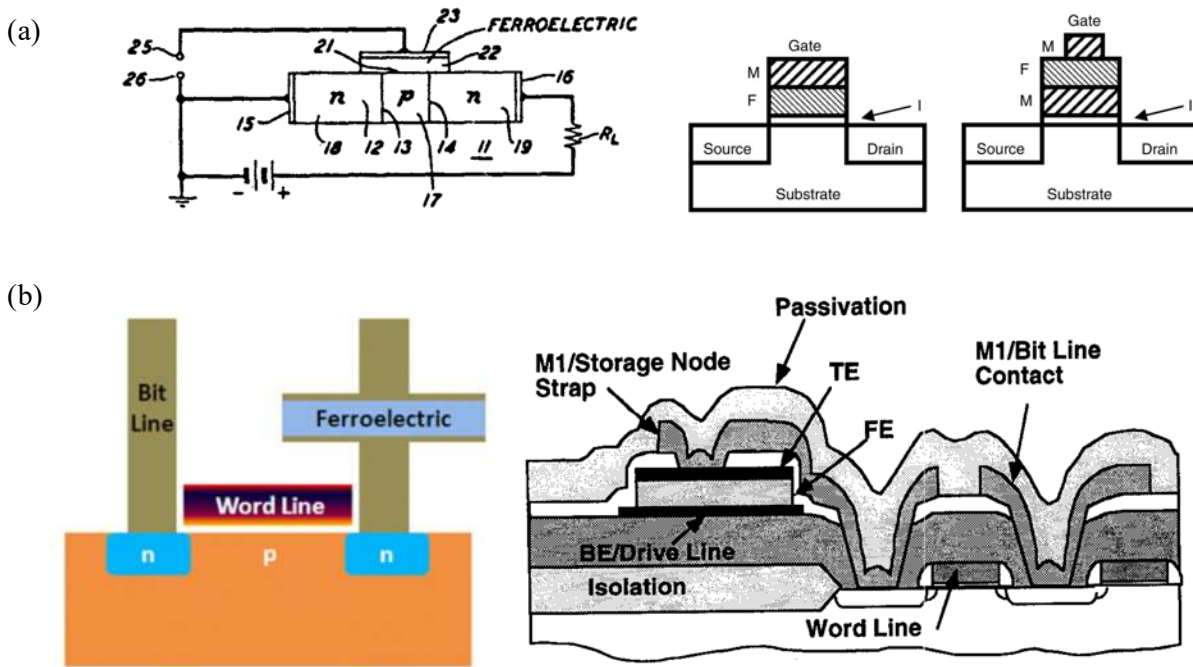


Figure 2.9 – (a) Proposed ferroelectric translating device proposed by Ross for data storage.⁴⁷ Metal-ferroelectric-insulator-semiconductor (MFS) and metal-ferroelectric-metal-insulator-semiconductor (MFMI) FET FeRAM schematics (b) Schematic FeRAM structure with a similar design as that of a DRAM device.^{60, 61}

Operation of a FeRAM is shown in Figure 2.10. The basic operation is to detect the charge given by the ferroelectric when the polarization is pointed either up or down relative to the substrate at the

bottom. This is done by utilizing an access transistor (the word line), a bit line, and a plate line to form the memory cell.⁶² The process begins with no voltage applied to the word line, bit line or plate line, and with the capacitor in an unknown polarization state.⁶² The capacitor is charged by applying a voltage to the word line and the plate line.⁶² In the case of Figure 2.10, the applied field causes a switch in polarization, which is detected by the bit line. If the polarization state had started up, there would have been no change in the current of the bit line.⁶² Utilizing this, either 0 or 1 bits are detected in Fe

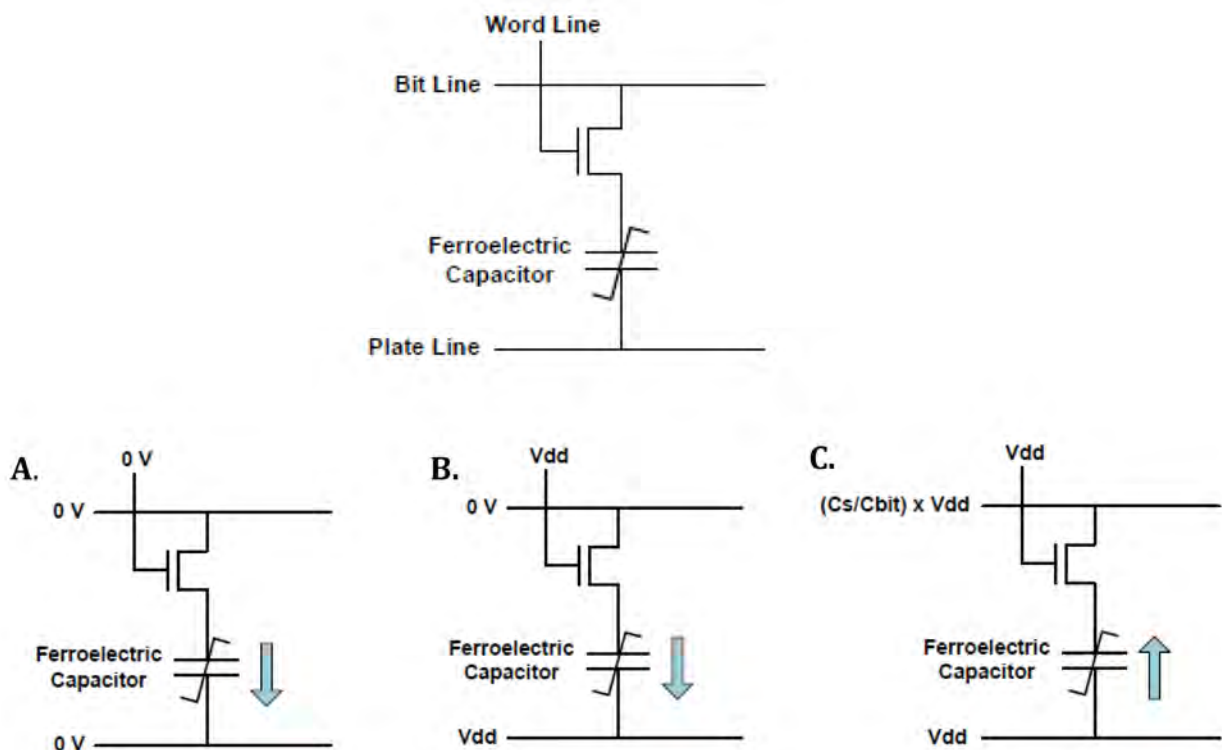


Figure 2.10 – Schematic operation of an FeRAM device based on a 1 Transistor / 1 Capacitor (1T1C) design. (A)-(C) Application of a voltage showing the switching of a ferroelectric capacitor with a 1T1C design. In this case the ferroelectric starts in the down polarization and is switched to the up polarization state when the word and plate line voltages are applied. C_s , C_{bit} , and V_{dd} are the capacitance of the switched ferroelectric, the capacitance of the parasitic bit line and the power supply voltage, respectively⁶²

Several properties are essential to the ferroelectric in an FeRAM device. Cycling endurance (fatigue resistance), retention, thickness scalability, remanent polarization, coercive field, imprint resistance, and high temperature performance determine the feasibility of a ferroelectric in an FeRAM device. Current state-of-the-art FeRAM utilize voltages similar to CMOS technology.⁶³ As such the

material utilized must either have a low coercive field and/or be scalable to a small thickness without loss of properties. The remanent polarization is directly proportional to the sensing signal margin of an FeRAM device.⁶⁴ The three main modes of failure in an FeRAM device are related to fatigue, imprint, and retention loss. In fatigue, there is loss of polarization with increasing number of switching cycles. The standard for FeRAM endurance is $10^{12} - 10^{14}$ cycles.^{57,60,65} This is necessary to ensure a long lifetime of the device because of the destructive read cycle of FeRAM. Imprint failure occurs when domains become preferentially oriented, leading to a lateral shift of the P-E loop.⁶⁶⁻⁶⁹ Device failure occurs either because the programming voltage becomes too large or because of an inability to distinguish between the two polarization states.⁶⁹ Finally, the most basic function of a FeRAM device is retaining a permanent polarization. Retention loss occurs due to depolarization; this can result if the material comes closer to the Curie temperature, or if there are internal fields which destabilize the polarization state. Retention failure is the main mode of failure in FeRAM devices, particularly in ferroelectric FET memory/logic devices.^{59,63,69}

The materials currently utilized for commercial FeRAM are PZT and $\text{SrBi}_2\text{Ta}_2\text{O}_9$ (SBT). The primary differences between these two materials are their reliability, their sensing signal margin, and their processing crystallization temperature. SBT has a $2P_r \approx 12$ to $24 \mu\text{C}/\text{cm}^2$ depending on doping, superior endurance to at least 10^{13} cycles on platinum electrodes, and potentially superior reliability.^{63, 70} PZT offers a $2P_r \approx 40 \mu\text{C}/\text{cm}^2$ with similar endurance to SBT when utilizing oxide electrodes, comparable reliability at high temperature to SBT and a lower crystallization temperature.^{70,71}

2.4 Bi-Based Solid Solutions

Figure 1.1 demonstrates that few end member ferroelectric perovskites exist with the higher Curie temperatures than PbTiO_3 . Several Mn and Cr based perovskites such as YMnO_3 and DyCrO_3 have high transition temperatures, but have multivalent ions allowing for electron hopping that would be expected to

be problematic in terms of conduction at elevated temperatures.⁷² Many $\text{BiMe}^{3+}\text{O}_3$ compounds are difficult to process without using high pressure.⁷³ An exception is BiFeO_3 , which can be processed phase pure under ambient conditions.^{74, 75} While BiFeO_3 has a transition temperature of $\approx 850^\circ\text{C}$, electron hopping conduction limits its use at high temperatures.⁷⁶

One strategy for finding candidate high temperature piezoelectric or ferroelectric materials is to utilize solid solutions. For piezoelectrics, solid solutions with a morphotropic phase boundary (MPB) are sought due to the enhanced piezoelectric properties. PZT, the most widely used ceramic piezoelectric, has a transition temperature of 385°C at the MPB. Prior to 2001, $\text{BiFeO}_3\text{-PbTiO}_3$ was known to provide a transition temperature higher than PbTiO_3 . The most well studied piezoelectric ceramics were solid solutions based on BaTiO_3 or PbTiO_3 which yield materials with T_c between the two end members.

Eitel *et al.* utilized the Goldschmidt tolerance factor to predict several Bi-based- PbTiO_3 solid solutions with a higher transition temperature than PZT at the MPB.¹¹ Figure 2.11 shows the relationship between the tolerance factor and the MPB transition temperature. While there is some data scatter, there is general agreement that as the end member tolerance factor decreases, the MPB transition temperature increases, particularly for the Bi-based solid solutions. This hypothesis was experimentally tested first with the $\text{BiScO}_3\text{-PbTiO}_3$ (BS-PT) solid solution.^{11, 77} Subsequently, multiple solid solutions have been reported with a higher MPB transition temperature than PZT or a T_c higher than PbTiO_3 in at least part of the solid solution range.^{18, 78-83}

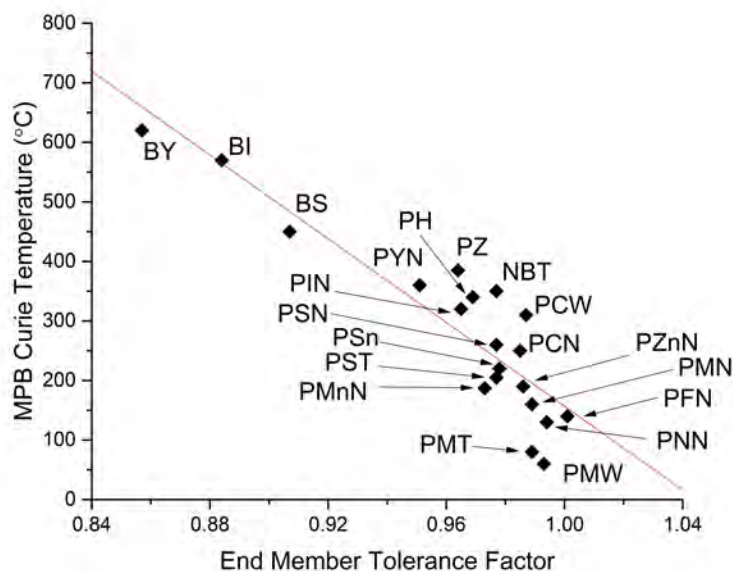


Figure 2.11 – MPB Curie temperature vs. end member tolerance factor in PbTiO_3 solid solutions.¹¹ The ionic radii are taken from Shannon and the ionic radius of Bi^{3+} in 12 coordination was extrapolated to be 1.34\AA .^{11, 84}

Suchomel *et al.* utilized the tolerance factor to provide a guide for determining the composition at which the MPB occurs for Bi-based- PbTiO_3 solid solutions.¹⁸ Figure 2.12 shows a plot of perovskite solid solutions either with both end members containing Pb and/or Bi or one end member containing neither Pb or Bi in the A site. Several conclusions were drawn from this work: 1) Despite some data scatter, the PbTiO_3 content at the MPB appears to converge as the tolerance factor decreases, 2) The presence of Pb or Bi on the A-site of the non- PbTiO_3 end member decreases the PbTiO_3 concentration needed to form an MPB and 3) the shaded region provides a range for predicting the MPB of unknown solid solutions.¹⁸

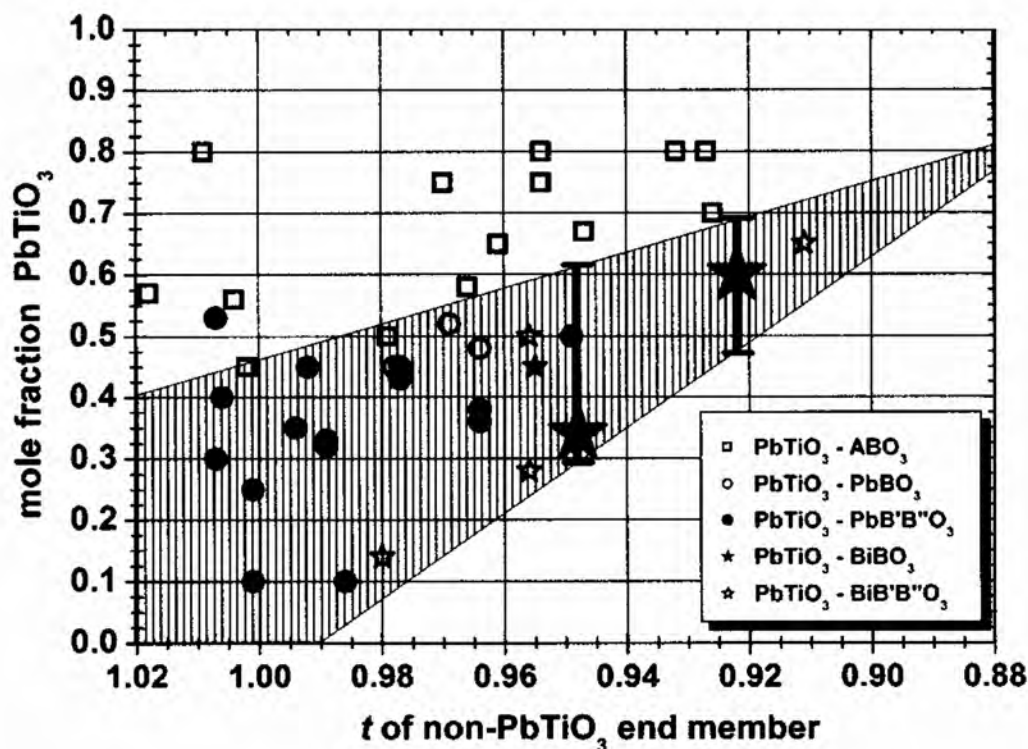


Figure 2.12 – Mole fraction of PbTiO_3 at the MPB of a solid solution vs the tolerance factor of the non- PbTiO_3 end member. Different data points correspond to different types of solid solutions (i.e. Pb, Bi, or a different cation on the A site and/or single/double cations on the B-site). The shaded region corresponds to the MPB for systems with Pb or Bi on the A-site of the non- PbTiO_3 end member.¹⁸

In some cases, the T_c does not vary monotonically between the end member T_c . Isupov brought attention to the need to explain the various trends in the T_c as a function of composition. He characterized the nonlinearity in T_c using a quadratic equation:

$$\Delta T_c = T_c(x = 0) - T_c(x) = ax + bx^2 \quad \text{Eq. 2.8}$$

where x is the mol fraction PbTiO_3 and a and b are fitting parameters. Care is needed in utilizing this method as the coefficients change depending on whether the PbTiO_3 or non- PbTiO_3 end member is set to equal 0. It was noted that several systems exhibit a positive value for the a coefficient, meaning T_c increases with reducing PbTiO_3 concentration. The increase in T_c for a system such as PbGeO_3 - PbTiO_3 can be explained due to smaller Ge^{4+} ion compared to Ti^{4+} , however other systems such as $(\text{K}_{0.5}\text{Bi}_{0.5})\text{TiO}_3$ - PbTiO_3 which show a maximum in T_c between the end members were left without explanation.¹⁵

Stringer proposed a slightly modified quadratic formula:⁸⁰

$$T_x(x) = a + bx + cx^2 \quad \text{Eq. 2.9}$$

where a is the transition temperature of PbTiO_3 (495°C), and b and c are fitting parameters. Three separate cases were determined based on the sign of b and c . For case 1, the signs of b and c are negative and thus the T_c decreases with decreasing PbTiO_3 content. This is the case for many PbTiO_3 -based solid solutions including PZT. In case 3, the signs of b and c are both positive and thus there is a continuous increase in T_c with decreasing PbTiO_3 content. This type of behavior is typified by BiFeO_3 , $\text{Bi}(\text{Zn}_{1/2}\text{Ti}_{1/2})\text{O}_3$, and $\text{Bi}(\text{Zn}_{3/4}\text{W}_{1/4})\text{O}_3$. For case 3, the reason for enhanced transition temperatures is related to the increase in tetragonality. In case 2, the sign of b is positive and the sign of c is negative. Figures 2.13-2.15 demonstrate the three basic classifications determined by Stringer *et al.* The following section will discuss case 2 materials in more depth with special attention paid to BiScO_3 and $\text{Bi}(\text{Mg}_{1/2}\text{Ti}_{1/2})\text{O}_3$ based solid solutions.

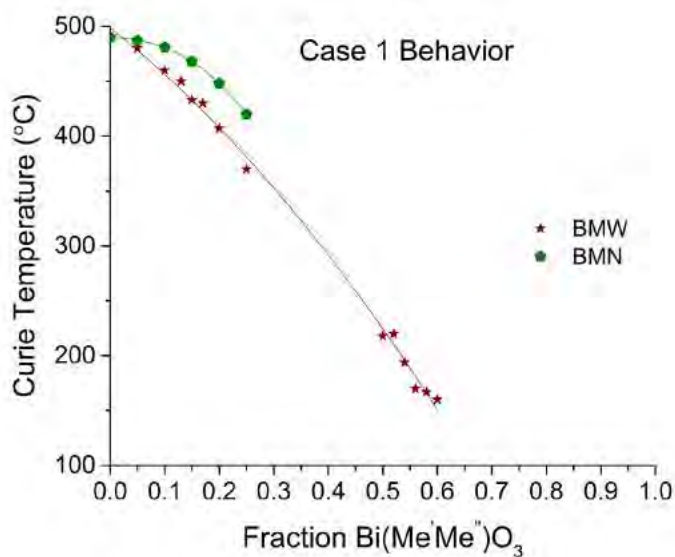


Figure 2.13 – Case 1 Bi-based- PbTiO_3 solid solutions showing a continuous decrease in T_c with decreasing PbTiO_3 . T_c vs composition data shown for $\text{Bi}(\text{Mg}_{3/4}\text{W}_{1/4})\text{O}_3$ (BMW) and $\text{Bi}(\text{Mg}_{2/3}\text{Nb}_{1/3})\text{O}_3$ (BMN) end members.⁸⁰

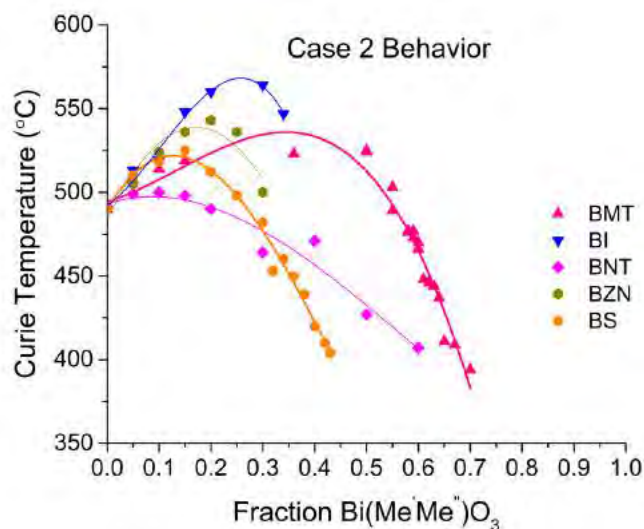


Figure 2.14 – Case 2 Bi-based-PbTiO₃ solid solutions showing a maximum in the T_c between the end members of the solid solution. T_c vs composition data shown for Bi(Mg_{1/2}Ti_{1/2})O₃ (BMT), BiInO₃ (BI), Bi(Ni_{1/2}Ti_{1/2})O₃ (BNT), Bi(Zn_{2/3}Nb_{1/3})O₃ (BZN), and BiScO₃ (BS).⁸⁰

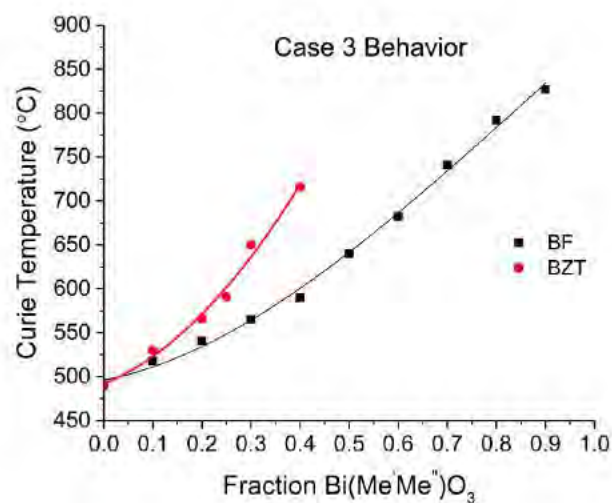


Figure 2.15 – Case 3 Bi-based-PbTiO₃ solid solutions showing a continuous increase in the T_c as the PbTiO₃ concentration decreases. T_c vs composition data shown for BiFeO₃ (BF) and Bi(Zn_{1/2}Ti_{1/2})O₃ (BZT).^{78,80}

2.4.1 Case 2 Bi-Based Solid Solutions

Stringer *et al.* proposed that the behavior seen in case 2 solid solutions is similar to transition temperatures observed in superconducting cuprates as reported by Attfield *et al.*^{80,85} Two factors were

correlated with the T_C behavior: 1) The spread of the tolerance factor within the solid solution (Δt) and 2) The variance of the B-site ionic radius (σ^2). Δt accounts for the maximum spread in unit cell lattice parameters assuming a unit cell was composed of one end member (PbTiO_3) or the other (BiMeO_3).⁸⁰ The difference between the two tolerance factor values is Δt . σ^2 is determined by:

$$\sigma^2 = \sum_i y_i r_i^2 - (\sum_i y_i r_i)^2 \quad \text{Eq. 2.10}$$

where y_i and r_i are the fraction of B-site ions present and ionic radii, respectively. T_C was found to change linearly with both Δt and σ^2 . Stringer *et al.* proposed that random electric fields resulting from random strain fields throughout the crystal lattice couple to the polarization, which accounts for the shift in T_C .⁸⁰

2.4.2 Case 2 Phase Diagrams - $\text{BiScO}_3\text{-PbTiO}_3$ and $\text{Bi}(\text{Mg}_{1/2}\text{Ti}_{1/2})\text{O}_3\text{-PbTiO}_3$ Solid Solutions

In the tetragonal phase field of case 1 and case 3 Bi-based- PbTiO_3 solid solutions, the c/a ratio is directly related to the transition temperature. For case 1 materials, the c/a ratio decreases with decreasing PbTiO_3 content, leading to a decrease in T_c .^{79,80} In case 3, the c/a ratio increases with decreasing PbTiO_3 , leading to an increase in T_c .⁷⁸⁻⁸⁰ However, no correlation between T_c and c/a ratio is found in case 2 solid solutions. BS-PT is the most well studied case 2 solid solution, and will be used as an exemplar. The phase diagram and lattice parameters for BS-PT are shown in Figure 2.16. The c/a ratio in BiScO_3 continuously decreases through the maximum in T_c vs composition.

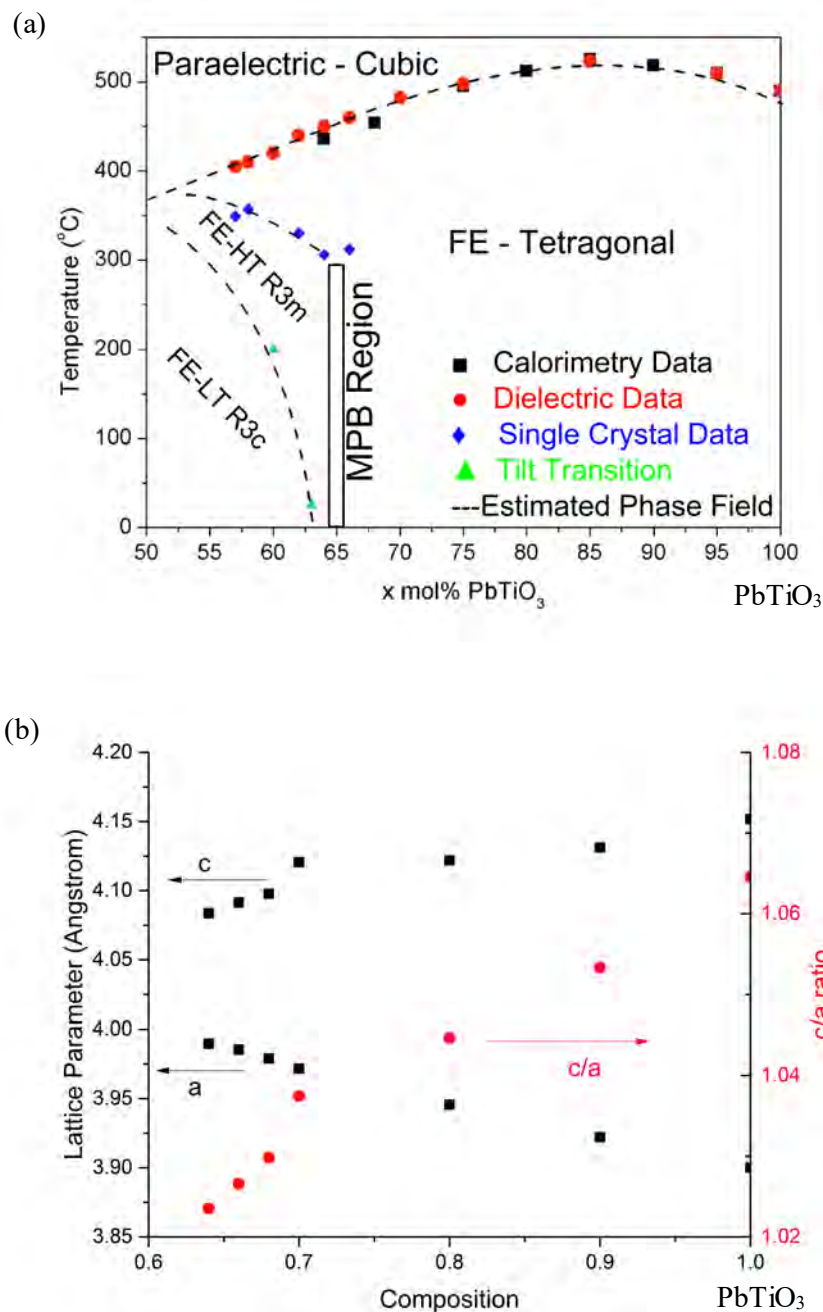


Figure 2.16 – (a) Phase diagram of BS-PT.⁸⁶ (b) Lattice parameter and c/a ratio for tetragonal BS-PT compositions.⁷⁷

The focus of this thesis is on another case 2 system, $\text{Bi}(\text{Mg}_{1/2}\text{Ti}_{1/2})\text{O}_3\text{-PbTiO}_3$ (BiMT-PT). The phase diagram for BiMT-PT is not as well studied as BS-PT, thus a comprehensive set of data is compiled here to update the phase diagrams. Figure 2.17 shows a phase diagram compiled from the data in the

literature.^{18,80,83,87} The most comprehensive data sets available are those published by Randall *et al.*⁸³ and Stringer *et al.*⁸⁰ and as those works were produced from the same group, they utilize some of the same samples/data and span the entire region of the phase diagram. Suchomel *et al.*¹⁸ independently investigated the BiMT-PT and other systems with data that fits reasonably well with the first group, although there are some inconsistencies. For example, there is a much quicker drop in the T_c transition temperature in Suchomel *et al.*'s¹⁸ data, particularly around the 50-50 composition, while the other data is much more diffuse in the T_c vs composition data. A single crystal produced by Liu *et al.*⁸⁷ matches reasonably well with that of the first group's data.

Suchomel and Davies utilized the tolerance factor of the non-PbTiO₃ end member of known systems to narrow the predicted region for the MPB location (close to $x = 62$ to 64 in BiMT-PT).¹⁸ Randall *et al.* refined the MPB compositional region utilizing piezoelectric (d_{33}), poled permittivity and X-ray diffraction measurements. They found that it was hard to pinpoint the exact MPB composition due to the propensity for formation of grains with core-shell structures associated with compositional gradients.⁸³

Figure 2.17 demonstrates that the focus of the literature has been on the compositions surrounding the MPB and that the circled region requires further study. Fitting was employed to estimate the composition for $T_{c,max}$ in the phase diagram. Two separate fitting methods were utilized. The first is according to the 2nd order polynomial (Eq. 2.9) proposed by Stringer *et al.*⁸⁰ Using a 2nd order polynomial for case 2, the b coefficient is positive and the c coefficient is negative. The original coefficients do not fit all of the available data well. Table 1 shows the parameters proposed by Stringer *et al.*⁸⁰ and proposed corrections based on Stringer *et al.*'s⁸⁰ data and all available T_c data. Figure 2.18 demonstrates the original fitting utilizing only the data from Stringer *et al.*'s⁸⁰ work. All 3 predict a maximum in $T_{c,max}$ at ≈ 25 - 27 mol% BiMT. The 2nd order polynomial model only appears to fit the ends of the composition range well.

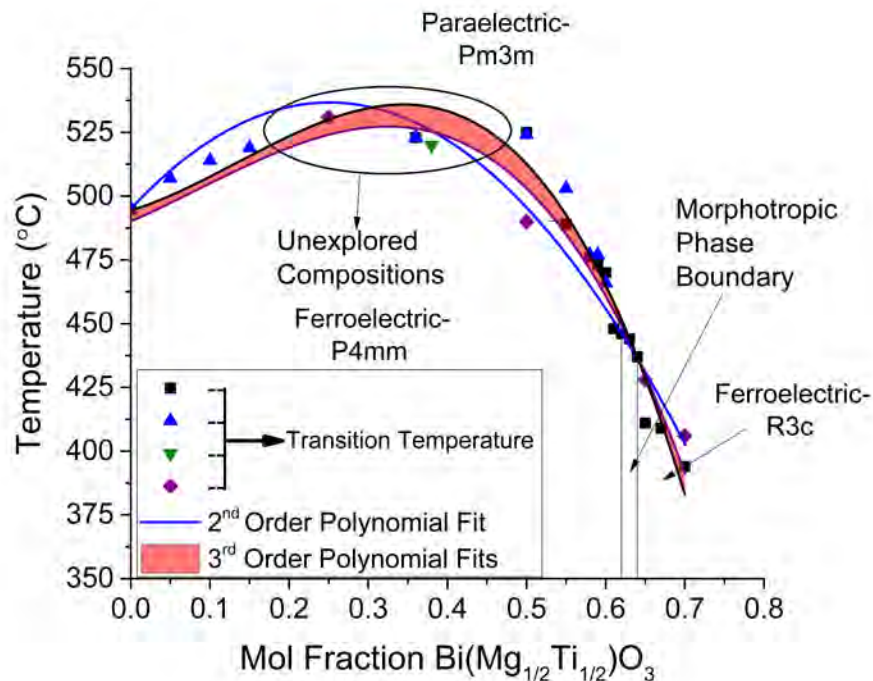


Figure 2.17 - Phase diagram of the BiMT-PT system. Reported data (black squares⁸³, blue upward triangle⁸⁰, green down triangle⁸⁷, and purple diamond¹⁸) is based on combined high temperature X-ray diffraction, differential scanning calorimetry and dielectric vs temperature measurements. The blue line corresponds to a 2nd order polynomial fit as performed by Stringer et al., but for all known data. The shaded region corresponds to 3rd order polynomial fits and the uncertainty in the transition temperature.

Table 2.1 - 2nd order polynomial fits: $a + bx + cx^2$ where “a” is assumed to be the PbTiO₃ Curie transition temperature of 495 °C. The predicted $T_{c,max}$ composition and $T_{c,max}$ are provided for each fitting.

| Fitting | b (°C/mole) | c (°C/mole) ² | BiMT Fraction at T_{max} (mol%) | $T_{c,max}$ (°C) |
|-----------------|-------------|--------------------------|-----------------------------------|------------------|
| Stringer | +430 | -800 | 27 | 553 |
| Refitted | +280 | -518 | 27 | 533 |
| Fit to All Data | +332 | -663 | 25 | 537 |

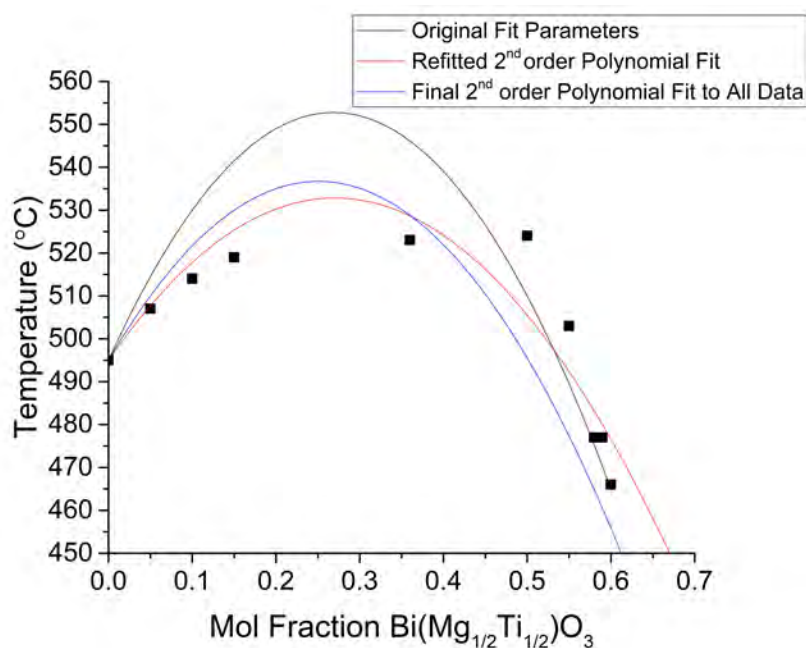


Figure 2.18 - BiMT-PT diagram replotted from Stringer *et al.*⁸⁰ The black line is the data fit according to Stringer's fitting parameters and the red line is the refitted data. The blue line corresponds a 2nd order polynomial fit to all reported data.

Randall *et al.* originally published a phase diagram with a T_c boundary that is not described, but is likely a 3rd order polynomial based on the fitting behavior. As seen in Figure 2.17 a third order polynomial fits the T_c behavior much better than the 2nd order polynomials. However, no physical meaning is currently ascribed to the fitting. For the 3rd order polynomial fits, the predicted $T_{c,max}$ is ≈ 527 - 535 °C depending on whether the fitting is performed with the data from Suchomel or not. $T_{c,max}$ is predicted to be ≈ 32 - 35 mol% BiMT. Further study is needed to assess the inconsistencies between Suchomel *et al.*'s and Randall/Stringer *et al.*'s T_c data. One potential source for the inconsistency is compositional gradients in the ceramics. It was noted that compositions near the MPB showed behavior consistent with a small increase in $PbTiO_3$ concentration near the grain boundaries.⁸³ However, this was noted only for the composition near the MPB, not the composition at $x=0.5$ PT. There is no evidence that the composition near $x=0.5$ could have a 25 mol% shift to match the data by Suchomel *et al.*. As such, none of the current data can be seen as outliers and the diagram is seen as having a very diffuse

maximum. Thus, a 3rd order polynomial is currently the better choice for modeling the T_c behavior, but more careful experiments are needed to verify this model and diagram.

2.5 References

- 1 A.J. Moulson and J.M. Herbert, "Elementary Solid State Science," pp. 5–93 in *Electroceramics*, Second Ed. 2003.
- 2 R.E. Newnham, *Properties of Materials: Anisotropy, Symmetry, Structure*. Oxford University Press, New York, 2005.
- 3 J.F. Nye, *Physical Properties of Crystals*. Oxford University Press, 1985.
- 4 B. Jaffe and W.R. Cook, *Piezoelectric Ceramics*. Academic Press, London and New York, 1971.
- 5 V.M. Goldschmidt, "Die Gesetze der Krystallochemie," *Naturwissenschaften*, **14** [21] 477–485 (1926).
- 6 P.M. Woodward, "Octahedral Tilting in Perovskites. I. Geometrical Considerations," *Acta Crystallogr. Sect. B Struct. Sci.*, **53** [1] 32–43 (1997).
- 7 A. Okazaki and Y. Suemune, "The Crystal Structure of $KCuF_3$," *J. Phys. Soc. Japan*, **16** [2] 176–183 (1961).
- 8 J. Goodenough, "Jahn-Teller Phenomena," *Annu. Rev. Mater. Sci.*, **28** 1–27 (1955).
- 9 A.M. Glazer, "The Classification of Tilted Octahedra in Perovskites," *Acta Crystallogr.*, **B28** 3384–3392 (1972).
- 10 A.M. Glazer, "Simple Ways of Determining Perovskite Structures," *Acta Crystallogr.*, **A31** 756–762 (1975).
- 11 R.E. Eitel, C.A. Randall, T.R. Shrout, P.W. Rehrig, W. Hackenberger, and S.-E. Park, "New High Temperature Morphotropic Phase Boundary Piezoelectrics Based on $Bi(Me)O_3$ - $PbTiO_3$ Ceramics," *Jpn. J. Appl. Phys.*, **40** 5999–6002 (2001).
- 12 V.A. Isupov, "Physical Phenomena in Complex Ferroelectric Perovskites," *Bull. Acad. Sci. U.S.S.R. Phys. Ser.*, **47** [3] 136–141 (1983).
- 13 R.E. Eitel, "Novel Piezoelectric Ceramics: Development of High Temperature, High Performance Piezoelectrics on the Basis of Structure," Ph.D. Dissertation, The Pennsylvania State University, 2003.
- 14 C.J. Stringer, "Structure-Property-Performance Relationships of New High Temperature Relaxors for Capacitor Applications," Ph.D. Dissertation, The Pennsylvania State University, 2006.
- 15 V.A. Isupov, "Nonlinearity of the Concentration Dependence of the Curie Temperature in Ferroelectric Perovskite Solid Solutions," *Phys. Status Solidi Appl. Res.*, **181** [1] 211–218 (2000).
- 16 I.M. Reaney, E.L. Colla, and N. Setter, "Dielectric and Structural Characteristics of Ba- and Sr-based Complex Perovskites as a Function of Tolerance Factor," *Jpn. J. Appl. Phys.*, **33** [7R] 3984 (1994).
- 17 H.D. Megaw, *Crystal Structures: A Working Approach*. W. B. Saunders Company, London, United Kingdom, 1973.
- 18 M.R. Suchomel and P.K. Davies, "Predicting the Position of the Morphotropic Phase Boundary in High Temperature $PbTiO_3$ - $Bi(B'B'')O_3$ Based Dielectric Ceramics," *J. Appl. Phys.*, **96** [8] 4405–4410 (2004).
- 19 J.B. Goodenough, "Colossal Magnetoresistance in $Ln_{1-x}A_xMnO_3$ Perovskites," *Aust. J. Phys.*, **52** [2] 155–186 (1999).
- 20 A. Navrotsky, *Structure and Bonding in Crystals*. Academic Press, New York, 1981.

- 21 S. Lee, W.H. Woodford, and C.A. Randall, "Crystal and Defect Chemistry Influences on Band
Gap Trends in Alkaline Earth Perovskites," *Appl. Phys. Lett.*, **92** [20] 1–4 (2008).
- 22 W. Merz, "The Effect of Hydrostatic Pressure on the Curie Point of Barium Titanate Single
Crystals," *Phys. Rev.*, **77** [7] 52–54 (1950).
- 23 Y. Yoneda, T. Okabe, K. Sakaue, H. Terauchi, H. Kasatani, and K. Deguchi, "Structural
Characterization of BaTiO₃ Thin Films Grown by Molecular Beam Epitaxy," *J. Appl. Phys.*, **83** [5]
2458 (1998).
- 24 K.J. Choi, M. Biegalski, Y.L. Li, A. Sharan, J. Schubert, R. Uecker, P. Reiche, Y.B. Chen, X.Q.
Pan, V. Gopalan, L.-Q. Chen, D.G. Schlom, and C.B. Eom, "Enhancement of Ferroelectricity in
Strained BaTiO₃ Thin Films," *Science*, **306** [November] 1005–1009 (2004).
- 25 Y.L. Li and L.Q. Chen, "Temperature-Strain Phase Diagram for BaTiO₃ Thin Films," *Appl. Phys.
Lett.*, **88** [7] 1–4 (2006).
- 26 R. Sommer, N.K. Yushin, and J.J. Van Der Klink, "Polar Metastability and an Electric-Field-
Induced Phase Transition in the Disordered Perovskite Pb(Mg_{1/3}Nb_{2/3})O₃," *Phys. Rev. B*, **48** [18]
13230–13237 (1993).
- 27 H.F. Kay and P. Vousden, "Symmetry Changes in Barium Titanate at Low Temperatures and their
Relation to its Ferroelectric Properties," *London, Edinburgh, Dublin Philos. Mag. J. Sci.*, **40**
[309] 1019–1040 (1949).
- 28 W.J. Merz, "The Electric and Optical Behavior of BaTiO₃ Single-Domain Crystals," *Phys. Rev.*,
76 [8] 1221–1225 (1949).
- 29 M.J. Haun, E. Furman, S.J. Jang, H.A. McKinstry, and L.E. Cross, "Thermodynamic Theory of
PbTiO₃," *J. Appl. Phys.*, **62** [8] 3331–3338 (1987).
- 30 W. Ma and L.E. Cross, "Flexoelectricity of Barium Titanate," *Appl. Phys. Lett.*, **88** [23] 2001–
2004 (2006).
- 31 J.P. Remeika and A.M. Glass, "The Growth and Ferroelectric Properties of High Resistivity Single
Crystals of Lead Titanate," *Mat. Res. Bull.*, **5** 37–46 (1970).
- 32 D.D. Fong, G.B. Stephenson, S.K. Streiffer, J.A. Eastman, O. Auciello, P.H. Fuoss, and C.
Thompson, "Ferroelectricity in Ultrathin Perovskite Films," *Science (80-.)*, **304** [June] 1650–
1653 (2004).
- 33 J.F. Ihlefeld, D.T. Harris, R. Keech, J.L. Jones, J.P. Maria, and S. Trolier-McKinstry, "Scaling
Effects in Perovskite Ferroelectrics: Fundamental Limits and Process-Structure-Property
Relations," *J. Am. Ceram. Soc.*, **99** [8] 2537–2557 (2016).
- 34 G. Arlt, D. Hennings, and G. De With, "Dielectric Properties of Fine-Grained Barium Titanate
Ceramics," *J. Appl. Phys.*, **58** 1619–1625 (1985).
- 35 D. Ghosh, A. Sakata, J. Carter, P.A. Thomas, H. Han, J.C. Nino, and J.L. Jones, "Domain Wall
Displacement is the Origin of Superior Permittivity and Piezoelectricity in BaTiO₃ at Intermediate
Grain Sizes," *Adv. Funct. Mater.*, **24** [7] 885–896 (2014).
- 36 Z. Zhao, V. Buscaglia, M. Viviani, M.T. Buscaglia, L. Mitoseriu, A. Testino, M. Nygren, M.
Johnsson, and P. Nanni, "Grain-Size Effects on the Ferroelectric Behavior of Dense
Nanocrystalline BaTiO₃ Ceramics," *Phys. Rev. B - Condens. Matter Mater. Phys.*, **70** [2] 1–8
(2004).
- 37 M.T. Buscaglia, M. Viviani, V. Buscaglia, L. Mitoseriu, A. Testino, P. Nanni, Z. Zhao, M.
Nygren, C. Harnagea, D. Piazza, and C. Galassi, "High Dielectric Constant and Frozen
Macroscopic Polarization in Dense Nanocrystalline BaTiO₃ Ceramics," *Phys. Rev. B - Condens.
Matter Mater. Phys.*, **73** [6] 1–10 (2006).
- 38 M.H. Frey, Z. Xu, P. Han, and D.A. Payne, "The Role of Interfaces on an Apparent Grain Size
Effect on the Dielectric Properties for Ferroelectric Barium Titanate Ceramics," *Ferroelectrics*,
206 [1] 337–353 (1998).
- 39 C.T. Shelton, P.G. Kotula, G.L. Brennecka, P.G. Lam, K.E. Meyer, J.P. Maria, B.J. Gibbons, and

- J.F. Ihlefeld, "Chemically Homogeneous Complex Oxide Thin Films via Improved Substrate Metallization," *Adv. Funct. Mater.*, **22** [11] 2295–2302 (2012).
- 40 M.M. Saad, P. Baxter, R.M. Bowman, J.M. Gregg, F.D. Morrison, and J.F. Scott, "Intrinsic Dielectric Response in Ferroelectric Nano-Capacitors," *J. Phys. Condens. Matter*, **16** [41] (2004).
- 41 K. Kinoshita and A. Yamaji, "Grain-Size Effects on Dielectric Properties in Barium Titanate Ceramics," *J. Appl. Phys.*, **47** [1] 371–373 (1976).
- 42 D.T. Harris, M.J. Burch, J. Li, E.C. Dickey, and J.P. Maria, "Low-Temperature Control of Twins and Abnormal Grain Growth in BaTiO₃," *J. Am. Ceram. Soc.*, **98** [8] 2381–2387 (2015).
- 43 J.F. Ihlefeld, W.J. Borland, and J.-P. Maria, "Enhanced Dielectric and Crystalline Properties in Ferroelectric Barium Titanate Thin Films," *Adv. Funct. Mater.*, **17** [7] 1199–1203 (2007).
- 44 D.A. Buck, "Ferroelectrics for Digital Information Storage and Switching," M.S. Thesis, Massachusetts Institute of Technology, 1952.
- 45 D.H. Looney, Semiconductive Translating Device, U.S. Patent 2 791 758, 1957.
- 46 W.L. Brown, Semiconductive Device, U.S. Patent 2 791 259, 1957.
- 47 I.M. Ross, Semiconductive Translating Device, U.S. Patent 2 791 760, 1957.
- 48 J.A. Morton, Electrical Switching and Storage, U.S. Patent 2 791 761, 1957.
- 49 J.L. Moll and Y. Tarui, "A New Solid State Resistor," *IEEE Trans. Electron Devices*, **10** [5] 338–339 (1963).
- 50 G.A. Rohrer, Thin Film Ferroelectric Device, US Patent 3728694 A, 1973.
- 51 S.-Y. Wu, "A New Ferroelectric Memory Device, Metal-Ferroelectric-Semiconductor Transistor," *IEEE Trans. Electron Devices*, **ED=21** [8] 499–504 (1974).
- 52 A. Okada, "Some Electrical and Optical Properties of Ferroelectric Lead-Zirconate-Lead-Titanate Thin Films," *J. Appl. Phys.*, **48** [7] 2905–2909 (1977).
- 53 A. Okada, "Electrical Properties of Lead-Zirconate-Lead-Titanate Ferroelectric Thin Films and Their Composition Analysis by Auger Electron Spectroscopy," *J. Appl. Phys.*, **49** [8] 4495–4499 (1978).
- 54 M. Ishida, H. Matsunami, and T. Tanaka, "Preparation and Properties of Ferroelectric PLZT Thin Films by RF Sputtering," *J. Appl. Phys.*, **48** 951–953 (1977).
- 55 T. Nakagawa, J. Yamaguchi, T. Usuki, Y. Matsui, M. Okuyama, and Y. Hamakawa, "Ferroelectric Properties of RF Sputtered PLZT Thin Film," *Jpn. J. Appl. Phys.*, **18** [5] 897–902 (1979).
- 56 J.T. Evans, W.D. Miller, and R.H. Womack, Non-Volatile Memory Circuit Using Ferroelectric Capacitor Storage Element, US Patent 8023308 B1, 1987.
- 57 Fujitsu Microelectronics, *FRAM Guide Book*, Fujitsu, (2008).
- 58 P.C. Lacaze and J. Lacroix, "Evolution of SSD Toward FeRAM, FeFET, CTM, and STT-RAM Memories," in *Non-Volatile Memories*. John Wiley & Sons, Inc., Hoboken, NJ, USA, 2014.
- 59 Y. Arimoto and H. Ishiwara, "Current Status of Ferroelectric Random Access Memory," *MRS Bull.*, **29** [11] 823–828 (2004).
- 60 J.S. Meena, S.M. Sze, U. Chand, and T.Y. Tseng, "Overview of Emerging Nonvolatile Memory Technologies," *Nanoscale Res. Lett.*, **9** [1] 1–33 (2014).
- 61 R.E. Jones, "Ferroelectric Nonvolatile Memories for Embedded Applications," *Proc. IEEE 1998 Cust. Integr. Circuits Conf. (Cat. No. 98CH36143)*, 431–438 (1998).
- 62 Cypress Semiconductor Corporation, *F-RAM™ Technology Brief*, [June] 1–5 (2016).
- 63 J. Rodriguez, K. Remack, J. Gertas, L. Wang, C. Zhou, K. Boku, K.R. Udayakumar, S. Summerfelt, T. Moise, D. Kim, J. Groat, J. Eliason, M. Depner, and F. Chu, "Reliability of Ferroelectric Random Access Memory Embedded within 130nm CMOS," pp. 750–758 in *Reliab. Phys. Symp. (IRPS), 2010 IEEE*. 2010.
- 64 F. Gan and Y. Wang, *Data Storage at the Nanoscale: Advances and Applications*. CRC Press, Boca Raton, FL, 2015.
- 65 B.A. Tuttle, "Pb(Zr,Ti)O₃ Based Thin Film Ferroelectric Memories," pp. 145–165 in *Thin Film*

- Ferroelectr. Mater. Devices.* 1997.
- 66 W.L. Warren, B.A. Tuttle, D. Dimos, G.E. Pike, H.N. Al-Shareef, R. Ramesh, and J.T. Evans,
 “Imprint in Ferroelectric Capacitors,” *Jpn. J. Appl. Phys.*, **35** 1521–1524 (1996).
- 67 N. Inoue and Y. Hayashi, “Effect of Imprint on Operation and Reliability of Ferroelectric Random
 Access Memory (FeRAM),” *IEEE Trans. Electron Devices*, **48** [10] 2266–2272 (2001).
- 68 W.L. Warren, D. Dimos, G.E. Pike, B. a. Tuttle, M. V. Raymond, R. Ramesh, and J.T. Evans,
 “Voltage Shifts and Imprint in Ferroelectric Capacitors,” *Appl. Phys. Lett.*, **67** [1995] 866 (1995).
- 69 M. Grossmann, O. Lohse, D. Bolten, U. Boettger, R. Waser, W. Hartner, M. Kastner, and G.
 Schindler, “Lifetime Estimation Due to Imprint Failure in Ferroelectric SrBi₂Ta₂O₉ Thin Films,”
Appl. Phys. Lett., **76** [2000] 363–365 (2000).
- 70 S. Kawashima and J.S. Cross, “FeRAM,” pp. 279–328 in *Embed. Memories Nano-Scale VLSIs*.
 2009.
- 71 H. Ishiwara, “Ferroelectric Random Access Memories,” *J. Nanosci. Nanotechnol.*, **12** 7619–7627
 (2012).
- 72 M.E. Lines and A.M. Glass, *Principles and Applications of Ferroelectrics and Related Materials*.
 Oxford University Press, 1977.
- 73 Y.Y. Tomashpol’skii, E. V. Zubova, K.P. Burdina, and Y.N. Venevtse, “X-Ray Investigations of
 New Perovskites Formed at High Pressures,” *Sov. Phys. Cryst.*, **13** [6] 859–861 (1969).
- 74 G.D. Achenbach, W.J. James, and R. Gerson, “Preparation of Single-Phase Polycrystalline
 BiFeO₃,” *J. Am. Ceram. Soc.*, **50** 437 (1967).
- 75 Y.Y. Tomashpol’skii, V.M. Skorikov, Y.N. Venevtsev, and E.I. Speranskaya, “On The Growth
 and Certain Structural Investigations of Single Crystals of Ferromagnetic BiFeO₃,” *Inorg. Mater.*,
2 [4] 607–611 (1966).
- 76 J.R. Giniewicz, R.E. Newnham, A. Safari, and D. Moffatt, “(Pb,Bi)(Ti,Fe,Mn)O₃ Polymer 0-3
 Composites for Hydrophone Applications,” *Ferroelectrics*, **73** [3–4] 405–417 (1987).
- 77 R.E. Eitel, C.A. Randall, T.R. Shrout, and S.-E. Park, “Preparation and Characterization of High
 Temperature Perovskite Ferroelectrics in the Solid-Solution (1-x)BiScO₃-xPbTiO₃,” *Jpn. J. Appl.*
Phys., **41** [Part 1, No. 4A] 2099–2104 (2002).
- 78 M.R. Suchomel and P.K. Davies, “Enhanced Tetragonality in (x)PbTiO₃-(1-x)Bi(Zn_{1/2}Ti_{1/2})O₃ and
 Related Solid Solution Systems,” *Appl. Phys. Lett.*, **86** [26] 1–3 (2005).
- 79 D.M. Stein, M.R. Suchomel, and P.K. Davies, “Enhanced Tetragonality in (x)PbTiO₃-(1-
 x)Bi(B’_{1/2}B’’_{1/2})O₃ Systems: Bi(Zn_{3/4}W_{1/4})O₃,” *Appl. Phys. Lett.*, **89** [13] 89–92 (2006).
- 80 C.J. Stringer, T.R. Shrout, C.A. Randall, and I.M. Reaney, “Classification of Transition
 Temperature Behavior in Ferroelectric PbTiO₃-Bi(Me’Me’’)O₃ Solid Solutions,” *J. Appl. Phys.*, **99**
 [2] 24106 (2006).
- 81 S.M. Choi, C.J. Stringer, T.R. Shrout, and C.A. Randall, “Structure and Property Investigation of a
 Bi-Based Perovskite Solid Solution: (1-x)Bi(Ni_{1/2}Ti_{1/2})O₃-xPbTiO₃,” *J. Appl. Phys.*, **98** [3] 34108
 (2005).
- 82 S. Zhang, C. Stringer, R. Xia, S.-M. Choi, C.A. Randall, and T.R. Shrout, “Investigation of
 Bismuth-Based Perovskite System: (1-x)Bi(Ni_{2/3}Nb_{1/3})O₃-xPbTiO₃,” *J. Appl. Phys.*, **98** [3] 34103
 (2005).
- 83 C.A. Randall, R. Eitel, B. Jones, T.R. Shrout, D.I. Woodward, and I.M. Reaney, “Investigation of
 a High T_c Piezoelectric System: (1-x)Bi(Mg_{1/2}Ti_{1/2})O₃-(x)PbTiO₃,” *J. Appl. Phys.*, **95** [7] 3633
 (2004).
- 84 R.D. Shannon, “Revised Effective Ionic Radii and Systematic Studies of Interatomic Distances in
 Halides and Chalcogenides,” *Acta Cryst.*, **A32** 751–767 (1976).
- 85 J.P. Attfield, A.L. Kharlanov, and J.A. McAllister, “Cation Effects in Doped La₂CuO₄
 Superconductors,” *Nature*, **394** 157–159 (1998).
- 86 R.E. Eitel, S.J. Zhang, T.R. Shrout, C.A. Randall, and I. Levin, “Phase Diagram of the Perovskite

- System $(1-x)\text{BiScO}_3-x\text{PbTiO}_3$,” *J. Appl. Phys.*, **96** [5] 2828–2831 (2004).
- ⁸⁷ J. Liu, X. Chen, G. Xu, D. Yang, Y. Tian, and X. Zhu, “Novel High-Temperature Ferroelectric Single Crystals $0.38\text{Bi}(\text{Mg}_{1/2}\text{Ti}_{1/2})\text{O}_3-0.62\text{PbTiO}_3$ with Good and Temperature-Stable Piezoelectric Properties,” *CrystEngComm*, **17** [30] 5605–5608 (2015).

Chapter 3 Experimental Procedures

This chapter discusses the experimental procedures and characterization techniques utilized in this thesis. 3 separate processing techniques are utilized in this thesis. Primarily, pulsed laser deposition (PLD) was utilized to deposit thin films. Second, all PLD targets with varying compositions were processed using standard ceramic processing. Third, chemical solution deposition was utilized to deposit seed undoped and doped PbTiO_3 seed layers. Films were structurally characterized utilizing x-ray diffraction (XRD), scanning electron microscopy (SEM), and transmission electron microscopy (TEM). Electrical and optical analysis is also discussed.

3.1 PLD Target Processing

Ceramic targets with varying compositions were batched using standard ball milling, calcination and sintering. Briefly, Pb_3O_4 , $4\text{MgCO}_3\text{Mg}(\text{OH})_2 \bullet 4\text{H}_2\text{O}$ (40-43.5% MgO, Alfa Aesar), TiO_2 (cr-el grade, 99.9%, Ishihara Sangyo Kaisha), and Bi_2O_3 (varistor grade, 99.99%, MCP Metal Specialties) were batched in a stoichiometric ratio and ball milled in ethanol for 24 hours. Ignition losses for each powder were taken into account for determining the batch composition. Powders were weighed after heating to 110-120 °C to limit adsorbed water. Batches were all $\geq 25\text{g}$ to limit minor nonstoichiometries related to errors weighing powders. All measured weights were $\leq 0.008\text{g}$ to the calculated stoichiometry. After drying at 85 °C, the powder was calcined at 775 °C for 4 hours. Varying amounts of Bi_2O_3 , PbO (Pb_3O_4 calcined at 700 °C for 1 hour), and MgCO_3 excesses were added to the stoichiometric batch to obtain the final target composition. Table 3.1 gives the batched compositions of the targets employed

throughout this thesis. The powders were vibratory milled for 12 hours, dried at 85 °C, pressed into pellets and sintered at 825 °C for 2 to 4 hours.

Table 3.1 – List of target compositions investigated throughout this thesis.

| Target Name | Pb Excess (mol%) | Bi Excess (mol%) | Mg Excess (mol%) |
|--------------|------------------|------------------|------------------|
| 20Pb10Bi0Mg | 20% | 10% | 0% |
| 30Pb15Bi5Mg | 30% | 15% | 5% |
| 48Pb20Bi10Mg | 48% | 20% | 10% |
| 65Pb20Bi10Mg | 65% | 20% | 10% |
| 85Pb20Bi10Mg | 85% | 20% | 10% |

3.2 PLD Substrate Processing

The 35BiMT-65PT films were deposited on PbTiO₃/Pt/Ti/SiO₂/Si substrates or Pt/Ti/SiO₂/Si substrates. An undoped PbTiO₃ or 5 mol% La-doped PbTiO₃ seed layer was deposited on the Pt-coated Si substrates using a chemical solution deposition technique to facilitate perovskite nucleation. Lead acetate trihydrate, titanium isopropoxide (97%), lanthanum acetate hydrate, 2-methoxyethanol (2-MOE) and acetylacetonate (ACAC) (all from Sigma-Aldrich Inc., St. Louis, MO) were used as raw materials. Lead acetate (40mol% excess) and lanthanum acetate were dissolved in 2-MOE and distilled in a rotary evaporator under Ar gas flow until precipitation. A solution was made by adding titanium isopropoxide and 2-MOE to the precipitated powder with half the molarity of the final solution. After refluxing for 3 hours, the solution was distilled, and ACAC and 2MOE was added to reach the final solution molarity. Figure 3.1 shows the process flow diagram for making undoped and La-doped PbTiO₃ solution. The solution was spun on the substrate at 3000 rpm for 45 seconds, pyrolyzed at 225 °C and 400 °C for 2 minutes each, and crystallized at 600 °C under oxygen flow for 1 minute in a rapid thermal annealing. The PbTiO₃ seed layer thickness was controlled by adjusting the solution molarity. Figure 3.2 shows the measured thickness of PbTiO₃ as a function of solution molarity.

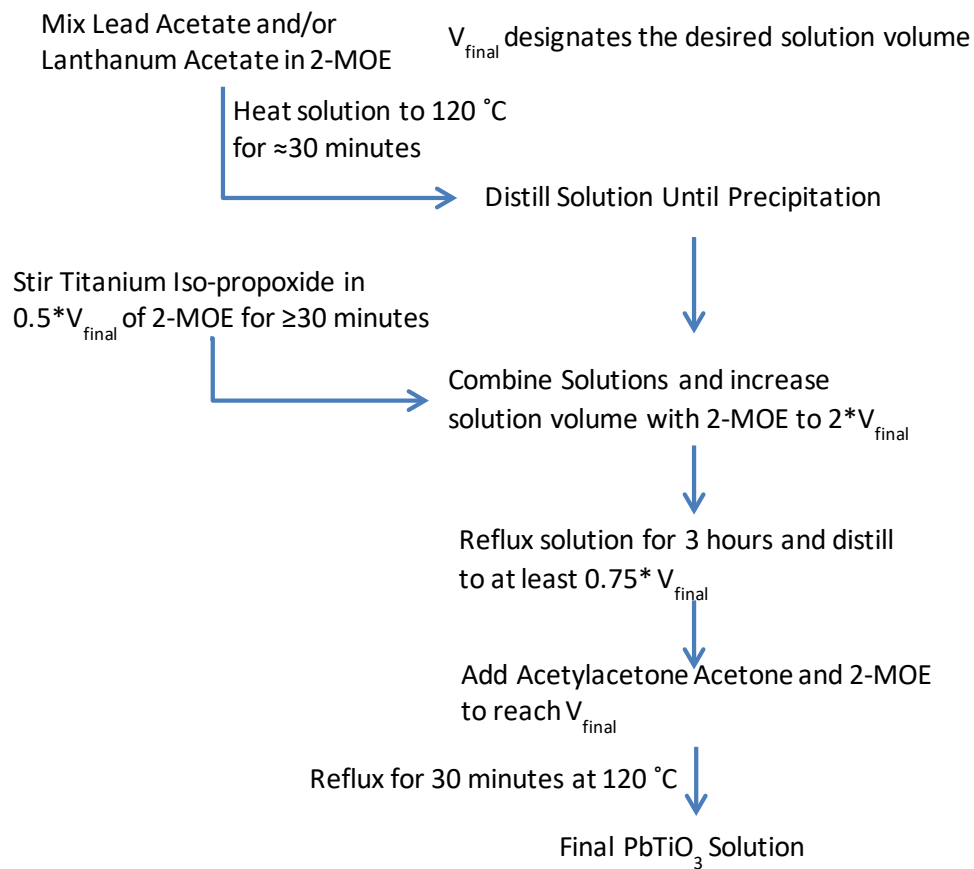


Figure 3.1- Process flow diagram for developing PbTiO_3 solutions.

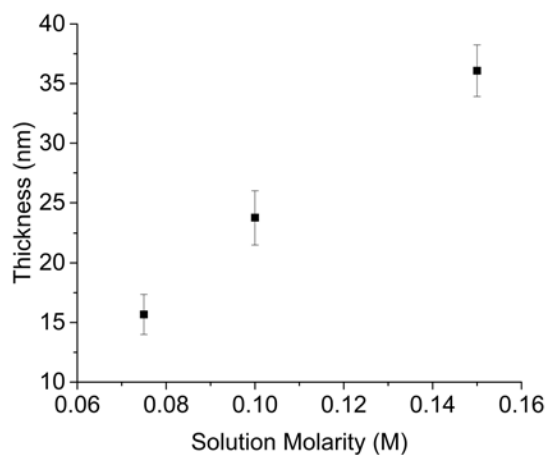


Figure 3.2 – Film thickness vs solution molarity of PbTiO_3 seed layers. Thickness measurements were determined via scanning electron microscope cross section images.

3.3 PLD Processing

Pulsed laser deposition (PLD) was used to deposit 35BiMT-65PT films on the seeded substrates and unseeded substrates. All substrates were diced into 5 mm X 5 mm squares after deposition of seed layers if utilized. For all depositions, substrates were cleaned via ultrasonication in acetone, ethanol and isopropyl alcohol for ≥ 5 minutes. Substrates were bonded to a substrate heater using a silver paste to insure good thermal contact. A KrF excimer laser (Lambda Physik Compex 102, Fort Lauderdale, FL) with an energy density of $\approx 1.6 \pm 0.1$ J/cm² was used for ablation. Targets were pre-ablated with 1200 pulses at 20 Hz. After aligning the substrate to the ablation spot, the chamber was pumped down to $\approx 10^6 - 10^7$ Torr. Several different atmospheres were utilized throughout this work. A 90%/10% O₂/O₃ mixed gas was employed as the background atmosphere in both seeded and seedless growths. An Ar/O₂ mixed gas was utilized for seedless growths where stated. During deposition, the chamber pressures were varied between 60 and 400 mTorr where specified. For all samples, the target to substrate distance was maintained at 6 cm and the substrate temperature was maintained at 700°C. These parameters were chosen based on conditions for growing BiS-PT and PMN-PT, as well as further optimization.^{1,2} The thin film growth rates for the most common growth conditions at 340 mTorr, 700 °C, and 6 cm target to substrate distance varied between ≈ 1.00 to 1.33 nm/s. Variations in the growth rate occurred due to inconsistencies with substrate alignment to the plume from sample to sample.

3.4 Structural and Composition Characterization

The films' phase purity was studied using a Philips Empyrean X-ray diffractometer with CuK α radiation. The film microstructures were observed using a Leo 1530 or a Merlin Field Emission Scanning Electron Microscope (FESEM) (Carl Zeiss Microscopy GmbH, Jena, Germany). Film compositions were determined from focused ion beam (FIB) milled cross-sections using energy dispersive x-ray

spectroscopy (EDS) on a FEI Talos transmission electron microscope (TEM) operated at 200 kV in scanning TEM (STEM) mode. High angular dark field (HAADF) images were collected; the resulting image primarily shows mass contrast approximately proportional to the square of the atomic number of the elements present. EDS data were collected using the Bruker Super-X quad x-ray detectors for 5 minutes with a beam current of approximately 0.25 nA.

3.5 Electrical Characterization

Electrical properties were tested using lithographically-defined Pt top electrodes. The electrodes were deposited in a Lesker CMS-18 sputter tool at an Ar pressure of 2.5 mTorr, and patterned by lift-off. All electrodes were annealed at 600 °C for 1 minute in flowing O₂. Prior to top electrode deposition, samples were wet etched to expose the bottom electrode. 1813 photoresist was painted on samples to define the area to be etched and cured at 105 °C for 2 minutes. A drop of 10:1 buffered oxide etch followed by a drop of hydrochloric acid were used to etch the film. The sample was washed in deionized water and the etching process was repeated until the bottom electrode was cleanly exposed. The photoresist was removed using acetone.

3.5.1 Ferroelectric Property Measurement and Retention

The thin film ferroelectric properties were studied using a Radiant Precision Multiferroic tester. Polarization – electric field (P-E) data were taken at 1 kHz and 10 kHz. Positive – up – negative – down (PUND)³ measurements were used to separate the ferroelectric switching and non-ferroelectric switching charges. Briefly, the PUND measurement is a series of 5 voltage pulses as demonstrated in Figure 3.3. The first pulse sets the ferroelectric into a known polarization state. The second voltage pulse applies the opposite sign voltage to switch the ferroelectric polarization resulting in a switching charge. The third

pulse applies the voltage of the same sign as the second pulse. Charges associated with this pulse are attributed to non-ferroelectric switching charges or backswitched domains. The fourth and fifth pulses repeat the same process, but for the opposite polarization state. All PUND data were acquired with a 1 ms pulse and 1 ms delays between pulses.

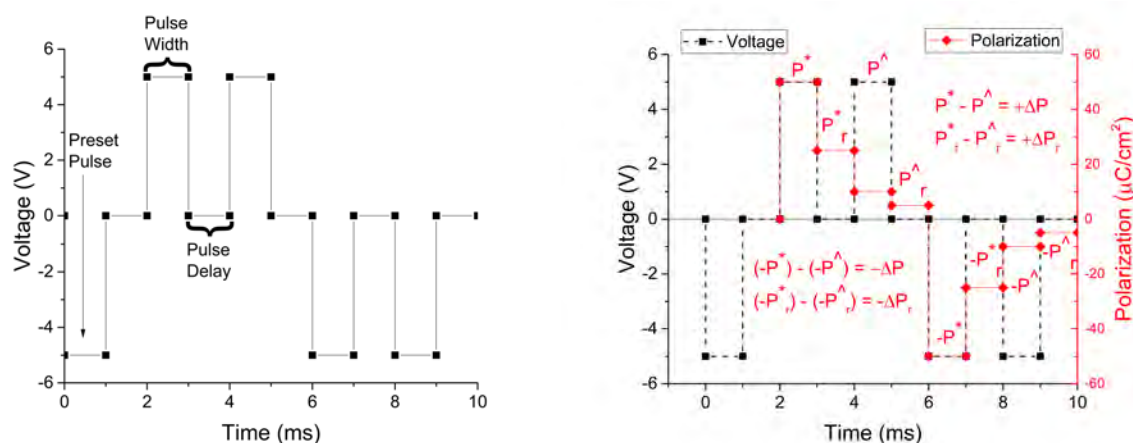


Figure 3.3 – Schematic PUND pulse sequence (left) and resulting charges when the field is applied and removed (right). P^* and P_r^* refer to charges from the total switching current. P^{\wedge} and P_r^{\wedge} refer to charges not associated with ferroelectric switching. The difference between the “*” and “^” calculates ΔP . Ideally ΔP and ΔP_r are equal.

Retention analysis was performed to determine the stability of the ferroelectric polarization without an electric field over time using the PUND test. Same state retention was done utilizing the first 3 pulses of the PUND test. The pulse width was maintained at 1 ms, but the pulse delay was varied.

3.5.2 Dielectric Property Measurements and I-V Measurements

Dielectric properties were measured using a 30 mV oscillation between 1 kHz – 1 MHz using an LCR meter (HP 4284 for room temperature and Agilent HP 4980 for high temperature). Current-voltage (I-V) measurements were measured using a pA meter (HP 4140B). The leakage current was measured using 5 kV/cm electric field steps after holding the dc field for 1 minute at each step. High temperature dielectric permittivity and I-V measurements were performed on a home built hot stage. The hot stage was built with fiberfrax insulation and ceramic bricks to insulate the side of the hot stage. The top was

insulated using silicone sandwiched between two fused quartz plates. The samples are electrically insulated from the copper heating block using an AlN ceramic plate. A K-type thermocouple was bonded to the surface near the sample to measure the temperature. To insure accuracy of the thermocouple measurement, a separate surface probe was utilized to measure the surface temperature. The variance in temperature between the bonded thermocouple and surface probe was within 5 °C up to 500 °C. Figure 3.4 shows a schematic diagram of the hot stage.

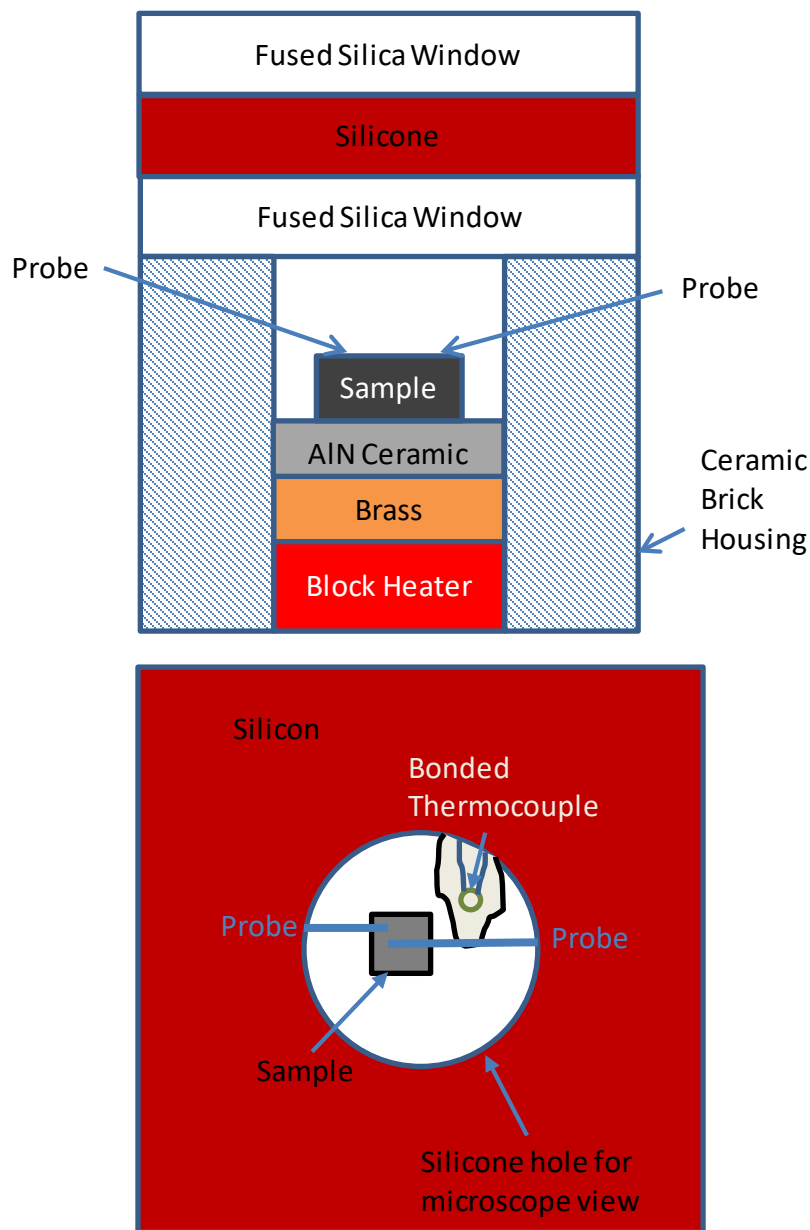


Figure 3.4 – Schematic diagram showing a cross-section of the home built high temperature probe station (top) and top-down view illustrating the microscope view (bottom). All samples were placed in the same position with respect to the bonded thermocouple.

3.5.3 Optical Property

Optical properties of 35BiMT-65PT were measured using a Woollam variable angle spectroscopic ellipsometer (VASE). Single crystal SrTiO₃ substrates (Crystec, Berlin, Germany) were used for the VASE measurements. Films were grown on SrTiO₃ utilizing the deposition parameters shown in Table 3.2. Optical properties were fitted between 500-1200 nm using a Sellmeier model:

$$n = \left(\varepsilon(\infty) + \frac{A\lambda^2}{\lambda^2 - B^2} - E\lambda^2 \right)^{\frac{1}{2}} \quad \text{Eq. 3.1}$$

where A is the amplitude, B is the wavelength of the central energy, E is position of the pole in the infrared, λ is the wavelength, and $\varepsilon(\infty)$ is the index offset (forced to equal 1). In addition, the surface roughness is also taken into account in the models by using a Bruggeman effective medium mixing of the optical coefficients of the film and air. The Sellmeier model parameters for the SrTiO₃ are shown in Table 3.3.

Table 3.2 - Deposition parameters for growing 35BiMT-65PT on single crystal SrTiO₃ substrates

| Parameter | Value |
|------------------------------|---|
| Target Composition | 20 mol% Pb and 10 mol% Bi excess |
| Energy Density | 1.6 J/cm ² |
| Deposition Temperature | 700 °C |
| Target to Substrate Distance | 6 cm |
| Deposition Pressure | 340 mTorr 90% O ₂ / 10% O ₃ |
| Laser Repetition Rate | 10 Hz |
| Substrate | SrTiO ₃ |

Table 3.3 - SrTiO₃ fitted Sellmeier model parameters. Parameter correlation was less than 0.9 for fitted parameters.

| Fitting Parameter | Value |
|--|--------------------|
| Amplitude (μm^2) | 4.158 ± 0.002 |
| Wavelength of Central Energy (μm) | 0.216 ± 0.0005 |
| IR Pole Amplitude (μm^{-2}) | 0 |
| $\varepsilon(\infty)$ | 1 |
| Thickness of Surface Roughness | 0.44 ± 0.01 nm |
| Mean Squared Error (MSE) | 2.01 |

3.6 References

- ¹ J.C. Nino and S. Trolier-McKinstry, "Dielectric, Ferroelectric, and Piezoelectric Properties of (001) BiScO₃-PbTiO₃ Epitaxial Films Near the Morphotropic Phase Boundary," *J. Mater. Res.*, **19** [2] 568–572 (2004).
- ² J. Maria, W. Hackenberger, and S. Trolier-McKinstry, "Phase Development and Electrical Property Analysis of Pulsed Laser Deposited Pb(Mg_{1/3}Nb_{2/3})O₃-PbTiO₃ (70/30) Epitaxial Thin Films," *J. Appl. Phys.*, **84** [9] 5147–5154 (1998).
- ³ J.A. Rodriguez, K. Remack, K. Boku, K.R. Udayakumar, S. Aggarwal, S.R. Summerfelt, F.G. Celii, S. Martin, L. Hall, K. Taylor, T. Moise, H. Mcadams, J. Mcpherson, S. Member, R. Bailey, G. Fox, and M. Depner, "Reliability Properties of Low-Voltage Ferroelectric Capacitors and Memory Arrays," *IEEE Trans. Device Mater. Reliab.*, **4** [3] 436–449 (2004).

Chapter 4

Influence of Processing on Composition, Microstructure and Ferroelectric Hysteresis

4.1 Introduction

Since the 1990's, lead zirconate titanate (PZT) has provided a stable platform for the production of non-volatile ferroelectric random access memory (FeRAM) technology, but new materials are being sought to replace it.¹ Currently, Texas Instruments produces state of the art embedded PZT FeRAM on 130 nm node CMOS, with an operating life of 10 years and 1000 hours at 85°C and 125°C.² Nonvolatile ferroelectric memories are also available from Cypress, Matsushita (Panasonic), Fujitsu, and Rohm.³⁻⁶ Increasing the operating temperature of FeRAM would extend its utility to harsher environments, including automotive applications. While a significant amount of research is dedicated to the scaling of thin film ferroelectrics for FeRAM,^{2, 7-12} high temperature functionality of the films has not been explored as extensively. Ultimately, the practical limiting use temperature is a fraction of the Curie Temperature (T_c). Films with high Curie temperatures and large switchable polarizations are of potential interest for high temperature FeRAM.

As discussed in Chapter 2, Eitel *et al.* predicted, based on the Goldschmidt tolerance factor, that several Bi-based-PbTiO₃ solid solutions should have higher transition temperatures than PZT at the morphotropic phase boundary (MPB).¹³⁻¹⁷ The following work focuses on the class II material Bi(Mg_{1/2}Ti_{1/2})O₃-PbTiO₃ based on Stringer *et al.*'s classification.^{18, 19} As seen in Figure 2.17, the bulk of the literature has focused on compositions around the MPB. Suchomel and Davies utilized the tolerance factor of the non-PbTiO₃ end member of known systems to narrow the predicted region for the MPB location (close to $x = 62$ to 64 in BiMT-PT).²⁰ Randall *et al.* refined the MPB compositional region utilizing piezoelectric (d_{33}), poled permittivity and X-ray diffraction measurements. They found that it was hard to pinpoint the exact MPB composition due to the propensity for formation of grains with core-

shell structures associated with compositional gradients.¹⁶ BiMT-PT ceramics were reported to have remanent polarizations of $\approx 33\text{-}38 \mu\text{C}/\text{cm}^2$ (at the MPB of $x=0.36$ PT)^{16,21} and $25 \mu\text{C}/\text{cm}^2$ (at $x=0.5$ PT)²². Compositions around the MPB had increased P_r and decreased the coercive field, E_c , and were resistant to thermal depoling to at least 175°C .^{21,23} Some reports suggest that there is limited domain wall mobility for some BMT-PT with high transition temperatures due to large lattice distortions²¹ or defects. Nonetheless, reasonable switchability is observed. In short, BiMT-PT materials demonstrate promise as an alternative high temperature piezoelectric without requiring use of scandium.

The literature on thin film Bi-based-PbTiO₃ solid solutions is considerably smaller than that on bulk ceramics. Zhong *et al.* grew 600 nm 100_c oriented 63BiMT-37PT thin films with a P_r of $24 \mu\text{C}/\text{cm}^2$ and a relative permittivity, ϵ_r , maximum at $\approx 415^\circ\text{C}$. Zhang *et al.* measured undoped and 0.5 mol% Mn doped 20BiMT-80PT thin films, reporting a stable polarization-electric field response to 125°C and fatigue resistance up to 10^8 cycles. Tanaka *et al.* and Oikawa *et al.* studied 111_c epitaxial BiMT films, a composition where the perovskite phase is metastable under ambient conditions. Oikawa *et al.*'s films demonstrated little change in P_r over the thickness range of 50-800nm.^{24,25} Other Bi(Me' Me'')O₃-PbTiO₃ solid solution thin films have also been produced, including BiScO₃-PbTiO₃ (BiS-PT)²⁶, BiInO₃ (BiI-PT)^{27,28}, BiAlO₃-PbTiO₃ (BiA-PT)²⁹, BiFeO₃-PbTiO₃ (BiF-PT),³⁰⁻³² and Bi(Zn_{1/2}Zr_{1/2})O₃-PbTiO₃ (BiZZ-PT)³³. Of the studied Bi(Me' Me'')O₃-PbTiO₃ thin films, BiS-PT, BiMT-PT, and BiI-PT are materials which may be able to withstand harsh environments for actuators, sensors and FeRAM devices. 0.5 mol% Mn-doped xBiI-(1-x)PT ($x=0.1\text{-}0.25$) exhibit high transition temperatures ($558^\circ\text{C}\text{-}633^\circ\text{C}$) and P_r ($25\text{-}44 \mu\text{C}/\text{cm}^2$), but a large frequency dispersion in $\tan(\delta)$ with temperature from 1 kHz to 1 MHz above 200°C . 001_c epitaxial 60BiScO₃-40PbTiO₃ demonstrate a $P_r \approx 42 \mu\text{C}/\text{cm}^2$, $\epsilon_{r,\text{max}}$ at $T \approx 455^\circ\text{C}$, and maintains a low loss (<0.1 at 100 kHz) up to 550°C .²⁶ BiMT-PT³⁴, BiA-PT²⁹ and BiZZ-PT³³ all demonstrate leakage currents of $10^{-5} \text{ A}/\text{cm}^2$ or less at 150 kV/cm, at least an order of magnitude less than that reported for 0.6BiFeO₃-0.4PbTiO₃ thin films,³⁰ presumably due to the lower likelihood of electron hopping in the iron-free compositions.

The possibility for BiMT-PT ferroelectrics with large remanent polarizations, a stable high temperature polarization, and a relatively thickness-independent P_r to film thicknesses of 50 nm are encouraging for developing next generation high temperature FeRAM. However, there is still a significant gap in knowledge in the development of BiMT-PT ferroelectrics. As noted in Figure 2.17, there is uncertainty in T_c as a function of composition, particularly near $T_{c,max}$. This is particularly notable for the thin film literature. For example, Liu *et al.* reported unseeded and seeded 63BiMT-37PT with $P_r \approx 18 \mu\text{C}/\text{cm}^2$ and $\approx 14\text{-}15 \mu\text{C}/\text{cm}^2$, respectively,^{35,36} but Zhong *et al.* report $\approx 8 \mu\text{C}/\text{cm}^2$ and $\approx 24 \mu\text{C}/\text{cm}^2$, respectively,³⁷ for the same composition. Liu *et al.*'s films show significantly increased leakage³⁸ compared to those in bulk ceramics. In addition, there are discrepancies between reported film and crystal properties.^{26,39-43}

This chapter investigates a relatively unexplored composition in the BiMT-PT solid solution, with an emphasis on processing-structure-property relationships. In particular, one aspect that has little attention in the literature is the defect chemistry of systems in which both Pb and Bi occupy the A site of the perovskite lattice, and the role of A-site point defects on electrical properties. Aliovalent point defects in Pb based perovskites play a significant role in controlling domain wall mobility, though V''_{Pb} have been shown to have only a minor influence on the electrical response in PZT.⁴⁴ 35BiMT-65PT was chosen as a model system, as it is near $T_{c,max}$ in the BiMT-PT system. This chapter focuses on the processing-composition-ferroelectric hysteresis response of these materials. The following chapter focuses on the thickness dependence of the electrical properties, high temperature P-E behavior, and charge injection of A-site deficient 35BiMT-65PT thin films.

4.2 35BiMT-65PT Thin Film Structure and Processing Window

In pulsed laser deposition, there are a wide variety of interrelated processing variables that control the plume-substrate interactions and influence the resulting film structure and properties. To explore this processing space, the substrate temperature was held fixed at 700°C, the target to substrate distance at 6

cm and the laser fluence at 1.6 ± 0.1 J/cm². The deposition pressure, target composition and laser deposition rate were then varied systematically. See appendix C for lattice parameter calculations as a function of each variable and comparison to film properties.

Figure 4.1 shows XRD patterns as a function of chamber pressure during deposition utilizing a target with 20 mol% excess Pb and 10 mol% excess Bi (called 20Pb10Bi0Mg from here on), along with a representative TEM cross-section showing the elemental map. For all of the processing conditions, unless stated otherwise, the films are $\{100\}_c$ oriented with a columnar grain structure. Film roughness decreases with lower deposition pressure due to an increase in bombardment energy as suggested by the Thornton structure zone model.⁴⁵ Figure 4.2 shows the film roughness decreases particularly as the deposition pressure decreases below 100 mTorr. AFM images in Figure 4.2 (d) and (e) show the RMS roughness decreases from ≈ 37 nm to ≈ 16 nm between as the deposition pressure decreased from 340 mTorr to 60 mTorr. EDS elemental mapping shows the films do not exhibit large spatial elemental segregation. Finally, Figure 4.2 (c) shows the seed layer of is still present in the films after deposition. As such, any models discussing electrical properties discussing capacitor in series models utilize measured seed layer thicknesses rather than assuming a dead layer at the platinum interface.

It is interesting to note the exceptionally wide processing window seen in Figure 4.1. The material is phase pure within the detection limits of XRD and secondary phases were not seen in TEM or SEM except where noted later in this chapter. To determine what potential limits there are the processing window, samples were made with a target utilizing only 10 mol% excess Pb and with both varying pressure and temperature. In lowering the excess compensation to only 10%, the material was expected to show some amount of secondary phase formation. Figure 4.3 shows the resulting XRD patterns from the examined deposition parameters. Several points are seen in this experiment. The perovskite phase is easily stabilized with relatively little compensation of either volatile PbO and Bi₂O₃ in the target. Changing the pressure is expected to change the bombardment energy, leading to greater loss of the volatile species, yet all materials are still phase pure when deposited on a PbTiO₃ seed layer. Changing

the deposition temperature to lower temperatures should increase the relative amount of volatile species in the growing film, yet no second phase is apparent in the X-ray patterns at temperatures as low as 600 °C. It is notable that in PZT films, it is often difficult to detect excess PbO, and it is possible that the same phenomenon is being observed here.

Ideally, a room temperature deposited film is significantly richer in volatile species than those deposited at high temperature. This might be expected to change the amount of secondary phase present, or possibly change the film orientation. As an initial test, samples were deposited at chamber pressures of 100 or 160 mTorr pressure for 45 seconds and crystallized in a rapid thermal annealer to create a BiMT-PT “seed” layer, rather than utilizing a sol-gel deposited PbTiO₃ seed. The samples were crystallized for 1 minute in 10 sccm flowing O₂ at various temperatures. Figure 4.4 shows the XRD patterns of the films deposited at 100 and 160 mTorr. There is an increase in the peak intensity as the pressure is decreased to 100 mTorr and secondary phases were not detected in XRD. This may suggest that the change in bombardment energy does change the amount of PbO/Bi₂O₃ in the as deposited film. Too much excess PbO/Bi₂O₃ may hinder the formation of the perovskite phase or limit preferential orientation in any specific direction.

Based on the improved orientation at lower deposition pressures, a more detailed study was performed at lower pressures and higher temperatures. Figure 4.5 shows the XRD profiles for films deposited at 60, 80 or 100 mTorr with RTA crystallization at temperatures between 700 °C and 760 °C. The resulting film microstructures are shown in Figure 4.6. Little change is seen in the XRD patterns as the pressure is changed. Similarly, there is only a modest change in the film microstructures with changing pressure and temperature. All films show grain sizes around 50 nm. There are some new microstructural features seen in the film grown at 60 mTorr and crystallized at 760 °C, but it is unclear at this point whether these belong to a second phase or not. Except for the 60 mTorr/760 °C sample, all other films were phase pure by XRD.

To assess if these layers may be utilized as seed layers, a BiMT-PT film was deposited on the 100 mTorr / 760 °C RTA crystallized sample at 700 °C and 100 mTorr. Figure 4.5 (c) and Figure 4.7 show the resulting XRD and microstructure, respectively. The film remains phase pure and the microstructure demonstrates a mixture of triangular, flat square-like, and long protruding rectangular grains which correspond to (111), (100)_c, and (110)_c oriented grains, based on symmetry. This microstructure is comparable to those of films prepared by depositing above 200 mTorr on a PbTiO₃ seed layer.

Based on the high temperature depositions and low temperature/RTA crystallized samples, 35BiMT-65PT is shown to have a very large processing window for forming the perovskite phase when utilizing either a PbTiO₃ or a “BiMT-PT” seed.

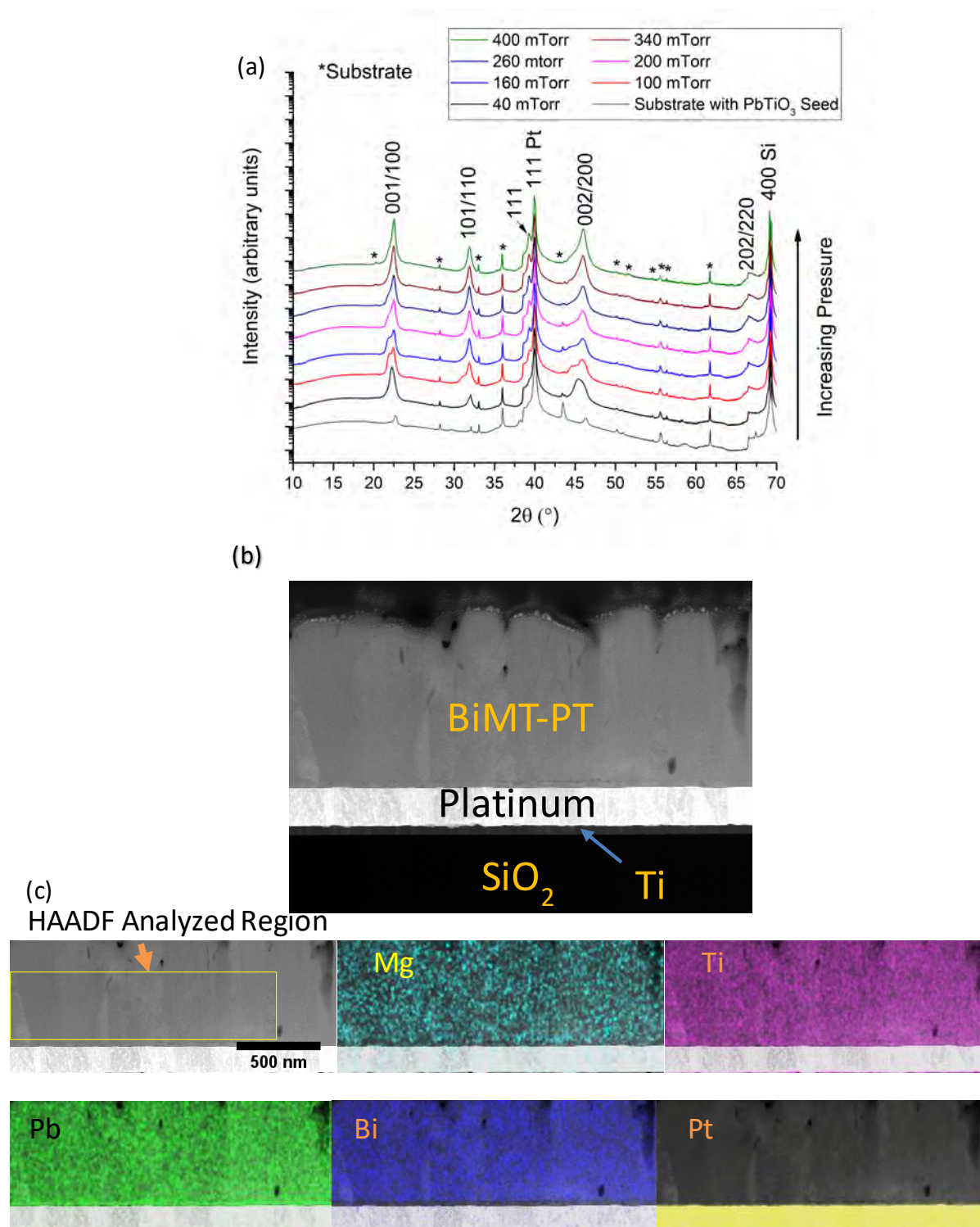


Figure 4.1 - (a) XRD patterns of films deposited between 40 and 400 mTorr background pressure. Peaks marked with a star come from the substrate. (b)-(c) STEM-HAADF image and STEM-HAADF image overlaid with color EDS elemental maps of elements of interest for a film grown at a chamber pressure of 340 mTorr. The thin layer between the Pt and Bi maps corresponds to the PbTiO_3 seed layer. TEM samples and analysis were provided by Wes Auker and Jenn Gray.

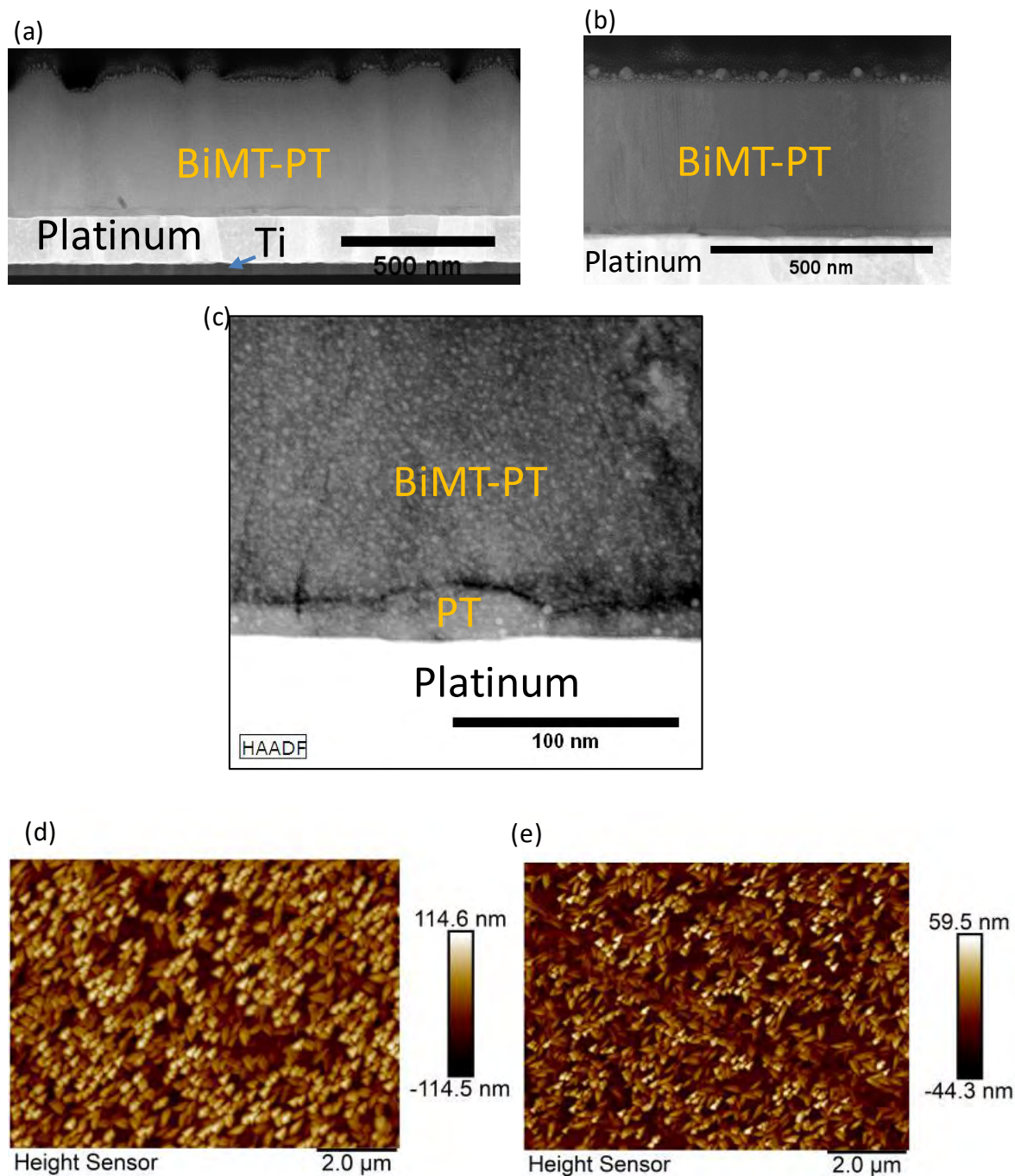


Figure 4.2 – TEM cross section of (a) 35BiMt-65PT deposited at 100 mTorr and (b) 60 mTorr oxygen (90%)/ozone (10%) pressure on 36 nm PbTiO_3 seed layers. Compared to Figure 4.1, the films show a reduced surface roughness with decreasing deposition pressure. (c) Shows the interface of the BiMT-PT showing the PT seed layer. Surface texture in (c) is expected to be due to beam damage at the very surface of the sample. The texture is only visible in STM-TEM mode. The bulk of the sample is undamaged by the beam. The very top of some samples have redeposited material / gallium induced defects. TEM samples and analysis were provided by Wes Auker and Jenn Gray. (d)-(e) AFM images of 35BiMT-65PT thin films deposited at 340 mTorr (d) and 60 mTorr (e) deposition background pressure.

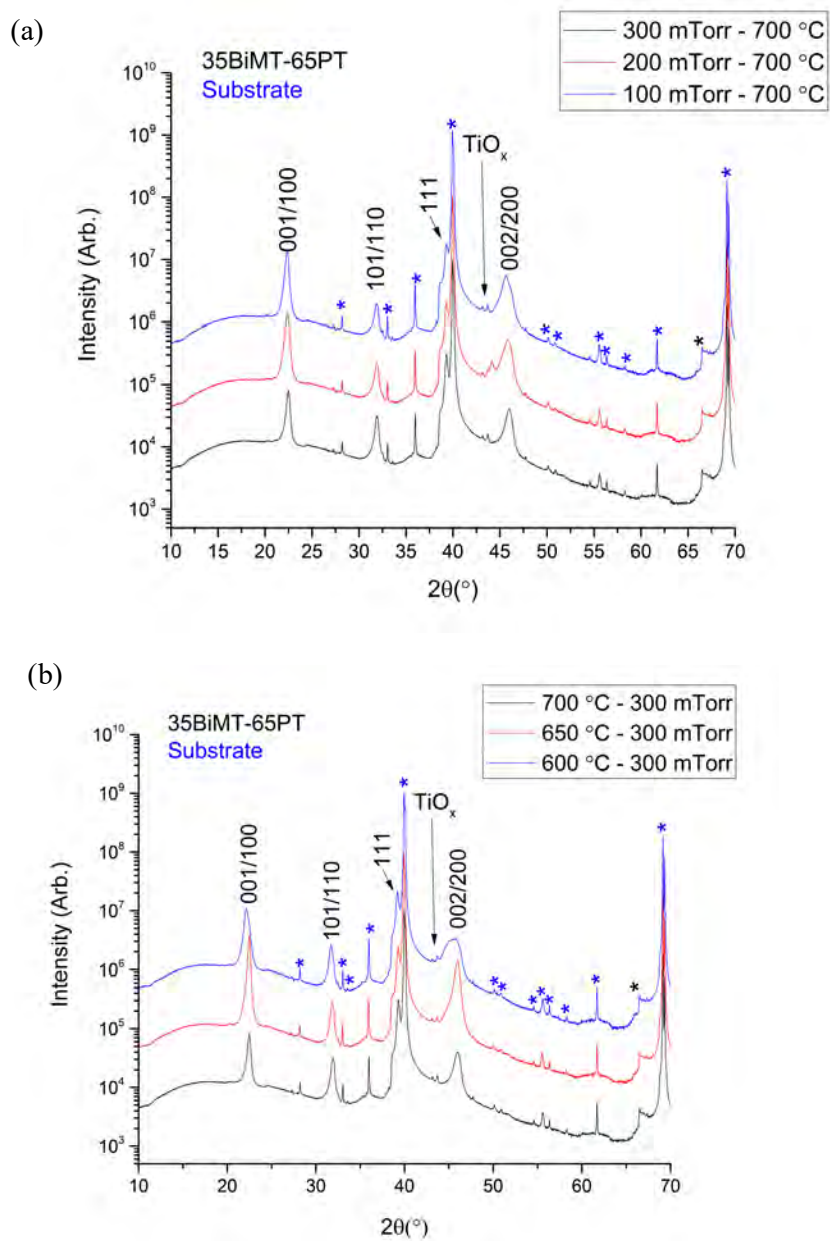


Figure 4.3 – (a) XRD patterns of samples deposited from a 10 mol% excess Pb target varying the deposition pressure from 100-300 mTorr. (b) XRD patterns of samples deposited from a 10 mol% excess Pb target varying the deposition temperature from 600 °C to 700 °C.

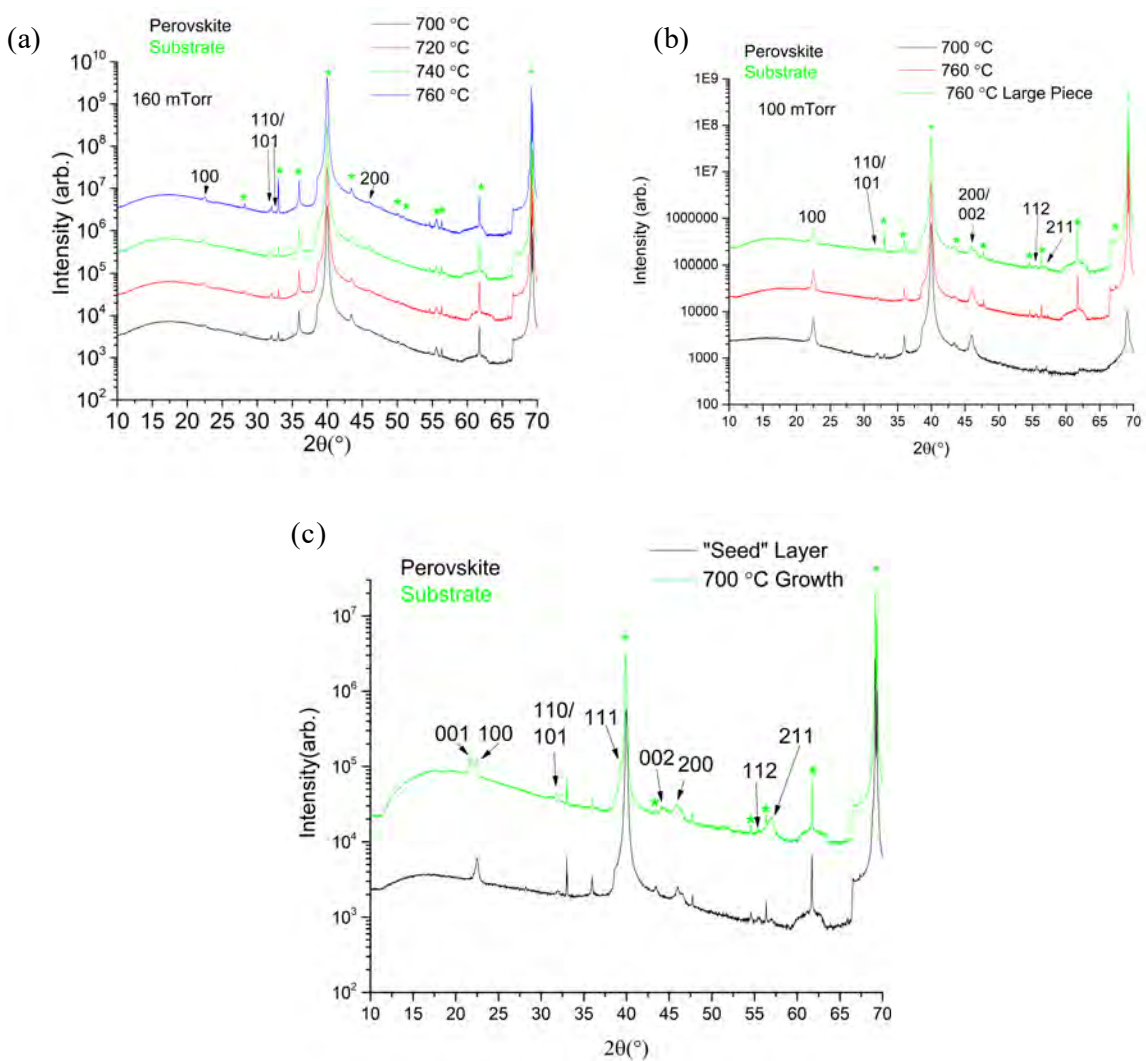


Figure 4.4 – (a) and (b) XRD patterns of room temperature deposited films at 160 mTorr and 100 mTorr, respectively. The films were crystallized between 700 °C and 760 °C. (c) Growth of 35BiMT-65PT from a 20Pb10Bi0Mg target (RTA crystallized film). The RTA crystallized film comes from a broken piece of the sample in (b) labeled 760 °C Large Piece.

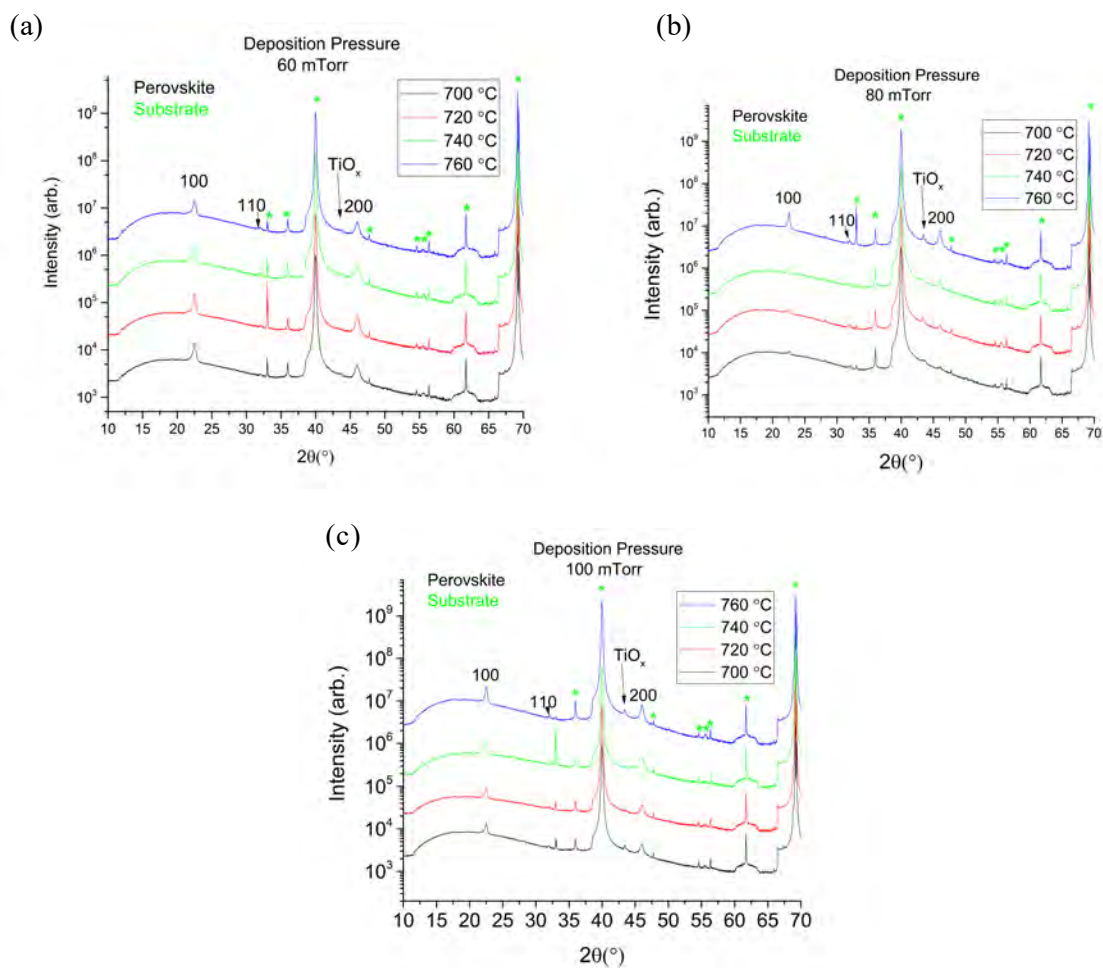


Figure 4.5 –XRD patterns of 35BiMT-65PT thin films deposited at room temperature for 45 seconds at chamber pressures of (a) 60 mTorr, (b) 80 mTorr, and (c) 100 mTorr. All films were crystallized between 700 °C and 760 °C as noted in the legend.

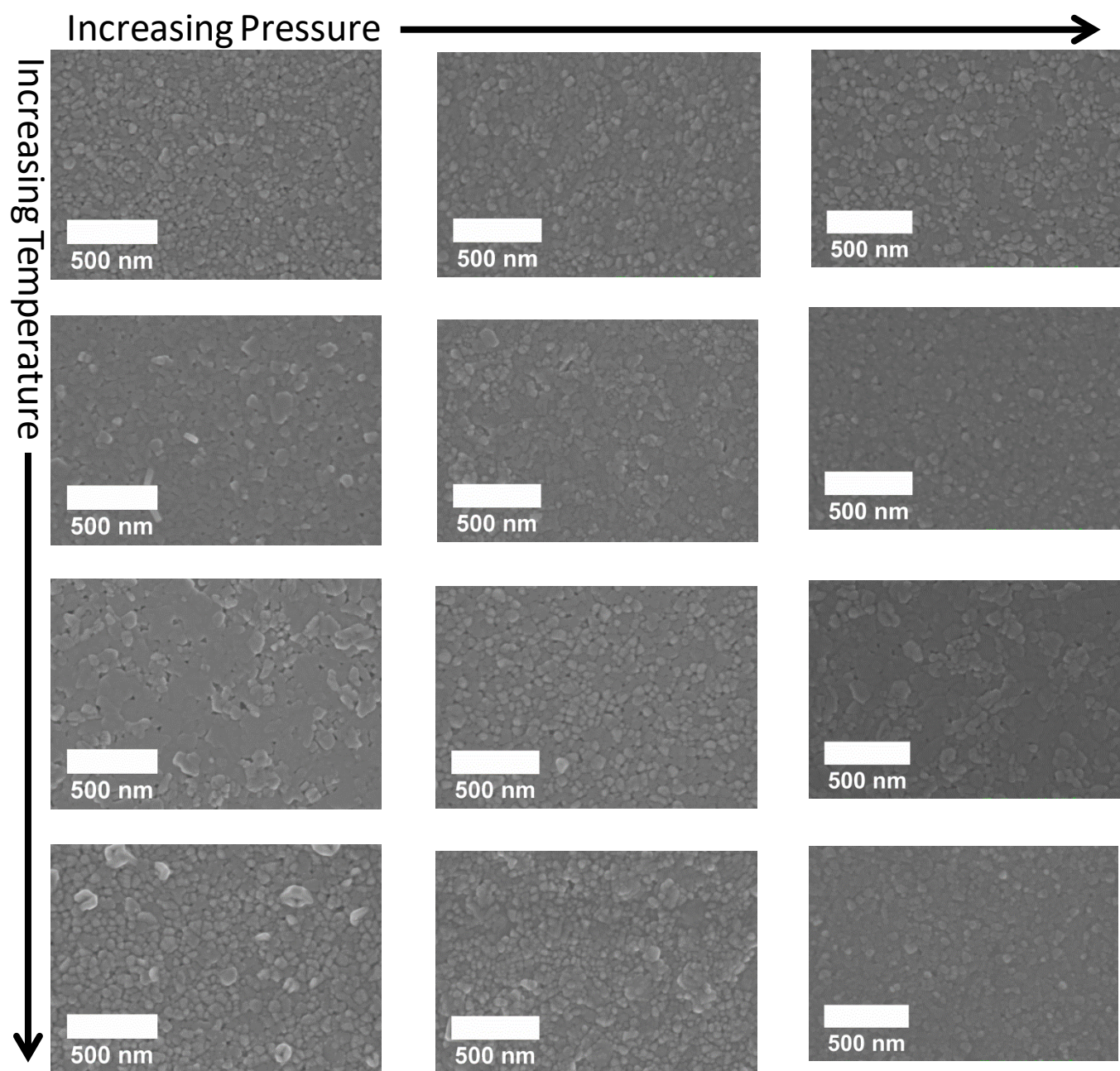


Figure 4.6 – SEM images of 35BiMT-65PT RTA crystallized for 1 minute in flowing O₂. The deposition pressures are 60, 80 and 100 mTorr from left to right. The deposition temperatures are 700 °C, 720 °C, 740 °C, and 760 °C from top to bottom respectively.

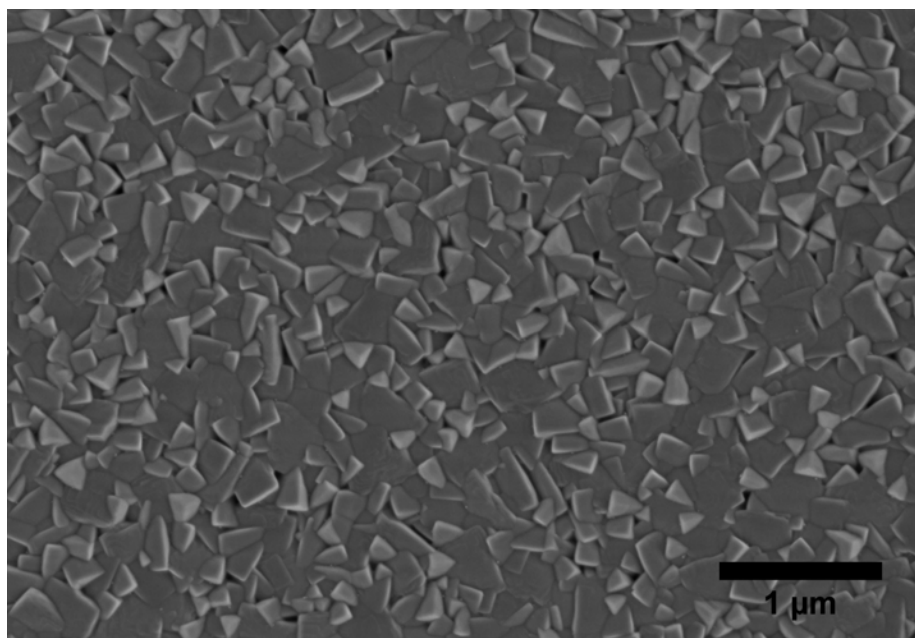


Figure 4.7 – Microstructure of a 700 °C film grown on top of the “seed” layer shown in Figure 4.6. The microstructure shows only perovskite grains where triangular grains, flat square-like grains, and long rectangular grains correspond to (111), (100)_c, and (110)_c oriented grains, respectively.

Due to the large processing window for forming the perovskite phase, a different metric is required to determine the best processing conditions for making 35BiMT-65PT thin films. In addition, a better understanding is needed as to why there is such a large processing window for the 35BiMT-65PT thin films. In the next section, TEM composition analysis and ferroelectric hysteresis response are utilized as metrics to assess the quality of the films deposited under various conditions and to probe the underlying process-property relationships.

4.3 Deposition Pressure – Composition – Ferroelectric Property Relationships

The background chamber pressure controls both the mean free path of the ablated species and the interaction of the ablated species with the background gas. These factors, in turn, determine the energy and chemical/physical state of species arriving at the substrate surface.⁴⁶ In general, high levels of bombardment can cause lattice expansion, imprint formation, and loss of volatile species.^{47–50}

To quantify the effect of pressure on the film composition, extensive composition analysis of the 35BiMT-65PT thin films was undertaken. BiMT-PT is a multicomponent system with the potential for a complex defect chemistry. To describe the film compositions, the cation concentrations were first normalized to the total cation content:

$$\text{Normalized Cation Concentration} = \frac{[A]}{\sum_A [Cations]} \quad \text{Eq. 4.1}$$

where [A] denotes the concentration of a cation. The cation concentration was then normalized to the ideal normalized cation concentration assuming a 35BiMT-65PT concentration.

$$\text{Fraction of Ideal Composition} = \frac{\text{Measured Normalized Cation Concentration}}{\text{Ideal Normalized Cation Concentration}} \quad \text{Eq. 4.2}$$

Finally, the data were normalized to the Ti concentration. It is noted that Ti shows little change in concentration with respect to the other cations as the chamber pressure during deposition changes, and Ti is expected to have a sticking coefficient of 1 on the substrate. Thus, Ti was used as a normalization factor:

$$\text{Fraction of Ideal Composition Adjusted to Ti} = \frac{\frac{\text{Measured Normalized Cation Concentration}}{\text{Ideal Normalized Cation Concentration}}}{\frac{\text{Measured Ti Concentration}}{\text{Ideal Ti Concentration}}} \quad \text{Eq. 4.3}$$

Figure 4.8(a) and (b) show the average composition for films deposited between 60 and 340 mTorr. The target utilized had 20 and 10 mol% excess Pb and Bi, respectively. As the deposition pressure decreased, the following phenomena were observed. First, the Mg concentration decreases with decreasing background pressure. The Mg loss is attributed to scattering out of the plume, as it is a light ion. Lichtenwalner demonstrated that the introduction of an ambient gas changes the angular distribution of species ejected from the target.⁴⁶ As the chamber pressure is increased, the angular distribution becomes confined. The plume expands at low pressures, and only the central portion of it directly deposits on the substrate. Secondly, the Pb content also decreases as the chamber pressure drops, presumably as the increased bombardment levels cause more re-sputtering from the growing film. Finally, the Bi concentration increases as the pressure decreases. This is contrary to what is expected

based on its comparatively high propensity for re-sputtering^{49,50}, suggesting that another mechanism must be involved. All films were determined to be A-site deficient, with a decrease in the overall A-site deficiency as the Bi-concentration increases.

The ferroelectric hysteresis loops shown in Figure 3(b) for films between 670 nm and 720 nm in thickness indicate that P_r and maximum polarization (P_{max}) correlate with improved film stoichiometry (Figure 3(a)). P_{max} , P_r , and leakage current (see chapter 5) increase with an increase in background deposition pressure. The increased P_{max} and P_r correlate with a counterclockwise rotation of the P-E loop, resulting in a P_r increase of 64% to 21.3 and -22.0 $\mu\text{C}/\text{cm}^2$. The correlation between deposition pressure and ferroelectric P-E response may be related to the excess Bi present at lower pressures. Bahri *et al.* and Skanavi *et al.* demonstrated that Bi doping lowers the Curie temperature in BaTiO_3 .^{51,52} This, in turn, decreases the remanent polarization, as demonstrated by Ogihara.⁵³ The polarization data suggests that the [Bi] strongly influences the P-E response in these films.

PUND measurements were used to quantify total switching (P^*) and nonswitching charges (P^\wedge), respectively, as shown in Figures 3(c) and 3(d). With increasing deposition pressure, at 500 kV/cm the total P^* increases by $\approx 32 \mu\text{C}/\text{cm}^2$, however, P^\wedge increases by $\approx 11-14 \mu\text{C}/\text{cm}^2$. While other sources may contribute to an increase in P^\wedge , the likely source is leakage, given to the relatively small differences in composition and structure from sample to sample. The increase in leakage is expected to be due to A-site vacancy-hole trapping and will be discussed in more detail in chapter 5.

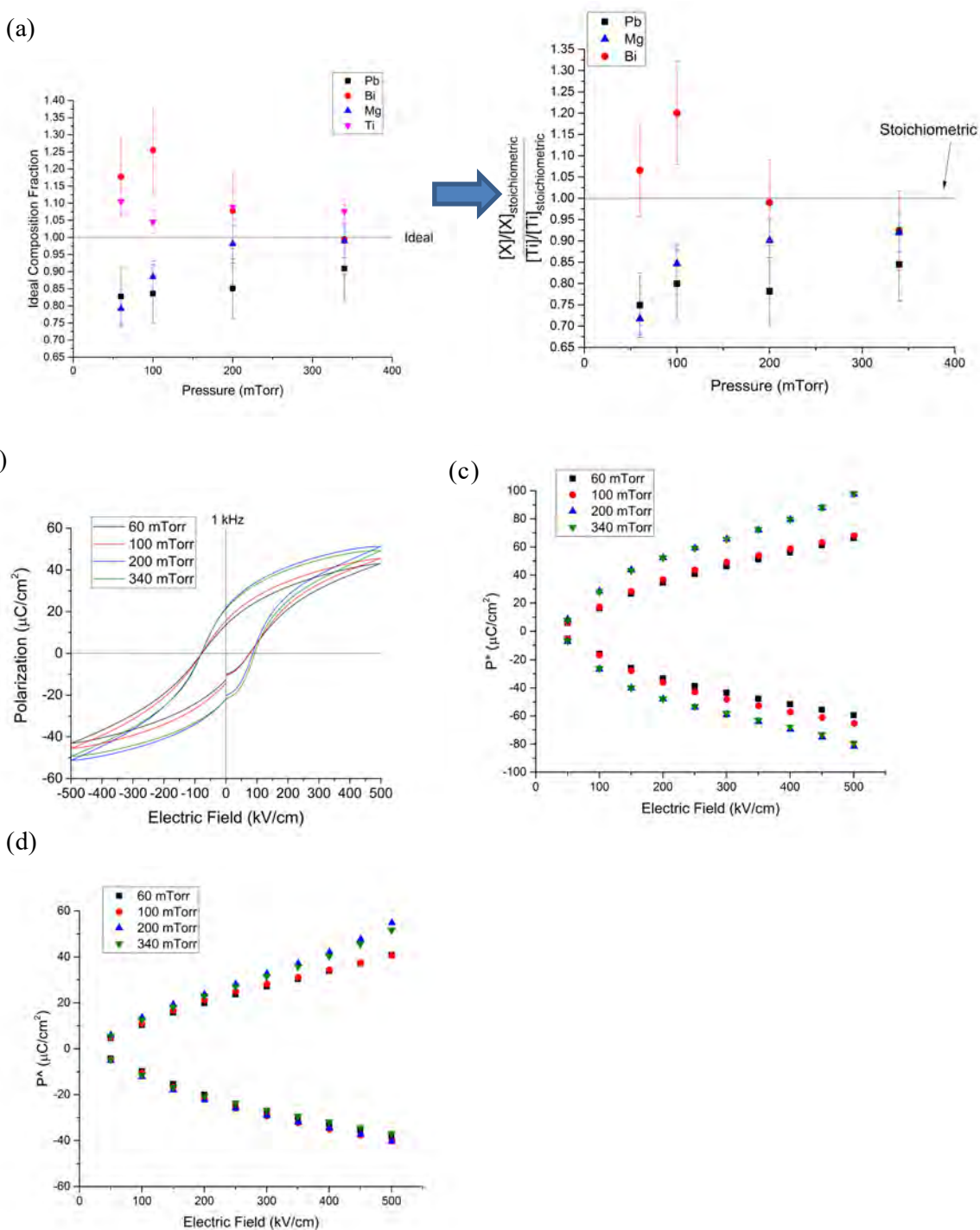


Figure 4.8 – (a) Ideal composition fraction without vs with adjusting to the Ti fraction as a function of the chamber background pressure in oxygen(90%)/ozone(10%). (a – right) ratio of species X, where X is Pb, Mg, or Bi as a function of chamber background pressure. The compositions are normalized to the Ti concentration. A stoichiometric composition would have the composition fractions for all cations equal to 1. (b) 1 kHz ferroelectric hysteresis response of 670-720 nm thick films with a 36 nm PbTiO₃ seed layer deposited between 60 and 340 mTorr. (c) PUND switching (P^*) and (d) non-switching (P^\wedge) charge with a 1ms pulse and 1 ms 0 V holds.

4.4 Target Composition – Ferroelectric Property Relationship

A series of targets was made to compensate for the stoichiometric deficiencies in the grown films. Table 4.1 lists the batched composition for these targets. If either volatility or resputtering of PbO or Bi₂O₃ is the primary source for the A-site deficiency, then it should be possible to compensate for the non-stoichiometry via the target. A series of films were deposited using each target. All films were deposited at 340 mTorr, a 6 cm target to substrate distance, and a laser deposition rate of 10 Hz. These films were deposited on a 16 nm 5 mol% La-doped PbTiO₃ to reduce the influence of the seed layers on the resulting electrical properties. Figure 4 shows the composition profile and ferroelectric response of the resulting films. Reducing the seed layer thickness resulted in a decrease in P_r to 14.4 and -15.2 μC/cm² using a 20Pb10Bi0Mg target.

Table 4.1 - List of target compositions investigated

| Target Name | Pb Excess (mol%) | Bi Excess (mol%) | Mg Excess (mol%) |
|--------------|------------------|------------------|------------------|
| 20Pb10Bi0Mg | 20% | 10% | 0% |
| 30Pb15Bi5Mg | 30% | 15% | 5% |
| 48Pb20Bi10Mg | 48% | 20% | 10% |
| 65Pb20Bi10Mg | 65% | 20% | 10% |
| 85Pb20Bi10Mg | 85% | 20% | 10% |

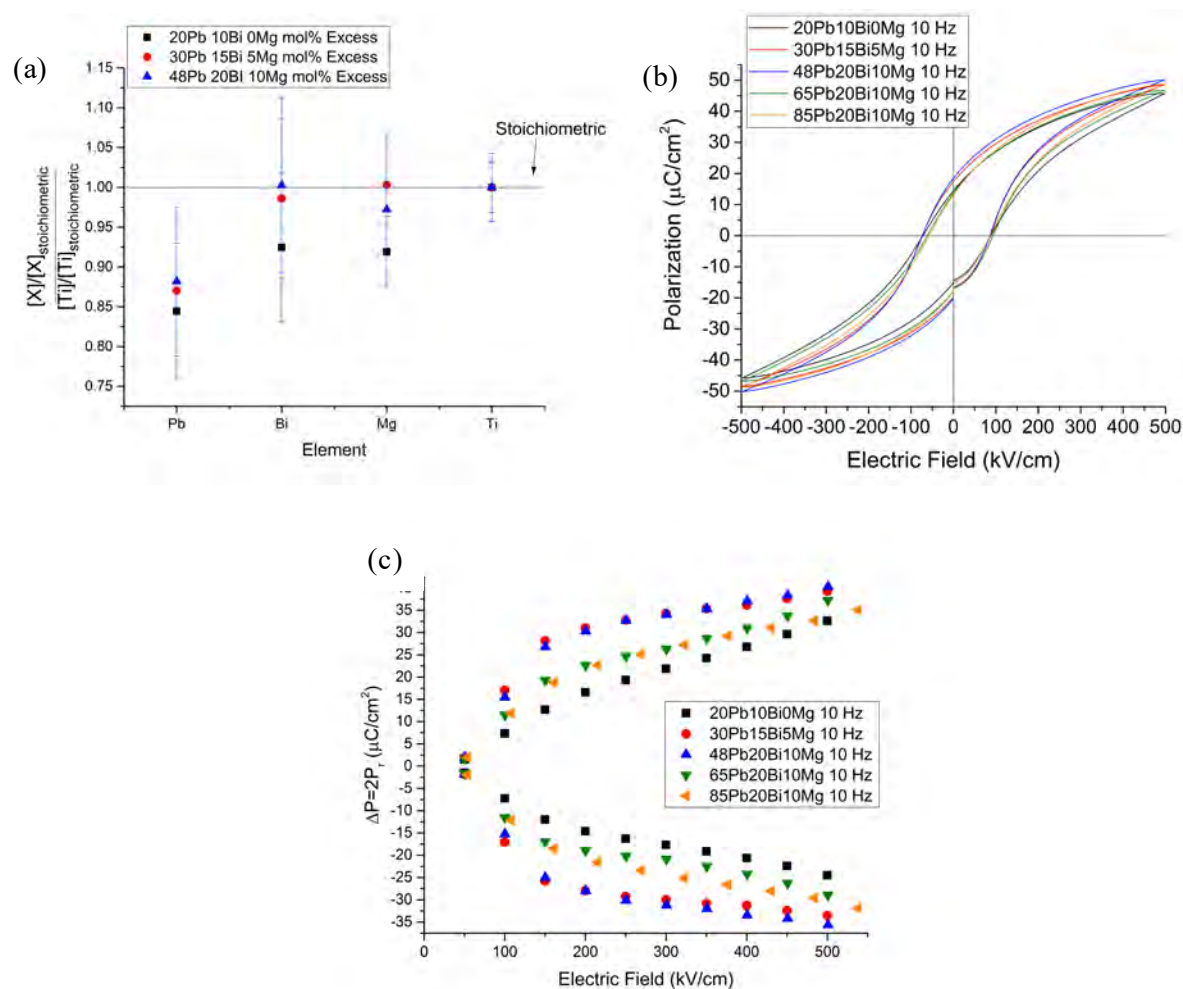


Figure 4.9 - (a) Normalized composition of 600-700 nm films grown using a 16 nm PbTiO_3 seed layer. The BiMT-PT film was deposited using a 20Pb10Bi0Mg target on a 36 nm PbTiO_3 seed for composition analysis. The seed layer was avoided during the cross-sectional analysis. (b) Ferroelectric hysteresis (1kHz) response as a function of target composition (all on 16 nm seed). (c) Sample PUND data for \approx 600-700 nm thick films measured using 1 ms pulses and 1 ms 0 V holds.

Figure 4.9(a) shows that compensation of cation deficiencies is possible for most of the cations. The Bi and Mg compositions approach the ideal concentrations with respect to the Ti concentration on adding 20 mol% and 10 mol% excess, respectively. However, the Pb concentration shows only minor increases regardless of the amount of excess PbO added to the target. It is hypothesized that this may be due to competition between Pb and Bi adsorption onto the A-site.

Figure 4.9(b) and 4.9(c) show the ferroelectric response of films deposited from all targets. The control samples deposited from the 20Pb10Bi0Mg target shows the lowest P_r based on P-E (1kHz) and

PUND measurements. As the cation concentration ratios approach ideal, the P_r increases. However, excessive amounts of PbO in the target lead to a decrease in P_r . It is believed that this is a consequence of a greater amount of disorder on the surface associated with the need to evolve more PbO from the surface during growth. The growing layers become more defective and the processing window shifts away from 10 Hz (see next section).

4.5 Laser Deposition Rate – Film Composition – Ferroelectric Property Relationships

The laser repetition rate also influences the film composition. Maria *et al.* demonstrated for PMN-PT films that lower laser repetition frequencies provide longer times for evolution of the most volatile species.^{54,55} Changing the laser repetition rate leads to a change in the growth rate as well, which can also change the crystalline quality of the resulting films. In particular, slower growth rates are expected to provide more time for atomic rearrangement, leading to improved ferroelectric properties.

Figure 4.10 shows film compositions and resulting ferroelectric properties for growth from a 48Pb20Bi10Mg target. It is evident that changing the laser frequency between 5-20 Hz does not yield a significant difference in the resulting film compositions. However, there is a significant change in the film properties. The maximum P_r and P_{max} occur at 3 and 5 Hz ($\approx 22 \mu\text{C}/\text{cm}^2$), while there is a continuous decrease in P_r and P_{max} as the laser frequency increases up to 20 Hz. The loop is noticeably lossier for growths at laser frequencies of 3 Hz or 1 Hz. Similar results were found when utilizing targets with greater PbO excess compensation.

Films deposited at frequencies of ≤ 5 Hz contain a Mg rich pyrochlore second phase (See Figure 4.11). Interestingly, P_r and P_{max} remain high for the films grown at 5 Hz, regardless of the presence a minor amount of second phase. A similar phenomenon is reported in systems such as PMN-PT.⁵⁴

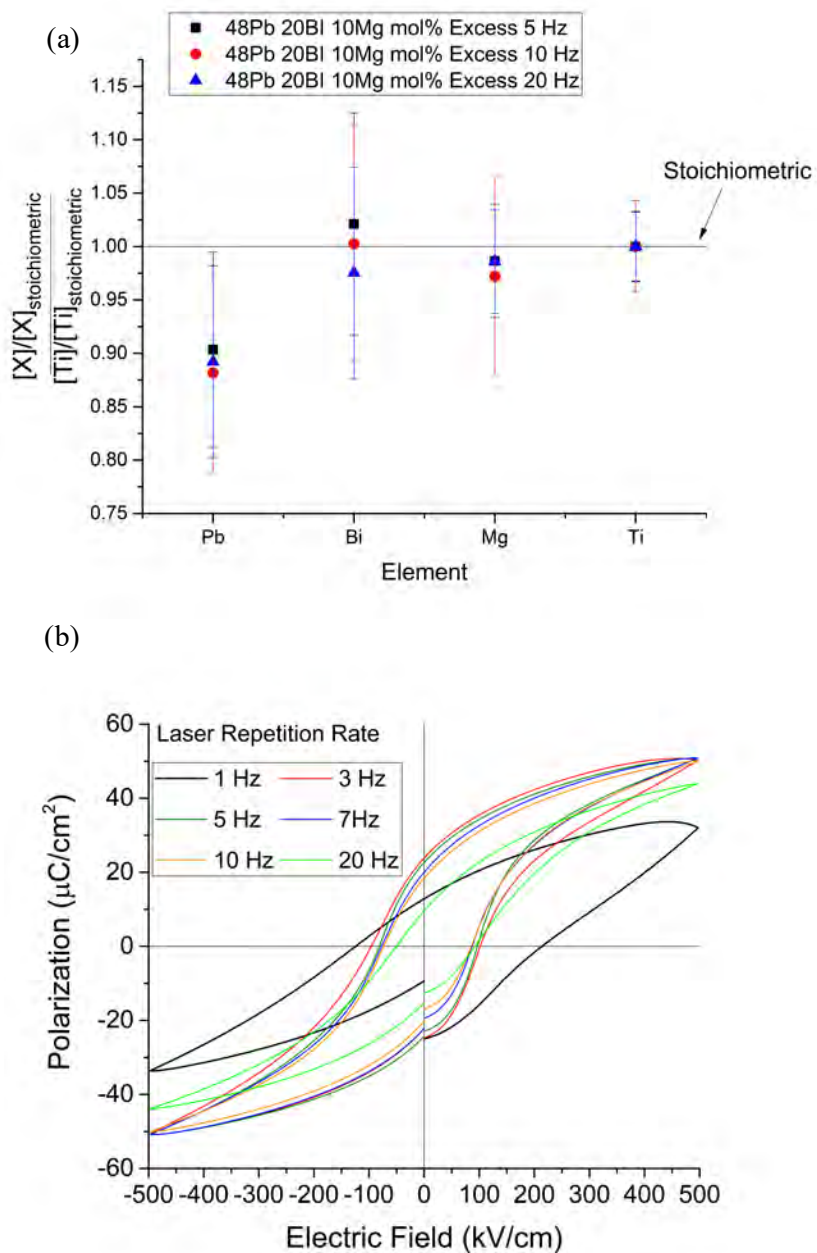


Figure 4.10 - (a) Composition of films deposited at laser pulse frequencies between 5 and 20 Hz. (b) Ferroelectric P-E hysteresis (1kHz) of films deposited between 1 and 20 Hz.

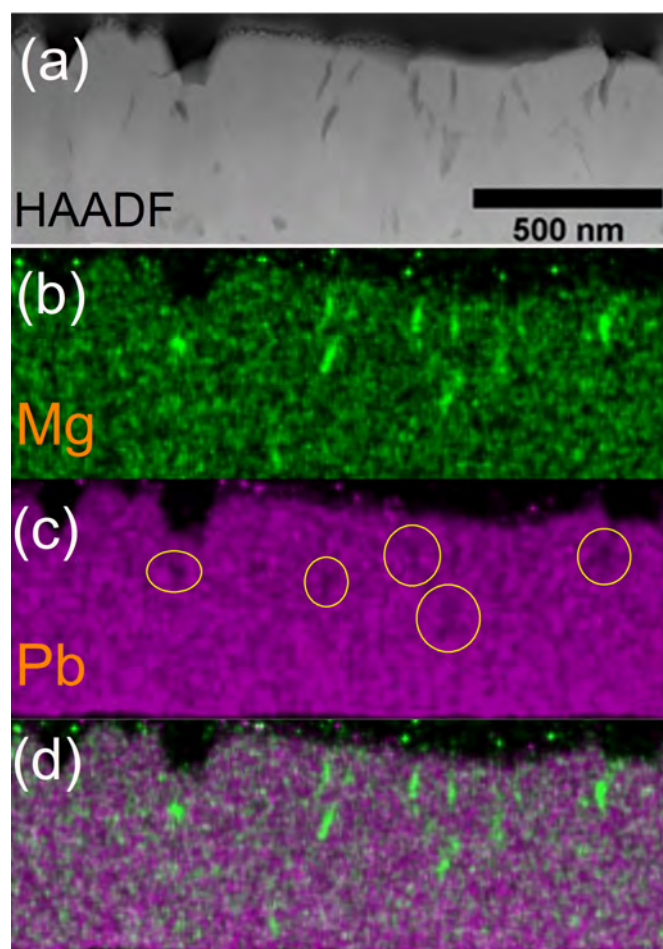


Figure 4.11 – (a) HAADF-STEM image of cross-section from sample from 35BiMT-65PT deposited at 5 Hz using a 48Pb20Bi10Mg target at 340 mTorr. Dark regions correspond to a Pb/Bi deficient secondary phase. (b) Mg quantitative EDS elemental map (atomic %). (c) Pb quantitative elemental EDS map (atomic %). Yellow circles highlight regions with decreased Pb concentrations. (d) Combined Pb and Mg elemental maps showing the overlap between Pb deficient regions and Mg rich regions.

If changing the frequency to lower deposition rates increases P_r , but results in secondary phase formation, then perhaps combining the variables of laser deposition rate and the target composition may shift the processing window. Figure 4.12 shows the hysteresis response of films deposited at different deposition laser frequencies and target composition. As the 48Pb20Bi10Mg target shows the best hysteresis behavior when depositing at 10 Hz, the 65Pb20Bi10Mg target is best at 5 Hz. The P_r increases from $22 \mu\text{C}/\text{cm}^2$ to $24\text{-}25 \mu\text{C}/\text{cm}^2$. This is due to a shift in the optimal PbO concentration in the target due to the slower growth rate. Slower growth rates evolve more PbO per laser pulse and give more time

for atomic rearrangement. Thus, controlling both the target composition and laser rate together can potentially yield further improved electrical properties.

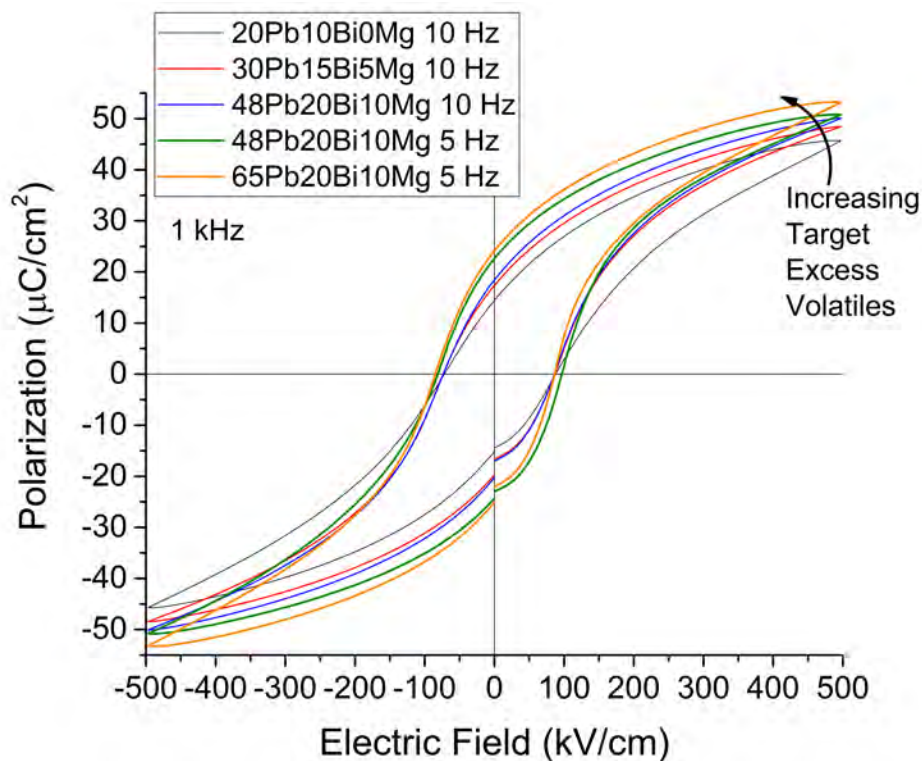


Figure 4.12 - Ferroelectric P-E hysteresis (1 kHz) of films deposited between 10 Hz and 5 Hz laser frequency with varying target compositions.

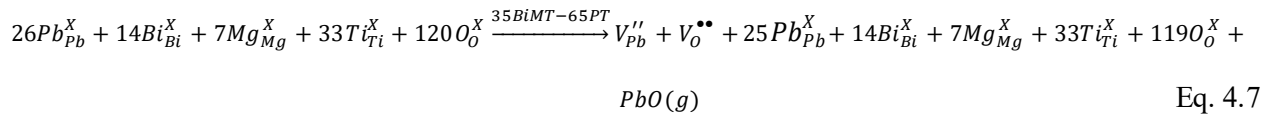
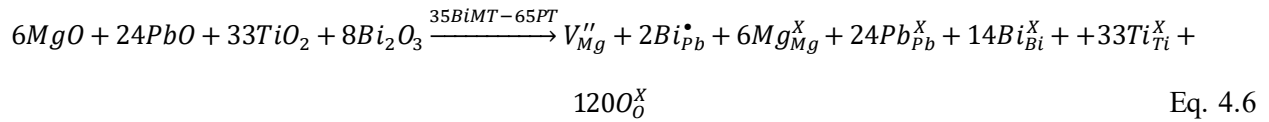
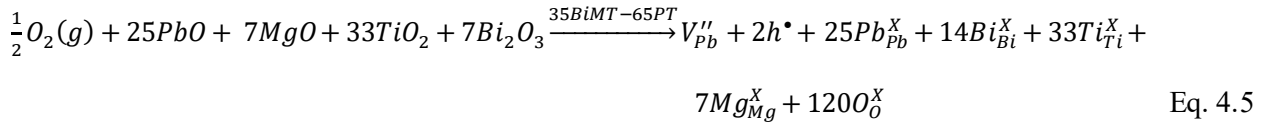
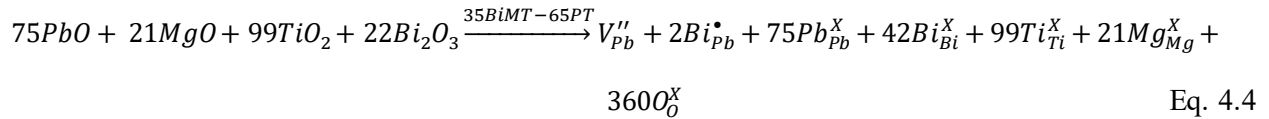
4.6 Defect Chemistry

The composition of films grown with volatile species can be either flux controlled or adsorption controlled. In flux-controlled growth, the film composition is dependent on the species provided to the growing film. In adsorption-controlled growth, the film composition is dependent on the adsorption kinetics, independent of the species flux. For PLD growth of BMT-PT films under the conditions investigated here, it was found that all films were nonstoichiometric. In particular, all films were Pb-deficient. Based on the composition data in Figures 4.9 and 4.10 it is clear that a mixture of flux and adsorption control exists in this system. The B-site cations (Mg and Ti) appear to be flux controlled, as

adding an excess of Mg leads to an increase in the Mg concentration. However, both A-site cations are adsorption controlled, where Bi adsorption controls the adsorption of Pb into the film. Pb and Bi have been shown to be adsorption controlled in PbTiO_3 , $\text{Bi}_4\text{Ti}_3\text{O}_{12}$, and other films grown by molecular beam epitaxy (MBE).⁵⁶⁻⁵⁹

Figure 4.9 demonstrates that Pb is adsorption controlled, as changing the flux of Pb leads to very little change in the overall Pb concentration. All films were sub-stoichiometric in Pb. Moreover, the Pb concentration in the film shows far less change than that of Bi with changes in target composition. It is hypothesized that preferential adsorption of Bi in the growing film leads to a fixed concentration of Pb-vacancies, in order to achieve electroneutrality. Considering the chemical formula as

$(\text{Bi}_{0.35}\text{Pb}_{0.65})(\text{Mg}_{0.175}\text{Ti}_{0.825})\text{O}_3$ and the observed defects, several defect reactions may be considered:



and the electroneutrality condition is:

$$[\text{Bi}^{\bullet}_{\text{Pb}}] + 2[V^{\bullet\bullet}_O] + p = 2[V''_{\text{Pb}}] + 2[V''_{\text{Mg}}] + n \quad \text{Eq. 4.8}$$

The lower volatility of Bi, with respect to Pb, is likely to favor excess Bi on Pb sites. Thus, to maintain electroneutrality, $[V''_{\text{Pb}}]$, $[V''_{\text{Mg}}]$ and/or the electron concentrations will increase. While the dominant defect reaction is not known, all of the films are reasonable insulators at low fields, suggesting that the compensation is predominantly ionic, or that any carriers are in deep traps. The observation of

increased leakage currents at high fields does suggest that at least some of the compensation is electronic. In Figure 4.8, as the [Mg] and, to a less extent, the [Pb] decreases, there is an increase in the Bi concentration, which is consistent with the defect reactions.

The complex defect chemistry of this system favors non-stoichiometry in films grown by pulsed laser deposition. A-site deficient films grown on PbTiO_3 seed layers to stabilize the perovskite phase showed P_r up to 24-25 $\mu\text{C}/\text{cm}^2$ for films on Si. In contrast, for bulk ceramics with similar compositions, P_r is reported to be 33-38 $\mu\text{C}/\text{cm}^2$.¹⁶ The decrease in the P_r with respect to bulk ceramics may be related to a combination of the tensile stress constraining the domain state, and the significant number of point defects in the grown films. More in depth electrical analysis on the electrical response of A-site deficient 35BiMT-65PT thin films is discussed in Chapter 5.

4.6 Conclusions

≈ 500 -700 nm 35BiMT-65PT thin films were deposited using pulsed laser deposition. The film composition was studied as a function of the film deposition pressure, target composition and laser deposition rate. Nearly all films were found to be phase pure perovskite within the explored processing space. EDS measurements showed that the [Mg] and [Pb] decreased with decreasing pressure, while the [Bi] increased. As the film target composition was adjusted, the [Bi] and [Mg] concentrations approached stoichiometric, but the [Pb] remained sub stoichiometric. Finally, the deposition rate showed no substantial effect on the film composition, but a significant impact on the ferroelectric properties. It was hypothesized that the preferential adsorption of Bi dictates the adsorption of Pb into the A-site. $2P_r$ increases 64% as the deposition pressure increased and the P-E loops rotated counterclockwise. The P_r increases as the target Pb excess increases to 48mol%. As the target Pb excess increased over 48 mol%, the P_r decreases possibly due to the need to evolve more PbO from defective growth layers. As the deposition rate decreased, the P_r increased due to enhanced crystalline quality. At laser frequencies of 5 Hz and below, a Mg-rich phase believed to be a pyrochlore begins to form. A-site deficient 35BiMT-

65PT thin films showed a maximum $P_r \approx 24\text{--}25 \mu\text{C}/\text{cm}^2$ when utilizing a combination of optimized laser deposition frequency and target composition.

4.7 References

- 1 C. Morandi, K.R. Udayakumar, S. Bhaskar, J. Rodriguez, and S. Trolier-McKinstry, "Exploring Next Generation High Temperature Ferroelectrics: $35\text{Bi}(\text{Mg}_{1/2}\text{Ti}_{1/2})\text{O}_3\text{--}65\text{PbTiO}_3$ Thin Films," in *IEEE Int. Symp. Appl. Ferroelectr. Int. Work. Acoust. Transduct. Mater. Devices Piezoresponse Force Microsc. Work.* 2017.
- 2 J. Rodriguez, K. Remack, J. Gertas, L. Wang, C. Zhou, K. Boku, K.R. Udayakumar, S. Summerfelt, T. Moise, D. Kim, J. Groat, J. Eliason, M. Depner, and F. Chu, "Reliability of Ferroelectric Random Access Memory Embedded within 130nm CMOS," pp. 750–758 in *Reliab. Phys. Symp. (IRPS), 2010 IEEE.* 2010.
- 3 Cypress, <http://www.cypress.com/products/f-ram-nonvolatile-ferroelectric-ram>, (n.d.).
- 4 Fujitsu, <http://www.fujitsu.com/us/products/devices/semiconductor/memory/fram/lineup/index.html>, (n.d.).
- 5 Rohm and LAPIS Semiconductor Co., <http://www.lapis-semi.com/en/semicon/memory/feram.html#TabPage1>, (n.d.).
- 6 Matsushita Electric Industry and Panasonic Corporation, <https://industrial.panasonic.com/ww/products/semiconductors/nfctags>, (n.d.).
- 7 J.H. Park, H.J. Joo, S.K. Kang, Y.M. Kang, H.S. Rhie, B.J. Koo, S.Y. Lee, B.J. Bae, J.E. Lim, H.S. Jeong, and K. Kim, "Fully Logic Compatible (1.6 V Vcc, 2 Additional FRAM Masks) Highly Reliable Sub 10F^2 Embedded FRAM with Advanced Direct Via Technology and Robust 100 nm Thick MOCVD PZT Technology," pp. 591–594 in *IEDM Tech. Dig. IEEE Int. Electroc Devices Meet.* 2004.
- 8 D.C. Yoo, B.J. Bae, D.H. Im, S.O. Park, H.S. Kim, J.T. Moon, and B.I. Ryu, "Highly Reliable 50nm-thick PZT Capacitor and Low Voltage FRAM Device using Ir/SrRuO₃ /MOCVD PZT Capacitor Technology," pp. 148–149 in *Symp. VLSI Technol.* 2005.
- 9 S.R. Gilbert, S. Hunter, D. Ritchey, C. Chi, D. V Taylor, J. Amano, S. Aggarwal, T.S. Moise, *et al.*, "Preparation of $\text{Pb}(\text{Zr},\text{Ti})\text{O}_3$ Thin Films by Metalorganic Chemical Vapor Deposition for Low Voltage Ferroelectric Memory," *J. Appl. Phys.*, **93** 1713–1717 (2003).
- 10 J.A. Rodriguez, K. Remack, K. Boku, K.R. Udayakumar, S. Aggarwal, S.R. Summerfelt, F.G. Celii, S. Martin, L. Hall, K. Taylor, T. Moise, H. Mcadams, J. Mcpherson, S. Member, R. Bailey, G. Fox, and M. Depner, "Reliability Properties of Low-Voltage Ferroelectric Capacitors and Memory Arrays," *IEEE Trans. Device Mater. Reliab.*, **4** [3] 436–449 (2004).
- 11 K.R. Udayakumar, T. San, J. Rodriguez, S. Chevacharoenkul, D. Frystak, J. Rodriguez-Latorre, C. Zhou, M. Ball, P. Ndai, S. Madan, H. McAdams, S. Summerfelt, and T. Moise, "Low-Power Ferroelectric Random access Memory Embedded in 180nm Analog Friendly CMOS Technology," *2013 5th IEEE Int. Mem. Work. IMW 2013*, 128–131 (2013).

- 12 B. Prince, "Trends in Scaled and Nanotechnology Memories," pp. 55–61 in *Non-Volatile Mem. Technol. Symp.* 2005.
- 13 R.E. Eitel, S.J. Zhang, T.R. Shrout, C.A. Randall, and I. Levin, "Phase Diagram of the Perovskite System $(1-x)\text{BiScO}_3-x\text{PbTiO}_3$," *J. Appl. Phys.*, **96** [5] 2828–2831 (2004).
- 14 R.E. Eitel, C.A. Randall, T.R. Shrout, P.W. Rehrig, W. Hackenberger, and S.-E. Park, "New High Temperature Morphotropic Phase Boundary Piezoelectrics Based on $\text{Bi}(\text{Me})\text{O}_3 - \text{PbTiO}_3$ Ceramics," *Jpn. J. Appl. Phys.*, **40** [10] 5999–6002 (2001).
- 15 R.E. Eitel, C.A. Randall, T.R. Shrout, P.W. Rehrig, W. Hackenberger, and S.-E. Park, "New High Temperature Morphotropic Phase Boundary Piezoelectrics Based on $\text{Bi}(\text{Me})\text{O}_3\text{-PbTiO}_3$ Ceramics," *Jpn. J. Appl. Phys.*, **40** 5999–6002 (2001).
- 16 C.A. Randall, R. Eitel, B. Jones, T.R. Shrout, D.I. Woodward, and I.M. Reaney, "Investigation of a High T_c Piezoelectric System: $(1-x)\text{Bi}(\text{Mg}_{1/2}\text{Ti}_{1/2})\text{O}_3-(x)\text{PbTiO}_3$," *J. Appl. Phys.*, **95** [7] 3633 (2004).
- 17 V.M. Goldschmidt, "Die Gesetze der Krystallochemie," *Naturwissenschaften*, **14** [21] 477–485 (1926).
- 18 C.J. Stringer, T.R. Shrout, C.A. Randall, and I.M. Reaney, "Classification of Transition Temperature Behavior in Ferroelectric $\text{PbTiO}_3\text{-Bi}(\text{Me}'\text{Me}'')\text{O}_3$ Solid Solutions," *J. Appl. Phys.*, **99** [2] 24106 (2006).
- 19 C.J. Stringer, "Structure-Property-Performance Relationships of New High Temperature Relaxors for Capacitor Applications," Ph.D. Dissertation, The Pennsylvania State University, 2006.
- 20 M.R. Suchomel and P.K. Davies, "Predicting the Position of the Morphotropic Phase Boundary in High Temperature $\text{PbTiO}_3\text{-Bi}(\text{B}'\text{B}'')\text{O}_3$ Based Dielectric Ceramics," *J. Appl. Phys.*, **96** [8] 4405–4410 (2004).
- 21 J. Chen, X. Tan, W. Jo, and J. Rödel, "Temperature Dependence of Piezoelectric Properties of High- T_c $\text{Bi}(\text{Mg}_{1/2}\text{Ti}_{1/2})\text{O}_3\text{-PbTiO}_3$," *J. Appl. Phys.*, **106** [3] 34109 (2009).
- 22 S. Sharma and D.A. Hall, "Ferroelectric and Antiferroelectric Polarisation Switching Characteristics of $\text{Bi}(\text{Mg}_{0.5}\text{Ti}_{0.5})\text{O}_3\text{-PbTiO}_3$ Ceramics," *J. Mater. Sci. Mater. Electron.*, **21** [4] 405–409 (2010).
- 23 Q. Zhang, Z. Li, F. Li, Z. Xu, and X. Yao, "Temperature Dependence of Dielectric/Piezoelectric Properties of $(1-x)\text{Bi}(\text{Mg}_{1/2}\text{Ti}_{1/2})\text{O}_3-x\text{PbTiO}_3$ Ceramics with an MPB Composition," *J. Am. Ceram. Soc.*, **93** [10] 3330–3334 (2010).
- 24 T. Oikawa, S. Yasui, T. Watanabe, H. Yabuta, Y. Ehara, T. Fukui, and H. Funakubo, "Film Thickness Dependence of Ferroelectric Properties of (111)-Oriented Epitaxial $\text{Bi}(\text{Mg}_{1/2}\text{Ti}_{1/2})\text{O}_3$ Films," *Jpn. J. Appl. Phys.*, **51** [09LA04] 09LA04 (2012).
- 25 H. Tanaka, T. Yamada, S. Yasui, K. Yamato, S. Wada, and H. Funakubo, "Growth of (111)-Oriented Epitaxial $\text{Bi}(\text{Mg}_{0.5}\text{Ti}_{0.5})\text{O}_3$ Films and their Characterization," *Key Eng. Mater.*, **485** 195–198 (2011).
- 26 J.C. Nino and S. Trolier-McKinstry, "Dielectric, Ferroelectric, and Piezoelectric Properties of (001) $\text{BiScO}_3\text{-PbTiO}_3$ Epitaxial Films Near the Morphotropic Phase Boundary," *J. Mater. Res.*, **19** [2] 568–572 (2004).

- 27 S.Y. Lee, S.W. Ko, S. Lee, and S. Trolier-McKinstry, "Mn-doped 0.15BiInO₃-0.85PbTiO₃ Piezoelectric Films Deposited by Pulsed Laser Deposition," *Appl. Phys. Lett.*, **100** [21] 212905 (2012).
- 28 S.Y. Lee, W. Wang, and S. Trolier-McKinstry, "High Curie Temperature BiInO₃-PbTiO₃ films," *J. Appl. Phys.*, **115** [22] 1–5 (2014).
- 29 G. Wu, H. Zhou, X. Zhou, N. Qin, and D. Bao, "Structural, Dielectric, and Ferroelectric Properties of BiAlO₃–PbTiO₃ Solid Solution Thin Films on Indium Tin Oxide-Coated Glass Substrates," *J. Am. Ceram. Soc. Society*, **927** 925–927 (2010).
- 30 M.A. Khan, T.P. Comyn, and A.J. Bell, "Large Remanent Polarization in Ferroelectric BiFeO₃ - PbTiO₃ Thin Films on Pt/Si Substrates," *Appl. Phys. Lett.*, **91** [3] 32901 (2007).
- 31 M.A. Khan, T.P. Comyn, and A.J. Bell, "Leakage Mechanisms in Bismuth Ferrite-Lead Titanate Thin Films on Pt/Si Substrates," *Appl. Phys. Lett.*, **92** [7] 90–93 (2008).
- 32 M.A. Khan, T.P. Comyn, and A.J. Bell, "Growth and Characterization of Tetragonal Bismuth Ferrite-Lead Titanate Thin Films," *Acta Mater.*, **56** [9] 2110–2118 (2008).
- 33 L. Zhang, J. Chen, H. Zhao, L. Fan, Y. Rong, J. Deng, R. Yu, and X. Xing, "Large Remanent Polarization and Small Leakage in Sol–Gel Derived Bi(Zn_{1/2}Zr_{1/2})O₃–PbTiO₃ Ferroelectric Thin Films," *Dalt. Trans.*, **42** [2] 585–590 (2013).
- 34 L. Zhang, J. Chen, H. Zhao, L. Fan, Y. Rong, J. Deng, R. Yu, and X. Xing, "Temperature-Independent Ferroelectric Property and Characterization of High-T_c 0.2Bi(Mg_{1/2}Ti_{1/2})O₃-0.8PbTiO₃ Thin Films," *Appl. Phys. Lett.*, **103** [8] 82902 (2013).
- 35 L. Liu and R. Zuo, "Fabrication and Electrical Properties of Sol-Gel Derived 0.63Bi(Mg_{1/2}Ti_{1/2})O₃-0.37PbTiO₃ Thin Films," *J. Am. Ceram. Soc.*, **94** [11] 3686–3689 (2011).
- 36 L. Liu, R. Zuo, and Q. Liang, "Effect of PbTiO₃ Seed Layer on the Orientation Behavior and Electrical Properties of Bi(Mg_{1/2}Ti_{1/2})O₃-PbTiO₃ Ferroelectric Thin Films," *Ceram. Int.*, **39** [4] 3865–3871 (2013).
- 37 C. Zhong, X. Wang, L. Guo, and L. Li, "Characterization of (100)-Oriented 0.63BiMg_{1/2}Ti_{1/2}O₃-0.37PbTiO₃ Piezoelectric Films by a Sol–Gel Process," *Thin Solid Films*, **580** 52–55 (2015).
- 38 L. Liu, R. Zuo, Q. Sun, and Q. Liang, "Structure and Electrical Properties of Mn Doped Bi(Mg_{1/2}Ti_{1/2})O₃-PbTiO₃ Ferroelectric Thin Films," *Appl. Surf. Sci.*, **268** 327–331 (2013).
- 39 H. Wen, X. Wang, C. Zhong, L. Shu, and L. Li, "Epitaxial Growth of Sol-Gel Derived BiScO₃-PbTiO₃ Thin Film on Nb-Doped SrTiO₃ Single Crystal Substrate," *Appl. Phys. Lett.*, **90** [20] 202902 (2007).
- 40 T. Yoshimura and S. Trolier-McKinstry, "Growth and Properties of (001) BiScO₃-PbTiO₃ Epitaxial Films," *Appl. Phys. Lett.*, **81** [11] 2065–2066 (2002).
- 41 S. Zhang, C.A. Randall, and T.R. Shrout, "High Curie Temperature Piezocrystals in the BiScO₃-PbTiO₃ Perovskite System," *Appl. Phys. Lett.*, **83** [15] 3150–2 (2003).
- 42 S.J. Zhang, C.A. Randall, and T.R. Shrout, "Electromechanical Properties in Rhombohedral BiScO₃-PbTiO₃ Single Crystals as a Function of Temperature," *Japanese J. Appl. Phys. Part 2-Letters*, **42** [10A] L1152–L1154 (2003).

- 43 S. Zhang, C.A. Randall, and T.R. Shrout, "Dielectric, Piezoelectric and Elastic Properties of Tetragonal BiScO₃-PbTiO₃ Single Crystal with Single Domain," *Solid State Commun.*, **131** [1] 41–45 (2004).
- 44 D.M. Marincel, S. Jesse, A. Belianinov, M.B. Okatan, S. V. Kalinin, T.N. Jackson, C.A. Randall, and S. Trolier-McKinstry, "A-site Stoichiometry and Piezoelectric Response in Thin Film PbZr_{1-x}Ti_xO₃," *J. Appl. Phys.*, **117** [20] (2015).
- 45 J.A. Thornton, "Structure-Zone Models of Thin Films," *Proc. SPIE 0821*, [1] 95–105 (1988).
- 46 D.J. Lichtenwalner, O. Auciello, R. Dat, and A.I. Kingon, "Investigation of the Ablated Flux Characteristics During Pulsed Laser Ablation Deposition of Multicomponent Oxides," *J. Appl. Phys.*, **74** [12] 7497–7505 (1993).
- 47 J.-P. Maria, S. Trolier-McKinstry, D.G. Schlom, M.E. Hawley, and G.W. Brown, "The Influence of Energetic Bombardment on the Structure and Properties of Epitaxial SrRuO₃ Thin Films Grown by Pulsed Laser Deposition," *J. Appl. Phys.*, **83** [8] 4373 (1998).
- 48 S.B. Krupanidhi, H. Hu, and V. Kumar, "Multi-Ion-Beam Reactive Sputter Deposition of Ferroelectric Pb(Zr,Ti)O₃ Thin Films," *J. Appl. Phys.*, **71** [1] 376–388 (1992).
- 49 M.P. Besland, H. Djani-Ait Aissa, P.R.J. Barroy, S. Lafane, P.Y. Tessier, B. Angleraud, M. Richard-Plouet, L. Brohan, and M.A. Djouadi, "Comparison of Lanthanum Substituted Bismuth Titanate (BLT) Thin Films Deposited by Sputtering and Pulsed Laser Deposition," *Thin Solid Films*, **495** [1–2] 86–91 (2006).
- 50 P.K. Ghosh, A.S. Bhalla, and L.E. Cross, "Surface Morphology of R.F. Sputtered Bismuth Titanate Thin Films," *J. Mater. Sci.*, **29** [17] 4659–4662 (1994).
- 51 F. Bahri, A. Simon, and H. Khemakhem, "Classical or Relaxor Ferroelectric Behaviour of Ceramics with Composition Ba_{1-x}Bi_{2x/3}TiO₃," *Phys. Status Solidi*, **464** [2] 459–464 (2001).
- 52 G.I. Skanavi, I.M. Ksendzov, V.A. Trigubenko, and V.G. Prokhvatilov, "Relaxation Polarization and Losses in Nonferroelectric Dielectrics with High Dielectric Constants," *Sov. J. Exp. Theor. Phys.*, **6** [2] 250 (1958).
- 53 H. Ogihara, C.A. Randall, and S. Trolier-McKinstry, "Weakly Coupled Relaxor Behavior of BaTiO₃-BiScO₃ Ceramics," *J. Am. Ceram. Soc.*, **92** [1] 110–118 (2009).
- 54 J. Maria, W. Hackenberger, and S. Trolier-McKinstry, "Phase Development and Electrical Property Analysis of Pulsed Laser Deposited Pb(Mg_{1/3}Nb_{2/3})O₃-PbTiO₃ (70/30) Epitaxial Thin Films," *J. Appl. Phys.*, **84** [9] 5147–5154 (1998).
- 55 J.-P. Maria, "Epitaxial Pb(Mg_{1/3}Nb_{2/3})O₃-PbTiO₃ Thin Films," PhD Thesis, The Pennsylvania State University, 1998.
- 56 C.D. Theis, J. Yeh, D.G. Schlom, M.E. Hawley, and G.W. Brown, "Adsorption-Controlled Growth of PbTiO₃ by Reactive Molecular Beam Epitaxy," *Thin Solid Films*, **325** [1–2] 107–114 (1998).
- 57 C.D. Theis, J. Yeh, D.G. Schlom, M.E. Hawley, G.W. Brown, J.C. Jiang, and X.Q. Pan, "Adsorption-Controlled Growth of Bi₄Ti₃O₁₂ by Reactive MBE," *Appl. Phys. Lett.*, **72** [22] 2817–2819 (1998).
- 58 J.F. Ihlefeld, A. Kumar, V. Gopalan, D.G. Schlom, Y.B. Chen, X.Q. Pan, T. Heeg, J. Schubert, X.

Ke, P. Schiffer, J. Orenstein, L.W. Martin, Y.H. Chu, and R. Ramesh, “Adsorption-Controlled Molecular-Beam Epitaxial Growth of BiFeO_3 ,” *Appl. Phys. Lett.*, **91** [7] 2005–2008 (2007).

- ⁵⁹ J.H. Lee, X. Ke, R. Misra, J.F. Ihlefeld, X.S. Xu, Z.G. Mei, T. Heeg, M. Roeckerath, J. Schubert, Z.K. Liu, J.L. Musfeldt, P. Schiffer, and D.G. Schlom, “Adsorption-Controlled Growth of BiMnO_3 Films by Molecular-Beam Epitaxy,” *Appl. Phys. Lett.*, **96** [26] 2008–2011 (2010).

Chapter 5

Influence of A-site Deficiency and Thickness Scaling on Electrical Properties

5.1 Introduction

Functional ferroelectric thin films have enabled numerous devices including actuators, sensors, transducers, and energy harvesters.¹ Commercially, ferroelectric films are used as the storage element in Ferroelectric Random Access Memory (FeRAM).^{2,3} Currently, FeRAM is utilized in consumer electronics, medical equipment and in numerous other applications.⁴ To further diversify the application of FeRAM, this work focuses on material systems with the potential to surpass the current limiting use temperature of 85 °C, specifically bismuth-based PbTiO₃ solid solution systems. Their high Curie temperatures show promise in this respect. These systems have not yet been widely investigated for non-volatile memory. Thus, mapping their underlying processing-microstructure-property relationships is essential to identify the most promising compositions. Although BiMT-PT films are potentially interesting for high temperature FeRAM, there is no study that reports essential film properties for the same film composition.

As discussed in Chapter 2 and Chapter 4, the 35BiMT-65PT system exhibits a broad maximum in the Curie temperature, between 26 and 35 mol% BiMT predicted to be between 525°C and 535°C.⁵⁻⁷ In bulk ceramics, the remanent polarization (P_r) at the morphotropic boundary ($x = 0.36$) is $\approx 33-38 \mu\text{C}/\text{cm}^2$ and the P_r at $x=0.5$ was shown to be $\approx 25 \mu\text{C}/\text{cm}^2$.^{5,8,9} The dielectric constant of bulk morphotropic phase boundary (MPB) BiMT-PT has been reported to be ≈ 1000 ^{5,6} or $\approx 300-950$ ^{5,6,9,10} across the tetragonal compositions between 25°C-100 °C (increasing towards as the composition approaches the MPB). Compositions around the MPB retain their properties up to at least 200°C.^{8,11} In both single crystal and ceramics, thermal depoling is notable at 300°C.^{8,12} All of these properties suggest that BiMT-PT is a potential candidate to replace PZT as a high temperature FeRAM material.

Research in BiMT and BiMT-PT thin films has recently increased. MPB BiMT-PT thin films were studied by Zhong *et al.* and Liu *et al.*^{13,14} 600 nm (100)_c oriented 63BiM-37PT thin films produced by Zhong *et al.* had a dielectric constant, T_{\max} , $d_{33,f}$ and P_r of 1060, 415 °C, 90 pm/V and 24 $\mu\text{C}/\text{cm}^2$, respectively.¹³ Tetragonal 20BiMT-80PT films have a ϵ_r of 620 and fatigue resistance up to 10^8 cycles (films doped with 0.5mol% Mn).¹⁵ In addition, the polarization-electric (P-E) hysteresis response is reported to be stable to temperatures of at least 125 °C.¹⁵ Metastable epitaxial {111} BiMT films produced by Oikawa *et al.* show little thickness dependence in polarization-electric field response from 50-800nm.¹⁶ Although BiMT-PT films are potentially interesting for high temperature FeRAM, there is no study that reports essential film properties for the same film composition.

Chapter 4 focused on the processing window-microstructure-composition-ferroelectric property relationships of 35BiMT-65PT thin films grown utilizing pulsed laser deposition. Under a wide range of processing conditions, films were found to be A-site deficient, particularly with Pb deficiency. The Pb deficiency is believed to be a result of preferential adsorption of Bi. With improved film composition, the remanent polarization, P_r , and maximum polarization, P_{\max} , increased.

Chapter 5 describes the effects of A-site deficiency on other electrical properties of 35BiMT-65PT thin films. For high temperature FeRAM technology, the material must be scalable to maintain a low driving voltage, show high temperature stability, low leakage and polarization retention. To determine if 35BMT-65PT is a feasible choice for FeRAM devices, each of these aspects were analyzed. Furthermore, the relationship between composition and high temperature-electric field leakage of the thin film properties was investigated.

5.2 Thickness dependence

It was shown in Chapter 4 that $\approx 600\text{-}700$ nm thick 35BiMT-65PT films had P_r values up to 24-25 $\mu\text{C}/\text{cm}^2$. However, current embedded FeRAM operates at thicknesses <100 nm in order to reduce the driving voltage. Thus, any potential candidate material must exhibit robust functional properties at thickness <100 nm. Figure 5.1(a) and (b) shows the P-E and PUND data, respectively, of 5 mol% La

doped PbTiO_3 seeded 35BiMT-65PT thin films as a function of 35BiMT-65PT film thickness. The thin films were deposited using the 20Pb10Bi0Mg target from Chapter 4, at 340 mTorr $\text{O}_2(90\%)/\text{O}_3(10\%)$ pressure, 6 cm target to substrate distance, 700 °C, and an energy density of 1.6 J/cm². A decrease in the maximum polarization is observed with decreasing thickness. P_r is relatively constant until the film thickness decreases to <200 nm. The PUND measurements in Figure 5.1(b) are in agreement with the P-E measurements.

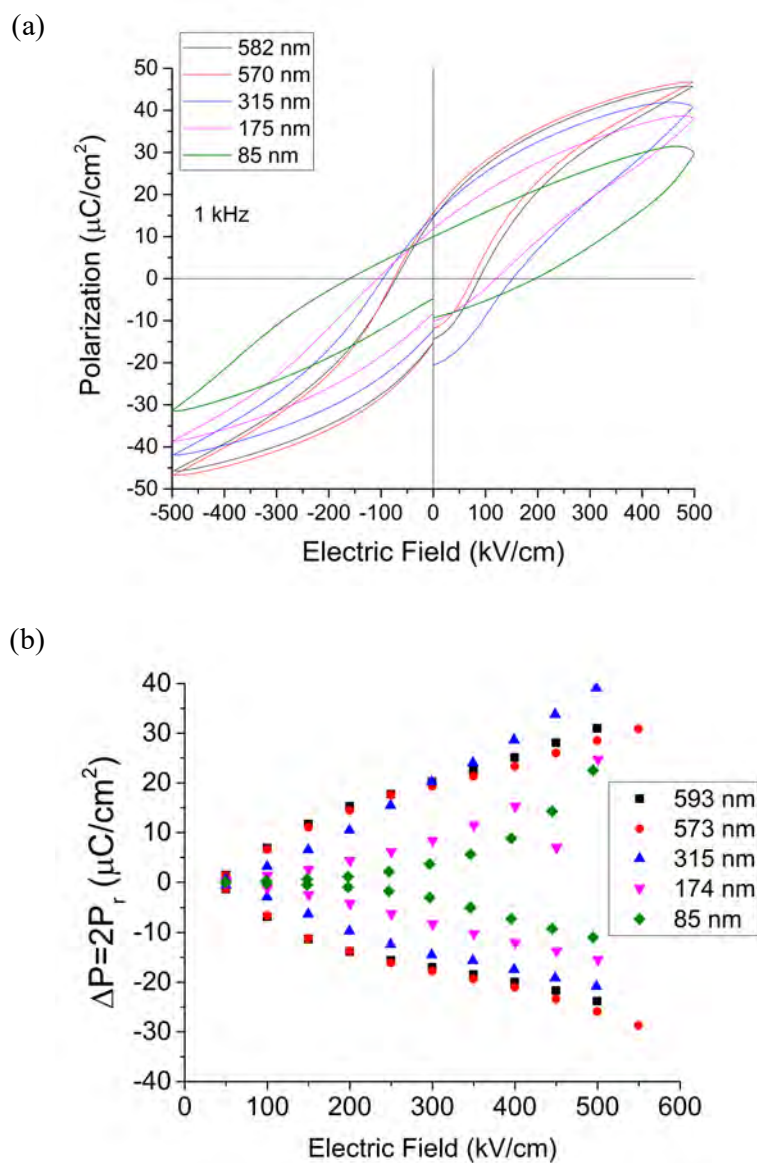


Figure 5.1 - Ferroelectric P-E (a) and PUND (b) of 35BiMT-65PT thin films grown on 16 nm 5 mol% La doped- PbTiO_3 seed layer as a function of thickness. The reported thickness is the total film thickness (seed and grown film).

The ferroelectric properties drop with film thickness; however, the seed layer is expected to play a role in the degradation of both dielectric and ferroelectric properties. In order to assess this, the dielectric response of the films was studied as a function of film thickness. The seed layer was treated as a capacitor in series:

$$\frac{1}{C_{Total}} = \frac{1}{C_{PbTiO_3}} + \frac{1}{C_{BiMT-PT}} \quad \text{Eq. 5.1}$$

where C_{total} , is the total capacitance, C_{PbTiO_3} is the capacitance of the seed layer, and $C_{BiMT-PT}$ is the capacitance of the 35BiMT-65PT thin film. Figure 5.2(a) shows the capacitance-film thickness relationship, confirming a capacitor in series. The total ϵ_r for an ≈ 600 nm film is ≈ 770 ; ϵ_r decreases to ≈ 360 for an 85 nm thick film. Figure 5.2(b) shows the total ϵ_r , along with the corrected value for the BiMT-PT layer vs. film thickness. The corrected ϵ_r is ≈ 960 , similar to the ϵ_r reported by Zhong *et al.* for 63BiMT-37PT thin films.¹³ The ϵ_r of the $PbTiO_3$ seed is calculated to be 99. The low ϵ_r seed is expected to contribute to lower net ferroelectric responses in these films.

To further elucidate the relationship between the seed layer and ferroelectric property degradation with thickness, the total switching charge (P^*) and non-switching charge (P^\wedge) are plotted as a function of effective electric field and thickness in Figure 5.3(a) and (b), respectively. To calculate the effective field, the voltage drop across the seed layer was assumed to be a constant proportion of the applied field at all electric fields. The effective field is only an estimation, as other sources such as domain wall motion, domain switching, and field dependent leakage may change the ratio. Several phenomena are concluded from these data. First, both positive and negative polarization states show increased leakage with decreasing thickness. The positive P^\wedge polarization charge shows greater amounts of leakage with increasing field and decreasing thickness than the negative polarization charge. Second, P^* is constant for all film thicknesses in the negative state. The changes in the positive state are attributed to the increase in P^\wedge . Finally, based on the modest change in $-P^*$, the effective coercive increases for thinner

films. This suppression supports the hypothesis that the seed layer contributes to the degradation of the P-E behavior in the BMT-PT with decreasing thickness.

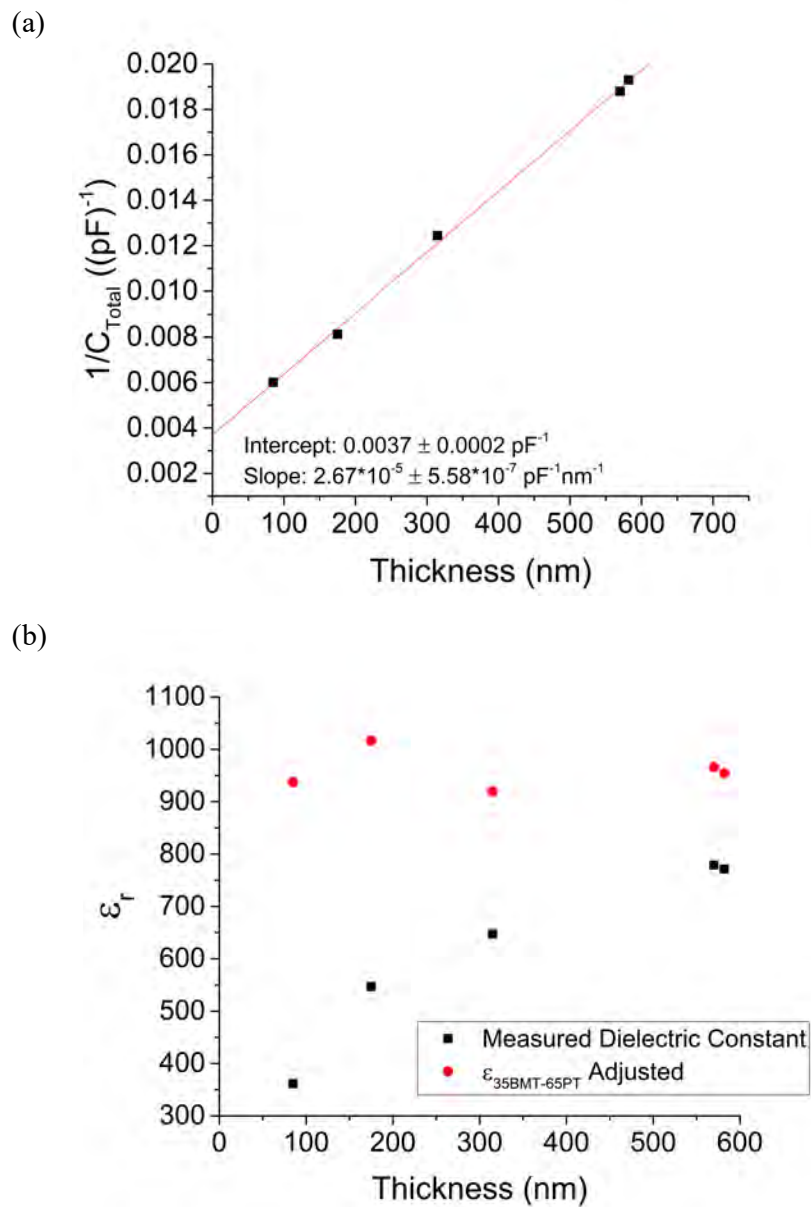


Figure 5.2 - (a) $1/C_{\text{Total}}$ vs thickness plot showing the capacitor in series relationship for seeded 35BiMT-65PT thin films. (b) Adjusted film ϵ_r vs total thickness

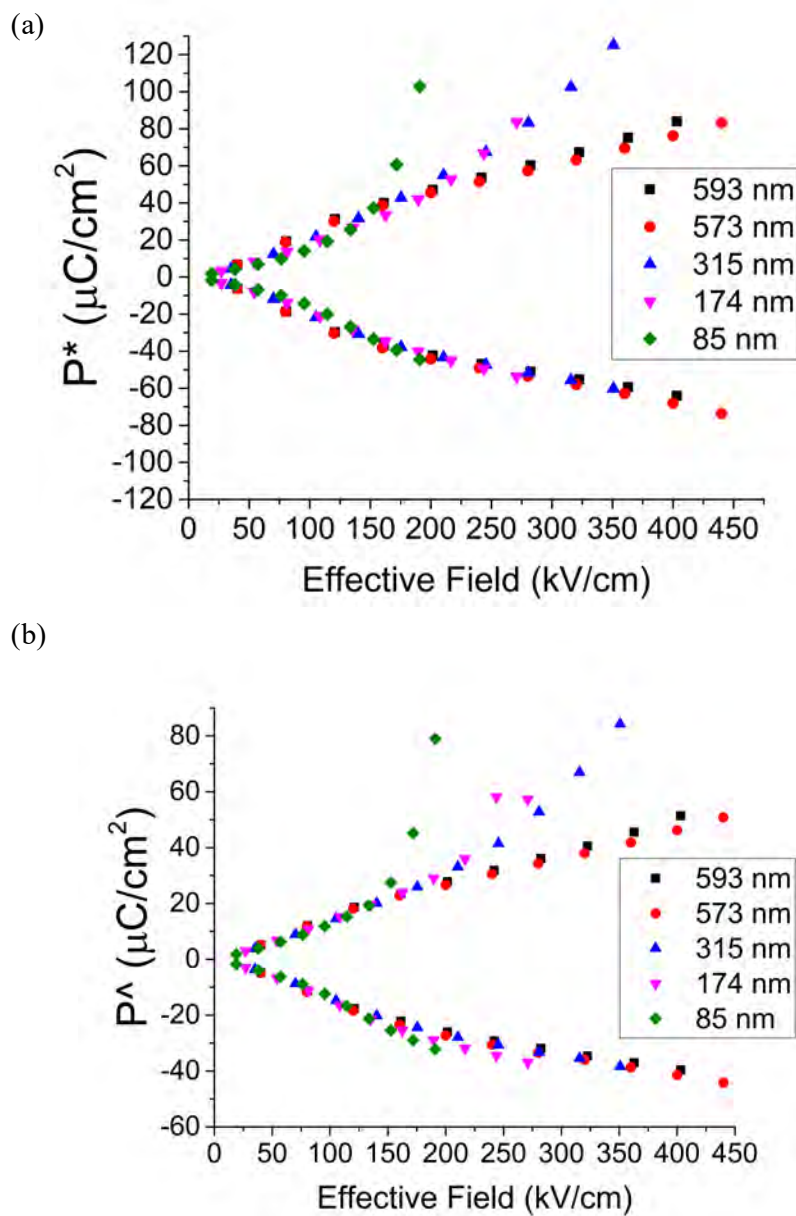


Figure 5.3 - Switching (P^*) and non-switching (P^A) charges vs the effective electric field across the BiMT-PT film of varying thickness. The effective field was calculated assuming the % voltage drop in the dielectric measurements is constant at all fields and then recalculating the new electric field.

5.3 Temperature Dependence

The high temperature behavior was investigated to determine the viability of BiMT-PT for high temperature FeRAM. First, the material must have a high T_c to be a viable choice. Figure 5.4(a) and (b)

shows the ϵ_r vs temperature behavior these films. The T_{\max} for an $\approx 600\text{nm}$ film is $\approx 430^\circ\text{C}$. The loss tangent ($\tan(\delta)$) remains $<15\%$ at 1 kHz up to 335°C and $<10\%$ up to 585°C at 1 MHz. These properties suggest a material that can be utilized in high temperature applications. It is notable, though that the T_{\max} is significantly below the expected value of $\sim 530^\circ\text{C}$. It is hypothesized that the reduction in T_{\max} is correlated with A-site deficiency, as reported in other perovskite systems. Lee and Randall observed that as the Ba/Ti ratio in BaTiO_3 deviated from 1, the Curie point decreases in the single phase region of the phase diagram.¹⁷ It is proposed here that a similar mechanism may occur in 35BiMT-65PT films. In Bi-based- PbTiO_3 solid solutions such as BiMT-PT and BiS-PT there is not a 1:1 correlation between tetragonality and the phase transition temperature, so it was not possible to use the lattice parameters as an independent indication of the phase transition temperatures. Partial correction of the non-stoichiometry (as reported elsewhere⁷) was achieved using a target with excess in Pb, Bi, and Mg. Figure 5.4(c) shows that the T_{\max} increases to 450°C for this film. It is possible that if the Bi:Pb ratio was fully corrected that T_{\max} would approach the predicted values.

Moreover, for high temperature FeRAM, the high T_{\max} must be maintained to small film thickness. Figure 4(d) shows the effect of thickness on the dielectric response (including the seed layer). All films exhibit T_{\max} between 430 and 440°C at 1 MHz indicating that the film transition temperature is independent of film thickness to 85 nm. Additionally, all films show a loss $<15\%$ at 1 MHz up to 585°C regardless of film thickness. The ϵ_r at T_{\max} becomes less pronounced with decreasing thickness. The suppression of ϵ_r at T_{\max} with decreasing thickness may be attributed to several factors: 1. The presence of the low dielectric permittivity layer in series with the 35BiMT-65PT flattens the permittivity peak progressively as film thickness is reduced. 2. The coupling of the domain state with the strain associated with the thermal mismatch between the substrate (Si) and the film.¹⁸ Finally, as T_{\max} does not change with thickness, it is anticipated that the polarization state is stable to high temperature regardless of thickness.

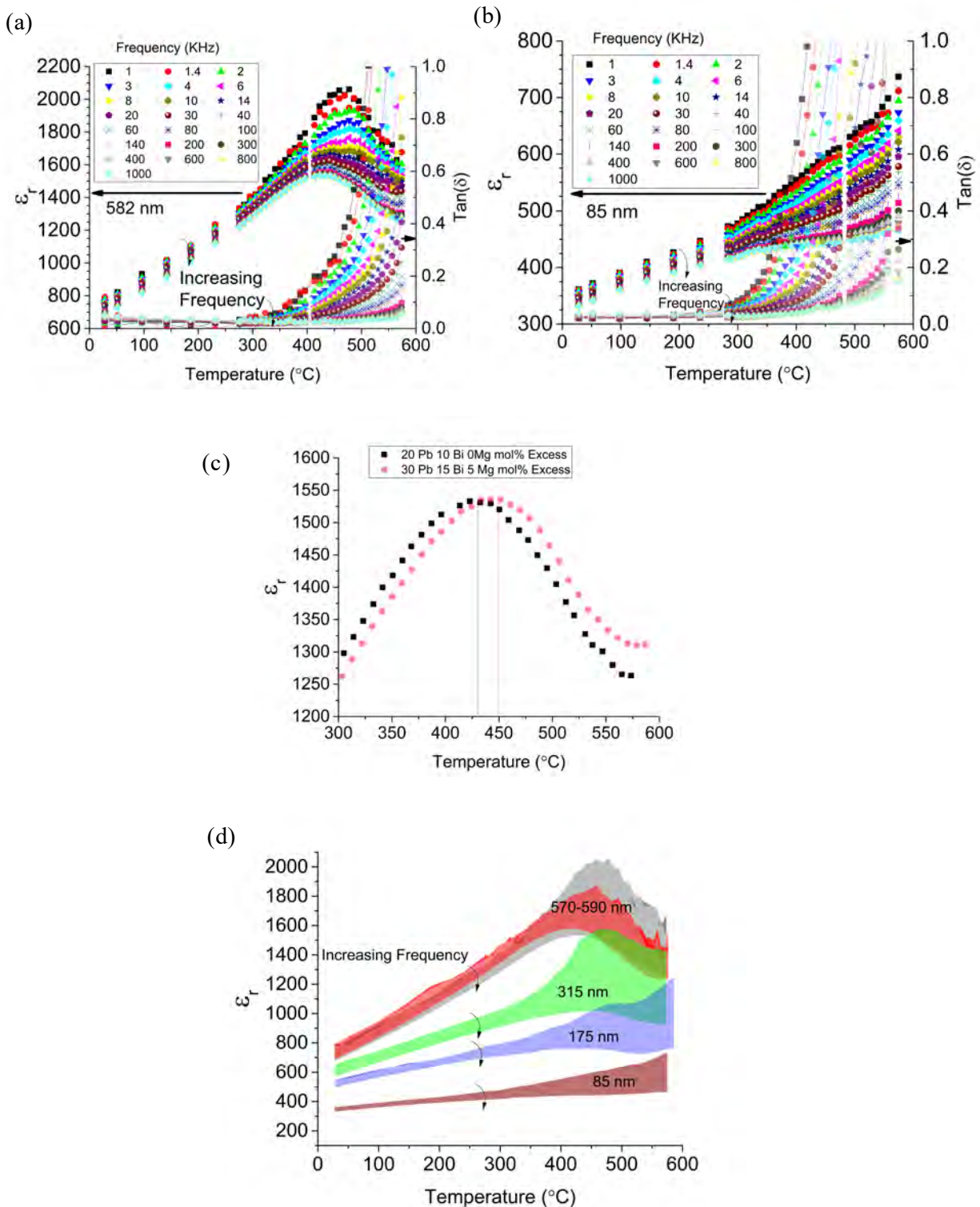


Figure 5.4 - (a) ϵ_r vs. temperature for a 582 nm thick film. (b) ϵ_r vs. temperature for an 85 nm thick film. (c) ϵ_r vs temperature for films deposited using targets of different compositions. The values refer to the mol% excess of each cation added to the target. Permittivity measurements are at 1 MHz with a 30 mV excitation. Film thicknesses are 582 nm (squares) and 632 nm (circles). (d) a variety of film thicknesses showing the thickness independence of T_{\max} in 35BiMT-65PT thin films

As the films show a high T_{max} , the P-E behavior was investigated as a function of temperature. Figure 5(a) shows the P-E behavior from room temperature to 200 °C for an ≈ 600 nm film. The P-E as a function of thickness show the same trend as Figure 5.1(a) when temperature is increased. Up to 50 °C, no change in P-E is seen. At temperature ≥ 100 °C, charge injection is seen for one polarity (driven from the bottom electrode – polarization pointing down). The source of the charge injection is discussed later. The opposite polarization state shows less leakage, and little change up to temperatures of 200 °C. The PUND data shown in Figure 5.5(b) for the negative polarization direction confirm the stability to ~ 200 C. While the leakage in the positive direction is problematic for a high temperature device, the negative polarization state suggests that the problem does not lie with the material, but rather is defect or interface mediated.

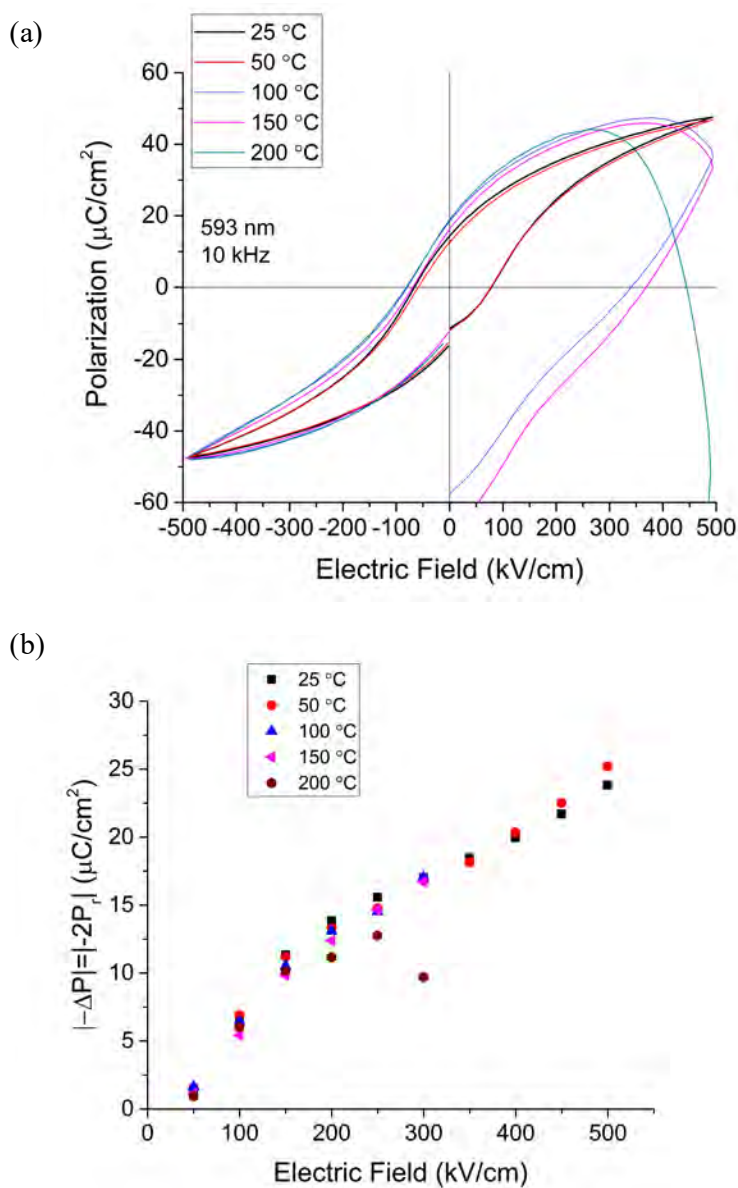


Figure 5.5- (a) High temperature P-E response for a ≈ 600 nm 35BiMT-65PT thin film. (b) Corresponding PUND for the negative polarization state vs. temperature showing temperature independence up to 200 °C.

5.4 High Voltage/Temperature Leakage

While all films have a low dielectric loss tangent (2-3%) at low field, they exhibit increased leakage with increasing field and temperature. To establish the underlying mechanisms of this behavior, I-V measurements were performed on a series of samples deposited at different deposition pressures on 36 nm

PbTiO₃ seeds. As discussed in Chapter 4, films deposited under different deposition pressures exhibit significant changes in film stoichiometry.⁷ Figure 5.6(a) shows the DC field dependence at room temperature of the leakage for films deposited at different pressures; the compositions are shown in Table 5.1. The leakage of these films was found to increase with increasing deposition pressure, which correlates with an increasing A-site deficiency in the films. For comparison, Figure 5.7(a) and (b) show the DC field dependence with increasing temperature for the 100 and 340 mTorr samples. The DC leakage increases with temperature and dielectric breakdown or a change in conduction mechanism begins to show in some samples at electric fields less than 250 kV/cm.

Table 5.1 - Compositions of films as a function of deposition pressure. The compositions were normalized such that the Ti concentration equals the ideal concentration. The oxygen concentration was calculated assuming typical valences for each cation.

| Pressure | Composition | A/B Site Ratio |
|-------------------|---|----------------|
| 60 | (Pb _{0.509} Bi _{0.390} □ _{0.100})(Mg _{0.137} Ti _{0.863})O _{2.958} | 0.90 |
| 100 | (Pb _{0.524} Bi _{0.439} □ _{0.036})(Mg _{0.157} Ti _{0.843})O _{3.026} | 0.96 |
| 200 | (Pb _{0.517} Bi _{0.439} □ _{0.130})(Mg _{0.160} Ti _{0.840})O _{2.885} | 0.87 |
| 340 | (Pb _{0.557} Bi _{0.328} □ _{0.115})(Mg _{0.163} Ti _{0.837})O _{2.886} | 0.88 |
| Ideal Composition | (Pb _{0.65} Bi _{0.35})(Mg _{0.175} Ti _{0.825})O ₃ | 1 |

Two possible sources for the increase in leakage were considered, Schottky emission (eq. 5.2) and Poole-Frenkel emission (eq. 5.3). Linear fits were done from 175 kV to breakdown fields on all samples and a refractive index value was calculated from the estimated permittivity:

$$\ln\left(\frac{J}{T^2}\right) = \ln(A) - \frac{q\phi_B}{kT} + \frac{q\sqrt{\frac{qE}{4\pi\epsilon_r\epsilon_0}}}{kT} \quad eq. 5.2$$

$$\ln\left(\frac{J}{E}\right) = \ln(q\mu N_c) - \frac{q\phi_T}{kT} + \frac{q\sqrt{\frac{qE}{\pi\epsilon_r\epsilon_0}}}{kT} \quad eq. 5.3$$

where J is current density, E is electric field, T is the temperature, A is the Richardson constant, q is the species charge, ϕ_B is the barrier height, ϕ_T is the trap energy level, k is Boltzmann's constant, ϵ_0 is the permittivity of free space and ϵ_r is the relative permittivity. The refractive index calculated from the fitting is shown in Figure 5.6(b) at room temperature and Figure 5.7(c) as a function of temperature.

Also shown in Figure 5.6(c) is the best fit refractive index from a spectroscopic ellipsometry measurement of a film grown at 340 mTorr under the same growth conditions using the same target on a SrTiO₃ substrate. Figure 5.7 shows the ellipsometry fit. The substrate and film were modeled using a Sellmeier model:

$$n = (\varepsilon(\infty) + \frac{A\lambda^2}{\lambda^2 - B^2} - E\lambda^2)^{\frac{1}{2}} \quad \text{Eq. 5.4}$$

where A, B, and E are fitting parameters, λ is the wavelength, $\varepsilon(\infty)$ was set to 1. Tables 3.3 and 5.2 shows the fitting parameters for the SrTiO₃ substrate and the 35BiMT-65PT thin film. The growth conditions are discussed in Chapter 3. At 633 nm, the refractive index is 2.58. The refractive index is similar to that of PbZr_{1-x}Ti_xO₃ (2.2 – 2.6), which is reasonable.¹⁹⁻³⁰ Thus, it is apparent from Figure 5.6(b) that for all deposition pressures, the Poole-Frenkel model has a more reasonable refractive index than the Schottky model. Figure 5.7(b) further validates this as the calculated refractive index is consistently around 2.0 to 2.4 for measurements done at high temperature. As deposition pressure increases the model does tend to disagree more, suggesting other phenomena may also contribute to the conduction. Particularly, the 200 mTorr sample shows a significant decrease in the calculated refractive index as temperature is increased above 25 °C. Given that the data suggest Poole-Frenkel conduction is the dominant conduction mechanism, traps dominate the conduction response; it is hypothesized that the traps are associated with point defects.

To elucidate how the PbTiO₃ seed layer influences the total film conduction, I-V measurements were performed on a 582 nm 35 BiMT-65PT with a 16 nm 5 mol% La-doped PbTiO₃ seed layer (Figure 5.9). The I-V measurements were taken with both polarities (positive polarity is driven from the bottom electrode, negative polarity is driven from the top electrode) on two electrodes. Compared to an equivalent film deposited on a 36 nm thick PbTiO₃ seed layer, the current density is moderately decreased in the positive polarity direction. The negative polarity exhibits significantly reduced leakage, but the slope of the plot at high fields is comparable to the data taken at positive polarity and the samples

deposited on the 36 nm film. The measured Poole-Frenkel slope and calculated permittivity for the negative polarity is $0.00104 \pm 1.5 \times 10^{-5}$ and ≈ 2.84 , respectively. The measured Schottky emission slope and calculated permittivity for the negative polarity is $0.00154 \pm 1.8 \times 10^{-5}$ and ≈ 0.92 . The Poole-Frenkel model is a better fit model to the measured values in Figure 5.6 (c) compared to the Schottky emission model. This also shows that the seed layer does not change the conduction mechanism determined by the I-V measurements.

Table 5.2 - 35BiMT-65PT fitted Sellmeier model parameters. Parameter correlation was less than 0.9 for fitted parameters.

| Fitting Parameter | Value |
|--|--------------------|
| Amplitude | 5.044 ± 0.005 |
| Central Energy (μm) | 0.211 ± 0.001 |
| IR Pole Amplitude (μm^{-2}) | 0 |
| $\epsilon(\infty)$ | 1 |
| Thickness of Surface Roughness | 4.74 ± 0.04 nm |
| Film Thickness | 297.5 ± 0.1 nm |
| MSE | 6.61 |

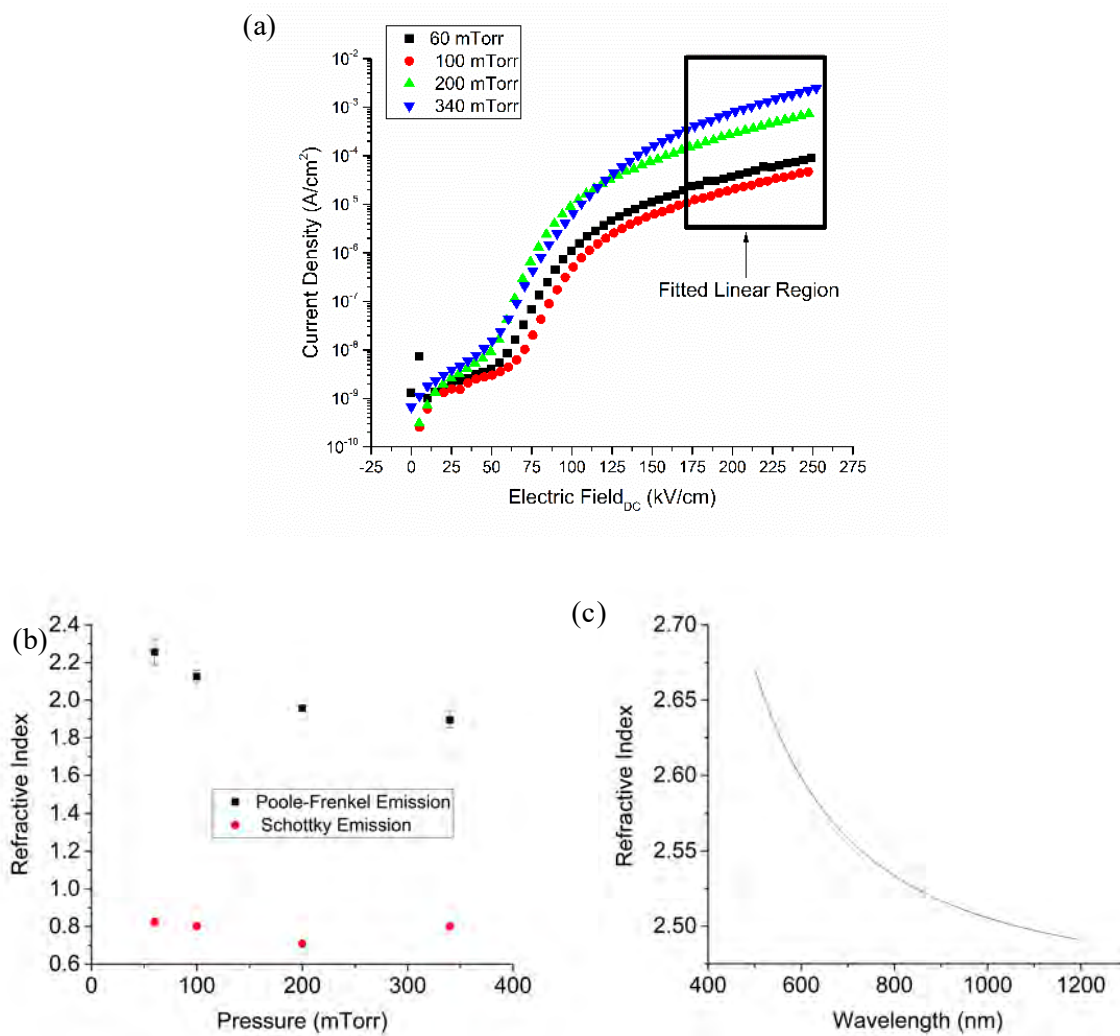


Figure 5.6 - (a) I-V measurement of 35BiMT-65PT thin films deposited under various deposition pressures. (b) Calculated refractive index based on linear fits using Poole-Frenkel and Schottky models vs deposition pressure. (c) Measured refractive index based on ellipsometry models.^{29,30}

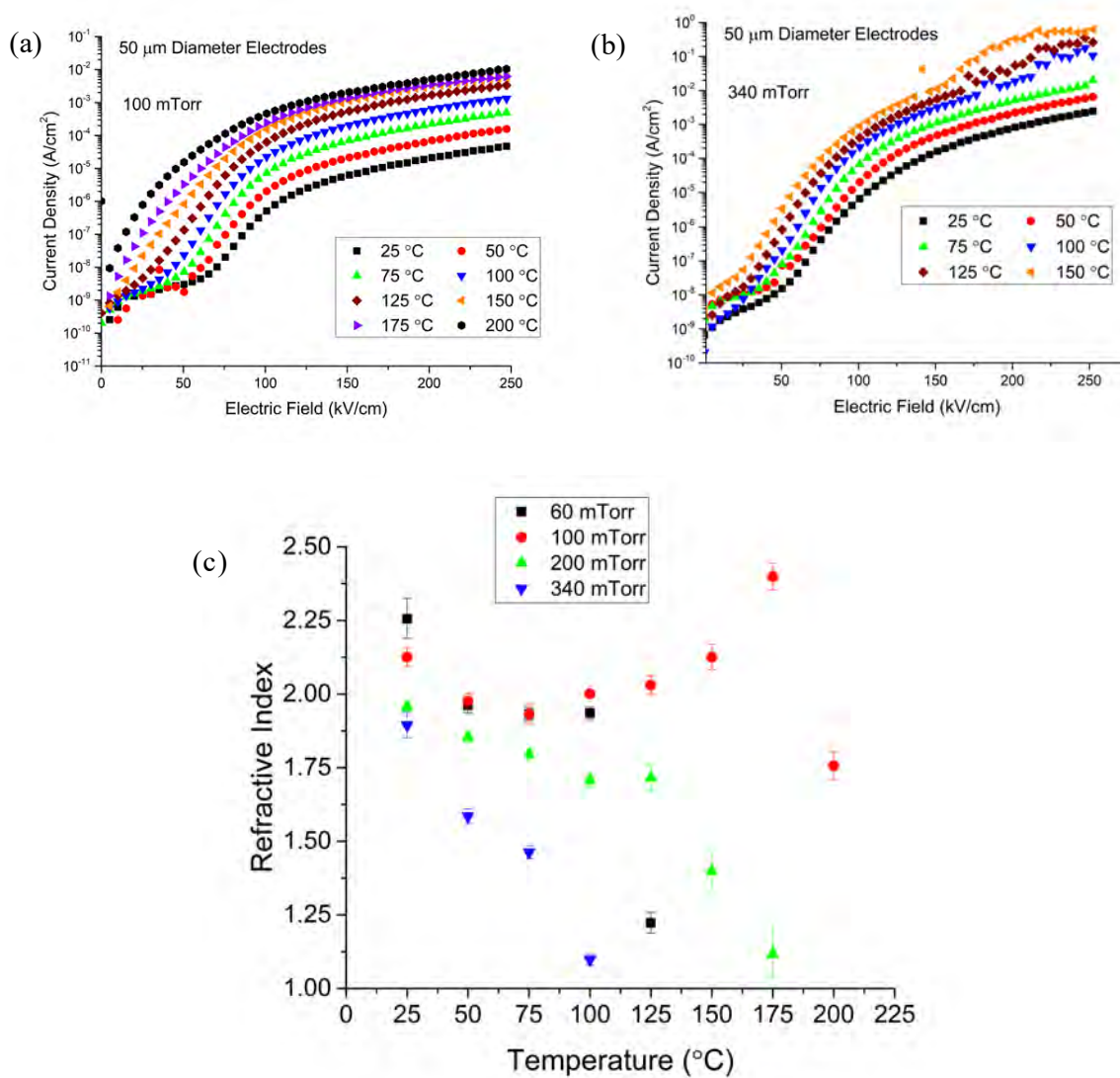


Figure 5.7 - (a)-(b) I-V measurement of 35BiMT-65PT thin films deposited at (a) 100 mTorr and (b) 340 mTorr. (c) Calculated refractive index based on linear fits using Poole-Frenkel and Schottky models for films grown at different deposition pressures. See appendix for fitted data in part (c).

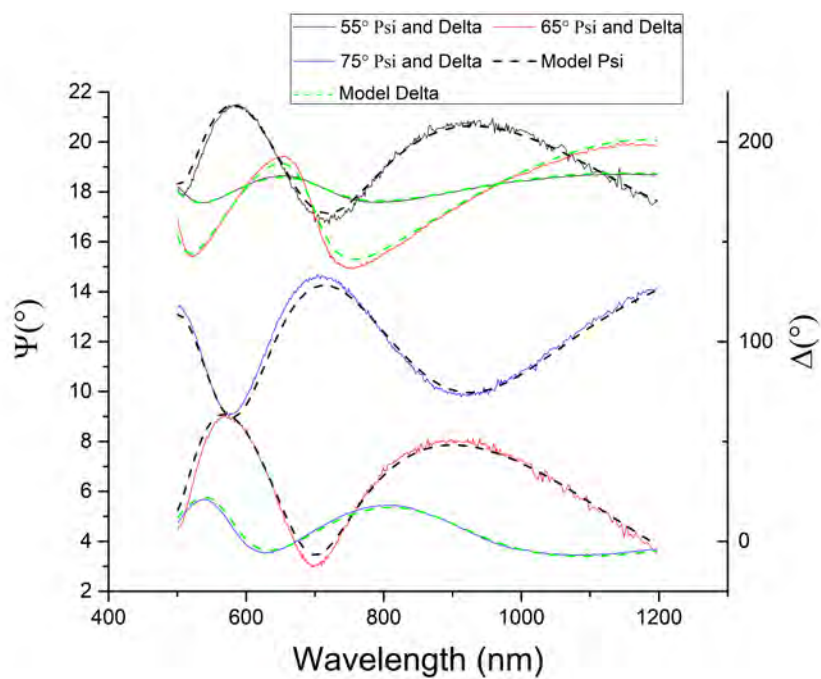


Figure 5.8 – ψ and Δ data and fits of 35BiMT-65PT on SrTiO₃. See chapter 3 for growth conditions.

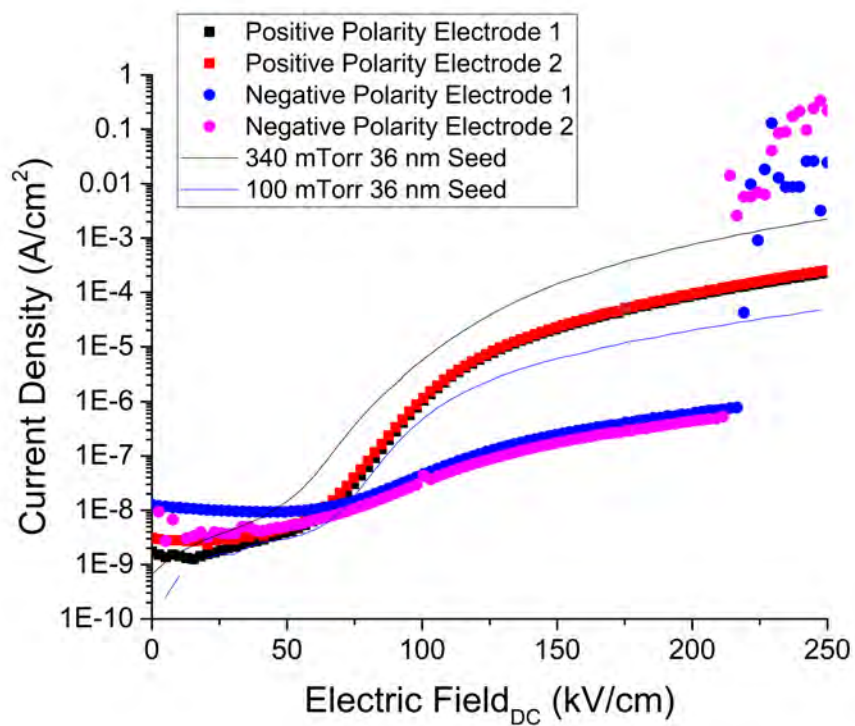


Figure 5.9 - I-V measurement of a 582 nm 35 BiMT-65PT deposited on a 16 nm 5 mol% La doped PbTiO₃ seed layer. The I-V measurements were done on 50 μ m electrodes. For comparison, the positive polarity measurements from a film deposited on 36 nm PbTiO₃ seeds are included in solid lines.

Using the refractive index calculated from the I-V measurements, the Poole-Frenkel barrier height (Figure 5.10) was determined to be close to 0.6 eV. The origin of the trap state is unknown, but it is reasonably close to the activation energy associated with V'_{pb} in PZT ceramics (≈ 0.8 eV). Given the large concentrations of lead vacancies in the 35BiMT-65PT films, this seems like a plausible source.

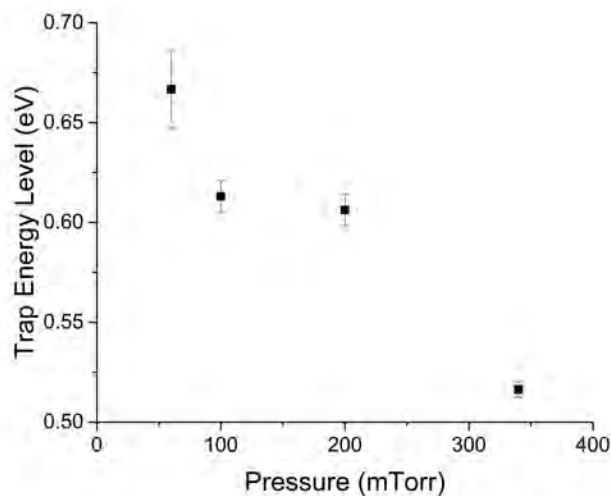


Figure 5.10 – Estimated trap energy level calculated from I-V vs T measurements.

5.5 Retention

The most basic function of any memory device is the ability to retain information, therefore as a further assessment of these materials in terms of their potential for FeRAM, their retention properties were evaluated. For this purpose, the same-state retention was explored at room temperature for films. Figure 5.11(a) shows the retention of several films deposited using different target compositions. Figure 5.11(b) and Figure 5.11(c) show the switching and non-switching charges for the retention test. Figure 5.11(b) shows that there is little systematic change in the switching charge behavior, except that the switching charge increases at small time scales with improved stoichiometry. All films show significant losses in switchable charge over time, which will need to be addressed in future work. It is possible that point defects in the material create internal fields which depole the films. Figure 5.9(a) shows that as the

Pb, Bi and Mg concentrations approach stoichiometry (see 7), the retention increased from $\approx 30\%$ to $>40\%$ of the initial ΔP values after a ≈ 280 min, 0V hold period. Likewise, Figure 5.11(c) shows a systematic decrease in the non-switching behavior as the film stoichiometry improves. Thus, it is anticipated with improved film stoichiometry, the same-state retention of 35BiMT-65PT films will improve.

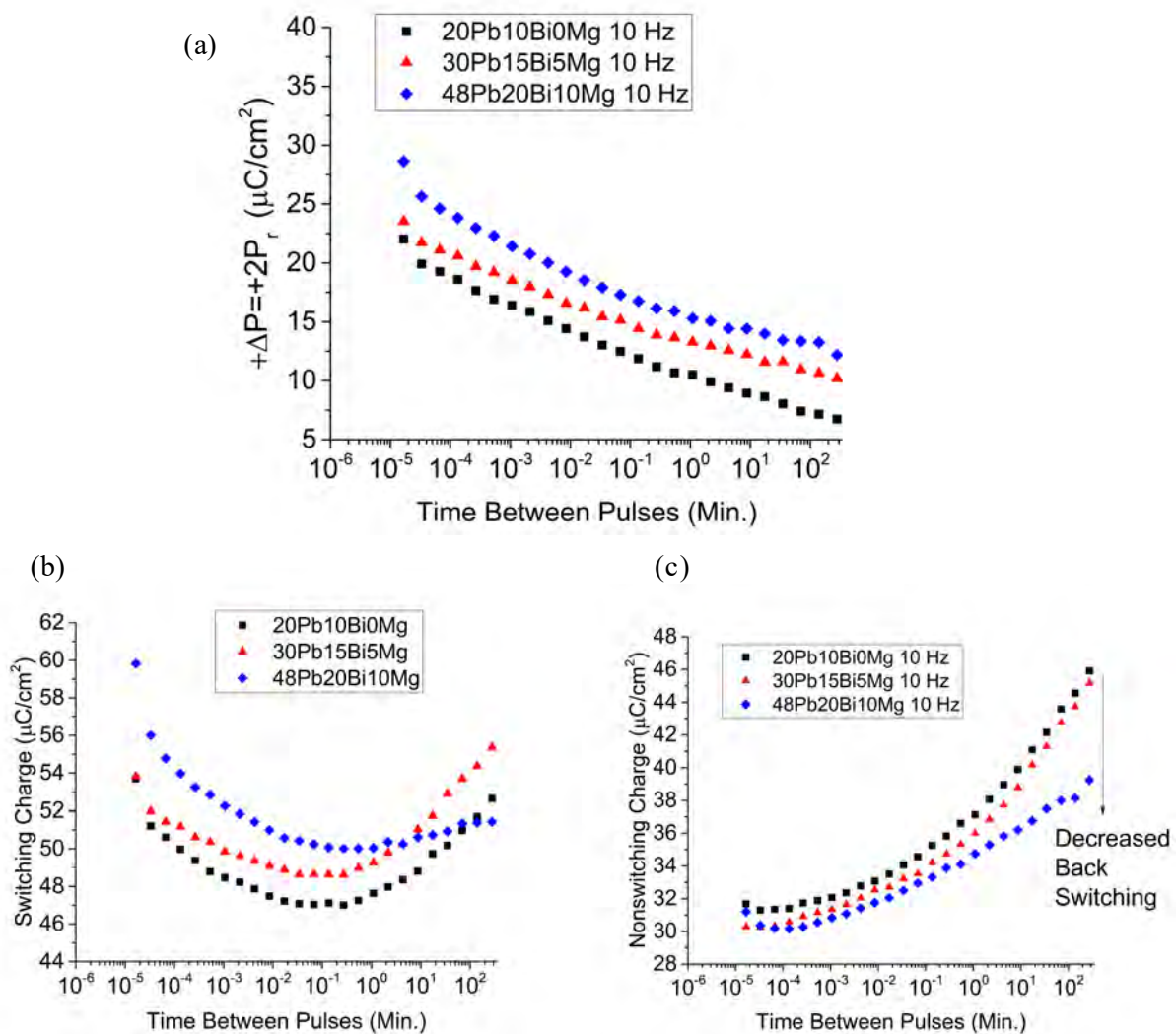


Figure 5.11 – Room temperature retention of 580-630 nm 35BiMT-65PT thin films as a function of target composition. Retention analysis was done with 300 kV/cm and 1 ms pulses. (a) The overall switching response. (b) The switching charge. (c) The non-switching charge.

5.6 Conclusions

Pulsed laser deposited 35BiMT-65PT thin films were investigated. The P-E hysteresis and dielectric permittivity were investigated as a function of thickness. With decreasing thickness, the P_r and dielectric permittivity decrease. A capacitor in series model shows that the film thickness dependent properties may be related to the presence of a low dielectric constant seed layer at the interface. Adjusting for the dielectric permittivity for the seed layer yields a thickness independent dielectric permittivity of ≈ 960 . High temperature permittivity measurements show a T_{\max} of ≈ 430 °C and $\tan(\delta) < 15\%$ at 1 MHz up to 585 °C for film thickness between 85 nm to ≈ 600 nm. The high temperature P-E response show charge injection with increasing temperature. PUND measurements show little change in P_r up to temperatures of 200 °C. I-V measurements show conduction consistent with Poole-Frenkel emission. The retention improves with improved film stoichiometry, suggesting the poor retention is due to defects within the material.

5.7 References

- 1 P. Muralt, R.G. Polcawich, and S. Trolier-McKinstry, "Piezoelectric Thin Films for Sensors, Actuators, and Energy Harvesting," *MRS Bull.*, **34** [September] 658–664 (2009).
- 2 J. Rodriguez, K. Remack, J. Gertas, L. Wang, C. Zhou, K. Boku, K.R. Udayakumar, S. Summerfelt, T. Moise, D. Kim, J. Groat, J. Eliason, M. Depner, and F. Chu, "Reliability of Ferroelectric Random Access Memory Embedded within 130nm CMOS," pp. 750–758 in *Reliab. Phys. Symp. (IRPS), 2010 IEEE*. 2010.
- 3 J.A. Rodriguez, K. Remack, K. Boku, K.R. Udayakumar, S. Aggarwal, S.R. Summerfelt, F.G. Celii, S. Martin, L. Hall, K. Taylor, T. Moise, H. McAdams, J. McPherson, S. Member, R. Bailey, G. Fox, and M. Depner, "Reliability Properties of Low-Voltage Ferroelectric Capacitors and Memory Arrays," *IEEE Trans. Device Mater. Reliab.*, **4** [3] 436–449 (2004).
- 4 K.R. Udayakumar, T. San, J. Rodriguez, S. Chevacharoenkul, D. Frystak, J. Rodriguez-Latorre, C. Zhou, M. Ball, P. Ndai, S. Madan, H. McAdams, S. Summerfelt, and T. Moise, "Low-Power Ferroelectric Random access Memory Embedded in 180nm Analog Friendly CMOS Technology," *2013 5th IEEE Int. Mem. Work. IMW 2013*, 128–131 (2013).
- 5 C.A. Randall, R. Eitel, B. Jones, T.R. Shrout, D.I. Woodward, and I.M. Reaney, "Investigation of a High T_c Piezoelectric System: $(1-x)\text{Bi}(\text{Mg}_{1/2}\text{Ti}_{1/2})\text{O}_3-(x)\text{PbTiO}_3$," *J. Appl. Phys.*, **95** [7] 3633 (2004).
- 6 M.R. Suchomel and P.K. Davies, "Predicting the Position of the Morphotropic Phase Boundary in High Temperature PbTiO_3 - $\text{Bi}(\text{B}'\text{B}')\text{O}_3$ Based Dielectric Ceramics," *J. Appl. Phys.*, **96** [8] 4405–4410 (2004).
- 7 C. Morandi, J.L. Gray, W. Aufer, and S. Trolier-McKinstry, "Pulsed Laser Deposited 35 $\text{Bi}(\text{Mg}_{1/2}\text{Ti}_{1/2})\text{O}_3$ - 65 PbTiO_3 Thin Films Part 1 - Influence of Processing on Composition, Microstructure, and Ferroelectric Hysteresis," 2018.

- 8 Q. Zhang, Z. Li, F. Li, Z. Xu, and X. Yao, "Temperature Dependence of Dielectric/Piezoelectric Properties of $(1-x)\text{Bi}(\text{Mg}_{1/2}\text{Ti}_{1/2})\text{O}_3$ - $x\text{PbTiO}_3$ Ceramics with an MPB Composition," *J. Am. Ceram. Soc.*, **93** [10] 3330–3334 (2010).
- 9 S. Sharma and D.A. Hall, "Ferroelectric and Antiferroelectric Polarisation Switching Characteristics of $\text{Bi}(\text{Mg}_{0.5}\text{Ti}_{0.5})\text{O}_3$ - PbTiO_3 Ceramics," *J. Mater. Sci. Mater. Electron.*, **21** [4] 405–409 (2010).
- 10 A. Moure, M. Alguero, L. Pardo, E. Ringgaard, and A.F. Pedersen, "Microstructure and Temperature Dependence of Properties of Morphotropic Phase Boundary $\text{Bi}(\text{Mg}_{1/2}\text{Ti}_{1/2})\text{O}_3$ - PbTiO_3 Piezoceramics Processed by Conventional Routes," *J. Eur. Ceram. Soc.*, **27** 237–245 (2007).
- 11 J. Chen, X. Tan, W. Jo, and J. Rödel, "Temperature Dependence of Piezoelectric Properties of High- T_c $\text{Bi}(\text{Mg}_{1/2}\text{Ti}_{1/2})\text{O}_3$ - PbTiO_3 ," *J. Appl. Phys.*, **106** [3] 34109 (2009).
- 12 J. Liu, X. Chen, G. Xu, D. Yang, Y. Tian, and X. Zhu, "Novel High-Temperature Ferroelectric Single Crystals $0.38\text{Bi}(\text{Mg}_{1/2}\text{Ti}_{1/2})\text{O}_3$ - 0.62PbTiO_3 with Good and Temperature-Stable Piezoelectric Properties," *CrystEngComm*, **17** [30] 5605–5608 (2015).
- 13 C. Zhong, X. Wang, L. Guo, and L. Li, "Characterization of (100)-Oriented $0.63\text{BiMg}_{1/2}\text{Ti}_{1/2}\text{O}_3$ - 0.37PbTiO_3 Piezoelectric Films by a Sol-Gel Process," *Thin Solid Films*, **580** 52–55 (2015).
- 14 L.X. Zhang and X. Ren, "In Situ Observation of Reversible Domain Switching in Aged Mn-doped BaTiO_3 Single Crystals," *Phys. Rev. B - Condens. Matter Mater. Phys.*, **71** [17] 1–8 (2005).
- 15 L. Zhang, J. Chen, H. Zhao, L. Fan, Y. Rong, J. Deng, R. Yu, and X. Xing, "Temperature-Independent Ferroelectric Property and Characterization of High- T_c $0.2\text{Bi}(\text{Mg}_{1/2}\text{Ti}_{1/2})\text{O}_3$ - 0.8PbTiO_3 Thin Films," *Appl. Phys. Lett.*, **103** [8] 82902 (2013).
- 16 T. Oikawa, S. Yasui, T. Watanabe, H. Yabuta, Y. Ehara, T. Fukui, and H. Funakubo, "Film Thickness Dependence of Ferroelectric Properties of (111)-Oriented Epitaxial $\text{Bi}(\text{Mg}_{1/2}\text{Ti}_{1/2})\text{O}_3$ Films," *Jpn. J. Appl. Phys.*, **51** [09LA04] 09LA04 (2012).
- 17 S. Lee, C.A. Randall, and Z.K. Liu, "Modified Phase Diagram for the Barium Oxide-Titanium Dioxide System for the Ferroelectric Barium Titanate," *J. Am. Ceram. Soc.*, **90** [8] 2589–2594 (2007).
- 18 J.F. Ihlefeld, D.T. Harris, R. Keech, J.L. Jones, J.P. Maria, and S. Trolier-McKinstry, "Scaling Effects in Perovskite Ferroelectrics: Fundamental Limits and Process-Structure-Property Relations," *J. Am. Ceram. Soc.*, **99** [8] 2537–2557 (2016).
- 19 J. Lappalainen, J. Hiltunen, and V. Lantto, "Characterization of Optical Properties of Nanocrystalline Doped PZT Thin Films," *J. Eur. Ceram. Soc.*, **25** [12 SPEC. ISS.] 2273–2276 (2005).
- 20 A. Deineka, M. Glinchuk, L. Jastrabik, and G. Suchanek, "Influence of Surface and Interface on PZT Film Optical Properties," *Phys. Status Solidi*, **443** 443–446 (1999).
- 21 G. Teowee, J.T. Simpson, T. Zhao, M. Mansuripur, J.M. Boulton, and D.R. Uhlmann, "Electro-Optic Properties of Sol-Gel Derived PZT and PLZT Thin Films," *Microelectron. Eng.*, **29** [1–4] 327–330 (1995).
- 22 C.H. Peng and S.B. Desu, "Low-Temperature Metalorganic Chemical Vapor Deposition of Perovskite $\text{Pb}(\text{Zr}_x\text{Ti}_{1-x})\text{O}_3$ Thin Films," *Appl. Phys. Lett.*, **61** [1] 33–36 (1992).
- 23 M.P. Moret, M.A.C. Devillers, K. Wörhoff, and P.K. Larsen, "Optical Properties of PbTiO_3 , $\text{PbZr}_x\text{Ti}_{1-x}\text{O}_3$, PbZrO_3 Films Deposited by Metalorganic Chemical Vapor on SrTiO_3 ," *J. Appl. Phys.*, **92** [1] 468–474 (2002).
- 24 C.H. Peng, J.-F. Chang, and S.B. Desu, "Optical Properties of PZT, PLZT and PNZT Thin Films," pp. 21–26 in *Mat. Res. Soc. Symp. Proc.* 1992.
- 25 G. Yi, Z. Wu, M. Sayer, G. Vi, and Z. Wu, "Preparation of $\text{Pb}(\text{Zr},\text{Ti})\text{O}_3$ Thin Films by Sol Gel Processing: Electrical, Optical, and Electro-Optic Properties," *J. Appl. Phys.*, **64** [5] 2717–2724 (1988).
- 26 C.M. Foster, G. Bai, R. Csencsits, J. Vetrone, R. Jammy, C.M. Foster, G. Bai, R. Csencsits, J.

- Vetrone, and R. Jammy, "Single-Crystal $\text{Pb}(\text{Zr}_x\text{Ti}_{1-x})\text{O}_3$ Thin Films Prepared by Metal-Organic Chemical Vapor Deposition: Systematic Compositional Variation of Electronic and Optical Properties," *J. Appl. Phys.*, **81** [5] 2349–2357 (1997).
- 27 B.G. Potter, M.B. Sinclair, and D. Dimos, "Electro-Optical Characterization of $\text{Pb}(\text{Zr},\text{Ti})\text{O}_3$ Thin Films by Waveguide Refractometry," *Appl. Phys. Lett.*, **63** [16] 2180–2182 (1993).
- 28 A. Deineka, L. Jastrabik, G. Suchanek, and G. Gerlach, "Ellipsometric Investigations of the Refractive Index Depth Profile in PZT Thin Films," *Phys. Status Solidi*, **188** [4] 1549–1552 (2001).
- 29 S. Trolier-McKinstry, J. Chen, K. Vedam, and R.E. Newnham, "In Situ Annealing Studies of Sol-Gel Ferroelectric Thin Films by Spectroscopic Ellipsometry," *J. Am. Ceram. Soc.*, **78** [7] 1907–1913 (1995).
- 30 S. Trolier-McKinstry, H. Hu, S.B. Krupanidhi, P. Chindaudom, K. Vedam, and R.E. Newnham, "Spectroscopic Ellipsometry Studies on Ion Beam Sputter Deposited $\text{Pb}(\text{Zr},\text{Ti})\text{O}_3$ Films on Sapphire and Pt-coated Silicon Substrates," *Thin Solid Films*, **230** 15–27 (1993).

Chapter 6

Development of Seedless 35 Bi(Mg_{1/2}Ti_{1/2})O₃-65PbTiO₃ Thin Films

6.1 Introduction

The electrical properties of 35BiMT-65PT thin films were examined as a function of film composition, thickness and temperature; these results were discussed in chapters 4 and 5. It was found that films of ≈ 600 -700 nm thickness show good ferroelectric properties with a P_r up to 24-25 $\mu\text{C}/\text{cm}^2$. However, the ferroelectric properties degrade with decreasing film thickness, limiting the usage of 35BiMT-65PT as a high temperature FeRAM material. Additionally, the films show significant retention loss at room temperature and significant charge injection with increasing temperature and/or voltage.

These limitations may be attributed to two sources: non-stoichiometry in the films (especially the large concentration of V_{pb}'') and the presence of a seed layer. The low permittivity seed layer was shown to significantly impact the dielectric and ferroelectric properties, as it acts like a capacitor in series with the 35BiMT-65PT thin film. Adjusting for the presence of the seed layer, the 35BiMT-65PT films have a thickness independent relative permittivity of ≈ 960 . The seed layer permittivity was calculated to be 99.

Due to the influence of the seed layer on the electrical properties, Chapter 6 focuses on the development of seedless growth of 35BiMT-65PT thin films on Pt/Si substrates. The processing, microstructure and electrical properties were investigated. As in chapter 5, high temperature polarization stability, low leakage and polarization retention were analyzed.

6.2 Seedless 35BiMT-65PT Thin Film Growth and Microstructure

As discussed in chapter 4, phase pure 35BiMT-65PT thin films can be grown directly on platinized silicon using room temperature PLD deposition, followed by crystallization in an RTA; the balance of the film can then be grown to thickness by high temperature deposition. However, this process may lead to inconsistencies in the film due to the different processing conditions for the two layers. Thus, a one-step high temperature growth was utilized here.

Platinized Si often hillocks during high temperature growths.¹ This creates shorts in dielectric films grown on top, limiting thickness scaling experiments. Thus, initial experiments were conducted to determine whether the Pt substrates utilized in this work were susceptible to hillocking, by analyzing the Pt surface after etching the 35BiMT-65PT grown on top. Figure 6.1 shows the platinum surface after removing films grown utilizing 20Pb10Bi0Mg or 30Pb15Bi5Mg targets; the growth conditions for the film are given in the caption. Neither surface shows the formation of hillocks in the platinum surface, confirming that thickness scaling experiments can be done without limitation by hillock formation.

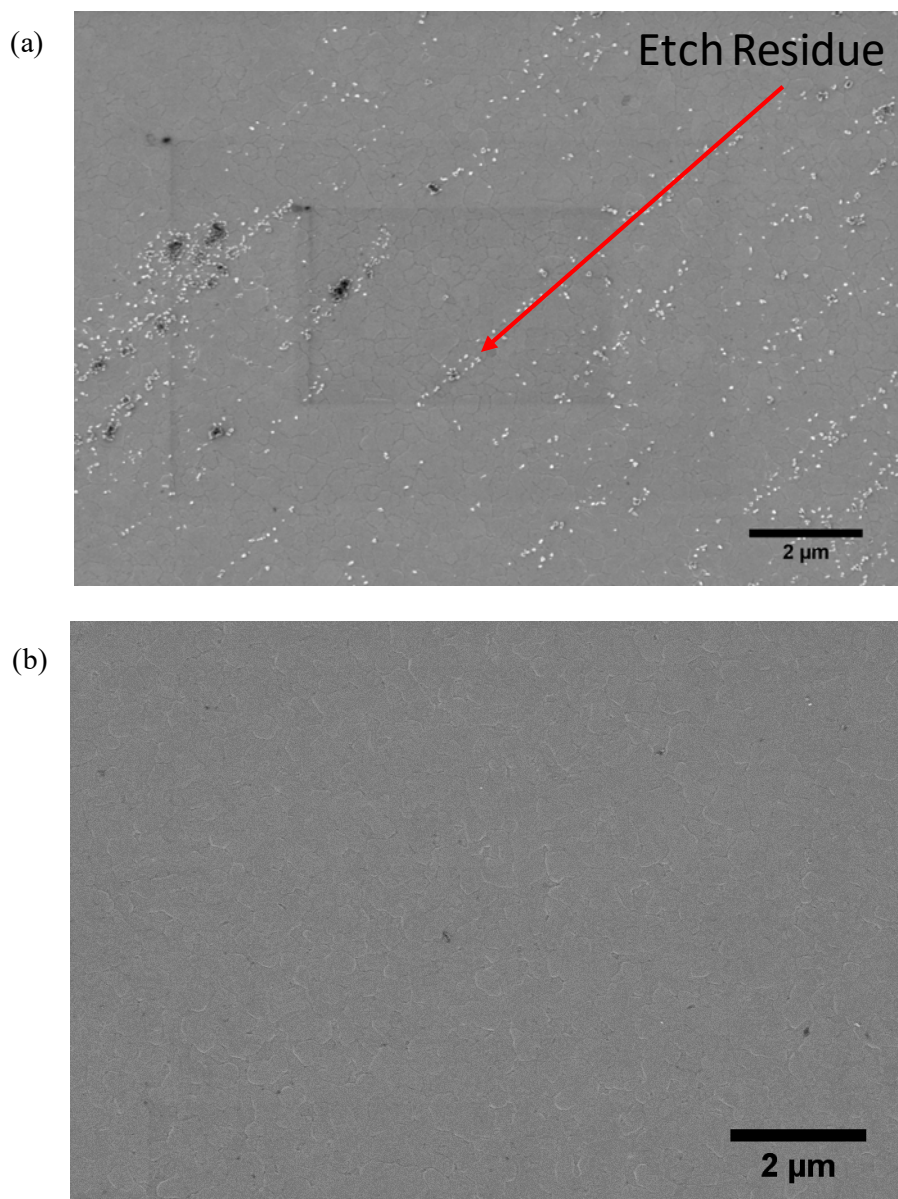


Figure 6.1 – SEM of the etched platinum surface after depositing 35BiMT-65PT at 340 mTorr, 700 °C, 6 cm target to substrate distance, 340 mTorr O₂/O₃, and 10 Hz. The targets utilized are (a) 20Pb10Bi0Mg and (b) 30Pb15Bi5Mg.

It has been demonstrated with PZT and PMN-PT that the presence of excess PbO favors the formation of (100)_c oriented films. Thus, films were deposited utilizing at 700 °C, 340 mTorr O₂/O₃, and 10 Hz for 10 minutes each utilizing the same target compositions developed for seeded growth. Figure 6.2 shows the XRD patterns for 600-650 nm thick films utilizing the different target compositions. All films are phase pure perovskite and have a (100)_c preferred orientation. However, no direct correlation is

found between the target composition and the film orientation. Figure 6.2 demonstrates that the change in PbO flux did not have a significant impact on the degree of (100)_c orientation. Instead, a maximum in the (100)_c orientation was found for the 48Pb20Bi10Mg target; the orientation decreases with higher amounts of excess PbO. As discussed in chapter 4, the optimum PbO content may change as the laser deposition frequency is changed.

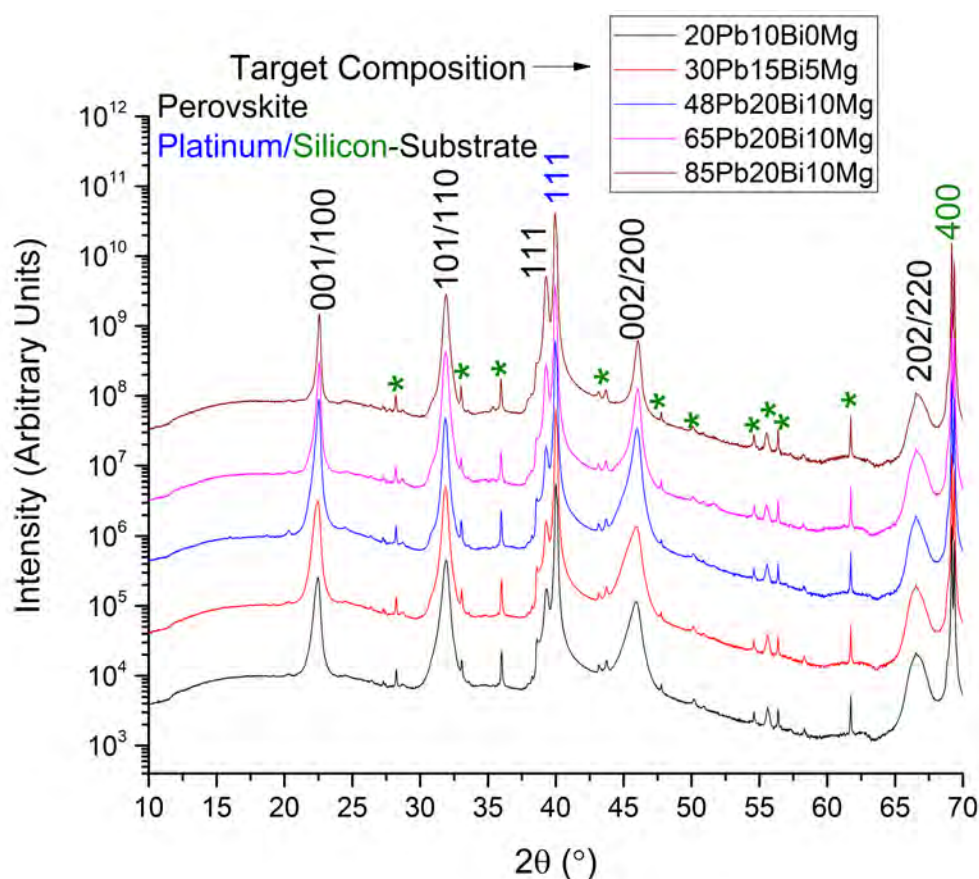


Figure 6.2 - XRD patterns of 35 BiMT-65PT 600-650 nm thick thin films deposited using the same target compositions as seeded growth.

Based on this result (and the electrical properties in Figure 6.5), the 48Pb20Bi10Mg target was selected for further growths. For the thickness scaling, films were grown between 100 nm to 700 nm in thickness. Figure 6.3 shows the resulting XRD patterns of the thickness series. Consistent with Figure 6.2, all films are phase pure and

(100)_c oriented. As the film thickness changes, there is some broadening of the peaks, particularly the (100)_c peaks, which may be due to either a change in film structure, crystalline quality, or a difference in the stress in the thin film.

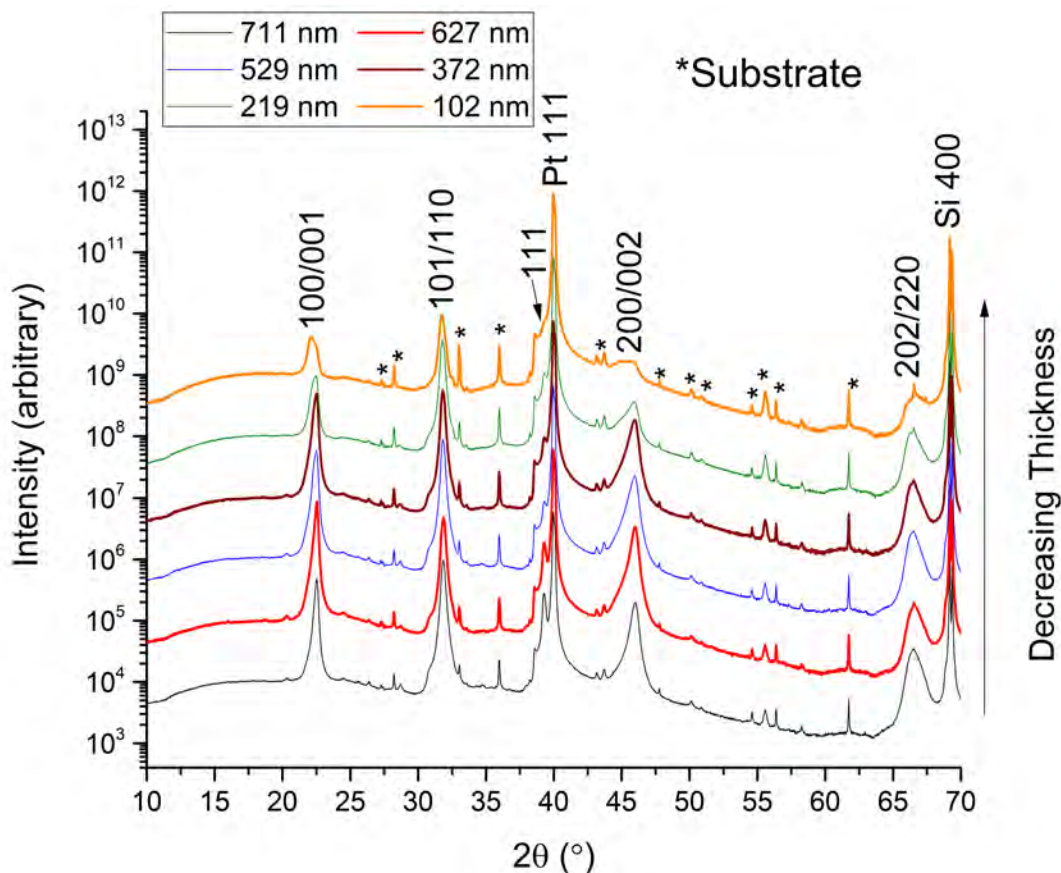


Figure 6.3 - XRD patterns of 35 BiMT-65PT 100-700 nm thick thin films deposited using the 48Pb20Bi10Mg composition target.

Some depositions were done in different background atmospheres (see below) as part of process optimization; this may influence the film composition and hence the conductivity and/or conduction mechanism (see section 6.4 for further details). Figure 6.4 shows the XRD patterns of 35BiMT-65PT thin films grown at 340 mTorr, 700 °C, 6 cm target to substrate distance from a 48Pb20Bi10Mg target composition at 10 Hz laser frequency for 10 minutes with varying amounts of O₂/Ar background gas amounts. The films were deposited with a constant flow rate of 50 sccm gas and no O₃ was utilized in the gas mixture to limit the number of variables and decrease the O₂ reactivity. The film thicknesses ranged from 580 nm – 630 nm, decreasing with decreasing O₂% possibly due to an increase in bombardment

with heavier Ar ions. At 100% Ar, no crystalline phase was detected and no film was seen on the surface suggesting bombardment increases with increasing Ar concentration.

All films were phase pure perovskite. (100)_c orientation increased with increasing Ar concentration in the atmosphere, likely due to the increase in bombardment energy. This is different compared to growths on seeded films where the film deposition pressure was varied. As discussed in chapter 4, decreasing the chamber pressure also leads to a change in bombardment energy. However, XRD of films of comparable thickness on 36 nm PbTiO₃ seeds did not show any correlation between film orientation and deposition pressure (Figure 6.4 (b)). Three possible reasons were considered to explain these datasets. First, the change in bombardment energy as a function of chamber pressure may not be as large as that seen with changing Ar concentration. It is believed that this is unlikely as the change in film thickness for equivalent time is much greater for different pressures, as seen in Figure 4.1. Second, the seed layer surface may differ slightly from deposition to deposition due to the variable heating time of the substrate heater; this could also influence the nucleation step. Finally, different batch seed layers used may have had slightly different orientations, ultimately changing the final film orientation. See appendix C for lattice parameter estimations of seedless films and comparisons to film properties.

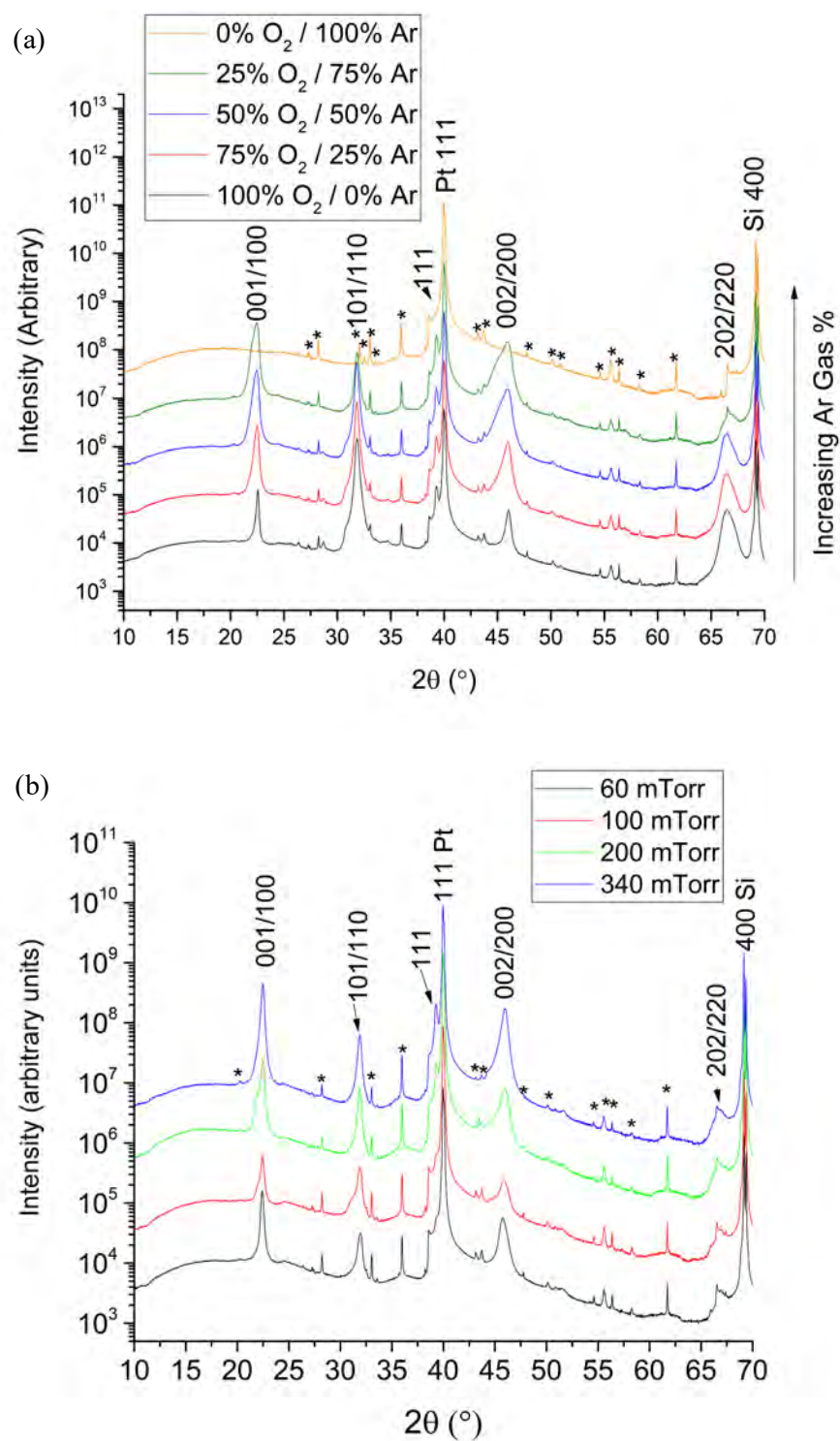


Figure 6.4 – (a) XRD patterns of 35 BiMT -65PT 580-630 nm thick films deposited with varying O₂/Ar background gas mixtures. Films were deposited from the 48Pb20Bi10Mg target at 340 mTorr and constant mass flow rate 50 sccm. (b) XRD patterns of 35BiMT-65PT ≈670 nm – ≈720 nm thick films deposited on 36 nm PbTiO₃ between 60 mTorr and 340 mTorr background deposition pressure (90% O₂/10% O₃). Films were deposited from a 20Pb10Bi0Mg target.

6.3 Ferroelectric Hysteresis and Thickness Dependence of Seedless Thin Films

Chapters 4 and 5 demonstrated the need for improved processing conditions to optimize the dielectric and ferroelectric properties of 35BiMT-65PT thin films. Elimination of the seed layer is also of interest in terms of potentially reducing the thickness dependence and improving the manufacturability of BMT-PT films. It was anticipated that the optimized conditions for seedless growth would be similar to that of seeded growth. For a growth at 10 Hz laser frequency, 700 °C, 6 cm target to substrate distance and 340 mTorr O₂/O₃ background pressure, the optimal target composition was found to be 48Pb20Bi10Mg, based on the composition and ferroelectric properties. Figure 6.5 demonstrates the ferroelectric hysteresis response as a function of the target composition compared to that of the seeded growth with a 48Pb20Bi10Mg target. Several phenomena can be noted in the ferroelectric hysteresis data. First, all seedless films exhibit significantly more charge injection, leading to bloated hysteresis on the positive axis. This demonstrates that the 5mol% La-doped PbTiO₃ seed layers suppress charge injection. Second, charge injection in the seeded films is detectable at fields exceeding 600 kV/cm at room temperature, while injection in seedless films begin for fields above 250 kV/cm-300 kV/cm. Third, the amount of charge injection reduces with increasing PbO content in the target up to 48 mol%, but the ferroelectric properties do not change substantively for films deposited from targets containing even more excess PbO. Finally, the PUND data in Figure 6.5 (c) demonstrates that the 48Pb20Bi10Mg seeded or unseeded deposited films show effectively the same ferroelectric properties. Thus, the 48Pb20Bi10Mg target composition was selected as the optimal target for the remainder of the experiments.

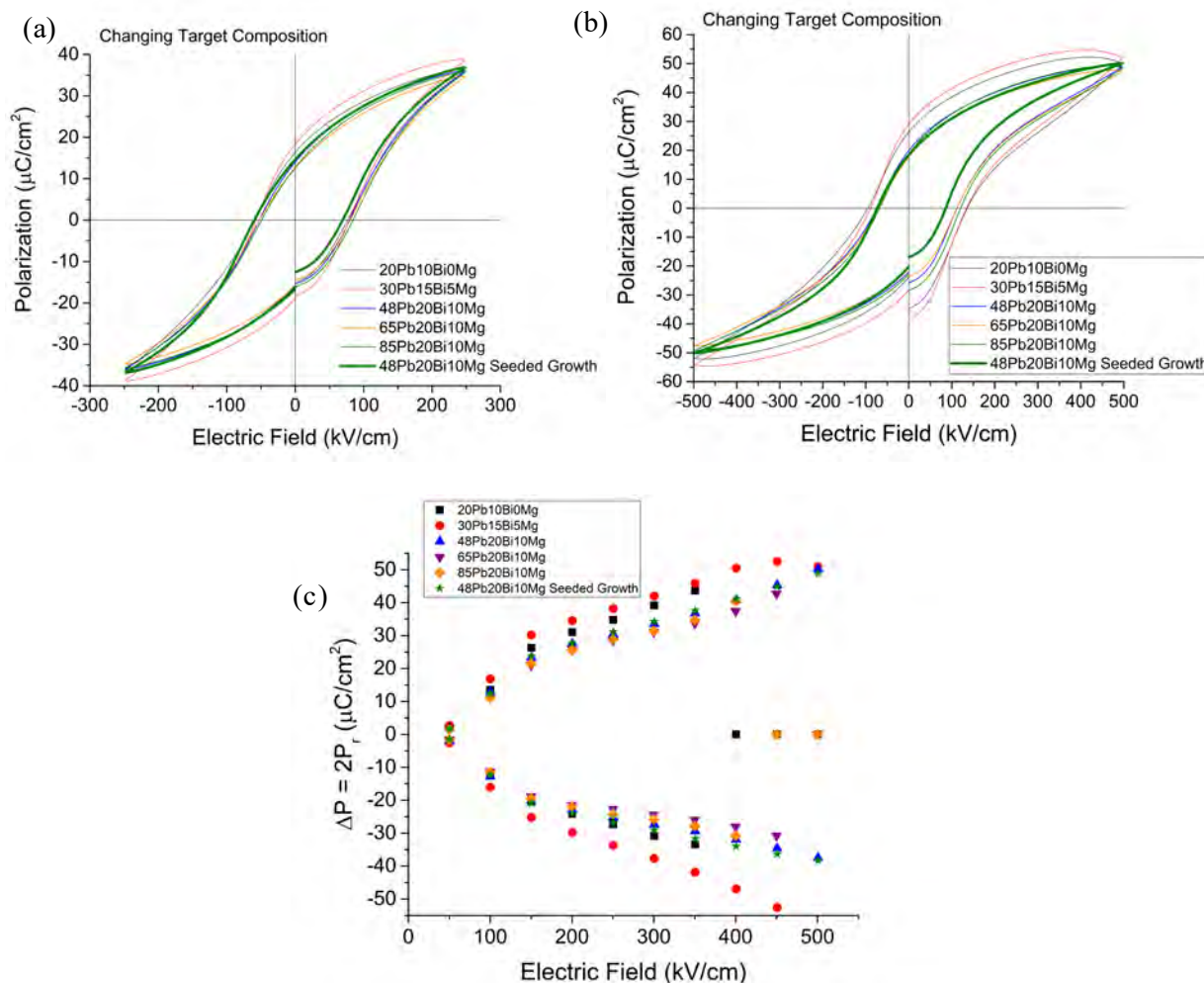


Figure 6.5 – Ferroelectric hysteresis of seedless 35BiMT-65PT thin films as a function of target composition at 1 kHz frequency, 250 kV/cm applied field (a), and 500 kV/cm (b). (c) Sample PUND data measured using 1 ms pulses and 1 ms 0 V holds.

A series of seedless films were grown with varying thicknesses using the 48Pb20Bi10Mg target. The resulting films are compared to those discussed in Chapter 5. Figure 6.6 shows the scaling behavior of ϵ_r of seedless 35BiMT-65PT thin films for thicknesses from ≈ 100 nm – ≈ 700 nm. The film series shows a non-zero intercept, indicating that the data can be described using a capacitor in series model. Figure 6.6(b) shows that the dielectric permittivity of the seedless films is only slightly improved with decreasing thickness, compared to the seeded films. Figure 6.6 (c) shows that accounting the interfacial capacitance, the ϵ_r of the seedless films is ≈ 970 .

It is interesting to note how similar the thickness dependence of the dielectric permittivity is between the seeded and seedless films. The intercept and slope of Figure 6.6 (a) were determined to be $0.0036 \pm 0.0008 \text{ pF}^{-1}$ and $2.67 \times 10^{-5} \pm 1.71 \times 10^{-6} \text{ pF}^{-1} \text{ nm}^{-1}$, respectively. These values are very close to the slope and intercept determined for the seeded films: $0.0037 \pm 0.0002 \text{ pF}^{-1}$ and $2.67 \times 10^{-5} \pm 5.58 \times 10^{-7} \text{ pF}^{-1} \text{ nm}^{-1}$. The adjusted permittivity for the seeded and seedless films is ≈ 960 and ≈ 970 , respectively. Due to the similarities in interfacial capacitance values, it is proposed that the thickness dependence in the seedless films is due to a PbTiO_3 rich interface at the bottom electrode. In PZT, it has been shown that PbTiO_3 can nucleate preferentially, causing segregation of the Ti^{4+} and Zr^{4+} species. A similar phenomenon may be occurring here, where a PbTiO_3 -rich interface is formed. It is suggested that transmission electron microscopy cross-sections be imaged to confirm whether there is a composition gradient in the seedless films.

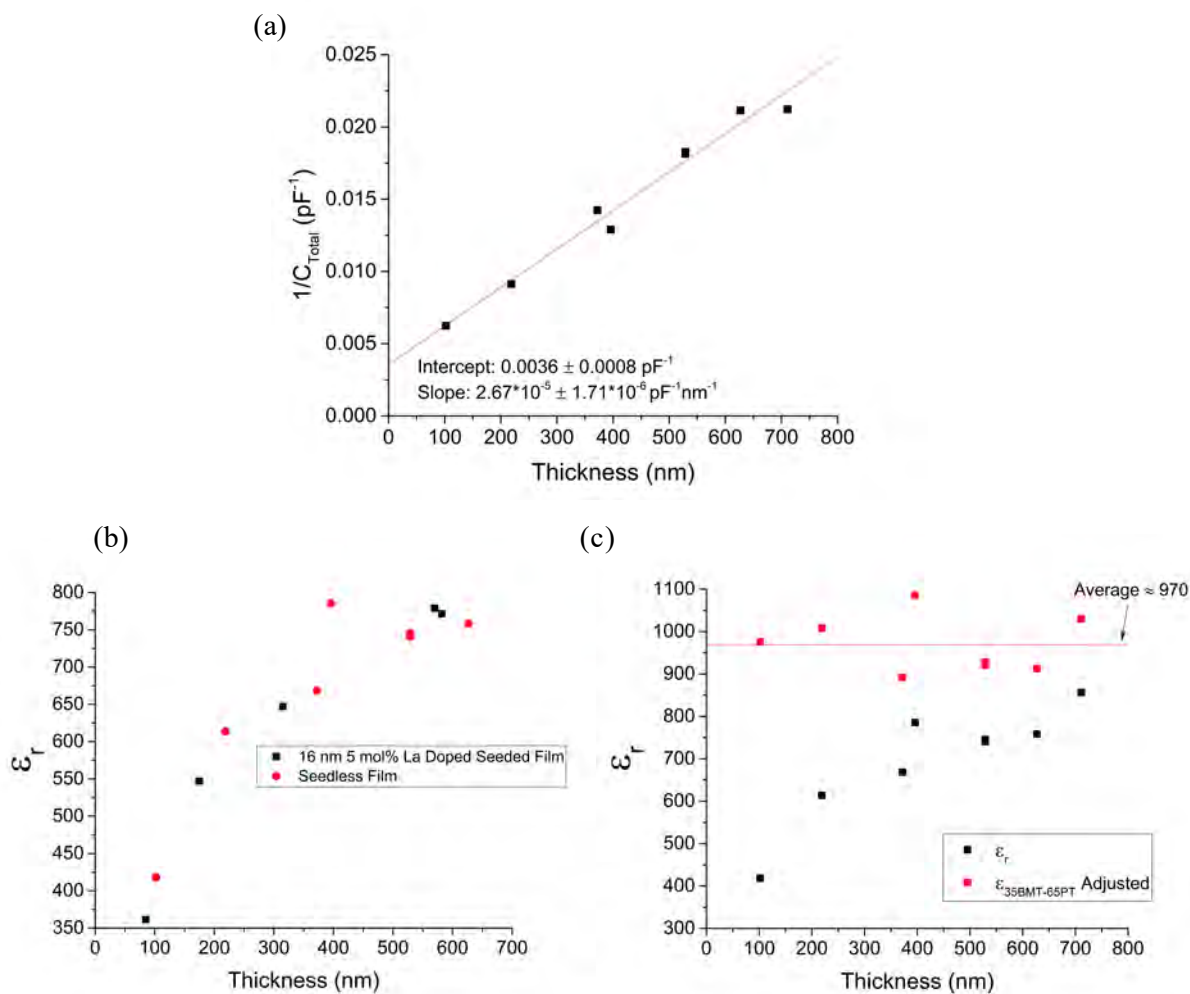


Figure 6.6 – (a) $1/C_{\text{total}}$ vs thickness plot showing the capacitor in series relationship for seedless 35BiMT-65PT thin films. (b) ϵ_r vs thickness comparison between seeded 35BiMT-65PT and seedless 35BiMT-65PT thin films. (c) Adjusted vs total film ϵ_r vs thickness

Figures 6.7, 6.8, and 6.9 compare the thickness dependence of the ferroelectric properties of seeded and unseeded films. The P_r in the seeded films is approximately thickness independent until the film thickness decreases below 200 nm. The P_r decreases from $\approx 15\text{-}16 \mu\text{C}/\text{cm}^2$ to $\approx 10 \mu\text{C}/\text{cm}^2$ ($+P_r$) and $\approx -5 \mu\text{C}/\text{cm}^2$ ($-P_r$) based on the ferroelectric hysteresis and PUND measurements when the thickness decreases from ≈ 600 nm to 85 nm in thickness. Films on 16 nm 5 mol% La-doped PbTiO_3 seed layers were deposited using a 20Pb10Mg0Mg target, thus the maximum possible polarizations found in chapter 4 are not seen; growth from other targets needs to be explored in future work. The seedless films demonstrate somewhat less thickness dependence on the ferroelectric properties. Based on the 10 kHz

and PUND measurements, P_r is approximately constant until the thickness approaches 100 nm. The P_r decreases from $\approx 22 - 25 \mu\text{C}/\text{cm}^2$ to $\approx 15.5 \mu\text{C}/\text{cm}^2$ between the thickness of 711 nm to 102 nm. The higher P_r in the seedless films compared to the seeded films is due to using a 48Pb20Bi10Mg target. Figure 6.9 shows that the effective coercive field of the thin films increases as the thickness decreases, particularly below 200 nm. In both the seedless and seeded films, there is a suppression in the PUND values, but the ΔP of thinner films approaches the value of thicker films as the electric field increases. In seedless films, ΔP of the 102 nm thick film equals that of the 711 nm thick film at 500 kV/cm. Thus, there is modest improvement in the thickness dependence of the ferroelectric properties with decreasing thickness.

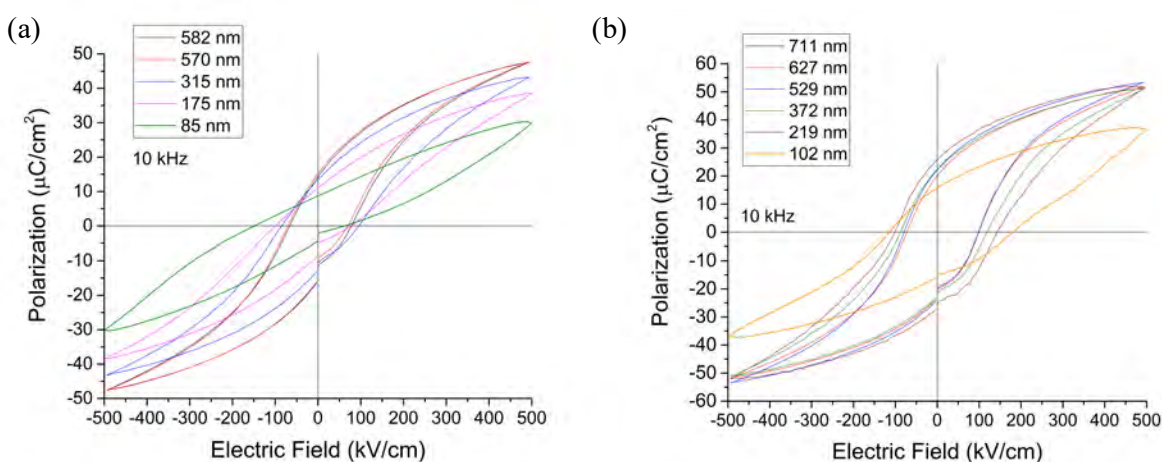


Figure 6.7 – Thickness dependence of ferroelectric hysteresis at 10 kHz for (a) 5 mol% La-doped PbTiO_3 seeded 35BiMT-65PT thin films and (b) Unseeded 35BiMT-65PT thin films

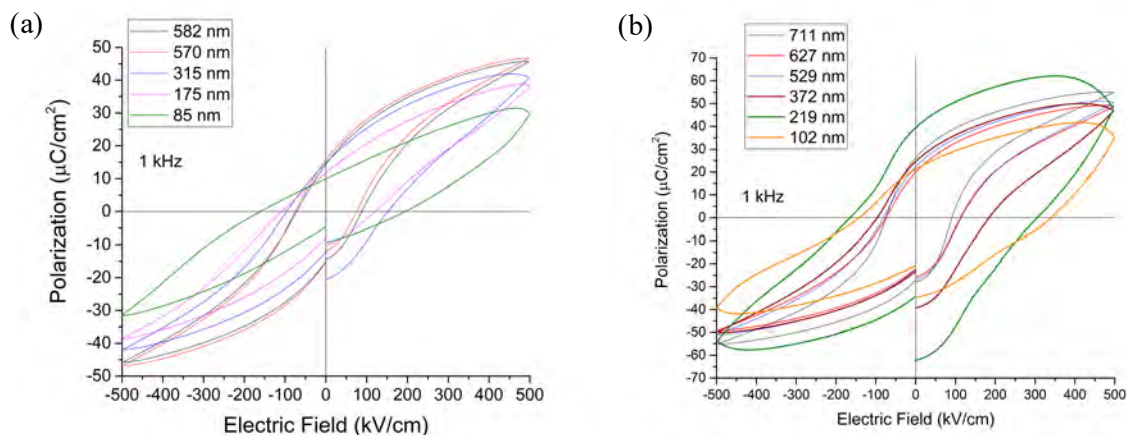


Figure 6.8 - Thickness dependence of ferroelectric hysteresis at 1 kHz for (a) 5 mol% La-doped PbTiO₃ seeded 35BiMT-65PT thin films and (b) Unseeded 35BiMT-65PT thin films.

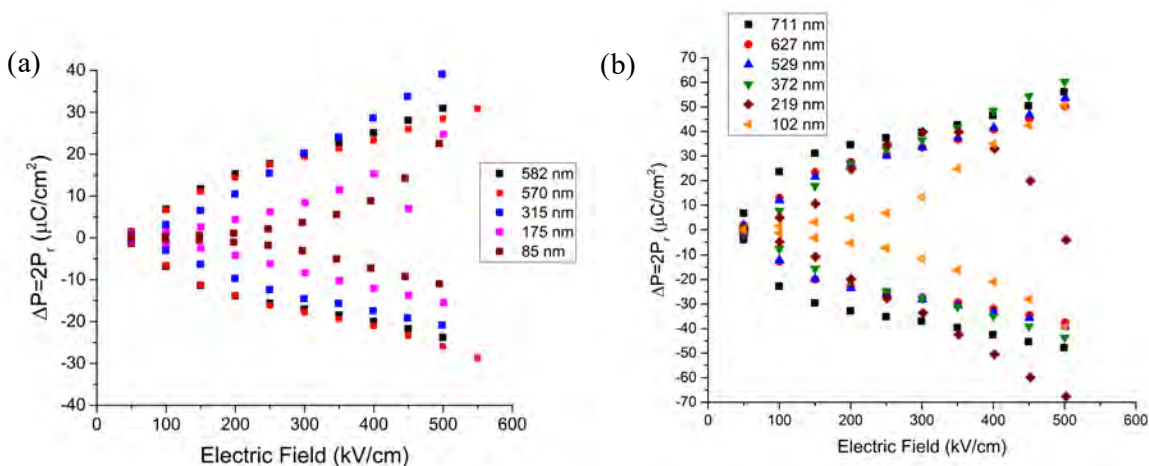
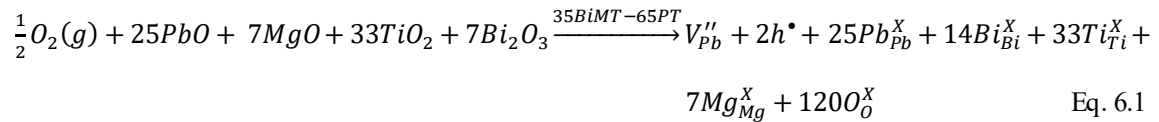


Figure 6.9 - Thickness dependence of ferroelectric PUND with 1 ms pulses and 0V hold times for (a) 5 mol% La-doped PbTiO₃ seeded 35BiMT-65PT thin films and (b) Unseeded 35BiMT-65PT thin films.

6.4 Controlling Defect Chemistry/Charge Injection in Seedless Films

As seen in Figures 6.5 and 6.8, there is significant charge injection in the seedless films compared to the seeded films. Chapters 4 and 5 discussed how the I-V characteristics are related to the defect chemistry of the 35BiMT-65PT thin films, particularly the A-site deficiency in Pb. Currently, the mechanism that controls the V''_{pb} concentration is unknown. Ultimately, the film composition is

dependent on several processes during growth. First a flux of material is brought to the surface by the plume. The material at the surface will either become incorporated into the growing film structure via adsorption or will desorb via sputtering or evaporation. Considering that the films are non-stoichiometric regardless of the target composition, it was proposed that the preferential adsorption of Bi in the growing film leads to a fixed concentration of V''_{Pb} in order to maintain electroneutrality. Thus, if the V''_{Pb} concentration is to be reduced, the adsorption of Bi and Pb must be controlled. Of the defect reactions considered, one reaction considered the formation of electronic defects as well as the formation of V''_{Pb} and is related to the PO_2 of the during deposition:



In Chapter 4, it was shown that regardless of the target composition, the films could not be made stoichiometric. Eq. 6.1 may or may not coexist with defect reactions associated with the preferential adsorption of Bi onto the Pb site. If Eq. 6.1 dominates the formation of V''_{Pb} then the magnitude and slope of the I-V measurements should change as a function of the oxygen partial pressure. In principle, the removal of the defects contributing to Poole-Frenkel emission will eventually lead to a change the conduction mechanism to something else such as Schottky emission. To assess this, depositions were done controlling the background gas atmosphere at a single deposition pressure (340 mTorr). To control the pO_2 during deposition, a mixture of O_2 and Ar gas (no O_3) was introduced such that the flow rate was maintained at 50 sccm for the mixed gas. There are two possible means by which this process could control the Pb stoichiometry. First, in PZT, Pb is removed at high temperatures due to $PbO(g)$ formation. Thus, using a lower PO_2 may reduce the amount of oxygen available, limiting the evaporation of $PbO(g)$ from the surface. Second, the change in oxidation state could change the adsorption rate.

It was found that as deposited films grown in O_2/Ar appeared similar to films deposited in an O_2/O_3 , suggesting that there was little reduced Pb. However, it is important to note that all films were

exposed to temperatures above 400 °C for a few minutes after deposition stops in the presence of oxygen gas. Thus, it is possible that any oxygen-deficiency present during growth was eliminated during cooling.

Figures 6.10 and 6.11 show the ferroelectric properties of seedless 35BiMT-65PT thin films as a function of the oxygen concentration measured for two different maximum fields. For modest electric fields (< 300 kV/cm) the maximum and remanent polarizations decrease with increasing Ar in the gas phase during growth. However, at high fields (< 500 kV/cm), charge injection in the P-E hysteresis significantly reduces with decreasing O₂ concentration in the deposition gas mixture. Correspondingly, the apparent P_r decreases from +P_r ≈ 30 μC/cm² to 18.5 μC/cm² and -P_r ≈ -30 μC/cm² to -22 μC/cm² for measurements at 500 kV/cm. Similarly, the P_r decreases from +P_r ≈ 23.7 μC/cm² to 13.5 μC/cm² and -P_r ≈ 21 μC/cm² to -13 μC/cm² at 300 kV/cm. The decrease in P_r is approximately linear over the concentration range studied as seen in Figure 6.10 (c).

PUND measurements provide further quantification of charge injection in the films deposited at higher O₂ concentrations at high fields. The switching charge (P*, Figure 6.11(b)) decreases with decreasing O₂ concentration. The non-switching charge (P[^], Figure 6.11(c)) on the positive polarization state is constant as function of pO₂ until the electric field increases above 300 kV/cm for the 100% O₂ sample and 450 kV/cm for the 75% O₂ / 25% Ar sample. On the other hand -P[^] is not a strong function of the gas mixture utilized. Changes in P[^] are indicative of changes in leakage behavior; i.e. increases in P[^] are increases in leakage. As ±P[^] is constant as a function pO₂ / Ar at 50% Ar concentration, no further benefit is achieved going to greater Ar concentrations. However, the continual decrease in P* indicates that polarization continuously decreases with increasing Ar concentration. For the high pO₂ samples (100% and 75% O₂), the discrepancy in PUND and hysteresis measured P_r is due to either increased time at field or leakage. The 100% O₂ / 0% Ar sample P_r determined by PUND at 500 kV/cm is +P_r ≈ 35 μC/cm² and -P_r ≈ -28.5 μC/cm². As the -P_r state is reasonably close to the hysteresis measurement, it is likely that the positive polarization PUND at 500 kV/cm is inflated, at least in part, due to increased leakage.

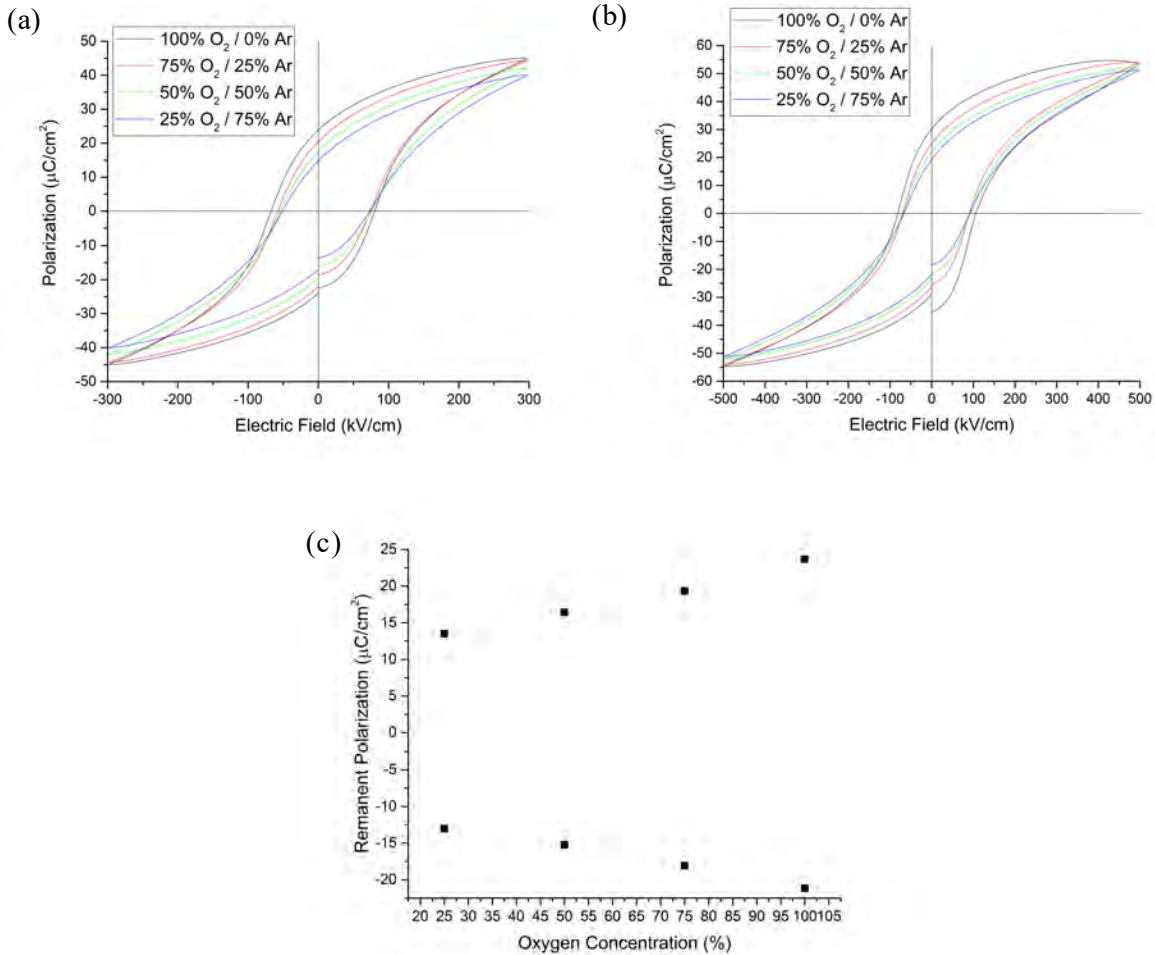


Figure 6.10 – Ferroelectric hysteresis (1kHz) of seedless films as function O₂/Ar background deposition gas mixture at 300 kV/cm (a) and 500 kV/cm (b). (c) Remanent polarization as a function of oxygen concentration measured at 300 kV/cm.

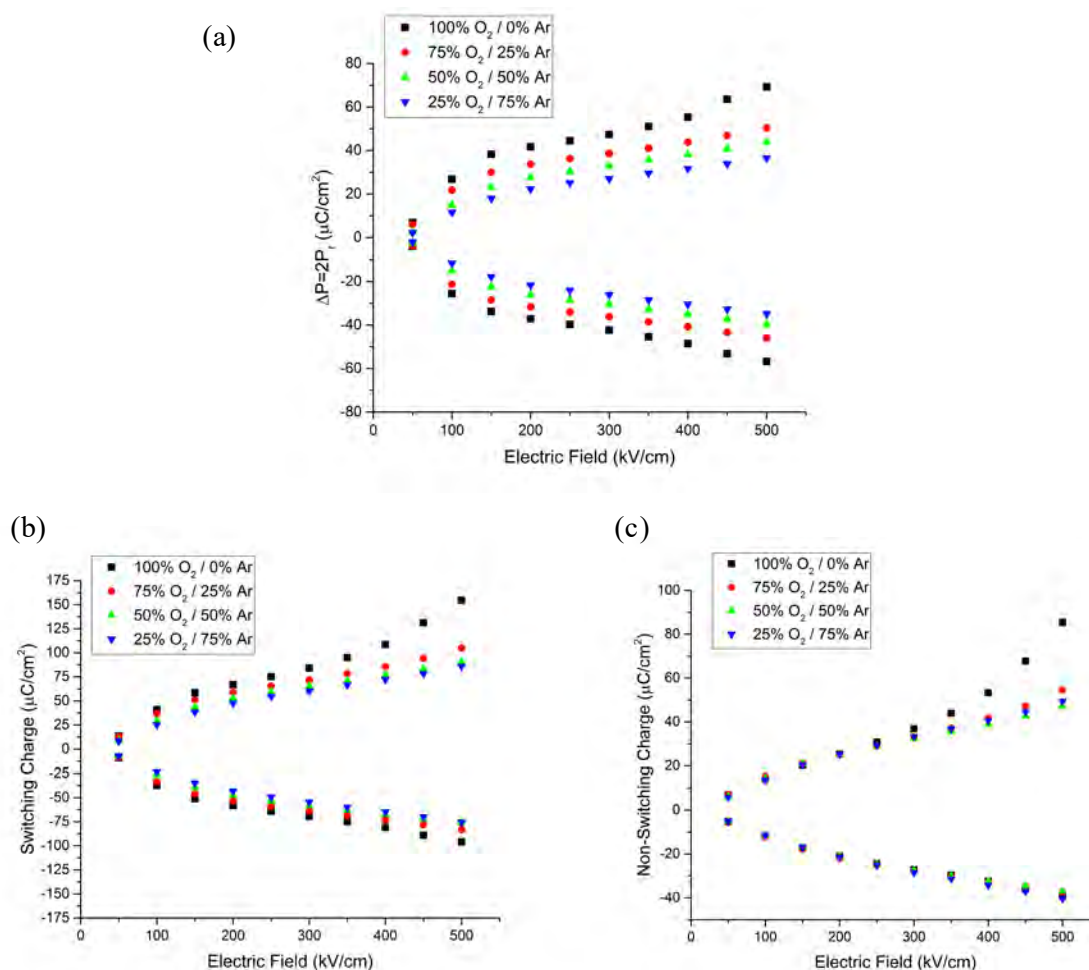


Figure 6.11 – PUND measurements as a function of electric field and oxygen concentration of seedless 35BiMT-65PT thin films. (b) and (c) Corresponding P^* (switching) and P^\wedge (non-switching) charges, respectively.

Figure 6.12 shows the I-V characteristics of 35BiMT-65PT thin films deposited under different O₂/Ar concentrations compared to the seeded growths. Similar to the hysteresis and PUND measurements, decreasing leakage is found with decreasing O₂ concentration. Interestingly, while the seedless growths show significantly increased charge injection at lower fields in the ferroelectric hysteresis measurements, the I-V measurements demonstrate similar leakage between the 100% O₂ and 340 mTorr seeded growth. The primary difference is the increased leakage at low electric fields. As the pO₂ decreases to 75% O₂, the leakage behavior at low fields (<100 kV/cm) and room temperature behave the same as the leakage of films grown on seed layers. Below 75% O₂, the I-V curve shifts to the right

and down, corresponding to decreased leakage. At 150 kV/cm, the leakage decreases by half an order of magnitude between the 100% O₂ film and the ≤50% O₂ concentration.

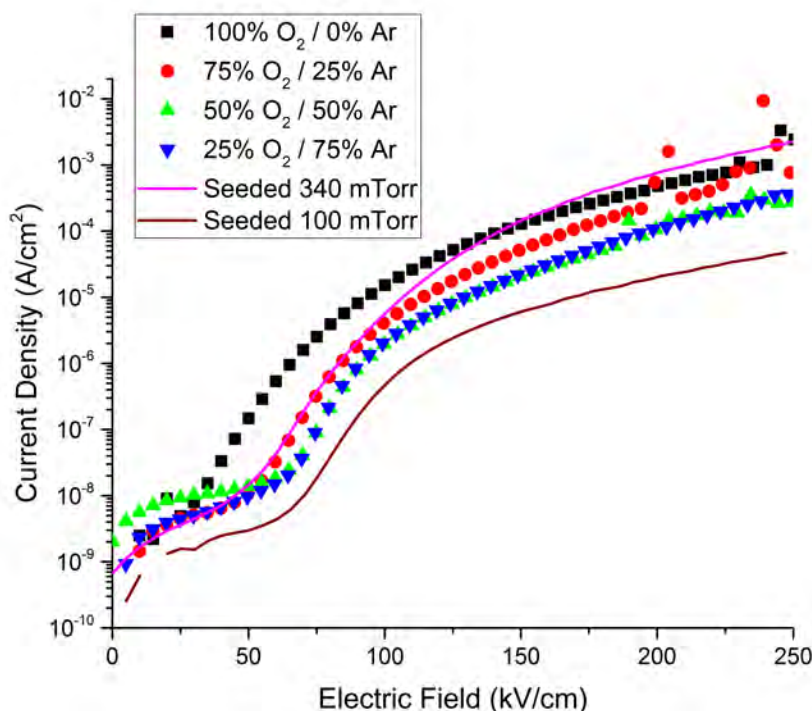


Figure 6.12 – Room temperature I-V measurement of 35BiMT-65PT thin films deposited under various O₂/Ar atmospheres during growth. The solid lines are data taken from 36 nm PbTiO₃ seeded 35BiMT-65PT films from Chapter 5. The seeded film data provides the maximum difference in leakage values seen in Chapter 5.

Based on Figures 5.6 and 6.12, decreasing the pO₂ via either decreasing the deposition pressure (pure O₂/O₃ atmosphere) or substitution with an inert gas during growth does not change the conduction mechanism. Ideally, reducing the V_{pb}'' concentration will change the leakage magnitude and the slope in the I-V which indicates a change in conduction mechanism. However, these films still exhibit Poole-Frenkel emission. The estimated refractive index for the film deposited at 25% O₂ / 75% Ar ≈ 1.8 , very close to the measurement for the 340 mTorr deposited sample on a 36 nm PbTiO₃ seed.

While the conduction mechanism did not change, the magnitude of the conductivity varies up to 50 times for films deposited at 60 mTorr and 340 mTorr (all other films fall in this range). Similar PUND, P*, and P^ behavior is seen between the films in Figure 4.8 and Figure 6.11. For films in Figure 4.8, as

the A:B site ratio approached 1, the film composition became rich in Bi. The mechanism controlling the decrease in P^* is not known, but it may be due to changes in composition such as those seen in chapter 4 and 5 where excess Bi correlated with decreases in P^* , P_r and leakage.

The Bi concentration on the A-site of the grown films may, in principle, be controlled by a change in Bi sticking coefficient. The sticking coefficient takes into account the amount of adsorption and desorption that occurs at the film surface. While all of the factors that control the sticking coefficient were not determined, the influence of bombardment energy and PO_2 were explored. Depositions were made between 40 mTorr and 400mTorr and from 100% Ar to 100% O_2 in the gas phase. While it was found that the 35BiMT-65PT thin films thickness could be changed considerably by bombardment (e.g. from $\approx 450 - 900$ nm, respectively, after a 10 minute deposition at growth pressures of 40 to 400 mTorr or from $\approx 580 - 0$ nm, respectively, after a 10 minute deposition at growth O_2 concentrations of 25% O_2 to 0% O_2 at 340 mTorr.), there were no conditions identified where massive quantities of second phases could be detected, as might have been expected if all of the A site cations had been resputtered.

Alternatively, a change in pO_2 may have changed the adsorption kinetics of the Bi species if the species is reduced under those conditions. For a chamber pressure of 340 mTorr, the pO_2 at 25% O_2 /75% Ar and 50% O_2 /50%Ar is 85mTorr and 170 mTorr, respectively. The difference in leakage at 250 kV/cm between these films and the 100 mTorr sample is ≈ 6 times. The difference in magnitude could be in part to the seed layer utilized in the 100 mTorr sample deposition. However, it would be important to grow a comparable set of films at these pressures in a pure oxygen atmosphere to clarify whether the oxidation state of the film or the bombardment during growth is more critical in controlling the Bi content.

6.5 High Temperature Leakage, Polarization and Retention of Seedless Films

As discussed in Chapter 5, the high temperature leakage, high temperature polarization and retention are important properties to study for a high temperature FeRAM device. In section 6.3, the seedless growth films were demonstrated to have comparable ferroelectric properties to PbTiO₃ seeded 35BiMT-65PT thin films. Under optimal O₂/Ar gas concentrations, the room temperature leakage of seedless films is also comparable to that of seeded growth. Thus, the high temperature and retention properties of seedless films were examined to determine their viability as a high temperature FeRAM material and compared to that of the PbTiO₃ seeded growths. To this end, the film deposited at 50% O₂ / 50% Ar background atmosphere was utilized because it exhibits the minimal leakage and maintains a reasonably high P_r.

Figure 6.13 shows the high temperature leakage behavior of the optimal seedless film. While the room temperature properties of the seedless film are similar to that of the PbTiO₃ seeded growths examined in Chapter 5, significant degradation occurs with increasing temperature. The DC electric field breakdown strength is approximately 250-300 kV/cm at room temperature and decreases with increasing temperature. At 50 °C, the 35 BiMT-65PT film show a change in leakage behavior around 200 kV/cm which soon lead to visible local breakdown events in the electrodes. The degradation of the breakdown strength increases faster with increasing temperature compared to seeded films is shown in Figure 5.7. While the room temperature properties are similar to the seeded growths, further understanding and optimization is required to achieve decreased leakage at high temperature.

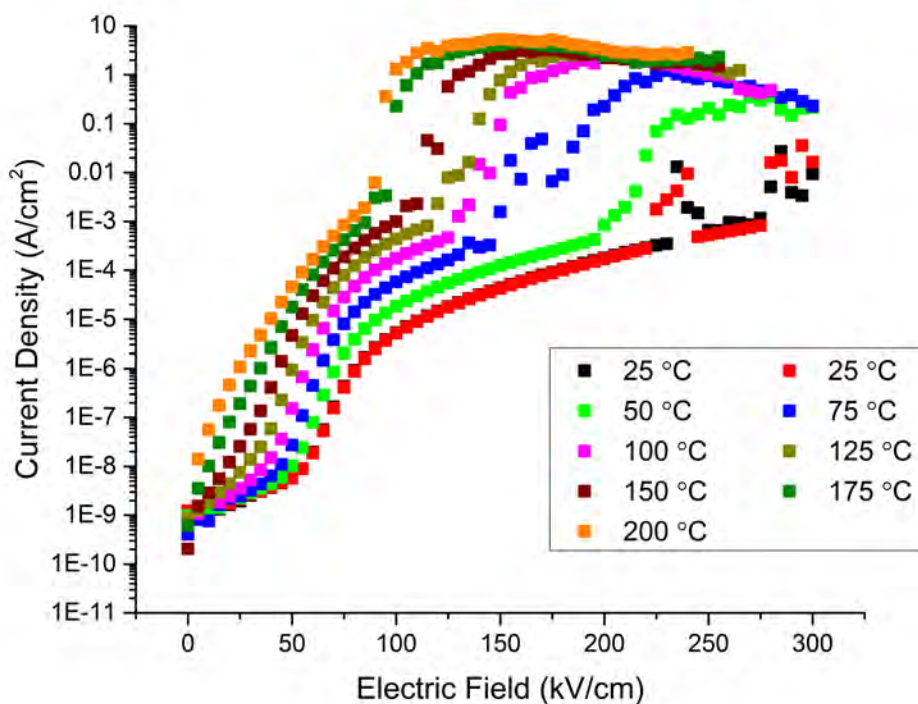


Figure 6.13 – I-V vs temperature measurements of a seedless 35BiMT-65PT thin film deposited under a 50% O₂ / 50% Ar background gas atmosphere.

Figure 6.14 shows the high temperature ferroelectric hysteresis properties of the 35BiMT-65PT thin films. In Chapter 5, seeded films exhibited significant charge injection at 500 kV/cm above ≥ 100 °C on the positive polarization state. Due to the lower dielectric breakdown strength and increased leakage, hysteresis measurements on seedless films were limited to 300 kV/cm at 10 kHz. Films exhibited little charge injection until the temperature reached 150 °C. The limited charge injection at high temperature is somewhat contrary to leakage measurements in Figure 6.13, where there is significant degradation in the I-V characteristics with increasing temperature. Based on these figures, two different time scales for the charge injection must be considered. Under DC field, the seedless films exhibit significant degradation in properties, but at high AC fields the charge injection is minimized. The mechanism for this change requires further investigation as the results here are unable to distinguish the conducting species.

Figure 6.14(b) demonstrates the P_r vs temperature of the optimized seedless film based on PUND. Similar to the $PbTiO_3$ seeded growth, the optimized seedless film shows little change in P_r with increasing temperature. At 300 kV/cm and 200 °C, the P_r decreases from ≈ 16 -17 $\mu C/cm^2$ to 12 $\mu C/cm^2$ on both the positive and negative polarization states. These P_r values are greater than or equal to two times the P_r at equivalent electric fields previously measured on $PbTiO_3$ seeded 35 BiMT-65PT thin films. Both $PbTiO_3$ seeded and seedless films exhibit stable P_r up to temperatures of 200 °C.

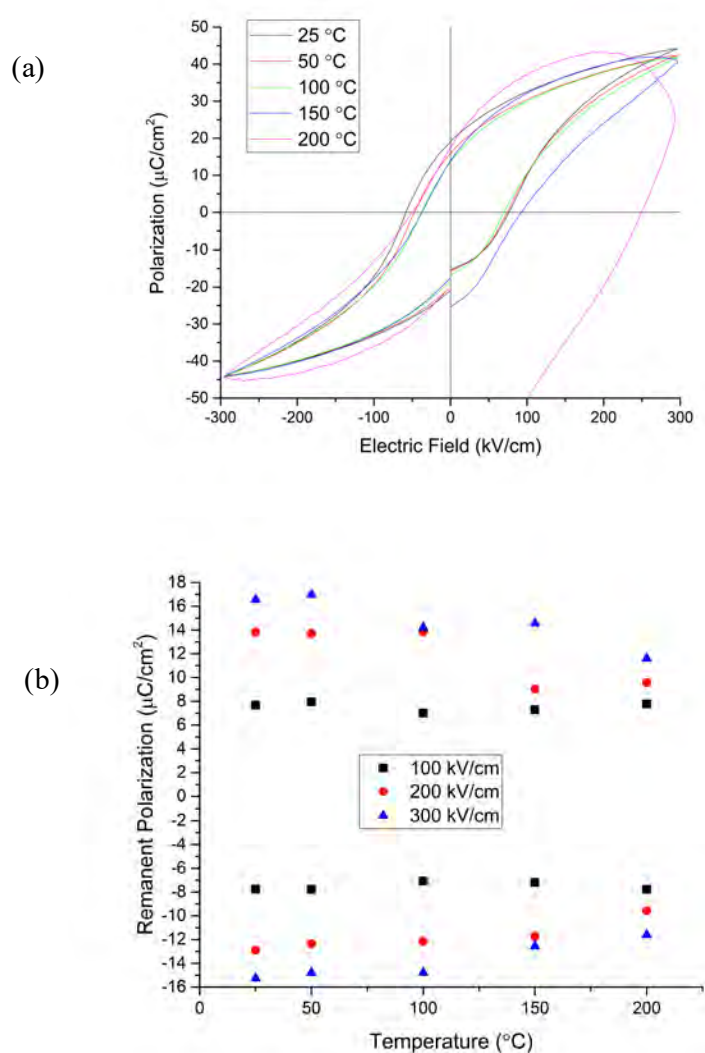


Figure 6.14 – (a) High temperature P-E of a seedless 35BiMT-65PT thin films at 10 kHz. The seedless film was deposited using a 50% O_2 / 50%Ar deposition background gas atmosphere. P-E is normalized at the maximum in electric field. (b) Corresponding P_r vs temperature as a function of electric field for the 35 BiMT-65Pt thin film. The P_r was determined from PUND measurements with 1 ms pulses and 1 ms 0V hold periods.

Figure 6.15 shows the retention properties of seedless 35 BiMT-65PT thin films at room temperature and high temperature. Both PbTiO₃ seeded and seedless films exhibit same state retention loss at room temperature. There is a ΔP loss of $\approx 15 \mu\text{C}/\text{cm}^2$ after a 4.65 hour hold time in both films. As discussed in Chapter 5, this is likely related to non-stoichiometric defects in the thin films, particularly the Pb A-site deficiency. Ultimately, 35 BiMT-65PT thin films must show retention in P_r at high temperatures as well as room temperature. Figure 6.15 (b) shows the same state retention of the optimized seedless 35 BiMT – 65 PT thin film at 85 °C. The loss in ΔP is accelerated with increasing temperature, but the ΔP remains > 0 for an equivalent time scale. Similar to the PbTiO₃ seeded films, it is expected that the retention loss will be reduced with improved film stoichiometry.

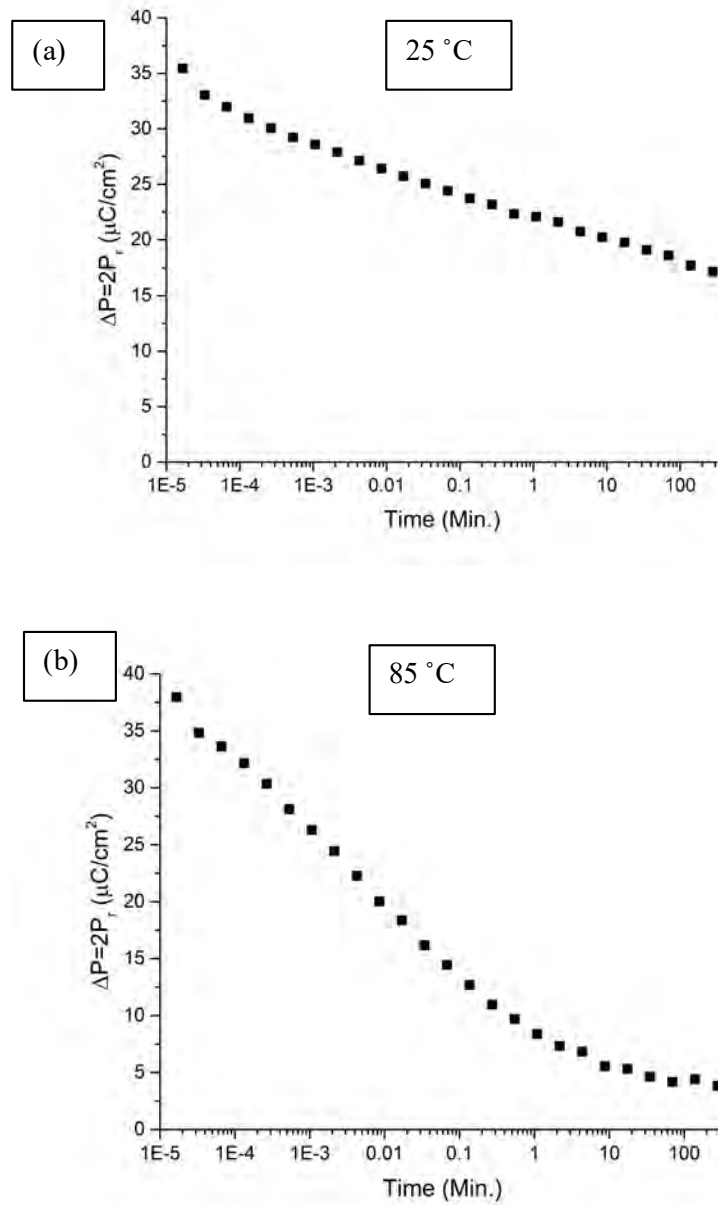


Figure 6.15 – (a) Room temperature retention of the optimized seedless 35 BiMT -65PT thin film. Same state retention at $85\text{ }^\circ\text{C}$ of the optimized seedless 35 BiMT - 65 PT thin film. The retention analysis was done at $300\text{ kV}/\text{cm}$ and 1 ms pulses / 0 V holds.

6.6 Conclusions

Pulsed laser deposited seedless 35 BiMT- 65 PT thin films were investigated. Phase pure perovskite films were formed within the investigated target composition range, film thickness range, and O₂/Ar gas atmosphere. The dielectric and ferroelectric properties of seedless 35 BiMT – 65 PT films were thickness dependent. The ϵ_r and P-E vs thickness were somewhat improved in the seedless 35 BiMT – 65 PT thin films compared to the 5 mol% La-doped PbTiO₃ seeded films. However, seedless films exhibited increased leakage when deposited under the same conditions as the seeded films. The O₂/Ar background atmosphere was utilized to control the PO₂ during deposition of the seedless films. With decreasing O₂ concentration, the leakage and P_r of the seedless films decrease. Optimized film growth was found at 50% O₂ / 50% Ar with a P_r \approx 15-16 $\mu\text{C}/\text{cm}^2$ at 300 kV/cm. The DC electric field strength was 250 – 300 kV/cm at room temperature and decreased with increasing temperature faster compared to the seeded films. Seedless and seeded film exhibit stable P_r up to temperatures of 200 °C. Seedless and seeded films exhibit room temperature same state retention loss of $\Delta P \approx 15 \mu\text{C}/\text{cm}^2$ over a 4.65 hour hold time. The retention loss is accelerated as the temperature increases. The seedless films properties are roughly equivalent to that of the seeded films except for the difference in leakage behavior. Improved properties are expected in seedless films with improved film stoichiometry.

6.7 References

- ¹ B.A. Tuttle, "Pb(Zr,Ti)O₃ Based Thin Film Ferroelectric Memories," pp. 145–165 in *Thin Film Ferroelectr. Mater. Devices*. 1997.

Chapter 7

Conclusions and Future Work

7.1 Conclusions

The goals of this thesis were to understand the underlying processing, microstructure, and electrical property relationships in pulsed laser deposited 35 BiMT - 65 PT thin films and to determine the feasibility of utilizing such materials in high temperature FeRAM. To meet these goals, four critical aspects were analyzed: 1) The possibility of measuring large remanent polarizations for films on Si, 2) The thickness dependence of the dielectric and ferroelectric response, 3) The high temperature dielectric, ferroelectric, and leakage characteristics, and 4) the retention properties of 35 BiMT – 65 PT thin films. Large remanent polarizations that can be preserved to small film thicknesses at high temperatures, along with acceptable retention behavior are all needed for high temperature FeRAM.

Chapter 4 explored the processing-composition-ferroelectric property relationships of PbTiO₃ seeded 35 BiMT – 65 PT thin films. The processing window for phase pure perovskite films was found to be very wide. All films were determined to be A-site deficient, likely due to preferential adsorption of Bi onto the A-site. The ferroelectric film properties varied depending on the deposition parameters; for example, the remanent polarization varied between $\approx 14 \mu\text{C}/\text{cm}^2$ and $25 \mu\text{C}/\text{cm}^2$ depending on the deposition pressure, target composition, and deposition rate. P_r increased as the film composition approached stoichiometry. Film stoichiometry improved with increasing deposition pressure and on utilizing targets with excess PbO, MgO, and Bi₂O₃. For all conditions explored, the films were determined to be deficient in Pb.

In Chapter 5, for films seeded with a PbTiO₃ layer, P_r and dielectric permittivity decreased with decreasing BiMT-PT film thickness. This was attributed to the presence of the low dielectric permittivity

seed layer in series with the BiMT-PT film. Based on the capacitor in series model, the adjusted dielectric permittivity of these thin films is ≈ 960 . The films showed a T_{\max} of ≈ 430 °C and $\tan(\delta) < 15\%$ at 1 MHz up to 585 °C for film thicknesses between 85 and ≈ 600 nm. P_r is stable up to temperatures of 200 °C. However, with increasing temperature or electric field, films show increasing charge injection. I-V measurements determined the film conduction is consistent with Poole-Frenkel emission and is correlated to the film stoichiometry. Finally, all films show poor retention, but the retention times increase with improved film stoichiometry.

In Chapter 6, for seedless 35 BiMT – 65 PT thin films, a wide processing window was determined for producing phase pure perovskite films. The ϵ_r and P-E vs thickness were somewhat improved in the seedless 35 BiMT – 65 PT thin films relative to films grown on doped PbTiO₃ seeds. The ϵ_r vs thickness were consistent with a capacitor in series with the BiMT-PT, possibly suggesting a PbTiO₃ rich nucleation layer at the Pt interface. Film leakage increased without the seed layer. To control the leakage, films were deposited in an O₂/Ar atmosphere. As the O₂ concentration decreases, the leakage and P_r of seedless films decrease. Optimized film growth was found at 50% O₂/ 50% Ar with a $P_r \approx 15$ -16 $\mu\text{C}/\text{cm}^2$ when measured at 300 kV/cm. The DC electric field strength was 250 – 300 kV/cm at room temperature and decreased with increasing temperature. Optimized films show stable P_r up to temperatures of 200°C. Seedless and seeded films exhibit room temperature same state retention loss of $\Delta P \approx 15$ $\mu\text{C}/\text{cm}^2$ over a 4.65 hour hold time. The retention loss is accelerated as the temperature increases. Ultimately, seedless films were determined to have roughly equivalent properties as the seeded films except for the increased leakage. Thus, improved properties are expected with improved film stoichiometry.

The data discussed in this thesis suggest that 35 BiMT – 65 PT thin films are a suitable material for FeRAM applications. The high temperature dielectric permittivity and P_r demonstrate that the material can be utilized at high temperatures. Films did exhibit thickness dependence, large leakage and poor retention. The thickness dependence found in this work is consistent with a capacitor in series and

did show signs of improvement with the removal of the seed layer. It is likely that reducing this thickness dependence will require better control of the nucleating layer. The leakage and retention limitations are shown to be related to composition defects. As such, these problems may not be inherent to the material itself, but processing controlled, as discussed in following future work.

7.2 Future Work – Developing Relationships Between A-Site stoichiometry Control, Electrical Properties and Retention

The hypothesis presented in this thesis is that the use of a higher temperature T_c material would correlate with improved retention of the ferroelectric polarization compared to PZT. However, poor composition control prevented fully testing this hypothesis, and thus future studies are required. In particular, no study other than this one has yet attempted to correlate the relationship between A-site stoichiometry, T_{max} in the ϵ_r vs temperature curve, and the retention properties of ferroelectrics for a single material. Thus, one key area to study further are these relationships. Three separate avenues are suggested for exploration with respect to retention and the A-site stoichiometry: 1) Bulk PZT at various compositions, 2) Bulk BiMT-PT and / or BiS-PT and 3) the “effective maximum retention temperature” of various ferroelectrics as a function of their Curie temperature.

First, PZT is a well-studied material in bulk and thin film where the stoichiometry can be easily controlled. Thus, it should serve as a model for how the A-site stoichiometry affects T_c and the retention behavior. The retention should be studied as a function of temperature. An “effective maximum retention temperature” could also be determined across the phase diagram. This temperature would correspond to something such as the highest temperature at which retention lasts for 10 years, one of the current guidelines for commercial FeRAM devices.

The second avenue looks at exploring Bi-based-PbTiO₃ solid solutions in their bulk form. Due to the complexity of controlling the A-site stoichiometry in thin films, more controlled studies using bulk materials may be necessary to better describe the mechanisms controlling the ferroelectric retention properties. Thus, BiMT-PT and BiS-PT ceramics should be studied for various Pb / Bi stoichiometries to better establish the effects of A-site non-stoichiometry on T_c and retention.

Finally, the “effective maximum retention temperature” could be explored across many ferroelectrics to establish whether there is a general relationship between retention and the Curie temperature for all ferroelectrics. While it is true that T_c limits the range over which the material is ferroelectric, its link to the stability of the domain state (e.g. retention) is not well established. Thus, categorizing the retention properties as a function of temperature for many ferroelectric materials is needed; knowledge of this relationship should guide the development of future high temperature FeRAM materials.

7.3 Future Work – Control of A-Site Stoichiometry in BiMT-PT Films

A critical factor discussed throughout this thesis has been the control of the A-site stoichiometry for BiMT-PT thin films. Poor stoichiometry control leads to degraded properties such as high field leakage and poor retention. Thus, one potential avenue for research is to determine a means to control the A-site stoichiometry of BiMT-PT thin films. If PLD is to be utilized, a parameter which controls the relative adsorption of Bi and Pb must be determined. Nino *et al.*¹ grew epitaxial BiScO₃-PbTiO₃ thin films that were reported to be Bi-rich on the A-site. In addition, the B-site was roughly stoichiometric, similar to the work in this thesis. They utilized similar energy densities compared to this work. Thus, there is no obvious explanation as to why the use of Sc would alter change the adsorption-kinetics behavior unless a complex with Pb/Bi and Sc forms prior to arriving at the surface. A factor that could be

studied to control this is the laser energy density as it determines the initial state and energy of the ablated species. In addition, there is a potential discrepancy in the observed phenomena between this thesis and Nino *et al.* In this work, significant reduction in P_r correlated with increases in Bi concentration above stoichiometric, but Nino *et al.* films had P_r greater than bulk BS-PT of the same composition. This may be attributed in part to the compressive stress applied to these epitaxial thin films, but further studies need to be done to determine if the correlation seen in this thesis is valid for other systems and if the P_r in epitaxial BS-PT increases as the Pb/Bi ratio approaches stoichiometry.

As adsorption-controlled kinetics limited the stoichiometry control in PLD BiMT-PT films, utilizing different deposition methods will avoid this problem. Zhang *et al.* utilized sol-gel to deposit 20BiMT-80PT thin films.² Although there is some concern about the magnitudes of the permittivity and polarization values in that work due to the use of shadow masks to define the top electrodes, their measurements show significantly improved leakage behavior at high electric fields relative to the PLD films grown here. Figure 7.1 shows I-V measurements on a 200 nm 20BiMT-80PT film. The leakage behavior is at least 2 orders of magnitude lower than those measured in this thesis. The decreased leakage suggests that the films were not as A-site deficient as the films produced in this work. Other processing techniques, such as chemical vapor deposition would also potentially avoid adsorption controlled kinetic problems.

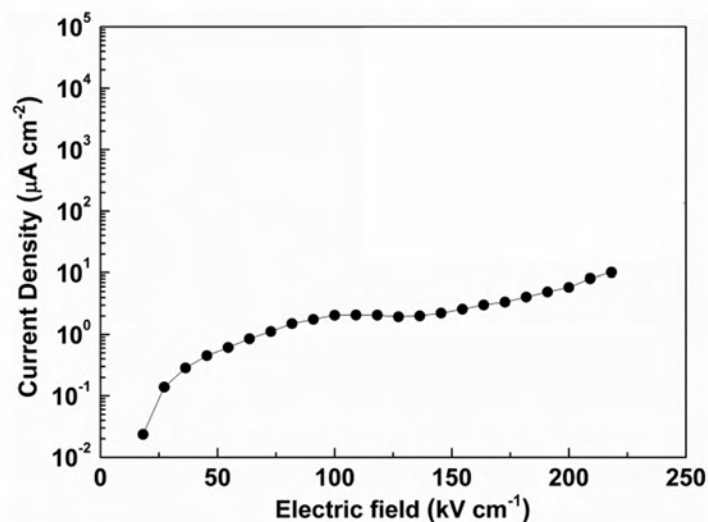


Figure 7.1 – I-V measurement of a 200 nm 20BiMT-80PT thin film by Zhang et al. (in supplemental section of the paper).²

7.4 Future Work – Other Bi-Based-PbTiO₃ Compositions

The BiMT-PT system studied here may act as a model system on how to develop other Bi-based-PbTiO₃ solid solution systems. There are a great number of possible Bi-based-PbTiO₃ solid solutions to study,^{3–10} few of which have been grown as thin films. There are several promising compositions reported for bulk ceramics that may be of interest for high temperature FeRAM or piezoelectric applications. As with the BiMT-PT system, these systems have not been studied at compositions near the maximum transition temperature. While many options exist, the best to choose are systems without multivalent cations (such as Fe and W). BiScO₃-PbTiO₃ (BiS-PT) has a similar T_{\max} , 500 °C at 85% PbTiO₃, as BiMT-PT and films have exhibited T_{\max} close to their bulk counterparts.^{1,11} The processing may be less strict compared to BiMT-PT based on Nino *et al.*'s films.¹ BiIO₃-PbTiO₃ (BiI-PT) is a system shows a much higher T_c than the BiS-PT system.⁷ Lee *et al.* grew BiI-PT films with BI concentrations up to 25 mol%, measuring transition temperatures between 558 °C and 633 °C.¹² While the P_r decreases with increasing BI concentration, the P_r is still 25 $\mu\text{C}/\text{cm}^2$ at 25% BI. However, the BiI-

PT films tend to show increased loss tangents at much lower temperatures compared to BiMT-PT and BiS-PT films, possibly limiting its high temperature usage. The BiYbO₃-PbTiO₃ (BiY-PT) is another system which potentially shows significantly higher T_c than BiS-PT, but the perovskite phase is not stable.⁷ Sometimes, epitaxial constraints facilitate preparation of phase-pure materials; thus, it may be of interest to grow BiY-PT through use of epitaxial stabilization.

Preliminary work was conducted on growth of thin films in the Bi(Zn_{1/2}Ti_{1/2})O₃-PbTiO₃ (BiZT-PT) system. BiZT-PT is similar to BiFeO₃-PbTiO₃ (BFO) in that it has a continuously increasing transition temperature with decreasing PbTiO₃ concentration due to enhanced tetragonality.⁴ If pure BiZT were stable and the T_c behavior continued, it would have a higher transition temperature than BFO.⁵ In addition, this material does not have the same electron hopping conduction problems seen in the BFO system. Under ambient conditions, the perovskite phase is only stable up to 40 mol% PbTiO₃.⁵ Pure BiZT can be processed at high pressures and is calculated to have a calculated ionic polarization of 150 μC/cm².¹³ Very few studies exist for the development of BiZT-PT thin films. Kwon *et al.* grew 20BiZT-80PT epitaxial thin films using off-axis rf sputtering, but only characterized the structural properties.¹⁴ Currently, Ahn and Son are the only group to have published electrical data on pure BiZT (none exist for BiZT-PT solid solutions).¹⁵ Their epitaxial films had a P_r ≈ 53 μC/cm² for a 150 nm thick film. Due to the high T_c and large ferroelectric properties, BiZT-PT compositions are of great potential interest.

A preliminary study is presented here for BiZT-PT to provide further information on developing this material in future studies. 20BiZT-80PT was selected as the composition due to the potential poor thermodynamic stability at higher BiZT concentrations. 20BiZT-80PT films were deposited on 5 mol% La-doped PbTiO₃ seed layers on the same Pt-Si substrates used for 35BiMT-65PT. BiZT-PT targets were processed using the same method as BiMT-PT targets. The stoichiometric powder was calcined up to 950 °C, and the targets were sintered at 850 °C. The film growth conditions are listed in Table 7.1. As Zn is a volatile, multiple targets were made with varying amounts of Zn excess (increments of 10 mol% Zn).

Table 7.1 – Process parameters for growing 20BiZT-80PT thin films.

| Processing Parameter | Value |
|---------------------------------|--|
| Laser Energy Density | 1.6 J/cm ² |
| Oxygen(90%)/Ozone(10%) Pressure | 340 mTorr |
| Target to Substrate Distance | 6 cm |
| Temperature | 700 °C |
| Laser Frequency | 10 Hz |
| Target Composition | 20 mol% excess Pb, 10 mol% excess Bi, 0-30 mol% excess Zn |

Figure 7.2 shows the XRD patterns of the resulting BiZT-PT thin films with varying Zn concentration. All films are phase pure based within the detection limits of XRD and all films show (100)_c preferred orientation. However, minor concentrations of a Zn rich, A-site deficient phase were detected in TEM micrographs of the film deposited using 0 mol% excess Zn (Figure 7.3) at the PbTiO₃ seed layer. As seen in Figure 7.3 (c), the secondary phase is deficient in both Pb and Bi while rich in Zn, suggesting it is a pyrochlore phase. While, no TEM images were taken of the samples deposited with greater amounts of excess Zn, it seems likely that these films are more likely to have a greater concentration of these secondary phases. However, the concentration is too low to be detected by XRD for all concentrations, so measured electrical properties are attributed primarily to the BiZT-PT film. Unfortunately, it is not known why a pyrochlore phase nucleated at the PbTiO₃ seed interface. 35BiMT-65PT deposited using the same excess compositions (20 mol% Pb, 10 mol% Bi, 0 mol% Mg) did not show any secondary phases. In future work, it may be necessary to increase the amount of excess Pb or Bi or increase the laser deposition rate to reduce the presence of second phases.

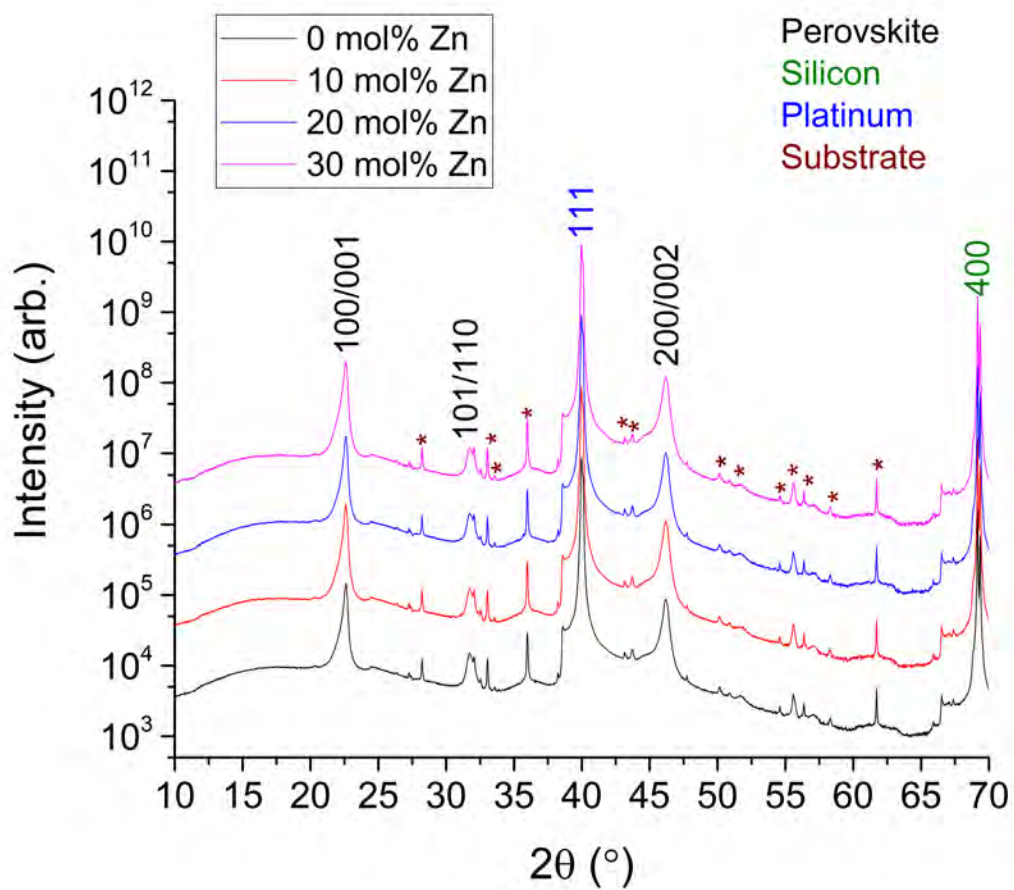


Figure 7.2 – XRD patterns of 20BiZT-80PT thin films deposited on 5 mol% La-doped PbTiO_3 seed layers. The film thickness varied from ≈ 580 nm – 630 nm.

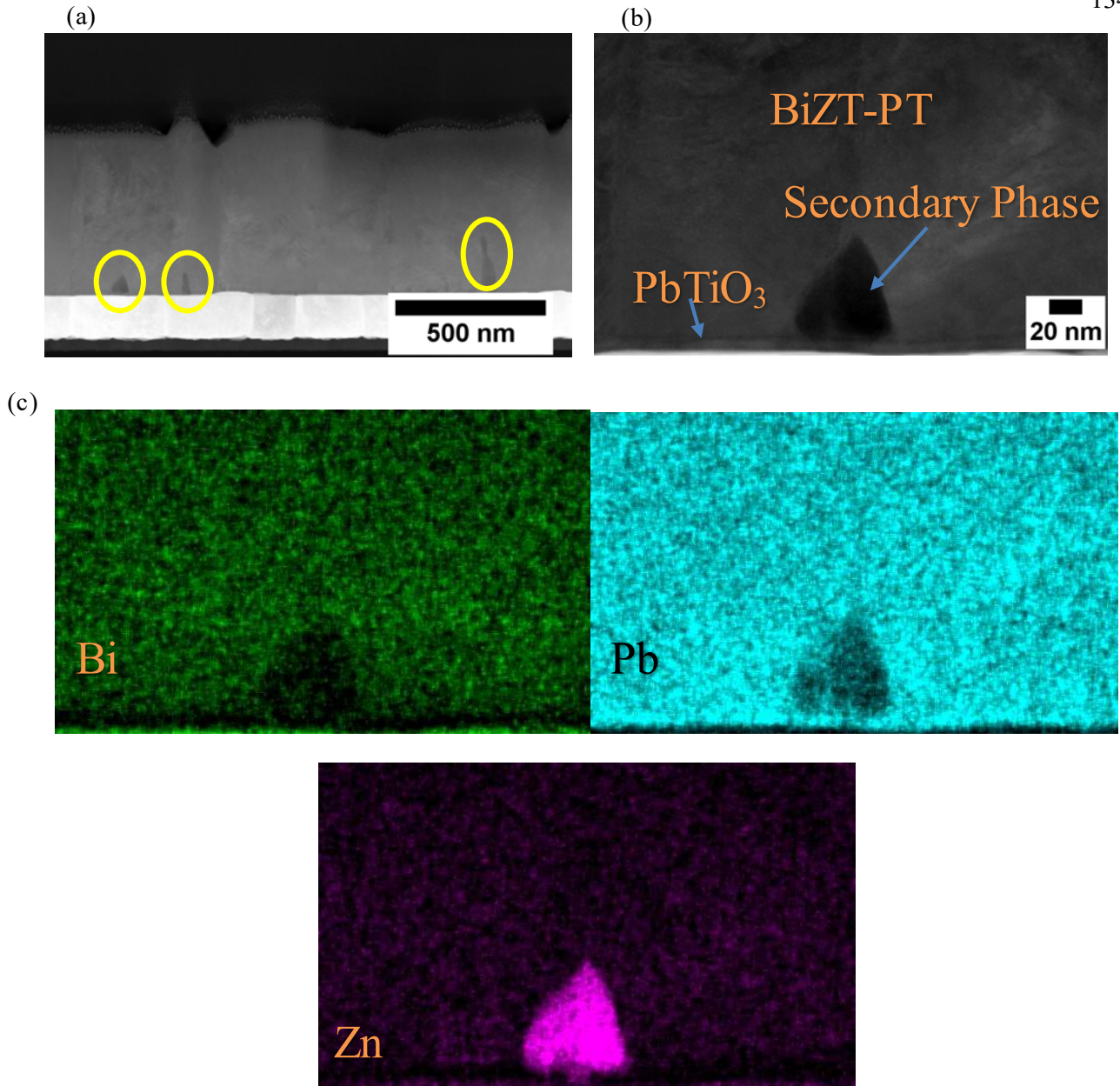


Figure 7.3 – STEM-HAADF images of 20 BiZT-80PT thin films at low (a) and high magnification (b). Yellow circles identify secondary phases in the film near the electrode interface. (c) Elemental maps of Bi, Pb and Zn at high magnification showing the contrast in composition between the BiZT-PT film and the secondary phases.

Figure 7.4 shows the room temperature permittivity and loss tangent as a function of the target Zn excess. No systematic variation in ϵ_r was seen as the Zn excess changed. ϵ_r was ≈ 510 and $\tan(\delta) \approx 2\%$ for the 20BiZT-80PT thin films. The dielectric permittivity of 20BiZT-80PT is significantly lower than 35BiMT-65PT ($\epsilon_r \approx 775$) of approximately the same thickness on the same seed layer. Figure 7.5 shows

the dielectric permittivity vs temperature data for the film deposited with using 30% excess Zn and compares the transition temperature to 35BiMT-65PT of equivalent thickness. The 20BiZT-80PT film shows a $T_{\max} \approx 520$ °C at 1 MHz, approximately 100 °C higher than the 35BiMT-65PT thin film. This significant increase in T_{\max} is expected to increase polarization temperature stability beyond that of 35BiMT-65PT. However, this is still well below the bulk $T_c \approx 565$ °C. The 20BiZT-80PT loss tangent is very similar to that of the 35BiMT-65PT thin films. At lower frequencies (1 and 10 kHz), the 20BiZT-80PT loss tangent rise somewhat faster than the 35BiMT-65PT thin film, but there is almost no difference between them at 100 kHz and 1 MHz.

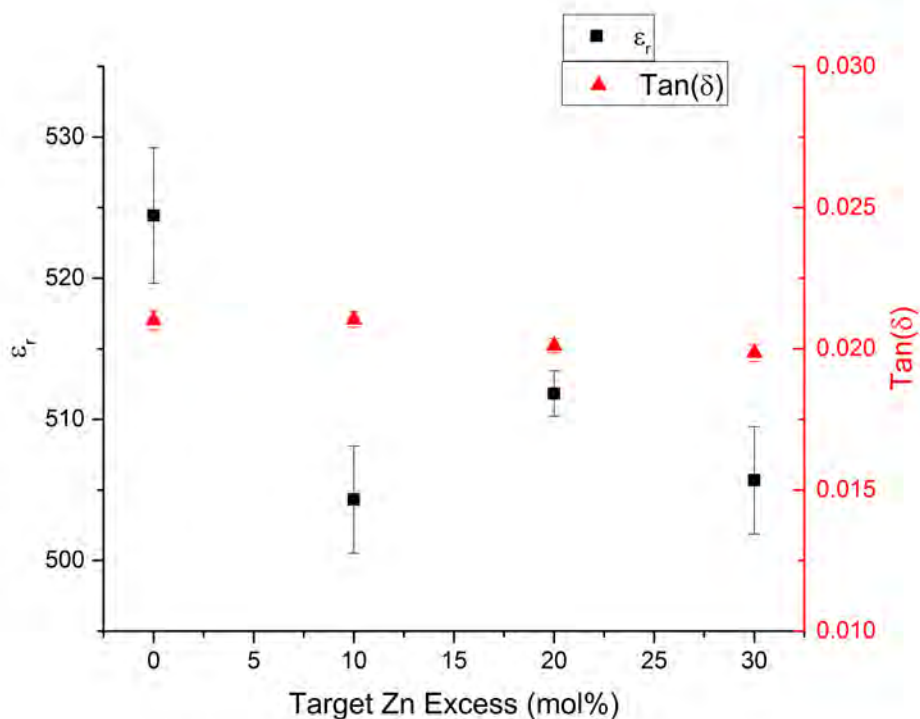


Figure 7.4 – Dielectric permittivity and loss tangent vs Target Zn excess (mol%) of 20BiZT-80PT thin films. Thin film thickness varied between 580 nm – 630 nm.

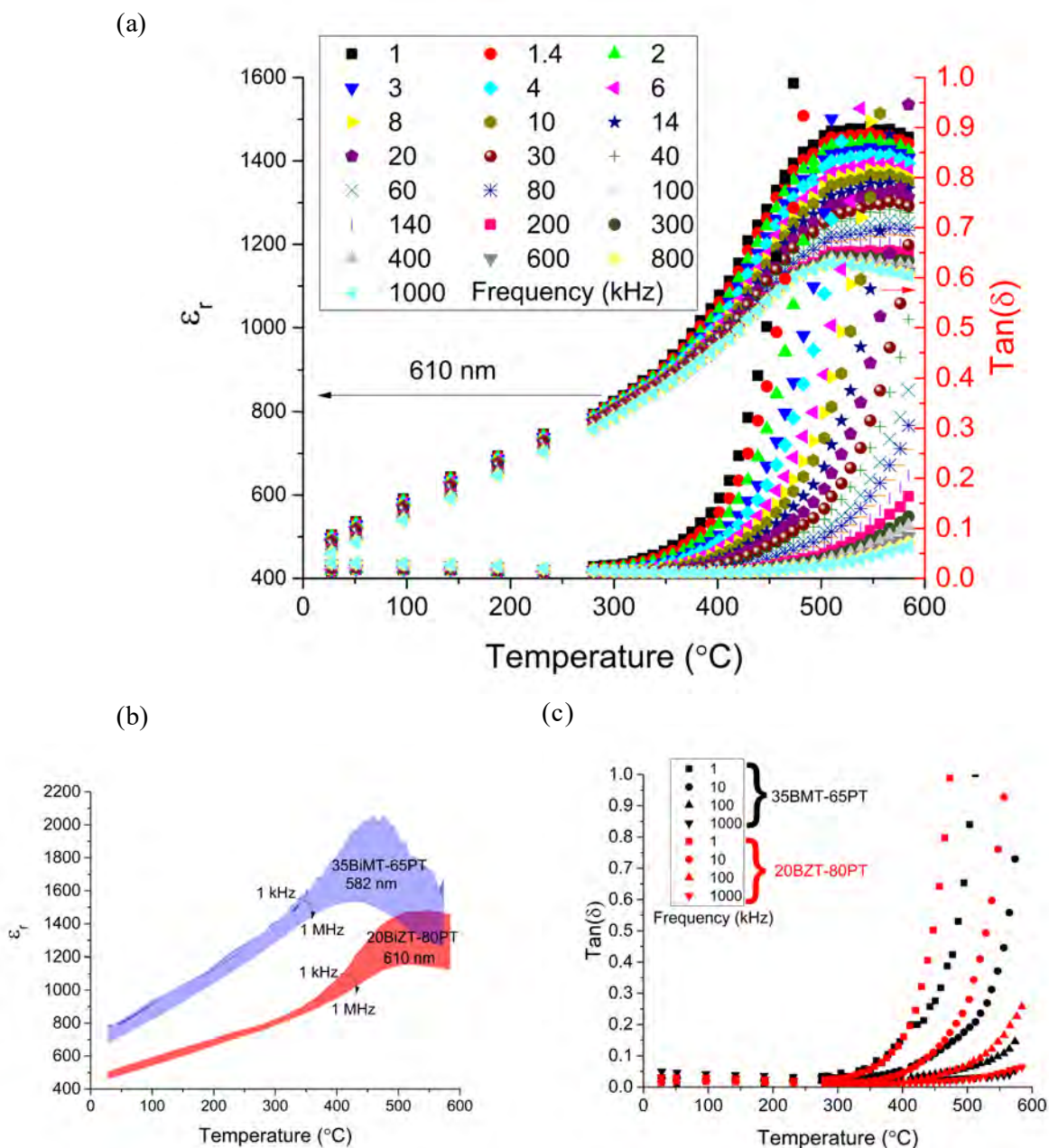


Figure 7.5 – (a) Dielectric permittivity and loss tangent vs temperature of a 610 nm thick 20BiZT-80PT thin film. (b) Comparison of ϵ_r vs temperature between 35BiMT-65PT and 20BiZT-80PT. (c) Comparison of $\tan(\delta)$ vs temperature between 35BiMT-65PT and 20BiZT-80PT

Figure 7.6 shows the ferroelectric hysteresis and PUND response of the 20BiZT-80PT films as a function of excess Zn concentration. Similar to the 35BiMT-65PT thin films, 20BiZT-80PT thin films show increased charge injection with increased applied voltage. However, all BiZT-PT films show significantly greater amounts of charge injection. While the 35BiMT-65PT films show no signs of charge

injection at 600 kV/cm with a 10 kHz hysteresis loop, all 20BiZT-80PT show charge injection on the positive electrode at 600 kV/cm with a 10 kHz hysteresis loop. Figure 7.7 shows the total charge (P^*) at 600 kV/cm for the positive voltage in the PUND measurement. With increasing Zn excess, P^* decreases, meaning less charge is injected. Two possible reasons exist for this. As mentioned earlier, a Zn rich phase is present in the film. If the concentration increases with increasing Zn excess, then this phase may act as higher resistivity phase in the film. Alternatively, the presence of the Zn rich phases may deplete the surrounding film of Zn. Thus, increasing the Zn acts to compensation for Zn deficiencies. Zn deficiencies may also occur due to Zn scattering out of the plume. The 20BiZT-80PT thin films show a $P_r \approx 25 \mu\text{C}/\text{cm}^2$ and $E_c \approx 150 \text{ kV}/\text{cm}$ based on the PUND data in figure 7.6(b). These values are comparable to 35BiMT-65PT which at a maximum $P_r \approx 25 \mu\text{C}/\text{cm}^2$ and $E_c \approx 75\text{-}100 \text{ kV}/\text{cm}$.

The greater charge injection behavior seen in the 20BiZT-80PT thin films compared to the 35BiMT-65PT thin films strongly suggests a large number of non-stoichiometric defects. Again, it is possible that the primary defect is A-site deficiency, specifically Pb deficiency. This would need to be proved with explicit measurements of the film composition.

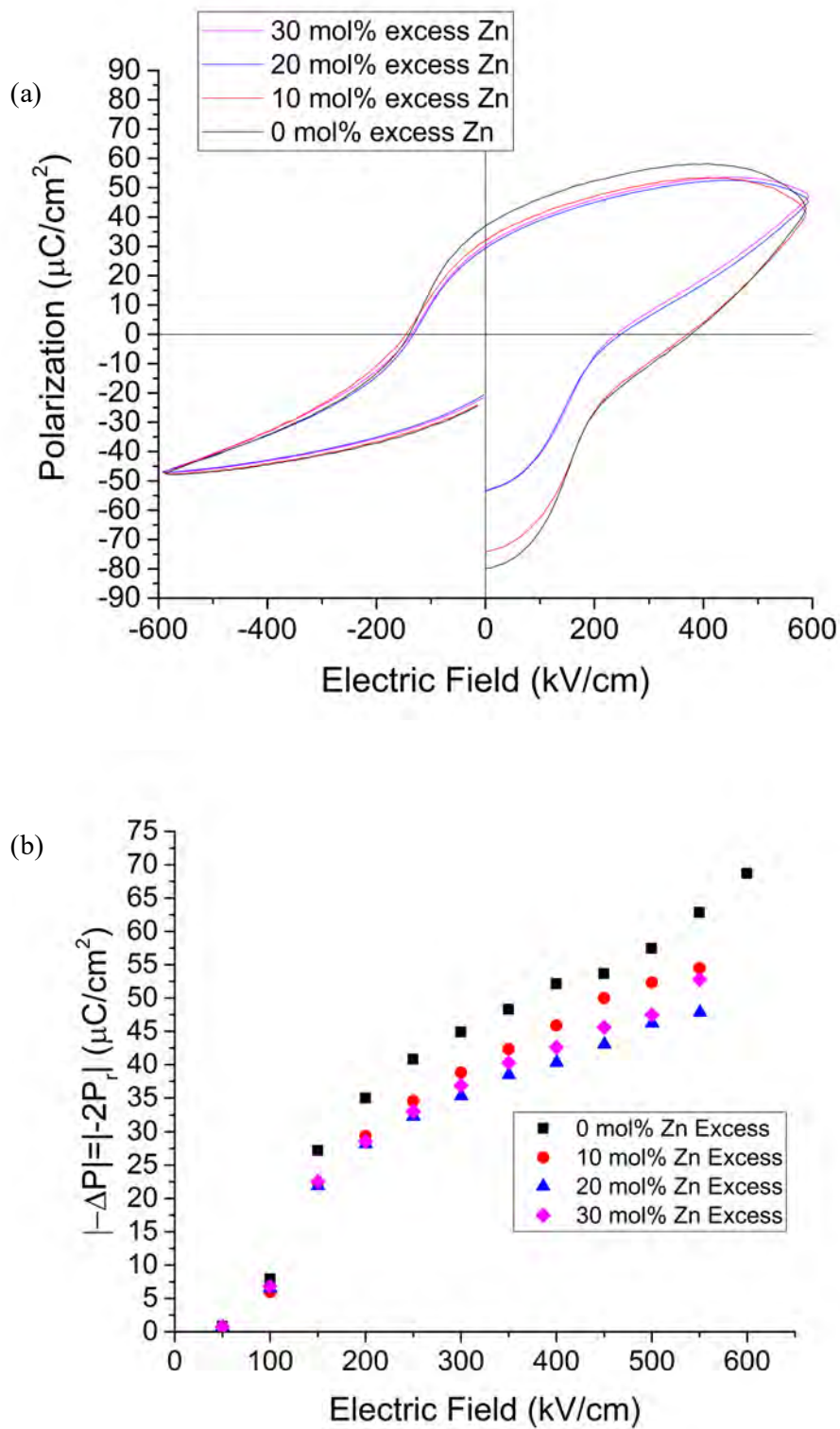


Figure 7.6 – (a) Ferroelectric hysteresis of 20BiZT-80PT thin films at 10 kHz as a function of the excess Zn in the targets. (b) Corresponding PUND measurements on the negative polarization state from with 1 ms pulses and 1 ms 0V holds.

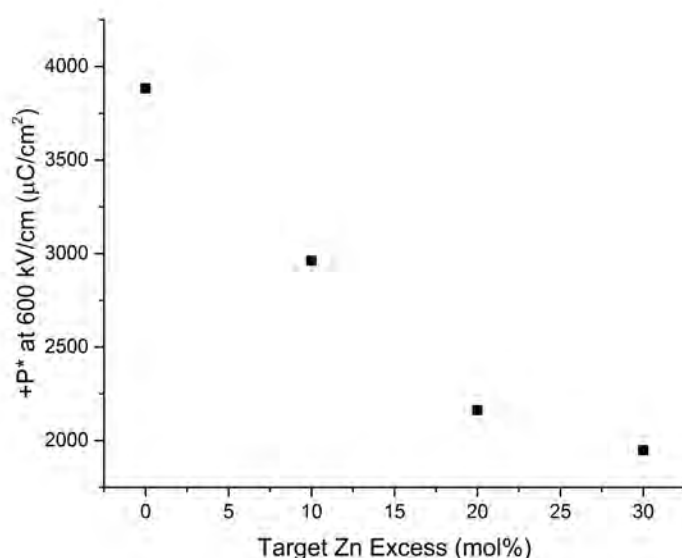


Figure 7.7 – Total charge (P^*) on the positive polarization state during the PUND measurement in Figure 7.6 (b) as a function to the target Zn excess.

7.5 Future Work – HfO₂-ZrO₂ Ferroelectric Thin Films

Recently, crystalline HfO₂-based thin films have been shown to exhibit ferroelectric properties.^{16–21} Ferroelectricity in these simple binary thin films is attributed to stabilization of the orthorhombic phase. One of the main advantages of these materials is the thickness scaling properties. These materials can be made at thicknesses at which most other conventional ferroelectrics lose their polarization. HfO₂-based films between 10-20 nm can exhibit near square hysteresis loops with P_r up to 15 $\mu\text{C}/\text{cm}^2$.^{18,21} In addition, Müller *et al.* have explored the possibility of this material being used as a Pb-free ferroelectric for non-volatile memory applications.¹⁸

However, many aspects of the optimization of these materials still need to be determined. Several of the main limiting factors are the high coercive field (>1 MV/cm), high fatigue and retention loss compared to PZT.^{18,21} Assuming a 1 MV/cm coercive field, and utilizing the same voltage as state of

the art commercial PZT FeRAM devices (≤ 1.5 V),²² would require the HfO₂-based film to have a thickness ≈ 5 nm such that on order of $3 \cdot E_c$ is applied and the maximum P_r is achieved. Müller *et al.* demonstrated HfO₂-based ferroelectrics with fatigue cycling up to 10^8 cycles without significant loss in the switchable polarization at 2V and that these films exhibited retention loss at 125 °C (at 3V) similar to PZT at 175 °C.^{18,22} There is still much that is unknown about the properties of HfO₂-based ferroelectrics as well as the processing optimization. The T_c of epitaxial 0.07 YO_{1.5}-doped HfO₂ films was estimated to be around 450 °C²³, which is greater than that of MPB PZT, but less than that of the Bi-based-PbTiO₃ solid solutions examined in this thesis. Thus, this material could potentially replace PZT as a high temperature FeRAM material. However, a comprehensive understanding of the high temperature properties as a function of the various dopants is still required to select optimal compositions for high temperature FeRAM.

7.6 References

- 1 J.C. Nino and S. Trolier-McKinstry, "Dielectric, Ferroelectric, and Piezoelectric Properties of (001) BiScO₃-PbTiO₃ Epitaxial Films Near the Morphotropic Phase Boundary," *J. Mater. Res.*, **19** [02] 568–572 (2004).
- 2 L. Zhang, J. Chen, H. Zhao, L. Fan, Y. Rong, J. Deng, R. Yu, and X. Xing, "Temperature-Independent Ferroelectric Property and Characterization of High- T_c 0.2Bi(Mg_{1/2}Ti_{1/2})O₃-0.8PbTiO₃ Thin Films," *Appl. Phys. Lett.*, **103** [8] 082902 (2013).
- 3 S.M. Choi, C.J. Stringer, T.R. Shrout, and C.A. Randall, "Structure and Property Investigation of a Bi-Based Perovskite Solid Solution: (1-x)Bi(Ni_{1/2}Ti_{1/2})O₃-xPbTiO₃," *J. Appl. Phys.*, **98** [3] 034108 (2005).
- 4 C.J. Stringer, T.R. Shrout, C.A. Randall, and I.M. Reaney, "Classification of Transition Temperature Behavior in Ferroelectric PbTiO₃-Bi(Me'Me'')O₃ Solid Solutions," *J. Appl. Phys.*, **99** [2] 024106 (2006).
- 5 M.R. Suchomel and P.K. Davies, "Enhanced Tetragonality in (x)PbTiO₃-(1-x)Bi(Zn_{1/2}Ti_{1/2})O₃ and Related Solid Solution Systems," *Appl. Phys. Lett.*, **86** [26] 1–3 (2005).
- 6 D.M. Stein, M.R. Suchomel, and P.K. Davies, "Enhanced Tetragonality in (x)PbTiO₃-(1-x)Bi(B'B'')O₃ Systems: Bi(Zn_{3/4}W_{1/4})O₃," *Appl. Phys. Lett.*, **89** [13] 89–92 (2006).
- 7 R.E. Eitel, C.A. Randall, T.R. Shrout, P.W. Rehrig, W. Hackenberger, and S.-E. Park, "New High Temperature Morphotropic Phase Boundary Piezoelectrics Based on Bi(Me)O₃ - PbTiO₃ Ceramics," *Jpn. J. Appl. Phys.*, **40** [10] 5999–6002 (2001).
- 8 C.A. Randall, R. Eitel, B. Jones, T.R. Shrout, D.I. Woodward, and I.M. Reaney, "Investigation of a High T_c Piezoelectric System: (1-x)Bi(Mg_{1/2}Ti_{1/2})O₃-(x)PbTiO₃," *J. Appl. Phys.*, **95** [7] 3633

- (2004).
- 9 R.E. Eitel, S.J. Zhang, T.R. Shrout, C.A. Randall, and I. Levin, "Phase Diagram of the Perovskite System $(1-x)\text{BiScO}_3-x\text{PbTiO}_3$," *J. Appl. Phys.*, **96** [5] 2828–2831 (2004).
- 10 R.E. Eitel, C.A. Randall, T.R. Shrout, and S.-E. Park, "Preparation and Characterization of High Temperature Perovskite Ferroelectrics in the Solid-Solution $(1-x)\text{BiScO}_3-x\text{PbTiO}_3$," *Jpn. J. Appl. Phys.*, **41** [Part 1, No. 4A] 2099–2104 (2002).
- 11 H. Wen, X. Wang, and L. Li, "Fabrication and Properties of Sol-Gel-Derived $\text{BiScO}_3\text{-PbTiO}_3$ Thin Films," *J. Am. Ceram. Soc.*, **89** [7] 2345–2347 (2006).
- 12 S.Y. Lee, W. Wang, and S. Trolier-McKinstry, "High Curie Temperature $\text{BiInO}_3\text{-PbTiO}_3$ films," *J. Appl. Phys.*, **115** [22] 1–5 (2014).
- 13 M.R. Suchomel, A.M. Fogg, M. Allix, H. Niu, J.B. Claridge, and M.J. Rosseinsky, " $\text{Bi}_2\text{ZnTiO}_6$: A Lead-Free Closed-Shell Polar Perovskite with a Calculated Ionic Polarization of $150 \mu\text{Ccm}^{-2}$," *Chem. Mater.*, **18** [21] 4987–4989 (2006).
- 14 D. Kwon, B. Kim, P. Tong, and B.G. Kim, "Growth and Structural Characterization of $(0.2)\text{Bi}(\text{Zn}_{1/2}\text{Ti}_{1/2})\text{O}_3\text{-}(0.8)\text{PbTiO}_3$ Epitaxial Thin Films by Off-Axis RF Sputtering," *Appl. Phys. Lett.*, **93** [4] 1–4 (2008).
- 15 Y. Ahn and J.Y. Son, "Epitaxial Perovskite $\text{Bi}_2\text{ZnTiO}_6$ Thin Film With High Tetragonality," *J. Cryst. Growth*, **433** 86–88 (2016).
- 16 T.S. Böske, J. Müller, D. Bräuhaus, U. Schröder, and U. Böttger, "Ferroelectricity in Hafnium Oxide Thin Films," *Appl. Phys. Lett.*, **99** [102903] (2011).
- 17 T.S. Böske, S. Teichert, D. Bräuhaus, J. Müller, U. Schröder, U. Böttger, and T. Mikolajick, "Phase Transitions in Ferroelectric Silicon Doped Hafnium Oxide," *Appl. Phys. Lett.*, **99** [112904] (2011).
- 18 J. Müller, T.S. Böske, S. Müller, E. Yurchuk, P. Polakowski, J. Paul, D. Martin, T. Schenk, *et al.*, "Ferroelectric Hafnium Oxide: A CMOS-Compatible and Highly Scalable Approach to Future Ferroelectric Memories," pp. 280–283 in *Electron Devices Meet.* 2013.
- 19 A. Onodera and M. Takesada, "Ferroelectricity in Simple Binary Crystals," *Crystals*, **7** [8] 232 (2017).
- 20 S.L. Weeks, A. Pal, V.K. Narasimhan, K.A. Littau, and T. Chiang, "Engineering of Ferroelectric $\text{HfO}_2\text{-ZrO}_2$ Nanolaminates," *ACS Appl. Mater. Interfaces*, **9** [15] 13440–13447 (2017).
- 21 S.W. Smith, A.R. Kitahara, M.A. Rodriguez, M.D. Henry, M.T. Brumbach, and J.F. Ihlefeld, "Pyroelectric Response in Crystalline Hafnium Zirconium Oxide ($\text{Hf}_{1-x}\text{Zr}_x\text{O}_2$) Thin Films," *Appl. Phys. Lett.*, **110** [072901] (2017).
- 22 J. Rodriguez, K. Remack, J. Gertas, L. Wang, C. Zhou, K. Boku, K.R. Udayakumar, S. Summerfelt, T. Moise, D. Kim, J. Groat, J. Eliason, M. Depner, and F. Chu, "Reliability of Ferroelectric Random Access Memory Embedded within 130nm CMOS," pp. 750–758 in *Reliab. Phys. Symp. (IRPS), 2010 IEEE*. 2010.
- 23 T. Shimizu, K. Katayama, T. Kiguchi, A. Akama, T.J. Konno, O. Sakata, and H. Funakubo, "The Demonstration of Significant Ferroelectricity in Epitaxial Y-doped HfO_2 Film," *Sci. Rep.*, **6** [32931] 1–8 (2016).

Appendix A

Material Tolerance Factor and Cubic Transition Temperature

Figure 1.1 plots the tolerance factor and cubic phase transition temperature for a set of perovskite materials. Table A.1 gives the calculated perovskite tolerance factor and cubic transition temperatures for all materials plotted.

Table A.1 – List of compounds, perovskite tolerance factor and cubic phase transformation temperature in Figure 1.1.

| Compounds | Perovskite Tolerance Factor | Cubic Transformation Temperature (°C) |
|--|-----------------------------|---------------------------------------|
| BaTiO ₃ | 1.062 | 135 |
| PbTiO ₃ | 1.019 | 490 |
| SrTiO ₃ | 1.002 | -163 |
| CdTiO ₃ | 0.956 | 110 |
| NaNbO ₃ | 0.967 | -200 |
| KNbO ₃ | 1.054 | 435 |
| NaTaO ₃ | 0.967 | 480 |
| KTaO ₃ | 1.054 | -271 |
| BiFeO ₃ | 0.947 | 850 |
| KIO ₃ | 0.915 | 212 |
| CsGeCl ₃ | 0.913 | 155 |
| AgNbO ₃ | 1.026 | 325 |
| AgTaO ₃ | 1.026 | 370 |
| DyCrO ₃ | 0.927 | 575 |
| HoCrO ₃ | 0.924 | 495 |
| YbCrO ₃ | 0.918 | 515 |
| LuCrO ₃ | 0.914 | 440 |
| PrCrO ₃ | 0.974 | 630 |
| YCrO ₃ | 0.930 | 550 |
| (K _{1/2} Bi _{1/2})TiO ₃ | 1.019 | 270 |
| (Na _{1/2} Bi _{1/2})TiO ₃ | 0.975 | 200 |
| Pb(Co _{1/2} W _{1/2})O ₃ | 1.022 | -190 |
| Pb(Sc _{1/2} Nb _{1/2})O ₃ | 0.977 | 90 |
| Pb(Fe _{1/2} Nb _{1/2})O ₃ | 1.001 | 114 |
| Pb(In _{1/2} Nb _{1/2})O ₃ | 0.964 | 90 |
| Pb(Sc _{1/2} Ta _{1/2})O ₃ | 0.977 | 26 |
| Pb(Fe _{1/2} Ta _{1/2})O ₃ | 0.969 | -40 |
| Pb(Mg _{1/3} Nb _{2/3})O ₃ | 0.989 | -8 |
| Pb(Zn _{1/3} Nb _{2/3})O ₃ | 0.986 | 140 |
| Pb(Co _{1/3} Nb _{2/3})O ₃ | 0.985 | -98 |
| Pb(Ni _{1/3} Nb _{2/3})O ₃ | 0.994 | -120 |
| Pb(Cd _{1/3} Nb _{2/3})O ₃ | 0.953 | 270 |

| Compounds | Perovskite Tolerance Factor | Cubic Transformation Temperature (°C) |
|---|-----------------------------|---------------------------------------|
| Pb(Mg _{1/3} Ta _{2/3})O ₃ | 0.989 | -90 |
| Pb(Co _{1/3} Ta _{2/3})O ₃ | 0.985 | -140 |
| Pb(Ni _{1/3} Ta _{2/3})O ₃ | 0.994 | -180 |
| Pb(Fe _{2/3} W _{1/3})O ₃ | 0.997 | -95 |
| Pb(Fe _{2/3} W _{1/3})O ₃ | 0.965 | -12 |
| Pb(Sc _{2/3} W _{1/3})O ₃ | 1.016 | 1200 |
| Ba(Cu _{1/2} W _{1/2})O ₃ | 1.028 | 470 |
| Ba(Cu _{1/3} Ta _{2/3})O ₃ | 0.972 | 920 |
| Sr(Cu _{1/2} W _{1/2})O ₃ | 0.970 | 1250 |
| Sr(Cu _{1/3} Ta _{2/3})O ₃ | 1.028 | 380 |
| Ba(Cu _{1/3} Nb _{2/3})O ₃ | 0.970 | 390 |
| Sr(Cu _{1/3} Nb _{2/3})O ₃ | 0.985 | 370 |
| BaBiO _{2.8} | 0.985 | 340 |
| BaBiO ₃ | 0.952 | 360 |
| Ba(Bi _{1/2} Nb _{1/2})O ₃ | 0.952 | 400 |
| Ba(Bi _{1/2} Ta _{1/2})O ₃ | 0.974 | 320 |
| Ba(Bi _{1/2} V _{1/2})O ₃ | 0.931 | 450 |
| Ba(Bi _{2/3} W _{1/3})O ₃ | 0.932 | 500 |
| Ba(Bi _{2/3} Mo _{1/3})O ₃ | 1.049 | 310 |
| Tl(Zr _{1/2} W _{1/2})O ₃ | 0.908 | 605 |
| CdHfO ₃ | 0.938 | 450 |
| Cd(Fe _{1/2} Nb _{1/2})O ₃ | 0.916 | 430 |
| Cd(Sc _{1/2} Nb _{1/2})O ₃ | 0.945 | 325 |
| Cd(Cr _{1/2} Nb _{1/2})O ₃ | 0.927 | 295 |
| Cd(Mg _{1/3} Nb _{2/3})O ₃ | 1.008 | 5 |
| Pb(Cr _{1/2} Nb _{1/2})O ₃ | 0.984 | -90 |
| Pb(Li _{1/4} Sc _{1/4} W _{1/2})O ₃ | 0.996 | -70 |
| Pb(Li _{1/4} Fe _{1/4} W _{1/2})O ₃ | 0.984 | 30 |
| Pb(Li _{1/4} Co _{1/4} W _{1/2})O ₃ | 0.978 | -5 |
| Pb(Li _{1/4} In _{1/4} W _{1/2})O ₃ | 0.966 | 5 |
| Pb(Li _{1/4} Y _{1/4} W _{1/2})O ₃ | 0.964 | 20 |
| Pb(Li _{1/4} Tb _{1/4} W _{1/2})O ₃ | 0.970 | -40 |
| Pb(Li _{1/4} Yb _{1/4} W _{1/2})O ₃ | 0.966 | 0 |
| Pb(Li _{1/4} Ho _{1/4} W _{1/2})O ₃ | 0.962 | 0 |
| Pb(Li _{1/4} Gd _{1/4} W _{1/2})O ₃ | 0.956 | -18 |
| Pb(Li _{1/4} Pr _{1/4} W _{1/2})O ₃ | 0.951 | -20 |
| Pb(Li _{1/4} La _{1/4} W _{1/2})O ₃ | 0.960 | -15 |
| Pb(Li _{1/4} Sm _{1/4} W _{1/2})O ₃ | 0.937 | 120 |
| Pb(Na _{1/4} Y _{1/4} W _{1/2})O ₃ | 0.937 | 150 |
| Pb(Na _{1/4} Ho _{1/4} W _{1/2})O ₃ | 0.986 | -30 |
| Pb(Li _{1/3} Zr _{1/6} W _{1/2})O ₃ | 0.982 | 495 |
| Pb(Li _{4/9} Nb _{2/9} W _{1/3})O ₃ | 0.976 | -170 |

| Compounds | Perovskite Tolerance Factor | Cubic Transformation Temperature (°C) |
|--|-----------------------------|---------------------------------------|
| $\text{Pb}(\text{Sc}_{5/9}\text{Nb}_{1/3}\text{W}_{1/9})\text{O}_3$ | 0.992 | 57 |
| $\text{Pb}(\text{Sc}_{1/4}\text{Cr}_{1/4}\text{Nb}_{1/2})\text{O}_3$ | 0.978 | 20 |
| $\text{Pb}(\text{Cd}_{1/4}\text{Mn}_{1/4}\text{Nb}_{1/2})\text{O}_3$ | 1.010 | 200 |
| $\text{Pb}(\text{Mg}_{1/4}\text{Mn}_{1/4}\text{Nb}_{1/2})\text{O}_3$ | 0.982 | 250 |
| $\text{Pb}(\text{Cd}_{1/4}\text{Mn}_{1/4}\text{W}_{1/2})\text{O}_3$ | 0.993 | 110 |
| $\text{Pb}(\text{Co}_{1/4}\text{Mn}_{1/4}\text{W}_{1/2})\text{O}_3$ | 1.000 | 100 |
| $\text{Pb}(\text{Ni}_{1/4}\text{Mn}_{1/4}\text{W}_{1/2})\text{O}_3$ | 1.009 | -25 |
| $\text{Pb}(\text{Co}_{1/4}\text{Mn}_{1/4}\text{Nb}_{1/2})\text{O}_3$ | 0.988 | -20 |
| $\text{Pb}(\text{Mg}_{1/4}\text{Mn}_{1/4}\text{Nb}_{1/2})\text{O}_3$ | 1.005 | 0 |
| $\text{Pb}(\text{Zn}_{1/4}\text{Mn}_{1/4}\text{Nb}_{1/2})\text{O}_3$ | 0.989 | 30 |
| $\text{Pb}(\text{Li}_{1/3}\text{Nb}_{1/3}\text{W}_{1/3})\text{O}_3$ | 0.989 | -45 |
| $\text{Pb}(\text{Mg}_{1/3}\text{Mn}_{1/3}\text{Ta}_{1/3})\text{O}_3$ | 1.007 | -135 |
| $\text{Pb}(\text{Ni}_{1/3}\text{Mn}_{1/3}\text{Ta}_{1/3})\text{O}_3$ | 1.012 | -180 |
| BiMnO_3 | 0.947 | 500 |

Appendix B

Refractive Index Estimation from High Temperature I-V Measurements

In Figure 5.6, the refractive index of 35 BiMT – 65 PT thin films on a 36 nm PbTiO₃ seed layer was estimated based on the I-V measurements by fitting the curves to the Poole-Frenkel equation (Eq. 5.3). Figure 5.7 shows the refractive index estimation for these films at between room temperature up to 200 °C. Figure B.1-B.4 below show the I-V measurements for the films deposited between 60 mTorr and 340 mTorr as a function of temperature. Figures B.5-B.8 show the resulting $\ln\left(\frac{J}{E}\right)$ vs $E^{1/2}$ plots for the I-V vs temperature plots and the fitted plot range for each curve. The resulting fit data is given in Table B.1. The fit range was done for the linear regions of each I-V measurement, generally between 175 kV/cm and 250 kV/cm.

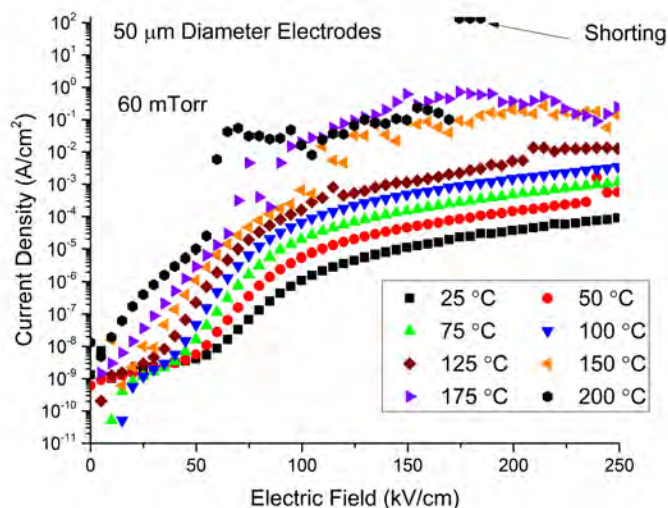


Figure B.1 –I-V measurement from 25 °C to 200 °C of a 35BiMT-65PT thin film deposited at 60 mTorr.

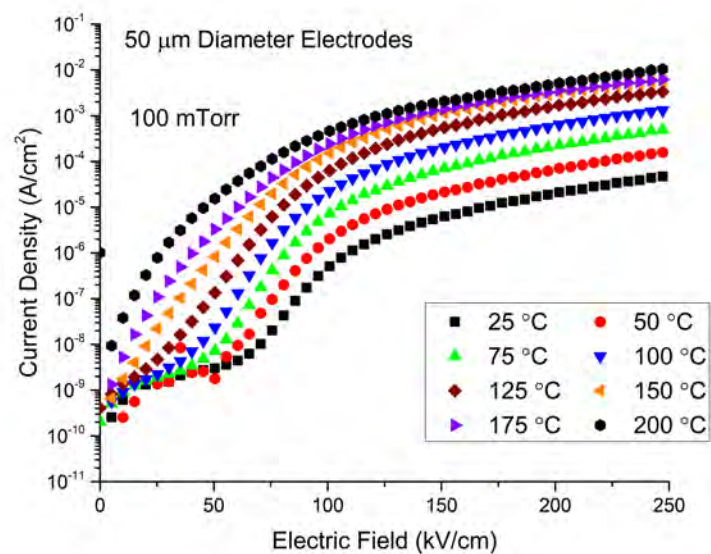


Figure B.2 –I-V measurement from 25 °C to 200 °C of a 35BiMT-65PT thin film deposited at 100 mTorr.

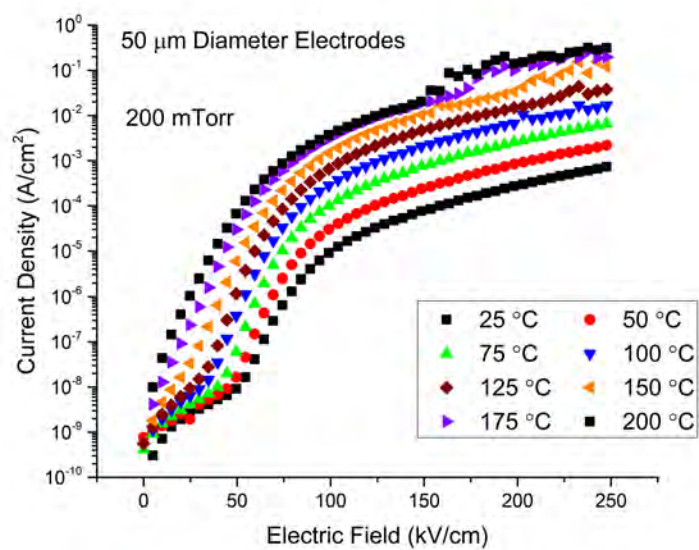


Figure B.3 –I-V measurement from 25 °C to 200 °C of a 35BiMT-65PT thin film deposited at 200 mTorr.

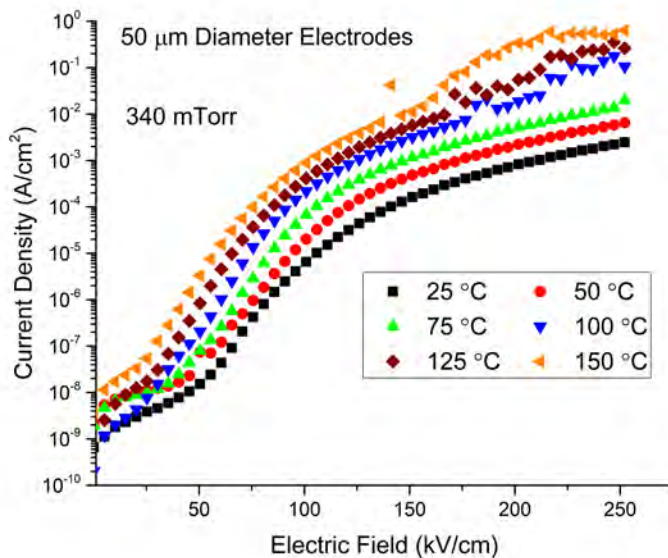


Figure B.4 –I-V measurement from 25 °C to 200 °C of a 35BiMT-65PT thin film deposited at 340 mTorr.

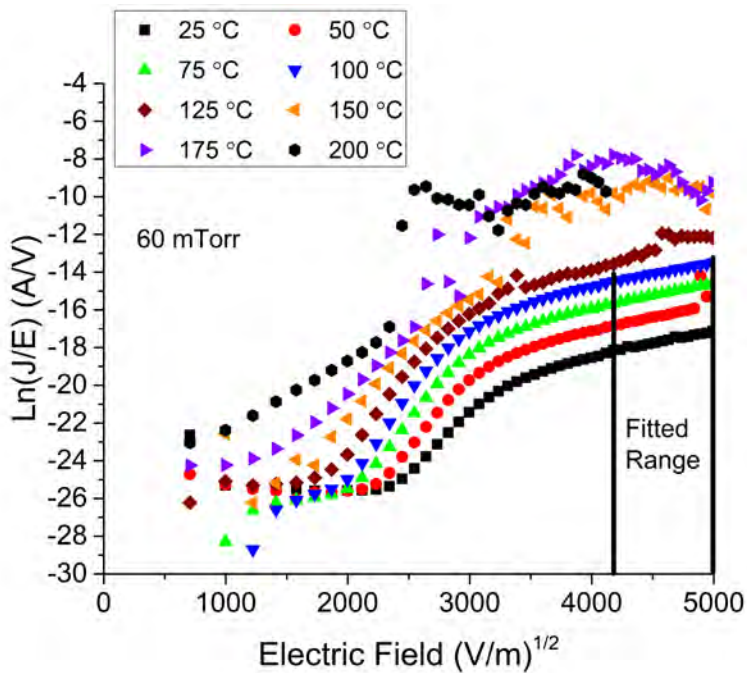


Figure B.5 – $\ln(J/E)$ vs $E^{1/2}$ for data in Figure B.1. Fitted linear region are indicated by the bold black lines.

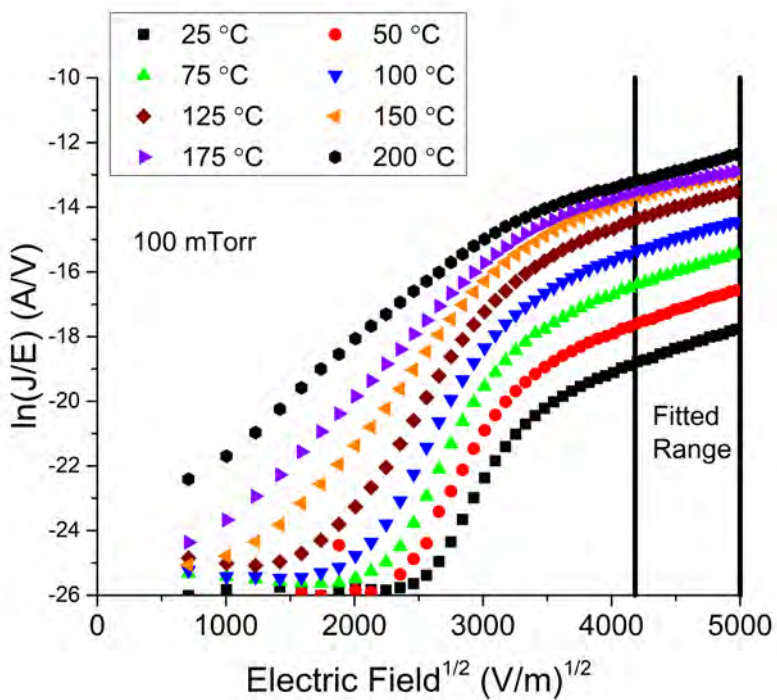


Figure B.6 $-\ln(J/E)$ vs $E^{1/2}$ for data in Figure B.2. Fitted linear region are indicated by the bold black lines.

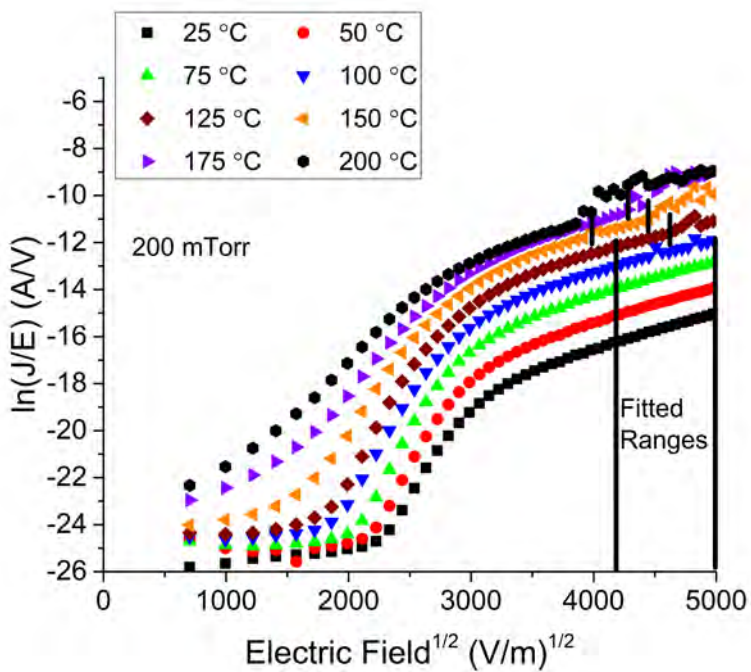


Figure B.7 $-\ln(J/E)$ vs $E^{1/2}$ for data in Figure B.3. Fitted linear region are indicated by the bold black lines.

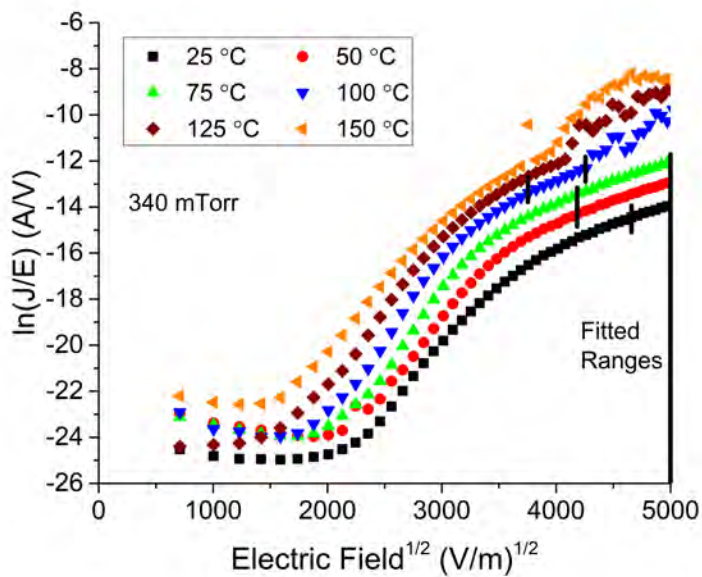


Figure B.8 $-\ln(J/E)$ vs $E^{1/2}$ for data in Figure B.4. Fitted linear region are indicated by the bold black lines.

Table B.1 – Fitted slopes and calculated refractive index for 35 BiMT– 65 PT thin films deposited between 60 m Torr and 340 m Torr in Figure 5.7.

| Deposition Pressure (mTorr) | Temperature (°C) | Fitted Slope ($\text{Am}^{1/2}/(\text{V}^{1.5})$) | Refractive Index |
|-----------------------------|------------------|---|------------------|
| 60 | 25 | 0.00131 | 2.26 |
| | 50 | 0.00139 | 1.96 |
| | 75 | 0.00131 | 1.93 |
| | 100 | 0.00122 | 1.94 |
| 100 | 25 | 0.00139 | 2.13 |
| | 50 | 0.00138 | 1.98 |
| | 75 | 0.00131 | 1.93 |
| | 100 | 0.00118 | 2.00 |
| | 125 | 0.00109 | 2.03 |
| | 150 | 0.00098 | 2.13 |
| | 175 | 0.00082 | 2.40 |
| | 200 | 0.00106 | 1.76 |
| 200 | 25 | 0.00151 | 1.96 |
| | 50 | 0.00147 | 1.85 |
| | 75 | 0.00141 | 1.79 |
| | 100 | 0.00138 | 1.71 |
| | 125 | 0.00129 | 1.72 |
| | 150 | 0.00149 | 1.40 |
| | 175 | 0.00176 | 1.12 |
| 340 | 25 | 0.00156 | 1.89 |
| | 50 | 0.00172 | 1.59 |
| | 75 | 0.00173 | 1.46 |
| | 100 | 0.00215 | 1.10 |

Appendix C

35BiMT-65PT Thin Film Processing-Composition-Lattice Parameter-Property Relationships

In chapters 4 and 6, various processing parameters were systematically explored as a means to control the phase, growth and properties of 35 BiMT-65PT films. As part of this work, XRD was utilized to characterize the films as a function of deposition pressure, target composition, laser repetition rate, and oxygen / argon background atmosphere. In addition, chapter 4 explored the resulting film compositions as a function of deposition pressure, target composition, and laser repetition rate. This section explores the possible relationships between the thin film processing parameters, the thin film lattice parameters and the resulting properties.

Lattice parameters were calculated by fitting 2 θ peaks using LIPRAS (Line-Profile Analysis Software) and assigning indices to the peaks. The Si substrate was used as an internal standard and the entire pattern was shifted such that the (400) Si peak occurred at $2\theta = 69.13^\circ$. Either Pearson VII or asymmetric Pearson VII functions were used to fit the peaks depending on the asymmetry of the peaks. The specific function is denoted in the captions of figures in this section. The peak background was fit manually using a 2nd order spline function due to the non-uniform background. All error bars are errors in the fitted peak position.

As the film compositions are deep in the tetragonal phase field, at least 2 peaks are needed to determine the a and c lattice parameters. Ideally, this would be done using the h00 and 00l peaks. Within the examined range, the 200 and 002 peaks have the largest peak separation and signal to noise ratio. However, due to the low peak intensity of the 00l peaks, peak overlap with the h00 peaks and the large non-uniform background, another peak was selected for fitting to insure the accuracy of the fits. The 111 peak was selected as it does not split and it was not possible to adequately determine if the 101 or 110

was the dominant peak around $2\theta \approx 31.5\text{-}32.0^\circ$. For 111 peaks, the a-lattice parameter was assumed to be equal to that from the fit of the 200 peak in order to complete the c-lattice parameter calculation.

Figure C.1 (a) and (b) shows the calculated lattice parameters for films deposited at different deposition pressures from Figure 6.4 (b) based on the 200 / 002 peak fits or the 200 / 111 peak fits. Films deposited at different pressures show the greatest change in 2θ among all variables examined and thus give the best possibility for examining the c/a ratio of these films. As seen in the Figure C.1, the c lattice parameters calculated from the 002 and the 111 peaks do not agree. Films deposited around 100 mTorr demonstrate the largest 200 / 002 peak separation and the highest intensity for the 002 peak. However, even in this case, the c-lattice parameter calculated from the 002 and 111 differ by $\approx 0.04 \text{ \AA}$. In addition, the opposite trend in the calculated c-lattice parameter vs deposition pressure is observed. It is believed that the difference in the c-lattice parameters is due to the inability to accurately resolve the 002 peak position due to the overlap with the 200, as well as the large, asymmetric background for the 111 peak. In particular, an incorrect subtraction of the large asymmetric backgrounds can shift the fitted peak position. Because of this uncertainty in the c lattice parameter, subsequent analysis was done only for the a-lattice parameter.

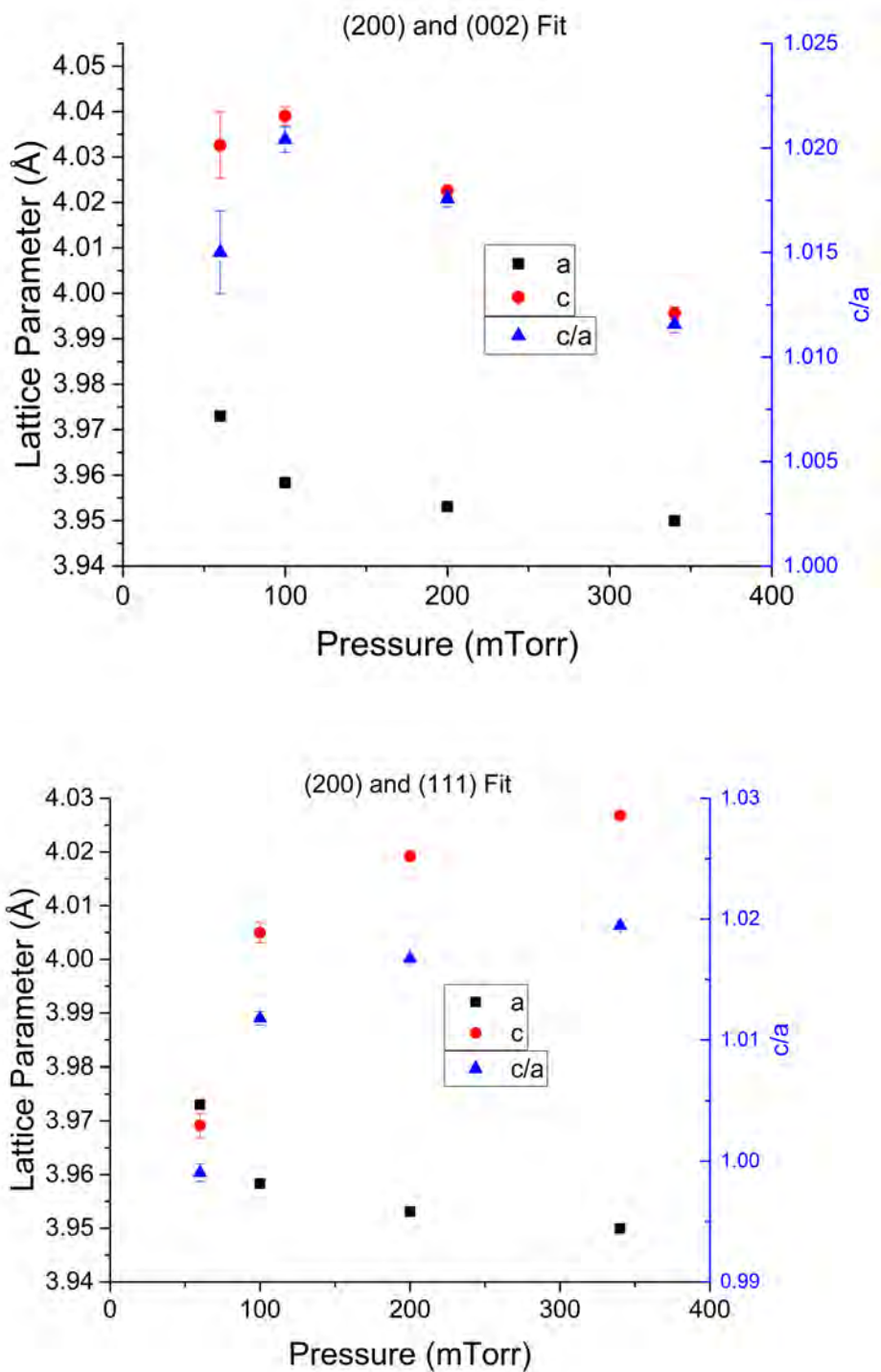


Figure C.1 - Estimated lattice parameters for 35 BiMT-65PT thin films deposited at different pressures from data in Figure 6.4 (b). The a-lattice parameter was calculated from the (200) peak while the c-lattice parameter was calculated from either the 002 peak (a) or the 111 peak (b). Error bars correspond to the error in the fitted peak position and the maximum possible error was used for all lattice parameter calculations. All peaks were fitted to a Pearson VII function except the 60 m Torr c-lattice parameter.

Figures C.1 – C.3 show the a-lattice parameter of 35BiMT-65PT thin films on PbTiO₃ seed layers as a function of deposition pressure, target composition, and laser repetition rate. In Figure C.1, the a-lattice parameter expands as the deposition pressure decreases. This is consistent with swelling of the lattice parameter as the bombardment energy is increased, as reported elsewhere.¹ In Figure C.2, the a-lattice parameter is calculated as a function of target composition. The composition for films were measured for targets with 20 mol% excess Pb to 48 mol% excess Pb. For these films, the Bi and Mg concentrations approach stoichiometry with respect to Ti, but the films are still significantly Pb deficient. However, it was found that the a-lattice parameter does not change significantly with target composition. There is a small decrease in the a-lattice parameter based on the fitted peak positions between 48 mol% excess Pb and 65 / 85 mol% excess Pb, but this could be due to fitting with a single peak. In figure C.3, the a-lattice parameter is calculated as a function of the laser repetition rate. Between 5-20 Hz, the a-lattice parameter varies little, but there is $\approx 0.01 \text{ \AA}$ decrease in the a-lattice parameter at 1 Hz. As the deposition rate decreases from 5 Hz to 1 Hz, there is an increasing amount of pyrochlore formation. As the pyrochlore forms, the composition of the surrounding perovskite material may further shift, changing the lattice parameter.

Considering the numerous processing parameters and compositions, it was not possible to establish a direct correlation between the a-lattice parameter and the observed material properties. The largest change in the a-lattice parameter is seen as a function of deposition pressure, where the a-lattice parameter increases with decreasing pressure and there is a subsequent loss in P_r and P_{\max} . While there is a consistent decrease in the P_r and P_{\max} in Figure 4.8, there are also changes in film stoichiometry. It is noted that there are significant changes in properties found in the cases of changing target composition and laser repetition rate where little or no change is seen in the lattice parameter. At 48 mol% excess Pb, P_r and P_{\max} reach a maximum as a function of target composition at a 10 Hz laser repetition rate. With decreasing laser repetition rate to 3 Hz, the P_r and P_{\max} continuously increase, but also become noticeably lossier. At 1 Hz, the P_r and P_{\max} decrease significantly due to increasing amounts of pyrochlore

formation. Furthermore, the decrease in the lattice parameter could be caused by a shift in composition of the perovskite portion of the film, as the pyrochlore phase may not have the same ratio of Bi, Mg and Ti cations as the perovskite phase. This should be explored in future work. Over all variables, shifts in lattice parameters do not form consistent trends with either the film compositions or the film properties likely due to the large number of point defects and complex nature of the defect chemistry present in the films.

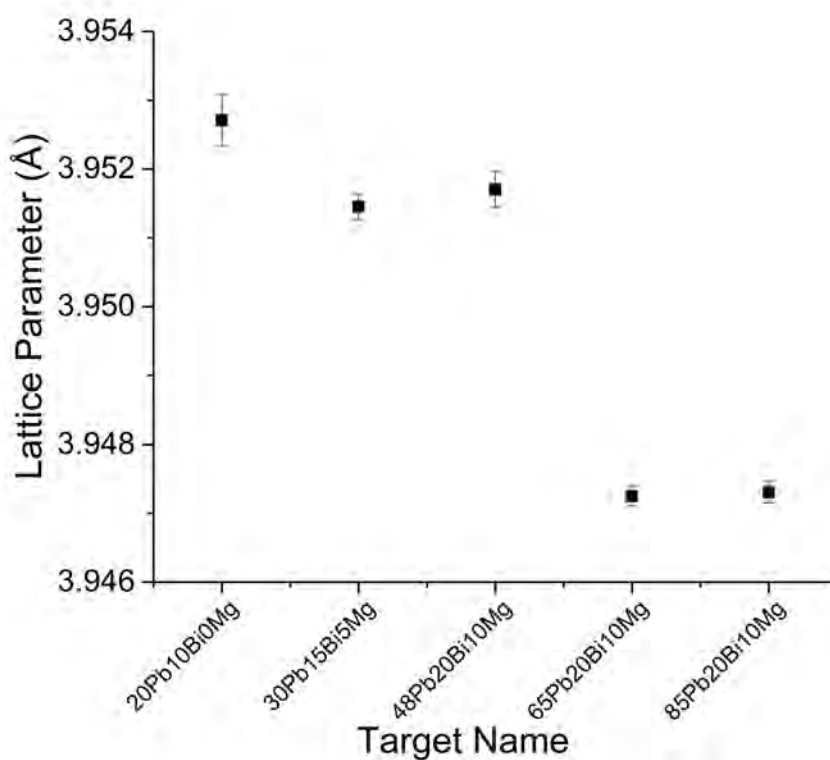


Figure C.2 – Estimated a-lattice parameter for 35BiMT-65PT thin films on 16 nm 5 mol% La-doped PbTiO_3 seed layers deposited as a function of target composition. All 200 peaks were fitted using a Pearson VII function.

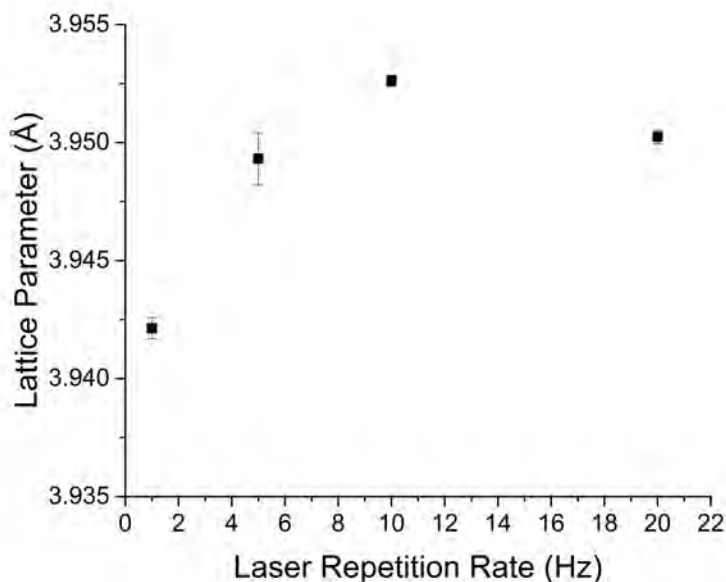


Figure C.3 - Estimated a-lattice parameter for 35BiMT-65PT thin films on 16 nm 5 mol% La-doped PbTiO₃ seed layers deposited as a function of the laser repetition rate. All (200) peaks were fitted using a Pearson VII function.

Figures C.4 and C.5 show the estimated a-lattice parameters for seedless 35 BiMT-65PT thin films deposited as a function of target composition and as a function of O₂/Ar concentration. Figure C.4 shows a more consistent decreasing lattice parameter trend with increasing Pb concentration, and the range of lattice parameters is slightly larger than that of Figure C.2. However, there is not a consistent trend between the a-lattice parameter and the properties that are measured. From Figure 6.5 (b) and (c), the 20 and 30 mol% excess Pb deposited films show large amounts of charge injection, while the PUND measurements show no change in P_r from 48 mol% to 85 mol% excess Pb. The 1 kHz hysteresis measurements in Figure 6.5 (a) and (b) do not show a consistent change in P_r and P_{max} for films between 48 mol% excess to 85 mol% excess Pb. Thus, no correlation is seen between the observed a-lattice parameter and the properties. Figure C.5 also shows that the lattice parameter varies little with changing background gas atmosphere from oxygen to argon. The film deposited at 100% O₂ does show a small decrease of 0.005 Å in the lattice parameter relative to nominally equivalent film data in Figures C.1-C.4 for films deposited at 340 mTorr in an ozone/oxygen mixture. Further experiments would need to be

conducted to assess if this is a sample to sample variation, or a function of the gas composition during growth.

As a function of oxygen-argon concentration, P_r , P_{max} and charge injection all decrease as seen in Figures 6.10-6.12. As such, no correlation exists between the a-lattice parameter and the observed material properties. This provides further evidence that the a-lattice parameter expansions in Figure C.1 are not directly correlated with film properties and stoichiometry changes observed in Chapter 4. It is possible the complex nature of the defect chemistry and /or the large Pb deficiency limit the observable changes in lattice parameter.

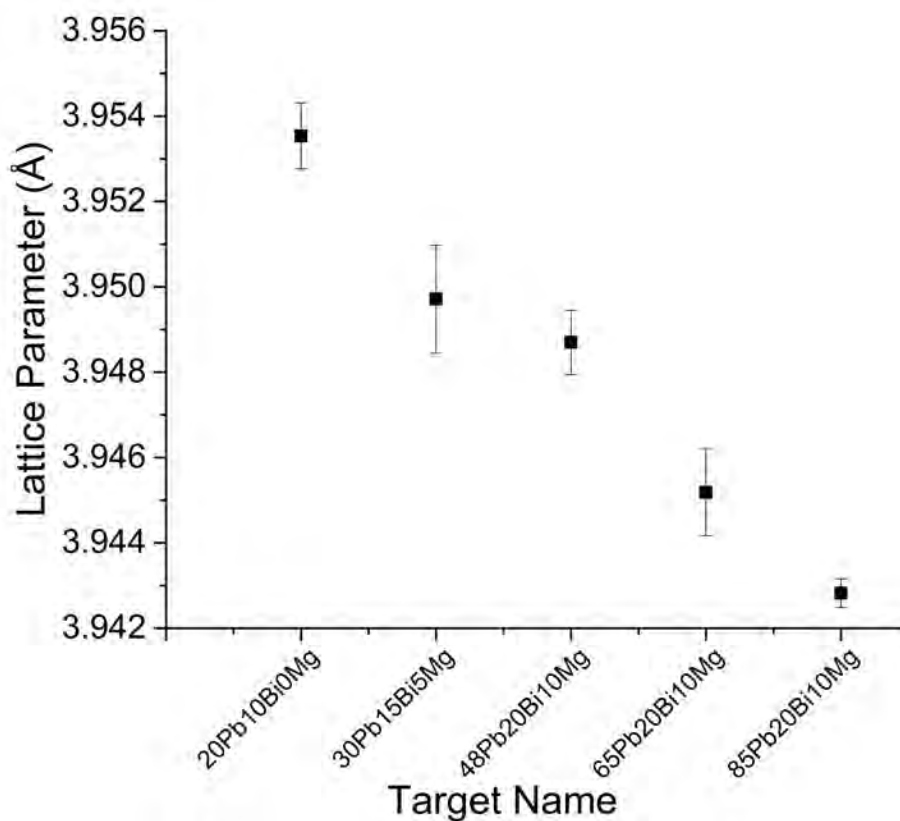


Figure C.4 - Estimated a-lattice parameter for seedless 35BiMT-65PT thin deposited as a function of target composition from figure 6.2. All (200) peaks were fitted using a Pearson VII function.

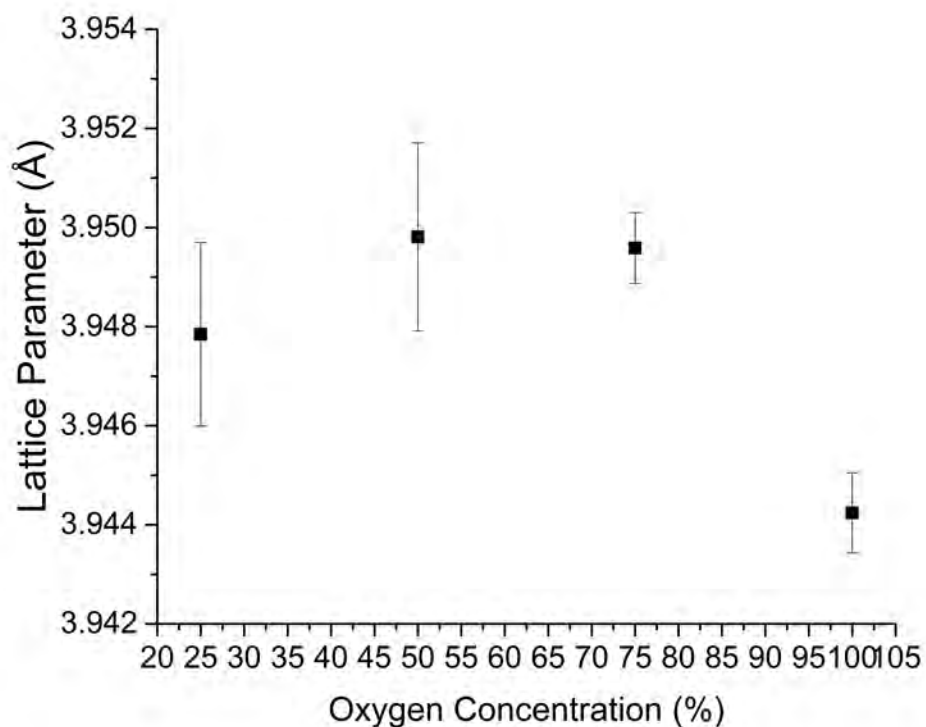


Figure C.5 - Estimated a-lattice parameter of 35 BiMT-65PT thin films deposited as a function of Oxygen/Argon concentration from figure 6.4(a). A Pearson VII function could not be used to fit all films as the peaks became more distorted at decreasing oxygen concentrations. An asymmetric Pearson VII function was used for all (200) peaks.

References

- ¹ J.-P. Maria, S. Trolier-McKinstry, D.G. Schlom, M.E. Hawley, and G.W. Brown, "The Influence of Energetic Bombardment on the Structure and Properties of Epitaxial SrRuO₃ Thin Films Grown by Pulsed Laser Deposition," *J. Appl. Phys.*, 83 [8] 4373 (1998).

VITA

Carl Sebastian Morandi

Carl Morandi was born in Houston, Texas on February 3, 1989. He graduated summa cum laude in Materials Science and Engineering from the University of North Texas in Denton, Texas in 2011.

During his undergraduate career, he obtained research experience under the guidance of Prof. Thomas Scharf, Dr. Richard Reidy, Prof. Srinivasan Srivilliputhur and Dr. Jicheng Du. In 2014, he received his Masters of Science in Materials Science and Engineering under the guidance of Prof. Gary Messing at the Pennsylvania State University. He began working towards his doctorate in Materials Science and Engineering at the Pennsylvania State University in 2014 under the guidance of Prof. Susan Troler-McKinstry. Dr. Morandi received his Ph.D. in winter 2018.